UNIVERSITY OF CALIFORNIA
RIVERSIDE

Vanadium Environmental Chemistry: Adsorption and Oxidation Processes

A Dissertation submitted in partial satisfaction
of the requirements for the degree of

Doctor of Philosophy

in

Environmental Toxicology

by

Macon Jedidiah Abernathy

September 2021

Dissertation Committee:
Dr. Samantha Ying, Chairperson
Dr. Jay Gan
Dr. Haizhou Liu
Dr. Matthew Polizzotto
.

The Dissertation of Macon Jedidiah Abernathy is approved:

_____

_____

_____

_____

Committee Chairperson

University of California, Riverside

ACKNOWLEDGEMENTS

I am lucky to have been able to be inspired and encouraged by many people over the course of my scientific journey whom I count as mentors. To each of you, I owe a debt of gratitude. Without your friendship, kindness, and encouragement I would not be here today writing this. My biggest thanks are for my wife, Catherine Heggie for her unending support and encouragement throughout these last 5 years. Catherine, you've been my rock during this chapter, and I know I couldn't have made it without you. Thanks also to my family, Scott and Jamie Abernathy and my brothers and sisters, Talon, Tanner, Madison and Haley, for their encouragement along the way.

I must thank Dr. Ruth Sofield for investing so much of her time and energy into myself and the rest of her undergraduate students. Not only would I not be in the sciences without her support and guidance, but I certainly would not have made it to graduate school. Ruth, you're an outstanding mentor and I'm so lucky to have wound up in WWU's ETOX program as an undergraduate. I also thank Ed Bain for being such an outstanding graduate student mentor to me during my time in Ruth's lab. Ed, you not only invested in my research abilities through SMoCS, but you made a very practical impact on my life when my work fell through, thank you for that. I also must thank Dr. Daniel Howard-Snyder, my first academic mentor and the one who introduced me to the formal, rigorous systems of thinking and writing that I've relied on throughout graduate school and will continue to rely on going forward. Thank you also to all of the professors and masters students in Western's Philosophy, Chemistry and Environmental Science

departments for your excellent tutelage and for creating an atmosphere that spurred learning, creativity and growth.

My formative years as an undergraduate could not have been spent at a better institution than Western. Many of the people I met during that time have left lasting impacts and have remained close friends. Wyatt, Nathan, Zach, men of the Home and the North Star, thank you for your friendship and the many conversations about philosophy, science, religion, and culture that we've shared over the years.

Sam, you've been an incredible mentor to me during my time at UCR. You stood out from the first lab meeting I attended as someone who really cared about her students as people, as well as scientists. You taught me how to think like a storyteller with my science, how to give compelling talks and write compelling proposals. You introduced me to x-ray spectroscopy, and a whole community of scientists who are also awesome people and fun at parties. You've also given me an incredible amount of freedom in my graduate school path; letting me travel to the Bay area more times than I can count, visit and do work at three separate synchrotron facilities across two countries. Travelling to Germany and participating in the biogeochemistry workshop at the University of Tübingen was hands-down the best experience of graduate school, and it wouldn't have been possible without you. Thank you for letting me pursue a hodge-podge of interests that included a trip to IUPUI for that electrochemistry thing. And crucially, thank you for helping me find ways to pay for a lot of it, and for covering the difference when my proposals came up short. All of the success I've had in graduate school is a direct result

of your mentorship, and I'm so grateful to have stumbled my way into your research group.

To all the current and former members of the Dirty lab, I can't express in words how much your friendship has meant to me over the years. Graduate school is a difficult time for everyone and having you all around to bounce ideas off of, grab coffee with, or just do some good old-fashioned complaint-therapy made it survivable. Claudia, You're an excellent scientist and a great friend. Thank you for your investment in me when I first joined the lab. Seeing as I knew basically nothing about soil, including me on your UCOP project (even if it was just for the electrodes!) meant a lot. Miranda, I can't put into words how much your friendship has meant to me during our time in Sam's lab. You're one of the best people I can think of to be sleep-deprived at the beam with, and you've always been a great person to talk with when the future was looking uncertain. Danielle, your presence has been such a huge gift to the lab. Your upbeat attitude and strong work ethic bring so much to the lab's work environment. Ben, when you reached out to talk about joining Sam's lab for grad school, I was ecstatic. You've got one of the best attitudes and work ethics of anyone I've meant, and you're influence on the lab was immediate and lasting. (Pre-covid) I really appreciated having someone else routinely around the lab and office "after hours" to chat with keep me motivated. BAMS forever. And finally, Mike I learned most of what I know about soil research from you. I was so lucky to have you as our post-doc the first couple years in the lab. You're an excellent teacher, a great mentor and I'm lucky to have you as a friend. Thank you for investing so much into Claudia, Miranda and myself during your time with us, and for still coming out

to the beam and stuff with us after you'd moved on to bigger and better things. Thanks for showing us all the best places to eat around Palo Alto and Saskatoon and making our trips to the beam successful.

I'd also like to thank Taylor Dennis, Yana Lyon, Dylan Riggs, James Bonner, Guy Quanrud, Ting Ting Wu, Connie Mitchell and Colton Vessey for their friendship. Each of you inspired me and helped me become a better scientist, and I'm grateful for your friendship during our time at UCR. Thank you also to all of the beamline scientists at SSRL for making our trips to SLAC successful and for showing us your tricks for better data collection. A special thanks to Matthew Latimer, Erik Nelson and Ryan Davis for their many hours of help and our many insightful conversations.

I'd like to end by thanking UC Riverside for giving me the opportunity do research, and for the many professors who have invested in me through their classes over the years. Thanks also to the Environmental Toxicology Program, and Dr. Wang for funding several years of my work through the NIH T32 grant, and to Sam, the Environmental Science department and UCR's Graduate Division for funding. Thanks also to Dr. Eastmond, Dr. Gan, Dr. Lin and Dr. Gill for their challenging and engaging ETOX courses.

The text in this dissertation is, in part a reprint of the materials as they appear in the following publication:

Chapter 3: Abernathy, M. J.; Schaefer, M. V.; Vessey, C. J.; Liu, H.; Ying, S. C. Oxidation of V(IV) by Birnessite: Kinetics and Surface Complexation. *Environ. Sci. Technol.* **2021**. https://doi.org/10.1021/acs.est.1c02464.

DEDICATION

To Catherine, my perpetual source of encouragement and motivation

And

To my parents, Scott and Jamie Abernathy who have never ceased in their encouragement

ABSTRACT OF THE DISSERTATION

Vanadium Environmental Chemistry: Soil Adsorption and Oxidation Processes

by

Macon Jedidiah Abernathy

Doctor of Philosophy, Graduate Program in Environmental Toxicology
University of California, Riverside, September 2021
Dr. Samantha Ying, Chairperson

Exposure to vanadium (V) results in adverse health outcomes in humans and a plethora of species in the environment across trophic levels. V is released from rock, slag and mine tailings, where it is able to oxidize to vanadate (V^{V}) ($H_nVO_4^{-3+n}$), which poses the greatest risk to human health. Vanadate is highly soluble unlike more reduced V^{III} or V^{IV} species, and is readily taken up by well systems, resulting in human exposure in areas where water treatment is minimal. However, the geochemical controls that determine the mobility of V in the environment are poorly understood, making the behavior of V in the subsurface difficult to predict. This dissertation addresses this knowledge gap by investigating the abiotic reactions of V with common iron and manganese mineral phases. These mineral phases are already known to play an important role in the fate and transport of similar contaminants, but many aspects of their specific reactivity towards V are unknown. To address this knowledge gap, the surface capacity, adsorption affinity and the ability to retain vanadate via surface complexation by iron and managanese oxides is investigated. The vanadate adsorption capacity and surface affinity are both

found to be inversely proportional to the crystallinity of the oxide examined. One manganese oxide, birnessite is also known to promote the oxidation of many trace metal contaminants. The oxidative capacity of birnessite towards V^{IV} is much greater than its surface capacity for V^{V}. At the aggregate scale, birnessite, V and Fe oxides coexist in close spatial proximity where rates of diffusion limit the transport of solutes. In such an environment, birnessite effectively oxidizes V^{IV} and retains more V^{V} than adjacent Fe oxide phases. Further, Fe^{II}-bearing oxides can reduce V^{V} back to V^{IV}. However, this pathway is slow compared to the oxidation rate of V^{IV} by birnessite. This suggests that surface complexation of vanadate, even by birnessite is a greater attenuation pathway than abiotic Fe^{II}-mediated reduction. The result of this research emphasizes the role of abiotic surface processes in constraining the mobility of V within the soil matrix which will improve the reliability of models implemented in the management and reclamation of V contaminated sites.

Table of Contents

List of Tables

List of Figures

Chapter 1: Introduction

I. Adverse Effects of Vanadium Exposure

Vanadium (V) is a d^5 transition metal which is commonly found in the +2, +3, +4 and +5 oxidation states under geologic and surficial conditions.[1] In the +5 oxidation state, V is present as the soluble oxyanion vanadate ($H_nVO_4^{-3+n}$) which is highly mobile and can contaminate groundwater sources used for human consumption.[2–6] Exposure to vanadate has been linked with adverse health outcomes in humans through the inhibition of Na, K and Ca ATPases and phosphotransferase enzymes, the generation of radical oxygen species and alteration of p53 function, among other pathways (Figure 1.1).[7–16] Vanadium contaminated water can also impact agricultural operations including crop quality and yield.[17,18] In response to evidence for its adverse effects in humans, a 50 μg L^{-1} notification limit for V has been established for drinking water by the United States Environmental Protection Agency and California Department of Public.[3,6,19,20] This limit is relatively high compared to what has been established by other governing bodies. California has discussed a 15 μg L^{-1} drinking water limit, although it has not yet been implemented, while North Carolina has established a groundwater standard of 7 μg L^{-1} V. Canada maintains water quality guidelines of 120 μg L^{-1} for freshwater and 5 μg L^{-1} for marine water, and the Netherlands has placed limits a 1.2 μg L^{-1} limit on V in freshwater.[19,21–23]

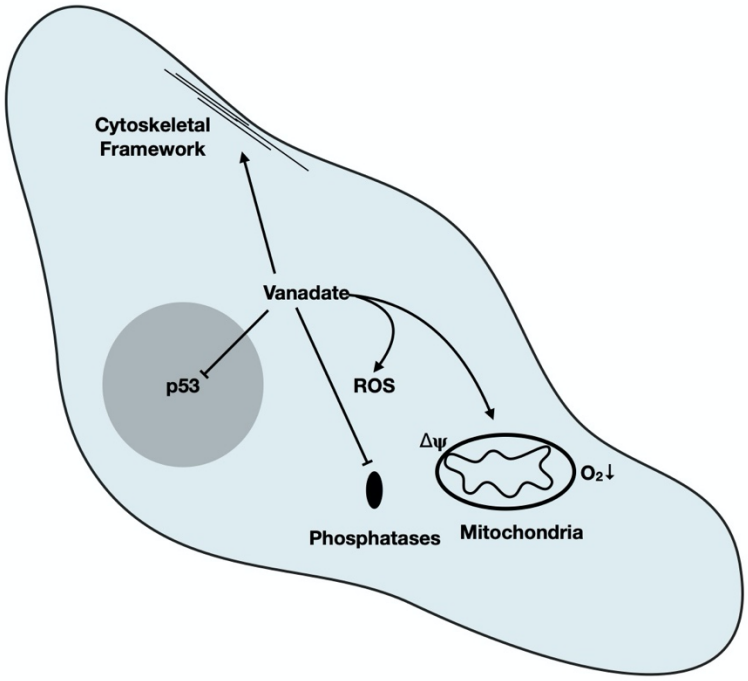

Figure 1.1 Examples of vanadate's effects in a human cell. Interferences with normal cell processes include inhibition of phosphatase enzymes, p53 function, mitochondrial O_2 utilization and membrane polarization stability, Radical Oxygen Species generation, and interreference with the function of the cytoskeleton.[7,9,24,25]

Elevated concentrations of V can negatively impact ecosystem health as a threat to an array of aquatic and terrestrial species. Species sensitivity distributions of aquatic species suggests that concentrations as low as 0.2 μg L^{-1} and 56 μg L^{-1} are hazardous to 5% and 50% of an ecosystem's species (the HC_5 and HC_{50} respectively). Sensitivities vary widely, however, up to 5 orders of magnitude within the same trophic level.[21] Using only aquatic species commonly used in toxicity assay, the acute and chronic toxicity of vanadate ranged from 0.6 – 63 mg L^{-1}. [26,27] Based on these findings, HC_5 values of 640 (acute) and 50 μg L^{-1} (chronic) were determined, indicating disagreement in the literature on the proper water quality benchmark value.

In terrestrial environments, the concentration of V in the soil solution is more important to consider when evaluating toxicological endpoints than the concentration within the mineral matrix.[28,29] At circumneutral pH, soluble V species are made up of predominately vanadate and demonstrate higher degrees of plant bioavailability than less soluble forms.[29] However, overall toxicity of vanadium towards plants is primarily determined by soil chemical processes including immobilization via adsorption.[28] In barley and tomato, EC_{50} ranging from 18-510 mg kg^{-1} were observed when assaying the effects of V^V shoot and root growth. However, when considering only the aqueous V in the soil solution, the measured EC_{50} decreased to 0.8 - 15 mg L^{-1}.[28]

Microbes can acquire energy for growth and other biological processes through V^V respiration.[30,31] However, elevated V concentrations in soils can also alter microbial community structure and function. Larsson et al. found that rates of microbial nitrification and respiration were reduced when V was added to soil to simulate anthropogenic contamination, yielding EC_{50} values as low as 28 mg kg^{-1} and 200 mg kg^{-1} respectively for these processes.[28] Simulating an anerobic groundwater environment, Zhang et al. similarly showed that V exposures as low as 25 ppm reduced microbial diversity and resulted in community succession. Overtime, the establishment of new synergistic relationships between autotrophic and heterotrophic species developed which had not existed prior to V exposure. This shift in community structure resulted in a community that was able to utilize aqueous V^V as a terminal electron acceptor which resulted in attenuation of aqueous V^V.[32,33] Taken together, these studies demonstrate that while V contamination can be detrimental to the native functioning and composition of

microbial communities, they can also adapt to that contamination in ways that lead to the attenuation of aqueous V^V.

II. Vanadium Geochemistry

Prominence in Surface Waters and Soils

The concentration of vanadium in terrestrial and aquatic environments varies widely due to variation in geogenic and anthropogenic sources.[1,34,35] In the absence of anthropogenic sources, reported V concentrations in surface and groundwaters range from 0.0005 – 180 μg L^{-1} .[1,34] In California, median groundwater concentrations are 5 μg L^{-1}, and generally range from less than 3 to 10.3 μg L^{-1} with some areas exceeding 50 μg L^{-1}.[6] Elevated concentrations were typically found in regions where aquifers had developed on mafic, gabbroic, or basaltic material that hosted V-bearing Fe minerals.[6,36] In the Truckee, Carson and Walker Rivers of the Sierra Nevada mountain range, V concentrations of 24 μg L^{-1} have been observed. Higher concentrations of V in these river systems were correlated with the weathering rates of the catchment parent material and aqueous Si.[37,38] These correlations indicate that the derivation of V and Si from siliceous rock occurs with similar efficiency.[37]

Groundwater vanadium concentrations in volcanically active regions, such as Mt. Fuji in Japan, have been studied for over 50 years. It has been shown that elevated groundwater V concentrations (0.1 to 91.4 μg L^{-1}) in aquifers around Mt. Fuji are due to weathering of the Shin-Fuji lavas.[39] Similarly, the volcanism of Mt Etna's in Italy has resulted in V concentrations as high as 182 μg L^{-1} in the drinking water of the

surrounding towns.[4] Similarly high groundwater concentrations have been reported throughout volcanically active regions of Argentina and Chile, ranging from 300 μg L^{-1} to 2.5 mg L^{-1}. [40–42]

Anthropogenic inputs generally increase the porewater vanadium concentration, as well as enrich local V loading in the soil. Mine tailings and blast furnace slag are the primary anthropogenic sources of V into terrestrial and aquatic environments.[35] One of the most notable instances of anthropogenic emission into a terrestrial environment was the breach of the red mud containment facility at the Ajkai Timfoldgyar Zrt Alumina plant in Western Hungary in 2010.[43,44] The red mud, a by-product of the extraction of Al from bauxite, affected approximately 40 km^2 of land and travelled 120 km downstream, carrying V concentrations exceeding 15 mg L^{-1} (963 mg kg^{-1}) and contaminating the Torna creek before reaching the Danube river.[44,45] Similarly, the 2014 Mount Polley mine tailings spill in British Columbia, Canada released material containing upwards of 295 mg kg^{-1} V into a catchment with soils initially containing only 40-33 mg kg^{-1} V.[46] As a result of this massive input, dissolved V in the surface water increased from 1 μg L^{-1} to 9 μg L^{-1}, while pore water reached concentrations as high as 1200 μg L^{-1}. The primary source of V in the tailings were identified as V-bearing magnetite and titanite containing approximately 0.25% w/w V. This study was critical to our understanding of V geochemical cycling between parent-minerals and the aqueous phase by establishing the direct connection between mineral grain weathering and elevated aqueous levels.[46] Comparable studies have demonstrated the leaching of V from steel slag and petroleum cokes.[47–49]

Vanadium Fate and Transport

Iron and Al-bearing mineral phases frequently contain isomorphic substitutions of V^{III} in nature, occasionally with small amounts of V^{IV} or V^{II}.[35,50–53] In secondary minerals such as goethite, hematite, and kaolinite, V can substitute for Fe and Al as V^{III} and V^{IV} respectively.[54–56] This phenomenon occurs in part because of the ease with which both V^{III} and Fe^{III} can form diaspore-like and spinel-type oxide structures.[52,55,57,58] As a result, V-substituted Fe oxides contribute to the fate and transport of V in Fe oxide-rich subsurface environments.[58] In igneous silicate formations, V is associated with silicate minerals, although which ones and in which ways has yet to be described.[37] Vanadium substitutes into a variety of other minerals as well, including: titanomagnetite,[46,59] roscoelite,[60] sepiolite[61] and gibbsite.[54] Likewise, the weathering of titanite to beidellite and anatase can release V under pH-neutral conditions.[46] Using magnetite as an example, it was shown that the release from V-substituted magnetite is a surface-controlled dissolution reaction capable of occurring at circumneutral pH and under dissolved oxygen conditions between 5% and 80% saturation.[62] It was also shown that millimolar concentrations of common ions such as Na, Ca, Mg, K, NO_3, Cl, SO_4 and CO_3 promoted the release of substituted V.[62]

Once released into the environment via weathering, the fate of V is dependent on pH, redox conditions, adjacent mineral phases and the presence of organic matter. Like many other aqueous transition metal species, reduced forms of V are stabilized against oxidation at low pH.[63] Considering aqueous V^{IV}, the oxidation half-life of the $V^{IV}OOH$ cation by dissolved O_2 at neutral pH increases from less than an hour to more than a year

when the pH is lowered below 6 and $V^{IV}O^{2+}$ becomes the dominant V^{IV} aqueous species.[63] Under reducing conditions, the +3 and +4 states of vanadium are predominant, with V^{III} susceptible to forming insoluble $V(OH)_{3(s)}$ at pH > 6.9.[64] The solubility of V^{IV} is also low at neutral pH, and its aqueous concentration is limited by the formation of V^{IV} oxyhydroxides.[1,65] One such oxyhydroxide, häggite ($V_2O_3(OH)_2$), has been observed in aquifers in the central United States[66] and was recreated in the experiments described below.

The presence of organic matter can stabilize V^{IV} against oxidation, even under moderately oxidizing conditions.[64,67] This results in V^{IV} being the primary form of V in acidic, organic-rich soil layers as would be encountered in the O horizon of pine forests, and in peat bogs.[1,68] Larsson et al. demonstrated that the oxidation state of vanadium once in a soil is independent of its oxidation state upon entering the soil solution. Thus, the observed oxidation state of V in soil reflects the soil's characteristics, such as organic matter content, redox potential and pH.[68,69] They found that the primary mechanisms for effecting this change in oxidation state are rapid and catalyzed by surface reactions, as predicted by Wehrli et al. 1989.[70]

Under oxic conditions V^{V} is the dominant oxidation state, present as the highly soluble oxyanion vanadate at pH's > 3.6, below which it forms the oxycation VO_2^+.[71] Under most environmental conditions (circumneutral pH, average global concentration of dissolved V = 0.71 μg L^{-1}) [72] $H_2VO_4^-$ is the dominant aqueous form of vanadate, with trace amounts of HVO_4^{2-} also present. Like Mo or W, V^{V} will undergo polymerization and condensation reactions with itself. This results the formation of dimers ($H_nV_2O_7^{4-n-}$),

trimers ($V_3O_{10}^{5-}$), tetramers ($H_nV_4O_{13}^{6-n-}$, $V_4O_{12}^{4-}$), pentamers ($V_5O_{15}^{5-}$), hexamers ($V_6O_{18}^{6-}$) and decamers ($H_nV_{10}O_{28}^{6-n-}$) depending on concentration and pH (Figure 1.2).[71,73,74] In environments with an abundance of humic substances and pH below 6, V^V can be reduced to organic matter stabilized V^{IV}.[67] Oxalic acid is one example of a simple organic acid that reduce V^V to V^{IV} and is leveraged by some species of saprotrophic fungi to dissolved V^V bearing minerals.[75,76]

Vanadate is strongly retained by many soil mineral phases through the formation of inner sphere complexes.[54,77–80] Aging and long-term studies of V amendments in various soil types suggest that overtime, V solubility, mobility, bioavailability and toxicity will decrease, primarily due to reduction of V^V to V^{IV}, complexation of V^V by organic matter and adsorption of $V^{V/IV}$ by soil mineral phases.[29,59,68,69] The low mobility of V in the soil column has likened comparisons to the comparably immobile Pb,[35] with the binding strength of VO^{2+} to metal oxide sorbents directly comparable to Pb^{2+}.[1]

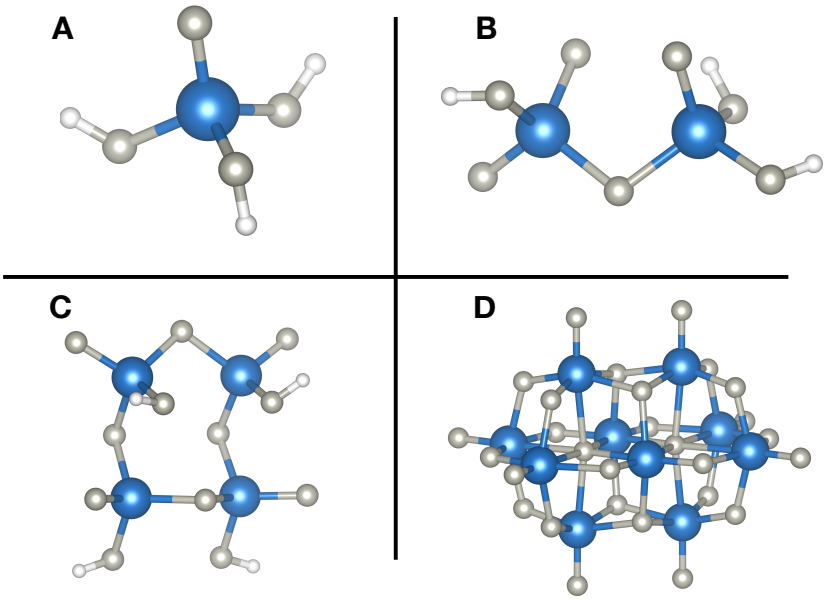

Figure 1.2 Polymers of vanadate. A) Orthovanadate (commonly "vanadate"). B) Pyrovanadate. C) Tetravanadate. D) Decavanadate. Vanadium is in blue, oxygen is light grey and hydrogen is white.

III. The Role of Manganese Oxides in Contaminant Attenuation

Manganese(IV) oxides are ubiquitous oxidants found in soils and sediments that act as scavengers of metal(loid)s in the environment (Figure 1.3, 1.4).[81–93] In soils and sediments, Mn^{II}-oxidizing fungi and bacteria catalyze the formation of layered, poorly crystalline Mn oxides resemble hexagonal birnessite in structure and reactivity.[92–99] When birnessite is reduced by trace metal(loid)s, stoichiometric ratios of Mn^{II} are produced.[81,100–102] Back reaction of the Mn^{II} and birnessite results in surface-passivation and the formation of new Mn^{III} oxyhydroxide phases.[81,88,103] The development of these new phases resulting from Mn^{II}-Mn^{IV} comproportionation can manifest as symmetry changes (e.g. the hexagonal to triclinic conversion of birnessite)[104] or the systematic development of new mineral phases like hausmannite, feiknechtite or manganite.[105,106]

Ions such as Ni and Zn can competitively substitute for Mn within Mn oxide minerals, but VO_3^- substitution has not been observed in nature, although it has been shown to alter the electrochemical properties of birnessite.[85,107,108] Manganese oxides, and in particular layered Mn oxides such as vernadite, birnessite and buserite[99] are of particular interest for their potential to react with V at redox interfaces. These interfaces are produced by redox fluctuations that occur through processes such groundwater withdrawal and recharge, or as a function of soil structure.[109–115] Manganese oxides have been observed at these interfaces, and can form in proximity to reduced forms of trace metal contaminants.[87,96,116]

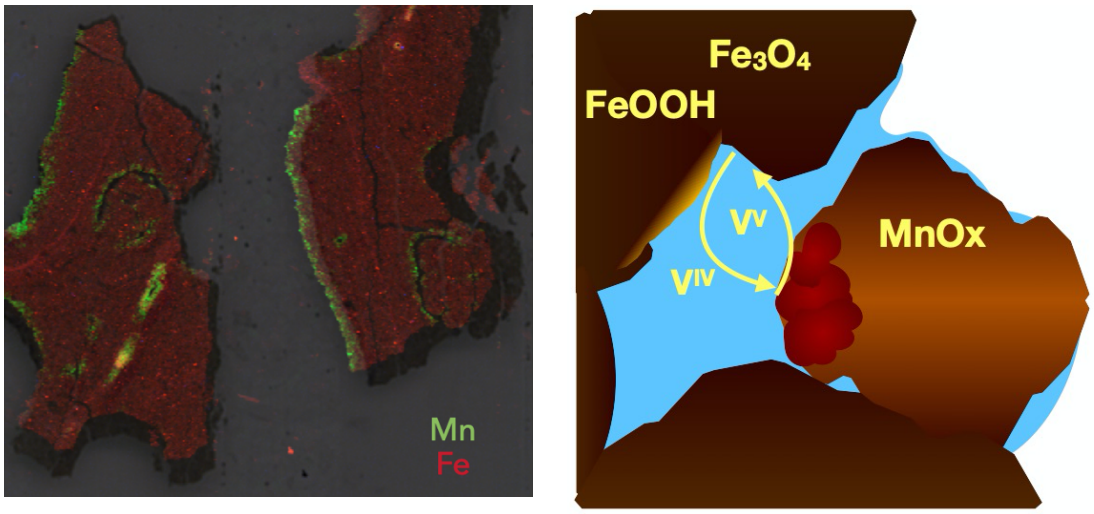

Figure 1.3 Left) A synchrotron μXRF image showing the distribution of Fe and Mn in a soil aggregate thin section. Data and image courtesy of Dr. Sam Ying. Right) Schematic of V cycling along a diffusion and redox gradient in an aggregate containing Mn and Fe oxides.

In California, birnessite and other Mn oxide phases have been observed throughout the state, either directly or inferred from their reduction to aqueous Mn^{II}.[117–120] These include locations where reduced contaminants such as Cr^{III} have been observed

[118,119,121] as well as locations that have elevated levels of V present in the groundwater and sediments.[3,6,117] The colocation of V and Mn at these redox interfaces indicates areas where V is likely to have enhanced mobility due to the oxidative interactions with Mn oxides. [3,6] While no studies of V^{V} or V^{IV} on Mn oxides has been done in the context of environmental applications, Yin et al. examined how birnessite synthesized with various degrees of V doping would affect the oxide's ability to scavenge metal cation contaminants.[122] They found that Pb^{2+} scavenging was enhanced in the doped birnessite and cited spectroscopic evidence to support the formation of an $Mn^{IV}O_6$-$V^{V}O_4$-Pb^{II} oxyanion bridge. They attribute this to a surface coating of hexameric vanadate polymers ($V_6O_{16}^{2-}$), yielding possible V-Mn distances of 2.97-3.06 and 3.43-3.5 Å.[122] While this is a great start to understanding the interactions of V with Mn oxides, much work is still needed to understand the processes of surface complexation that are occurring in the environment.

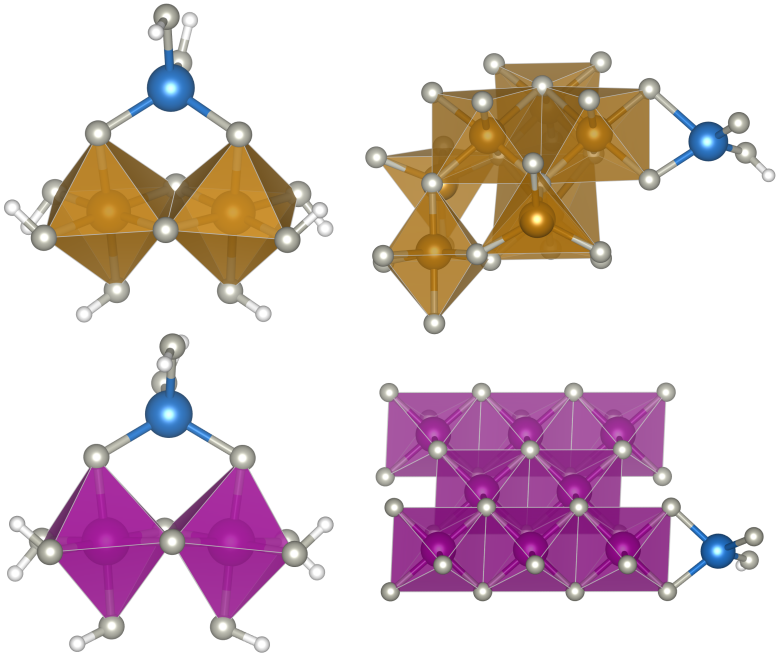

Figure 1.4 Adsorption modes of vanadate onto Fe and Mn oxides.

IV. The Role of Iron Oxides in Contaminant Attenuation

The role of Fe oxides in contaminant retention and transformation has been the subject of extensive study.[123] Iron oxides such as hematite, goethite and ferrihydrite are effective sorbents for contaminants such as As,[124–128] Sr,[129] Cr,[130] Ni,[130] U,[131–133] Cd,[134] Zn,[134] and Pb[134] as well as a variety of organic compounds.[135–140] In soils throughout California, Fe has been directly implicated in the retention and release of As[141–143] and U.[144] Iron (hydr)oxide phases have been implicated in controlling the abundance of vanadium in a variety of environments, including seawater,[145,146] tropical soils,[54] austral soils,[147] and temperate and boreal soils.[17,148–151]

Figure 1.5 A small erosion cut along a hillside on Tiger Mountain near Issaquah, Washington taken at the end of a summer drought. Top left) The extent of the groundwater is seen in the contrast of light and dark soil near the yellow arrow. Top Right) The direction of groundwater exfiltration is denoted by the blue arrow. The red circle denotes an area of pooling and Fe oxidation. Bottom right) A close-up of that same Fe oxidation pool, show casing the formation of ferrihydrite from Fe^{II} weathered out of the surrounding soil minerals. Bottom left) The same Fe oxide pool and an adjacent exfiltration site containing a dark material. Whether this material is algae, organic matter, Fe oxides or some combination is unknown.

Only a few spectroscopic and modelling studies have interrogated the molecular and kinetic associations of V with Fe oxides (Figure 1.4). They have focused predominately on goethite and ferrihydrite due to their ubiquity (Figures 1.3, 1.5). Spectroscopic evidence in these studies reveals that vanadate predominately forms bidentate corner-sharing complexes on goethite,[79] bidentate edge-sharing complexes on 2-line ferrihydrite.[77,78] The difference in these two adsorption modes is likely due to the difference in Fe-OH abundance at the major truncating faces of these minerals (Figure

1.4).[1] However, these studies demonstrates that vanadate has a broad sorption envelope on both ferrihydrite and goethite between pH 3 and 10, making it one of the most strongly adsorbing oxyanions on Fe^{III}.[1,79,152] Recently, Vessey and Lindsay explored the adsorption of vanadate onto ferrihydrite and hematite, providing the first spectroscopic evidence of polyvanadate adsorption.[153] This was soon followed by a study examining the kinetics of adsorption and subsequent reduction of vanadate by Fe^{II} bearing compounds.[77] They demonstrated that Fe^{II}-bearing iron oxides reduced vanadate through a surface-mediated electron transfer mechanism, a process theorized about previously[154] that results in retention and in some cases, structural incorporation of V^{IV} into the Fe oxide matrix. Despite these studies, however much work is still to be done to describe the interactions of V with other Fe oxides, particularly in the realms of sorption affinity and surface capacity.

V. Measurement Techniques for V in Environmental Samples

X-ray absorption spectroscopy (XAS) encompasses a wide array of analytical techniques that typically rely on the high energy-resolution and photon flux offered by synchrotron facilities that allows the user to obtain detailed geometric and electronic information about specific elements in heterogenous samples, even at low concentrations.[155,156] Common methods, such as extended x-ray absorption fine structure spectroscopy (EXAFS) and x-ray absorption near edge structure spectroscopy (XANES) are typically non-destructive for samples, and do not require significant alteration of the sample to be analyzed. These traits make XAS techniques very well suited to the study of environmental samples regardless of the matrix (soil, sediment, slurry, mineral, etc).[157]

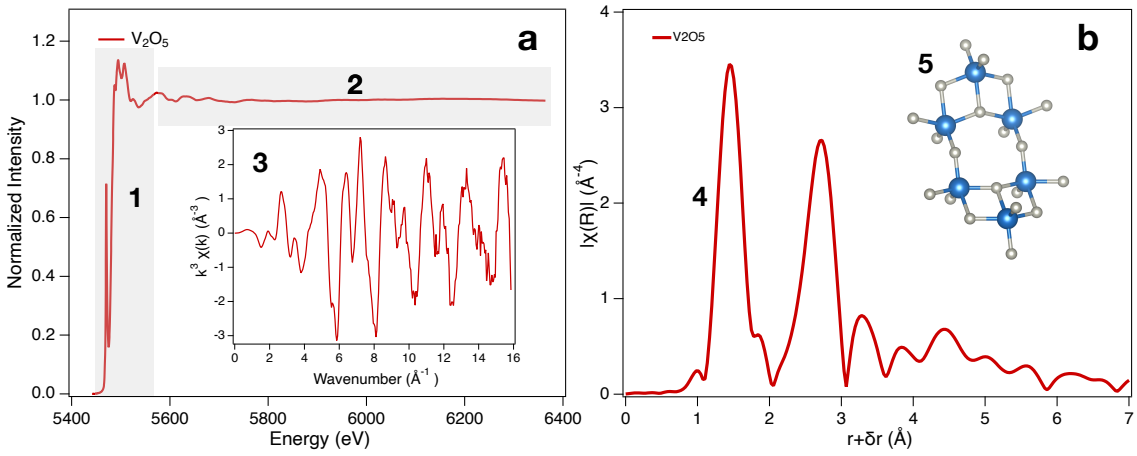

Figure 1.6 a,b) The XAS spectrum of V_2O_5 collected in transmission mode. 1) The XANES region. 2) The EXAFS region in energy-space. 3) k^3 weighted $\chi(k)$ spectrum inset showing the magnitude of the EXAFS oscillations obtained by transforming plot 2 into k-space. 4) The pseudo radial structure function plot obtained by taking the Fourier transform of plot 3. 5) the structure of V_2O_5 obtained from plot 4.

EXAFS and XANES are closely related techniques that are both obtainable from the same spectrum for a given element and sample (Figure 1.6). Although different

underlying processes give rise to the phenomena observed in each region, they both occur as a result of photoelectron scattering. Briefly, the XANES and EXAFS phenomena occur as a core electron in the 1s shell absorbs an incident x-ray of equal or greater energy to the energy that binds the electron to the nucleus, exciting it to the point of ejection from the absorbing atom. The primary difference in the two techniques is one of energy. At lower energies characteristic of the XANES region, the photoelectron is promoted from the 1s shell to holes in higher-energy orbitals. For the Vanadium K-edge, these include the 1s → 3d, 1s → 4p shakedown, 1s → $4p_z$ and 1s → $4p_{xy}$ transitions (Figure 1.7),[1] with higher V oxidation states having greater 1s → 3d intensity due to increased vanadium *p-d* orbital mixing (Figure 1.7, 1.8).[158] When the incident photon energy is high enough (but still within the XANES region), the photoelectron is ejected from the parent atom altogether, albeit with a low momentum. This low momentum subjects the photoelectron to a truly astounding number of scattering events with neighboring atoms which make the XANES computationally intensive to model.[159,160] As the energy of the incident photon is increased, the momentum of the ejected photoelectron also increases. This results in a predominance of single-scattering events, and a much narrower subset of multiple-scattering events, which make it much more feasible to model.[155,156] The information obtainable by XANES and EXAFS are constrained to short-range information about the absorbing atom and its neighbors due to limitations on the ejected photoelectron's mean-free path (< 10 Å, although typically < 6 Å from the absorbing atom is more common).[155–157]

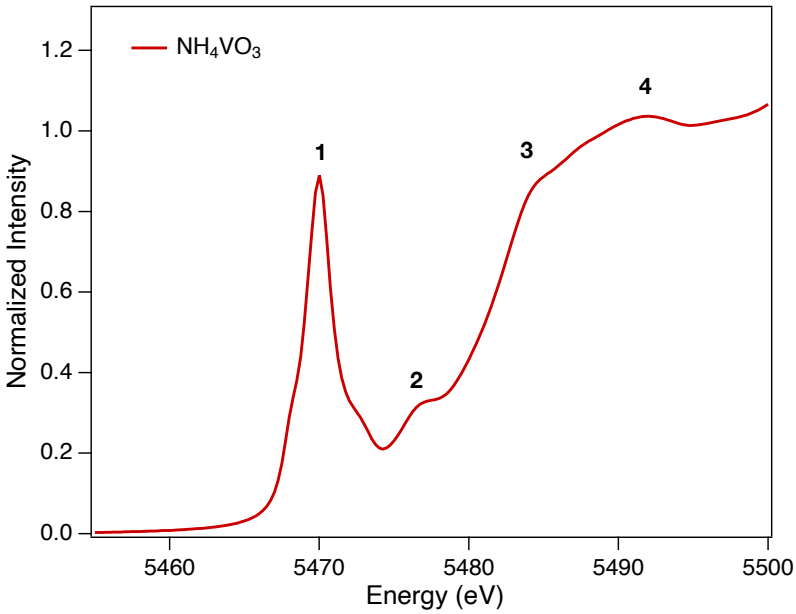

Figure 1.7 Electronic transitions that contribute to the V XANES spectra. 1) 1s → 3d. 2) 1s → 4p shakedown. 3) 1s → $4p_z$. 4) 1s → $4p_{xy}$. The Shoulders on the pre-edge feature (1s → 3d) are contributions from quadrupolar transitions.

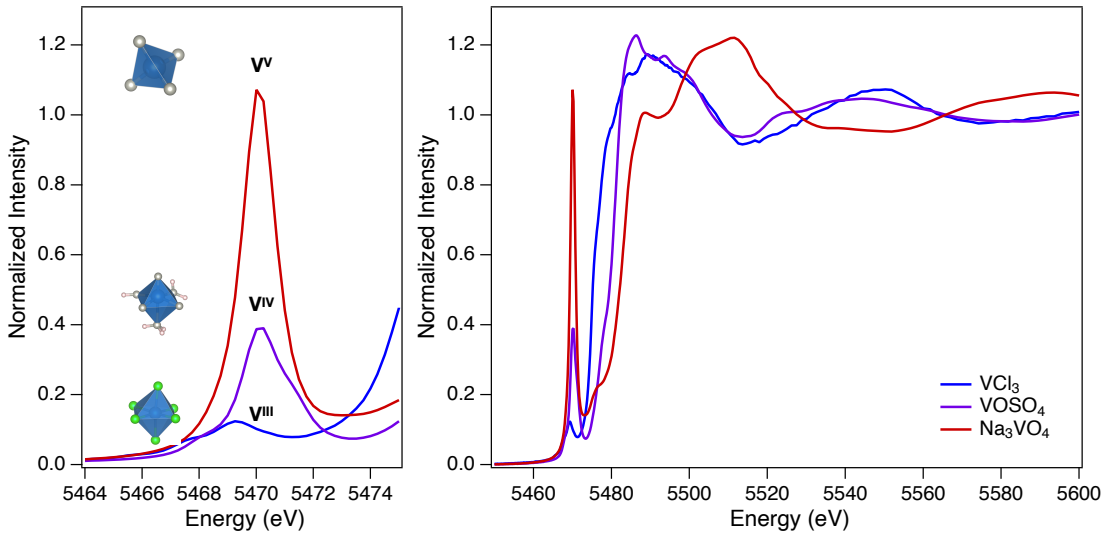

Figure 1.8 Left) The pre-edge feature of V across 3 oxidation states (+3, +4 and +5). Geometries of the corresponding V species are shown as polyhedral. Note that the increase in the pre-edge feature intensity tracks with a loss of centrosymmetry in the V compounds. Right) The full XANES spectra for V^{III}, V^{IV} and V^{V} reference compounds

(VCl_3, $VOSO_4$•$5H_2O$ and Na_3VO_4 respectively). Note the rightward shift of the edge with increasing oxidation state.

The information obtainable from XANES and EXAFS include average oxidation state, coordination environment/geometry, bond lengths, information on the nearest neighbors, mean disorder, degeneracy, asymmetry in distance distributions (3rd cumulant) and the deviation from a gaussian distribution of the distances to neighboring atoms in a given shell (4th cumulant). In the environmental sciences, XANES has typically been used for oxidation state determination[161] (Figure 1.8), while EXAFS has been utilized for determining bond lengths, coordination, and sorption geometry, among other endpoints.[79,156,162–166] However, this soon may change with the ongoing development of full-multiple scattering theory which will allow a recovery of the local geometry from just the XANES region.[167–169] At the moment however, XANES is particularly useful for instances where the element of interest is present in low concentrations (such as trace metal contamination) due to its high signal to noise ratio.[54,82,84,87,96,102,144,170] EXAFS has proven incredibly useful for determining adsorption behavior, monitoring the formation of new mineral phases, and deconvoluting the interactions of metal oxides.[91,129,163,171–173]

EXAFS can be quite difficult to analyze .[164] Part of this problem is the high number of scattering contributions that have the potential to contribute to the $\chi(k)$ signal (Figure 1.6 plot 3), relative to the limited number of independent points contained in any one spectrum (Ravel 2009).[174] Generally, each scattering contribution, or path requires five variables to model using the EXAFS equation. In practice, as implemented in the programs Artemis or Larch, these variables are:

CN - coordination number (path degeneracy)

S_0^2 – Passive electron (amplitude) reduction factor

ΔE – difference between reference energy of the data and theory

ΔR – change in the half-path length relative to a defined path

σ^2 – pseudo Debye-Waller factor

Common constraints on these parameters are available in Scott Calvin's EXAFS for Everyone (2013).[155] Constraints are necessary due considering five variables per path and a maximum information content of most EXAFS spectra of < 20 independent points. The information content of EXAFS is calculated according to the following equation:

$$N_{idp} = \frac{2(k_{max} - k_{min})(R_{max} - R_{min})}{\pi}$$

Where $k_{max} - k_{min}$ is the range of the data in k-space (χ(k)) and $R_{max} - R_{min}$ is the range of the Fourier-transform of the data used in a given fit of paths to the data (Figure 1.6, plots 3 and 4). Likewise, the spatial resolution of EXAFS in distinguishing different backscattering atoms from one another is given by:

$$\Delta R = \frac{\pi}{2(k_{max} - k_{min})}$$

This is all relevant to the study of V using EXAFS, as V spectra are rarely obtained past 11-12 $Å^{-1}$ in χ(k) space in environmental studies.[77–79,122] This inherently limits the information content obtainable from such spectra and may result in data that are over-fit. A common reason for this is the presence of glitches in the Si(111) crystals often used for energy selection by monochromators at tender-x-ray beamlines that are capable of doing V K-edge EXAFS. Alternatively, several elements have competing edges that

can interrupt V EXAFS if present. One such element is the barium L_2-edge at 5624 eV, which is only 159 eV away from the V K-edge at 5465 eV and is a common contaminant. Both obstacles have been encountered in the literature,[1,77] as well as in the course of collecting the data presented in this document.

For more information, the reader is referred to the works of S. Calvin (Sarah Lawrence College), J.J. Rehr (U. Washington), B. Ravel (NIST, NSLS-II), M. Newville (U. Chicago) and S. Kelly (UOP LLC) for further information.[155,156,159,175–177] As of this writing, additional material is available on Matt Newville's YouTube channel (https://www.youtube.com/user/mattnewville) as well as from Bruce Ravel's Summer school at the Diamond Lightsource (https://www.youtube.com/watch?v=8jjGXYvTzpA&list=PLyzX_pouV65vbohf_puwlg9fGNjJGpKpd) and in Matt Siebecker's fitting tutorial from his time at the University of Delaware (https://www.youtube.com/watch?v=Il_wRqhqFM4&list=PLynzdDBtjYa_6KWzRlzwB8pWQqYo9hBTp) .

VI. Research Objectives

The overarching goal of the research presented in this dissertation is to characterize a subset of the most important geochemical processes that are expected to govern the mobility of V in the subsurface by examining the interactions of V^{V} and V^{IV} with ubiquitous Fe and Mn oxides. The specific objectives are as follows:

1. To understand the affinity and capacity of common Fe and Mn oxide minerals to attenuate aqueous vanadate contamination via surface complexation pathways.

2. To understand the mechanism of and extent to which a common Mn oxide, birnessite promotes the oxidation of V^{IV} and mobility of V^{V}.
3. To understand the influence of diffusion-limited transport on the oxidation, reduction, and competitive retention of V between Mn and Fe oxides.

VII. References

(1) Gustafsson, J. P. Vanadium Geochemistry in the Biogeosphere –Speciation, Solid-Solution Interactions, and Ecotoxicity. *Appl. Geochem.* **2019**, *102*, 1–25. https://doi.org/10.1016/j.apgeochem.2018.12.027.

(2) Brima, E. I. Physicochemical Properties and the Concentration of Anions, Major and Trace Elements in Groundwater, Treated Drinking Water and Bottled Drinking Water in Najran Area, KSA. *Appl. Water Sci.* **2017**, *7* (1), 401–410. https://doi.org/10.1007/s13201-014-0255-x.

(3) Wright, M. T.; Stollenwerk, K. G.; Belitz, K. Assessing the Solubility Controls on Vanadium in Groundwater, Northeastern San Joaquin Valley, CA. *Appl. Geochem.* **2014**, *48*, 41–52. https://doi.org/10.1016/j.apgeochem.2014.06.025.

(4) Arena, G.; Copat, C.; Dimartino, A.; Grasso, A.; Fallico, R.; Sciacca, S.; Fiore, M.; Ferrante, M. Determination of Total Vanadium and Vanadium(V) in Groundwater from Mt. Etna and Estimate of Daily Intake of Vanadium(V) through Drinking Water. *J. Water Health* **2015**, *13* (2), 522–530. https://doi.org/10.2166/wh.2014.209.

(5) Gerke, T. L.; Scheckel, K. G.; Maynard, J. B. Speciation and Distribution of Vanadium in Drinking Water Iron Pipe Corrosion By-Products. *Sci. Total Environ.* **2010**, *408* (23), 5845–5853. https://doi.org/10.1016/j.scitotenv.2010.08.036.

(6) Wright, M. T.; Belitz, K. Factors Controlling the Regional Distribution of Vanadium in Groundwater. *Ground Water* **2010**, *48* (4), 515–525. https://doi.org/10.1111/j.1745-6584.2009.00666.x.

(7) Aureliano, M.; Crans, D. C. Decavanadate (V10O286-) and Oxovanadates: Oxometalates with Many Biological Activities. *J. Inorg. Biochem.* **2009**, *103* (4), 536–546. https://doi.org/10.1016/j.jinorgbio.2008.11.010.

(8) Capella, L. S.; Gefé, M. R.; Silva, E. F.; Affonso-Mitidieri, O.; Lopes, A. G.; Rumjanek, V. M.; Capella, M. A. M. Mechanisms of Vanadate-Induced Cellular Toxicity: Role of Cellular Glutathione and NADPH. *Arch. Biochem. Biophys.* **2002**, *406* (1), 65–72. https://doi.org/10.1016/S0003-9861(02)00408-3.

(9) Capella, M. A. M.; Capella, L. S.; Valente, R. C.; Gefé, M.; Lopes, A. G. Vanadate-Induced Cell Death Is Dissociated from H2O2 Generation. *Cell Biol. Toxicol.* **2007**, *23* (6), 413–420. https://doi.org/10.1007/s10565-007-9003-4.

(10) Goodno, C. C. Inhibition of Myosin ATPase by Vanadate Ion. *Proc. Natl. Acad. Sci.* **1979**, *76* (6), 2620–2624. https://doi.org/10.1073/pnas.76.6.2620.

(11) Huang, C.; Zhang, Z.; Ding, M.; Li, J.; Ye, J.; Leonard, S. S.; Shen, H.-M.; Butterworth, L.; Lu, Y.; Costa, M.; Rojanasakul, Y.; Castranova, V.; Vallyathan, V.; Shi, X. Vanadate Induces P53 Transactivation through Hydrogen Peroxide and Causes Apoptosis. *J. Biol. Chem.* **2000**, *275* (42), 32516–32522. https://doi.org/10.1074/jbc.M005366200.

(12) Costa Pessoa, J.; Garribba, E.; Santos, M. F. A.; Santos-Silva, T. Vanadium and Proteins: Uptake, Transport, Structure, Activity and Function. *Coord. Chem. Rev.* **2015**, *301–302*, 49–86. https://doi.org/10.1016/j.ccr.2015.03.016.

(13) Rehder, D. Biological and Medicinal Aspects of Vanadium. *Inorg. Chem. Commun.* **2003**, *6* (5), 604–617. https://doi.org/10.1016/S1387-7003(03)00050-9.

(14) Srivastava, A. K. Anti-Diabetic and Toxic Effects of Vanadium Compounds. *Mol. Cell. Biochem.* **2000**, *206* (1), 177–182. https://doi.org/10.1023/A:1007075204494.

(15) Wang, J.; Huang, X.; Zhang, K.; Mao, X.; Ding, X.; Zeng, Q.; Bai, S.; Xuan, Y.; Peng, H. Vanadate Oxidative and Apoptotic Effects Are Mediated by the MAPK-Nrf2 Pathway in Layer Oviduct Magnum Epithelial Cells. *Metallomics* **2017**, *9* (11), 1562–1575. https://doi.org/10.1039/C7MT00191F.

(16) Yu, Y.; Yang, J. Oral Bioaccessibility and Health Risk Assessment of Vanadium(IV) and Vanadium(V) in a Vanadium Titanomagnetite Mining Region by a Whole Digestive System in-Vitro Method (WDSM). *Chemosphere* **2019**, *215*, 294–304. https://doi.org/10.1016/j.chemosphere.2018.10.042.

(17) Martin, H. W.; Kaplan, D. I. Temporal Changes in Cadmium, Thallium, and Vanadium Mobility in Soil and Phytoavailability under Field Conditions. *Water. Air. Soil Pollut.* **1998**, *101* (1), 399–410. https://doi.org/10.1023/A:1004906313547.

(18) Singh, B. B. Effect of Vanadium on the Growth, Yield and Chemical Composition of Maize (Zea Mays L.). *Plant Soil* **1971**, *34* (1), 209–213. https://doi.org/10.1007/BF01372773.

(19) Howd, R. palvanadium.pdf https://oehha.ca.gov/media/downloads/water/chemicals/nl/palvanadium.pdf (accessed 2019 -02 -15).

(20) Tabri, A.; Daunt, P.; Zwayer, B. *Health Effects Assessinent Sumtnary Tables FY-1997 UPDATE*; 1997.

(21) Smit, C. Environmental Risk Limits for Vanadium in Water : A Proposal for Water Quality Standards in Accordance with the Water Framework Directive. *Milieurisicogrenzen voor vanadium : Een voorstel voor waterkwaliteitsnormen volgens de Kaderrichtlijn water* **2012**.

(22) *Amendments to 15A NCAC 02L .0202 Groundwater Quality Standards: Part 1*; 2020.

(23) *Environment and Climate Change Canada. Canadian Environ- Mental Protection Act (1999)*; Federal Environmental Quality Guidelines: Vanadium, 2016.

(24) Morita, A.; Yamamoto, S.; Wang, B.; Tanaka, K.; Suzuki, N.; Aoki, S.; Ito, A.; Nanao, T.; Ohya, S.; Yoshino, M.; Zhu, J.; Enomoto, A.; Matsumoto, Y.; Funatsu, O.; Hosoi, Y.; Ikekita, M. Sodium Orthovanadate Inhibits P53-Mediated Apoptosis. *Cancer Res.* **2010**, *70* (1), 257–265. https://doi.org/10.1158/0008-5472.CAN-08-3771.

(25) Seargeant, L. E.; Stinson, R. A. Inhibition of Human Alkaline Phosphatases by Vanadate. *Biochem. J.* **1979**, *181* (1), 247–250. https://doi.org/10.1042/bj1810247.

(26) Schiffer, S.; Liber, K. Estimation of Vanadium Water Quality Benchmarks for the Protection of Aquatic Life with Relevance to the Athabasca Oil Sands Region Using Species Sensitivity Distributions. *Environ. Toxicol. Chem.* **2017**, *36* (11), 3034–3044. https://doi.org/10.1002/etc.3871.

(27) Schiffer, S.; Liber, K. Toxicity of Aqueous Vanadium to Zooplankton and Phytoplankton Species of Relevance to the Athabasca Oil Sands Region. *Ecotoxicol. Environ. Saf.* **2017**, *137*, 1–11. https://doi.org/10.1016/j.ecoenv.2016.10.040.

(28) Larsson, M. A.; Baken, S.; Gustafsson, J. P.; Hadialhejazi, G.; Smolders, E. Vanadium Bioavailability and Toxicity to Soil Microorganisms and Plants. *Environ. Toxicol. Chem.* **2013**, *32* (10), 2266–2273. https://doi.org/10.1002/etc.2322.

(29) Baken, S.; Larsson, M. A.; Gustafsson, J. P.; Cubadda, F.; Smolders, E. Ageing of Vanadium in Soils and Consequences for Bioavailability. *Eur. J. Soil Sci.* **2012**, *63* (6), 839–847. https://doi.org/10.1111/j.1365-2389.2012.01491.x.

(30) Ortiz-Bernad, I.; Anderson, R. T.; Vrionis, H. A.; Lovley, D. R. Vanadium Respiration by Geobacter Metallireducens: Novel Strategy for In Situ Removal of

Vanadium from Groundwater. *Appl Env. Microbiol* **2004**, *70* (5), 3091–3095. https://doi.org/10.1128/AEM.70.5.3091-3095.2004.

(31) Carpentier, W.; Sandra, K.; De Smet, I.; Brige, A.; De Smet, L.; Van Beeumen, J. Microbial Reduction and Precipitation of Vanadium by Shewanella Oneidensis. *Appl. Environ. Microbiol.* **2003**, *69* (6), 3636–3639. https://doi.org/10.1128/AEM.69.6.3636-3639.2003.

(32) Zhang, B.; Qiu, R.; Lu, L.; Chen, X.; He, C.; Lu, J.; Ren, Z. J. Autotrophic Vanadium(V) Bioreduction in Groundwater by Elemental Sulfur and Zerovalent Iron. *Environ. Sci. Technol.* **2018**, *52* (13), 7434–7442. https://doi.org/10.1021/acs.est.8b01317.

(33) Zhang, B.; Hao, L.; Tian, C.; Yuan, S.; Feng, C.; Ni, J.; Borthwick, A. G. L. Microbial Reduction and Precipitation of Vanadium (V) in Groundwater by Immobilized Mixed Anaerobic Culture. *Bioresour. Technol.* **2015**, *192*, 410–417. https://doi.org/10.1016/j.biortech.2015.05.102.

(34) Schlesinger, W. H.; Klein, E. M.; Vengosh, A. Global Biogeochemical Cycle of Vanadium. *Proc. Natl. Acad. Sci.* **2017**, *114* (52), E11092–E11100. https://doi.org/10.1073/pnas.1715500114.

(35) Huang, J.-H.; Huang, F.; Evans, L.; Glasauer, S. Vanadium: Global (Bio)Geochemistry. *Chem. Geol.* **2015**, *417*, 68–89. https://doi.org/10.1016/j.chemgeo.2015.09.019.

(36) Groover, K. D.; Izbicki, J. A. Selected Trace-Elements in Alluvium and Rocks, Western Mojave Desert, Southern California. *J. Geochem. Explor.* **2018**. https://doi.org/10.1016/j.gexplo.2018.09.005.

(37) Shiller, A. M.; Mao, L. Dissolved Vanadium in Rivers: Effects of Silicate Weathering. *Chem. Geol.* **2000**, *165* (1), 13–22. https://doi.org/10.1016/S0009-2541(99)00160-6.

(38) Johannesson, K. H.; Lyons, W. B.; Welch, K. A. Oxyanion Concentrations in Eastern Sierra Nevada Rivers – 3. Boron, Molybdenum, Vanadium, and Tungsten. 28.

(39) Ono, M.; Machida, I.; Ikawa, R.; Kamitani, T.; Oyama, K.; Muranaka, Y.; Ito, A.; Marui, A. Regional Groundwater Flow System in a Stratovolcano Adjacent to a Coastal Area: A Case Study of Mt. Fuji and Suruga Bay, Japan. *Hydrogeol. J.* **2019**, *27* (2), 717–730. https://doi.org/10.1007/s10040-018-1889-9.

(40) Fiorentino, C. E.; Paoloni, J. D.; Sequeira, M. E.; Arosteguy, P. The Presence of Vanadium in Groundwater of Southeastern Extreme the Pampean Region Argentina. *J. Contam. Hydrol.* **2007**, *93* (1–4), 122–129. https://doi.org/10.1016/j.jconhyd.2007.02.001.

(41) Farnfield, H. R.; Marcilla, A. L.; Ward, N. I. Arsenic Speciation and Trace Element Analysis of the Volcanic Río Agrio and the Geothermal Waters of Copahue, Argentina. *Sci. Total Environ.* **2012**, *433*, 371–378. https://doi.org/10.1016/j.scitotenv.2012.05.098.

(42) Nicolli, H. B.; García, J. W.; Falcón, C. M.; Smedley, P. L. Mobilization of Arsenic and Other Trace Elements of Health Concern in Groundwater from the Salí River Basin, Tucumán Province, Argentina. *Environ. Geochem. Health* **2012**, *34* (2), 251–262. https://doi.org/10.1007/s10653-011-9429-8.

(43) Lehoux, A. P.; Lockwood, C. L.; Mayes, W. M.; Stewart, D. I.; Mortimer, R. J. G.; Gruiz, K.; Burke, I. T. Gypsum Addition to Soils Contaminated by Red Mud: Implications for Aluminium, Arsenic, Molybdenum and Vanadium Solubility. *Environ. Geochem. Health* **2013**, *35* (5), 643–656. https://doi.org/10.1007/s10653-013-9547-6.

(44) Burke, I. T.; Mayes, W. M.; Peacock, C. L.; Brown, A. P.; Jarvis, A. P.; Gruiz, K. Speciation of Arsenic, Chromium, and Vanadium in Red Mud Samples from the Ajka Spill Site, Hungary. *Environ. Sci. Technol.* **2012**, *46* (6), 3085–3092. https://doi.org/10.1021/es3003475.

(45) Burke, I. T.; Peacock, C. L.; Lockwood, C. L.; Stewart, D. I.; Mortimer, R. J. G.; Ward, M. B.; Renforth, P.; Gruiz, K.; Mayes, W. M. Behavior of Aluminum, Arsenic, and Vanadium during the Neutralization of Red Mud Leachate by HCl, Gypsum, or Seawater. *Environ. Sci. Technol.* **2013**, *47* (12), 6527–6535. https://doi.org/10.1021/es4010834.

(46) Hudson-Edwards, K. A.; Byrne, P.; Bird, G.; Brewer, P. A.; Burke, I. T.; Jamieson, H.; Macklin, M.; Williams, R. Origin and Fate of Vanadium in the Hazeltine Creek Catchment Following the 2014 Mount Polley Mine Tailings Spill, British Columbia, Canada. *Environ. Sci. Technol.* **2019**. https://doi.org/10.1021/acs.est.8b06391.

(47) Nesbitt, J. A.; Lindsay, M. B. J. Vanadium Geochemistry of Oil Sands Fluid Petroleum Coke. *Environ. Sci. Technol.* **2017**, *51* (5), 3102–3109. https://doi.org/10.1021/acs.est.6b05682.

(48) Hobson, A. J.; Stewart, D. I.; Bray, A. W.; Mortimer, R. J. G.; Mayes, W. M.; Rogerson, M.; Burke, I. T. Mechanism of Vanadium Leaching during Surface

Weathering of Basic Oxygen Furnace Steel Slag Blocks: A Microfocus X-Ray Absorption Spectroscopy and Electron Microscopy Study. *Environ. Sci. Technol.* **2017**, *51* (14), 7823–7830. https://doi.org/10.1021/acs.est.7b00874.

(49) Chaurand, P.; Rose, J.; Briois, V.; Olivi, L.; Hazemann, J.-L.; Proux, O.; Domas, J.; Bottero, J.-Y. Environmental Impacts of Steel Slag Reused in Road Construction: A Crystallographic and Molecular (XANES) Approach. *J. Hazard. Mater.* **2007**, *139* (3), 537–542. https://doi.org/10.1016/j.jhazmat.2006.02.060.

(50) Balan, E.; Villiers, J. P. R. D.; Eeckhout, S. G.; Glatzel, P.; Toplis, M. J.; Fritsch, E.; Allard, T.; Galoisy, L.; Calas, G. The Oxidation State of Vanadium in Titanomagnetite from Layered Basic Intrusions. *Am. Mineral.* **2006**, *91* (5–6), 953–956. https://doi.org/10.2138/am.2006.2192.

(51) Sutton, S. R.; Karner, J.; Papike, J.; Delaney, J. S.; Shearer, C.; Newville, M.; Eng, P.; Rivers, M.; Dyar, M. D. Vanadium K Edge XANES of Synthetic and Natural Basaltic Glasses and Application to Microscale Oxygen Barometry. *Geochim. Cosmochim. Acta* **2005**, *69* (9), 2333–2348. https://doi.org/10.1016/j.gca.2004.10.013.

(52) Canil, D. Vanadium in Peridotites, Mantle Redox and Tectonic Environments: Archean to Present. *Earth Planet. Sci. Lett.* **2002**, *195* (1), 75–90. https://doi.org/10.1016/S0012-821X(01)00582-9.

(53) Schofield, P. F.; Henderson, C. M. B.; Cressey, G.; van der Laan, G. 2p X-Ray Absorption Spectroscopy in the Earth Sciences. *J. Synchrotron Radiat.* **1995**, *2* (2), 93–98. https://doi.org/10.1107/S0909049595000598.

(54) Wisawapipat, W.; Kretzschmar, R. Solid Phase Speciation and Solubility of Vanadium in Highly Weathered Soils. *Environ. Sci. Technol.* **2017**, *51* (15), 8254–8262. https://doi.org/10.1021/acs.est.7b01005.

(55) Schwertmann, U.; Pfab, G. Structural Vanadium and Chromium in Lateritic Iron Oxides: Genetic Implications. *Geochim. Cosmochim. Acta* **1996**, *60* (21), 4279–4283. https://doi.org/10.1016/S0016-7037(96)00259-1.

(56) Gehring, A. U. The Chemical Form of Vanadium (IV) in Kaolinite. *Clays Clay Miner.* **1993**, *41* (6), 662–667. https://doi.org/10.1346/CCMN.1993.0410604.

(57) Bordage, A.; Balan, E.; de Villiers, J. P. R.; Cromarty, R.; Juhin, A.; Carvallo, C.; Calas, G.; Sunder Raju, P. V.; Glatzel, P. V Oxidation State in Fe–Ti Oxides by High-Energy Resolution Fluorescence-Detected X-Ray Absorption Spectroscopy. *Phys. Chem. Miner.* **2011**, *38* (6), 449–458. https://doi.org/10.1007/s00269-011-0418-3.

(58) Kaur, N.; Singh, B.; Kennedy, B. J.; Gräfe, M. The Preparation and Characterization of Vanadium-Substituted Goethite: The Importance of Temperature. *Geochim. Cosmochim. Acta* **2009**, *73* (3), 582–593. https://doi.org/10.1016/j.gca.2008.10.025.

(59) Yang, J.; Tang, Y.; Yang, K.; Rouff, A. A.; Elzinga, E. J.; Huang, J.-H. Leaching Characteristics of Vanadium in Mine Tailings and Soils near a Vanadium Titanomagnetite Mining Site. *J. Hazard. Mater.* **2014**, *264*, 498–504. https://doi.org/10.1016/j.jhazmat.2013.09.063.

(60) Wong, J.; Lytle, F. W.; Messmer, R. P.; Maylotte, D. H. K -Edge Absorption Spectra of Selected Vanadium Compounds. *Phys. Rev. B* **1984**, *30* (10), 5596–5610. https://doi.org/10.1103/PhysRevB.30.5596.

(61) Gehring, A. U.; Fry, I. V.; Luster, J.; Sposito, G. Vanadium in Sepiolite: A Redox-Indicator for an Ancient Closed Brine System in the Madrid Basin, Central Spain. *Geochim. Cosmochim. Acta* **1994**, *58* (16), 3345–3351. https://doi.org/10.1016/0016-7037(94)90090-6.

(62) Hu, X.; Yue, Y.; Peng, X. Release Kinetics of Vanadium from Vanadium Titano-Magnetite: The Effects of PH, Dissolved Oxygen, Temperature and Foreign Ions. *J. Environ. Sci.* **2018**, *64*, 298–305. https://doi.org/10.1016/j.jes.2017.07.001.

(63) Wehrli, B.; Stumm, W. Vanadyl in Natural Waters: Adsorption and Hydrolysis Promote Oxygenation. *Geochim. Cosmochim. Acta* **1989**, *53* (1), 69–77. https://doi.org/10.1016/0016-7037(89)90273-1.

(64) Wanty, R. B.; Goldhaber, M. B. Thermodynamics and Kinetics of Reactions Involving Vanadium in Natural Systems: Accumulation of Vanadium in Sedimentary Rocks. *Geochim. Cosmochim. Acta* **1992**, *56* (4), 1471–1483. https://doi.org/10.1016/0016-7037(92)90217-7.

(65) Besnardiere, J.; Petrissans, X.; Ribot, F.; Briois, V.; Surcin, C.; Morcrette, M.; Buissette, V.; Le Mercier, T.; Cassaignon, S.; Portehault, D. Nanoparticles of Low-Valence Vanadium Oxyhydroxides: Reaction Mechanisms and Polymorphism Control by Low-Temperature Aqueous Chemistry. *Inorg. Chem.* **2016**, *55* (21), 11502–11512. https://doi.org/10.1021/acs.inorgchem.6b02059.

(66) CHRISTENSON, S.; HAVENS, J. Ground-Water-Quality Assessment of the Central Oklahoma Aquifer, Oklahoma: Results of Investigations. **1998**.

(67) Lu, X.; Johnson, W. D.; Hook, J. Reaction of Vanadate with Aquatic Humic Substances: An ESR and 51V NMR Study. *Environ. Sci. Technol.* **1998**, *32* (15), 2257–2263. https://doi.org/10.1021/es970930r.

(68) Larsson, M. A.; D'Amato, M.; Cubadda, F.; Raggi, A.; Öborn, I.; Kleja, D. B.; Gustafsson, J. P. Long-Term Fate and Transformations of Vanadium in a Pine Forest Soil with Added Converter Lime. *Geoderma* **2015**, *259–260*, 271–278. https://doi.org/10.1016/j.geoderma.2015.06.012.

(69) Larsson, M. A.; Baken, S.; Smolders, E.; Cubadda, F.; Gustafsson, J. P. Vanadium Bioavailability in Soils Amended with Blast Furnace Slag. *J. Hazard. Mater.* **2015**, *296*, 158–165. https://doi.org/10.1016/j.jhazmat.2015.04.034.

(70) Wehrli, B.; Sulzberger, B.; Stumm, W. Redox Processes Catalyzed by Hydrous Oxide Surfaces. *Chem. Geol.* **1989**, *78* (3), 167–179. https://doi.org/10.1016/0009-2541(89)90056-9.

(71) Cruywagen, J. J. PROTONAT1ON, OLIGOMERIZATlON, AND CONDENSATION REACTIONS OF VANADATE(V), MOLYBDATE(VI), AND TUNGSTATE(V1). **2000**, 56.

(72) Shiller, A. M.; Boyle, E. A. Dissolved Vanadium in Rivers and Estuaries. *Earth Planet. Sci. Lett.* **1987**, *86* (2–4), 214–224. https://doi.org/10.1016/0012-821X(87)90222-6.

(73) McCann, N.; Wagner, M.; Hasse, H. A Thermodynamic Model for Vanadate in Aqueous Solution – Equilibria and Reaction Enthalpies. *Dalton Trans.* **2013**, *42* (7), 2622–2628. https://doi.org/10.1039/C2DT31993D.

(74) Crans, D. C.; Tracey, A. S. The Chemistry of Vanadium in Aqueous and Nonaqueous Solution. In *Vanadium Compounds*; ACS Symposium Series; American Chemical Society, 1998; Vol. 711, pp 2–29. https://doi.org/10.1021/bk-1998-0711.ch001.

(75) Bruyère, V. I. E.; Rodenas, L. A. G.; Morando, P. J.; Blesa, M. A. Reduction of Vanadium(V) by Oxalic Acid in Aqueous Acid Solutions. *J. Chem. Soc. Dalton Trans.* **2001**, No. 24, 3593–3597. https://doi.org/10.1039/B103320B.

(76) Ceci, A.; Rhee, Y. J.; Kierans, M.; Hillier, S.; Pendlowski, H.; Gray, N.; Persiani, A. M.; Gadd, G. M. Transformation of Vanadinite [Pb5(VO4)3Cl] by Fungi. *Environ. Microbiol.* **2015**, *17* (6), 2018–2034. https://doi.org/10.1111/1462-2920.12612.

(77) Vessey, C. J.; Lindsay, M. B. J. Aqueous Vanadate Removal by Iron(II)-Bearing Phases under Anoxic Conditions. *Environ. Sci. Technol.* **2020**. https://doi.org/10.1021/acs.est.9b06250.

(78) Larsson, M. A.; Persson, I.; Sjöstedt, C.; Gustafsson, J. P. Vanadate Complexation to Ferrihydrite: X-Ray Absorption Spectroscopy and CD-MUSIC Modelling. *Environ. Chem.* **2017**, *14* (3), 141–150. https://doi.org/10.1071/EN16174.

(79) Peacock, C. L.; Sherman, D. M. Vanadium(V) Adsorption onto Goethite (α-FeOOH) at PH 1.5 to 12: A Surface Complexation Model Based on Ab Initio Molecular Geometries and EXAFS Spectroscopy. *Geochim. Cosmochim. Acta* **2004**, *68* (8), 1723–1733. https://doi.org/10.1016/j.gca.2003.10.018.

(80) Motschi, H.; Rudin, M. 27Al ENDOR Study of VO2+ Adsorbed on ?-Alumina: Direct Evidence for Inner Sphere Coordination with Surface Functional Groups. *Colloid Polym. Sci.* **1984**, *262* (7), 579–583. https://doi.org/10.1007/BF01451522.

(81) Lafferty, B. J.; Ginder-Vogel, M.; Zhu, M.; Livi, K. J. T.; Sparks, D. L. Arsenite Oxidation by a Poorly Crystalline Manganese-Oxide. 2. Results from X-Ray Absorption Spectroscopy and X-Ray Diffraction. *Environ. Sci. Technol.* **2010**, *44* (22), 8467–8472. https://doi.org/10.1021/es102016c.

(82) Ginder-Vogel, M.; Landrot, G.; Fischel, J. S.; Sparks, D. L. Quantification of Rapid Environmental Redox Processes with Quick-Scanning x-Ray Absorption Spectroscopy (Q-XAS). *Proc. Natl. Acad. Sci.* **2009**, *106* (38), 16124–16128. https://doi.org/10.1073/pnas.0908186106.

(83) Zhu, M.; Ginder-Vogel, M.; Sparks, D. L. Ni(II) Sorption on Biogenic Mn-Oxides with Varying Mn Octahedral Layer Structure. *Environ. Sci. Technol.* **2010**, *44* (12), 4472–4478. https://doi.org/10.1021/es9037066.

(84) Landrot, G.; Ginder-Vogel, M.; Sparks, D. L. Kinetics of Chromium(III) Oxidation by Manganese(IV) Oxides Using Quick Scanning X-Ray Absorption Fine Structure Spectroscopy (Q-XAFS). *Environ. Sci. Technol.* **2010**, *44* (1), 143–149. https://doi.org/10.1021/es901759w.

(85) Lefkowitz, J. P.; Elzinga, E. J. Impacts of Aqueous Mn(II) on the Sorption of Zn(II) by Hexagonal Birnessite. *Environ. Sci. Technol.* **2015**, *49* (8), 4886–4893. https://doi.org/10.1021/es506019j.

(86) Manceau, A.; Lanson, B.; Drits, V. A. Structure of Heavy Metal Sorbed Birnessite. Part III: Results from Powder and Polarized Extended X-Ray Absorption Fine Structure Spectroscopy. *Geochim. Cosmochim. Acta* **2002**, *66* (15), 2639–2663. https://doi.org/10.1016/S0016-7037(02)00869-4.

(87) McClain, C. N.; Fendorf, S.; Webb, S. M.; Maher, K. Quantifying Cr(VI) Production and Export from Serpentine Soil of the California Coast Range. *Environ. Sci. Technol.* **2017**, *51* (1), 141–149. https://doi.org/10.1021/acs.est.6b03484.

(88) Mock, R. P.; Schaefer, M. V.; Pacheco, J. L.; Lake, L.; Lee, I.; Ying, S. C. Influence of Fe(II) on Arsenic(III) Oxidation by Birnessite in Diffusion-Limited Systems. *ACS Earth Space Chem.* **2019**, *3* (4), 550–561. https://doi.org/10.1021/acsearthspacechem.8b00184.

(89) Scott, M. J.; Morgan, J. J. Reactions at Oxide Surfaces. 2. Oxidation of Se(IV) by Synthetic Birnessite. *Environ. Sci. Technol.* **1996**, *30* (6), 1990–1996. https://doi.org/10.1021/es950741d.

(90) Takematsu, N.; Sato, Y.; Okabe, S.; Nakayama, E. The Partition of Vanadium and Molybdenum between Manganese Oxides and Sea Water. *Geochim. Cosmochim. Acta* **1985**, *49* (11), 2395–2399. https://doi.org/10.1016/0016-7037(85)90239-X.

(91) Toner, B.; Manceau, A.; Webb, S. M.; Sposito, G. Zinc Sorption to Biogenic Hexagonal-Birnessite Particles within a Hydrated Bacterial Biofilm. *Geochim. Cosmochim. Acta* **2006**, *70* (1), 27–43. https://doi.org/10.1016/j.gca.2005.08.029.

(92) Villalobos, M.; Lanson, B.; Manceau, A.; Toner, B.; Sposito, G. Structural Model for the Biogenic Mn Oxide Produced by Pseudomonas Putida. *Am. Mineral.* **2006**, *91* (4), 489–502. https://doi.org/10.2138/am.2006.1925.

(93) Webb, S. M. Structural Characterization of Biogenic Mn Oxides Produced in Seawater by the Marine Bacillus Sp. Strain SG-1. *Am. Mineral.* **2005**, *90* (8–9), 1342–1357. https://doi.org/10.2138/am.2005.1669.

(94) Bargar, J. R.; Tebo, B. M.; Bergmann, U.; Webb, S. M.; Glatzel, P.; Chiu, V. Q.; Villalobos, M. Biotic and Abiotic Products of Mn(II) Oxidation by Spores of the Marine Bacillus Sp. Strain SG-1. *Am. Mineral.* **2005**, *90* (1), 143–154. https://doi.org/10.2138/am.2005.1557.

(95) Bargar, J. R.; Fuller, C. C.; Marcus, M. A.; Brearley, A. J.; Perez De la Rosa, M.; Webb, S. M.; Caldwell, W. A. Structural Characterization of Terrestrial Microbial Mn Oxides from Pinal Creek, AZ. *Geochim. Cosmochim. Acta* **2009**, *73* (4), 889–910. https://doi.org/10.1016/j.gca.2008.10.036.

(96) Jones, M. E.; Nico, P. S.; Ying, S.; Regier, T.; Thieme, J.; Keiluweit, M. Manganese-Driven Carbon Oxidation at Oxic–Anoxic Interfaces. *Environ. Sci. Technol.* **2018**, *52* (21), 12349–12357. https://doi.org/10.1021/acs.est.8b03791.

(97) Santelli, C. M.; Webb, S. M.; Dohnalkova, A. C.; Hansel, C. M. Diversity of Mn Oxides Produced by Mn(II)-Oxidizing Fungi. *Geochim. Cosmochim. Acta* **2011**, *75* (10), 2762–2776. https://doi.org/10.1016/j.gca.2011.02.022.

(98) Spiro, T. G.; Bargar, J. R.; Sposito, G.; Tebo, B. M. Bacteriogenic Manganese Oxides. *Acc. Chem. Res.* **2010**, *43* (1), 2–9. https://doi.org/10.1021/ar800232a.

(99) Tebo, B. M.; Bargar, J. R.; Clement, B. G.; Dick, G. J.; Murray, K. J.; Parker, D.; Verity, R.; Webb, S. M. BIOGENIC MANGANESE OXIDES: Properties and Mechanisms of Formation. *Annu. Rev. Earth Planet. Sci.* **2004**, *32* (1), 287–328. https://doi.org/10.1146/annurev.earth.32.101802.120213.

(100) Lafferty, B. J.; Ginder-Vogel, M.; Sparks, D. L. Arsenite Oxidation by a Poorly Crystalline Manganese-Oxide 1. Stirred-Flow Experiments. *Environ. Sci. Technol.* **2010**, *44* (22), 8460–8466. https://doi.org/10.1021/es102013p.

(101) Landrot, G.; Ginder-Vogel, M.; Livi, K.; Fitts, J. P.; Sparks, D. L. Chromium(III) Oxidation by Three Poorly-Crystalline Manganese(IV) Oxides. 1. Chromium(III)-Oxidizing Capacity. *Environ. Sci. Technol.* **2012**, *46* (21), 11594–11600. https://doi.org/10.1021/es302383y.

(102) Landrot, G.; Ginder-Vogel, M.; Livi, K.; Fitts, J. P.; Sparks, D. L. Chromium(III) Oxidation by Three Poorly Crystalline Manganese(IV) Oxides. 2. Solid Phase Analyses. *Environ. Sci. Technol.* **2012**, *46* (21), 11601–11609. https://doi.org/10.1021/es302384q.

(103) Lafferty, B. J.; Ginder-Vogel, M.; Sparks, D. L. Arsenite Oxidation by a Poorly-Crystalline Manganese Oxide. 3. Arsenic and Manganese Desorption. *Environ. Sci. Technol.* **2011**, *45* (21), 9218–9223. https://doi.org/10.1021/es201281u.

(104) Zhao, H.; Zhu, M.; Li, W.; Elzinga, E. J.; Villalobos, M.; Liu, F.; Zhang, J.; Feng, X.; Sparks, D. L. Redox Reactions between Mn(II) and Hexagonal Birnessite Change Its Layer Symmetry. *Environ. Sci. Technol.* **2016**, *50* (4), 1750–1758. https://doi.org/10.1021/acs.est.5b04436.

(105) Elzinga, E. J. Reductive Transformation of Birnessite by Aqueous Mn(II). *Environ. Sci. Technol.* **2011**, *45* (15), 6366–6372. https://doi.org/10.1021/es2013038.

(106) Lefkowitz, J. P.; Rouff, A. A.; Elzinga, E. J. Influence of PH on the Reductive Transformation of Birnessite by Aqueous Mn(II). *Environ. Sci. Technol.* **2013**, *47* (18), 10364–10371. https://doi.org/10.1021/es402108d.

(107) Lefkowitz, J. P.; Elzinga, E. J. Structural Alteration of Hexagonal Birnessite by Aqueous Mn(II): Impacts on Ni(II) Sorption. *Chem. Geol.* **2017**, *466*, 524–532. https://doi.org/10.1016/j.chemgeo.2017.07.002.

(108) Liu, L.; Min, M.; Liu, F.; Yin, H.; Zhang, Y.; Qiu, G. Influence of Vanadium Doping on the Supercapacitance Performance of Hexagonal Birnessite. *J. Power Sources* **2015**, *277*, 26–35. https://doi.org/10.1016/j.jpowsour.2014.12.004.

(109) Bostick, B. C.; Hansel, C. M.; Fendorf, S. Seasonal Fluctuations in Zinc Speciation within a Contaminated Wetland. *Environ. Sci. Technol.* **2001**, *35* (19), 3823–3829. https://doi.org/10.1021/es010549d.

(110) Schaefer, M. V.; Ying, S. C.; Benner, S. G.; Duan, Y.; Wang, Y.; Fendorf, S. Aquifer Arsenic Cycling Induced by Seasonal Hydrologic Changes within the Yangtze River Basin. *Environ. Sci. Technol.* **2016**, *50* (7), 3521–3529. https://doi.org/10.1021/acs.est.5b04986.

(111) Schaefer, M. V.; Guo, X.; Gan, Y.; Benner, S. G.; Griffin, A. M.; Gorski, C. A.; Wang, Y.; Fendorf, S. Redox Controls on Arsenic Enrichment and Release from Aquifer Sediments in Central Yangtze River Basin. *Geochim. Cosmochim. Acta* **2017**, *204*, 104–119. https://doi.org/10.1016/j.gca.2017.01.035.

(112) Ying, S. C.; Schaefer, M. V.; Cock-Esteb, A.; Li, J.; Fendorf, S. Depth Stratification Leads to Distinct Zones of Manganese and Arsenic Contaminated Groundwater. *Environ. Sci. Technol.* **2017**, *51* (16), 8926–8932. https://doi.org/10.1021/acs.est.7b01121.

(113) Stuckey, J. W.; Schaefer, M. V.; Kocar, B. D.; Benner, S. G.; Fendorf, S. Arsenic Release Metabolically Limited to Permanently Water-Saturated Soil in Mekong Delta. *Nat. Geosci.* **2016**, *9* (1), 70–76. https://doi.org/10.1038/ngeo2589.

(114) Masue-Slowey, Y.; Ying, S. C.; Kocar, B. D.; Pallud, C. E.; Fendorf, S. Dependence of Arsenic Fate and Transport on Biogeochemical Heterogeneity Arising from the Physical Structure of Soils and Sediments. *J. Environ. Qual.* **2013**, *42* (4), 1119. https://doi.org/10.2134/jeq2012.0253.

(115) Ying, S. C.; Masue-Slowey, Y.; Kocar, B. D.; Griffis, S. D.; Webb, S.; Marcus, M. A.; Francis, C. A.; Fendorf, S. Distributed Microbially- and Chemically-Mediated Redox Processes Controlling Arsenic Dynamics within Mn-/Fe-Oxide Constructed Aggregates. *Geochim. Cosmochim. Acta* **2013**, *104*, 29–41. https://doi.org/10.1016/j.gca.2012.08.020.

(116) Fandeur, D.; Juillot, F.; Morin, G.; Olivi, L.; Cognigni, A.; Webb, S. M.; Ambrosi, J.-P.; Fritsch, E.; Guyot, F.; Brown, Jr., G. E. XANES Evidence for

Oxidation of Cr(III) to Cr(VI) by Mn-Oxides in a Lateritic Regolith Developed on Serpentinized Ultramafic Rocks of New Caledonia. *Environ. Sci. Technol.* **2009**, *43* (19), 7384–7390. https://doi.org/10.1021/es900498r.

(117) Fram, M. *Groundwater Quality in the Western San Joaquin Valley Study Unit, 2010: California GAMA Priority Basin Project*; Scientific Investigations Report; 2017.

(118) Gonzalez, A. R.; Ndung'u, K.; Flegal, A. R. Natural Occurrence of Hexavalent Chromium in the Aromas Red Sands Aquifer, California. *Environ. Sci. Technol.* **2005**, *39* (15), 5505–5511. https://doi.org/10.1021/es048835n.

(119) Hausladen, D. M.; Fendorf, S. Hexavalent Chromium Generation within Naturally Structured Soils and Sediments. *Environ. Sci. Technol.* **2017**, *51* (4), 2058–2067. https://doi.org/10.1021/acs.est.6b04039.

(120) Brown, F. H.; Pabst, A.; Sawyer, D. L. BIRNESSITE ON COLEMANITE A T BORON. CALIFORNIA. *Am. Mineral.* **1971**, *56*, 8.

(121) Ndung'u, K.; Friedrich, S.; Gonzalez, A. R.; Flegal, A. R. Chromium Oxidation by Manganese (Hydr)Oxides in a California Aquifer. *Appl. Geochem.* **2010**, *25* (3), 377–381. https://doi.org/10.1016/j.apgeochem.2009.12.004.

(122) Yin, H.; Feng, X.; Tan, W.; Koopal, L. K.; Hu, T.; Zhu, M.; Liu, F. Structure and Properties of Vanadium(V)-Doped Hexagonal Turbostratic Birnessite and Its Enhanced Scavenging of Pb2+ from Solutions. *J. Hazard. Mater.* **2015**, *288*, 80–88. https://doi.org/10.1016/j.jhazmat.2015.01.068.

(123) Borch, T.; Kretzschmar, R.; Kappler, A.; Cappellen, P. V.; Ginder-Vogel, M.; Voegelin, A.; Campbell, K. Biogeochemical Redox Processes and Their Impact on Contaminant Dynamics. *Environ. Sci. Technol.* **2010**, *44* (1), 15–23. https://doi.org/10.1021/es9026248.

(124) Manning, B. A.; Fendorf, S. E.; Goldberg, S. Surface Structures and Stability of Arsenic(III) on Goethite: Spectroscopic Evidence for Inner-Sphere Complexes. *Environ. Sci. Technol.* **1998**, *32* (16), 2383–2388. https://doi.org/10.1021/es9802201.

(125) Ona-Nguema, G.; Morin, G.; Juillot, F.; Calas, G.; Brown, G. E. EXAFS Analysis of Arsenite Adsorption onto Two-Line Ferrihydrite, Hematite, Goethite, and Lepidocrocite. *Environ. Sci. Technol.* **2005**, *39* (23), 9147–9155. https://doi.org/10.1021/es050889p.

(126) Sowers, T. D.; Harrington, J. M.; Polizzotto, M. L.; Duckworth, O. W. Sorption of Arsenic to Biogenic Iron (Oxyhydr)Oxides Produced in Circumneutral Environments. *Geochim. Cosmochim. Acta* **2017**, *198*, 194–207. https://doi.org/10.1016/j.gca.2016.10.049.

(127) Xiu, W.; Yu, X.; Guo, H.; Yuan, W.; Ke, T.; Liu, G.; Tao, J.; Hou, W.; Dong, H. Facilitated Arsenic Immobilization by Biogenic Ferrihydrite-Goethite Biphasic Fe(III) Minerals (Fh-Gt Bio-Bi-Minerals). *Chemosphere* **2019**. https://doi.org/10.1016/j.chemosphere.2019.02.098.

(128) Ying, S. C.; Kocar, B. D.; Fendorf, S. Oxidation and Competitive Retention of Arsenic between Iron- and Manganese Oxides. *Geochim. Cosmochim. Acta* **2012**, *96*, 294–303. https://doi.org/10.1016/j.gca.2012.07.013.

(129) Fuller, A. J.; Shaw, S.; Peacock, C. L.; Trivedi, D.; Burke, I. T. EXAFS Study of Sr Sorption to Illite, Goethite, Chlorite, and Mixed Sediment under Hyperalkaline Conditions. *Langmuir* **2016**, *32* (12), 2937–2946. https://doi.org/10.1021/acs.langmuir.5b04633.

(130) Singh, B.; Sherman, D. M.; Gilkes, R. J.; Ells, M. A. W.; Mosselmans, J. F. W. Incorporation of Cr, Mn and Ni into Goethite (a-FeOOH): Mechanism from Extended X-Ray Absorption Fine Structure Spectroscopy. **2002**, 11.

(131) Ginder-Vogel, M.; Stewart, B.; Fendorf, S. Kinetic and Mechanistic Constraints on the Oxidation of Biogenic Uraninite by Ferrihydrite. *Environ. Sci. Technol.* **2010**, *44* (1), 163–169. https://doi.org/10.1021/es902452u.

(132) Hiemstra, T.; Riemsdijk, W. H. V.; Rossberg, A.; Ulrich, K.-U. A Surface Structural Model for Ferrihydrite II: Adsorption of Uranyl and Carbonate. *Geochim. Cosmochim. Acta* **2009**, *73* (15), 4437–4451. https://doi.org/10.1016/j.gca.2009.04.035.

(133) Stewart, B. D.; Nico, P. S.; Fendorf, S. Stability of Uranium Incorporated into Fe (Hydr)Oxides under Fluctuating Redox Conditions. *Environ. Sci. Technol.* **2009**, *43* (13), 4922–4927. https://doi.org/10.1021/es803317w.

(134) Martínez, C. E.; McBride, M. B. Dissolved and Labile Concentrations of Cd, Cu, Pb, and Zn in Aged Ferrihydrite−Organic Matter Systems. *Environ. Sci. Technol.* **1999**, *33* (5), 745–750. https://doi.org/10.1021/es980576c.

(135) Dannenberg, A.; Pehkonen, S. O. Investigation of the Heterogeneously Catalyzed Hydrolysis of Organophosphorus Pesticides. *J. Agric. Food Chem.* **1998**, *46* (1), 325–334. https://doi.org/10.1021/jf970368o.

(136) Eusterhues, K.; Wagner, F. E.; Häusler, W.; Hanzlik, M.; Knicker, H.; Totsche, K. U.; Kögel-Knabner, I.; Schwertmann, U. Characterization of Ferrihydrite-Soil Organic Matter Coprecipitates by X-Ray Diffraction and Mössbauer Spectroscopy. *Environ. Sci. Technol.* **2008**, *42* (21), 7891–7897. https://doi.org/10.1021/es800881w.

(137) Eusterhues, K.; Rumpel, C.; Kleber, M.; Kögel-Knabner, I. Stabilisation of Soil Organic Matter by Interactions with Minerals as Revealed by Mineral Dissolution and Oxidative Degradation. *Org. Geochem.* **2003**, *34* (12), 1591–1600. https://doi.org/10.1016/j.orggeochem.2003.08.007.

(138) Keiluweit, M.; Bougoure, J. J.; Zeglin, L. H.; Myrold, D. D.; Weber, P. K.; Pett-Ridge, J.; Kleber, M.; Nico, P. S. Nano-Scale Investigation of the Association of Microbial Nitrogen Residues with Iron (Hydr)Oxides in a Forest Soil O-Horizon. *Geochim. Cosmochim. Acta* **2012**, *95*, 213–226. https://doi.org/10.1016/j.gca.2012.07.001.

(139) Keiluweit, M.; Kleber, M. Molecular-Level Interactions in Soils and Sediments: The Role of Aromatic π-Systems. *Environ. Sci. Technol.* **2009**, *43* (10), 3421–3429. https://doi.org/10.1021/es8033044.

(140) Müller, S.; Totsche, K. U.; Kögel-Knabner, I. Sorption of Polycyclic Aromatic Hydrocarbons to Mineral Surfaces. *Eur. J. Soil Sci.* **2007**, *58* (4), 918–931. https://doi.org/10.1111/j.1365-2389.2007.00930.x.

(141) Bostick, B. C.; Chen, C.; Fendorf, S. Arsenite Retention Mechanisms within Estuarine Sediments of Pescadero, CA. *Environ. Sci. Technol.* **2004**, *38* (12), 3299–3304. https://doi.org/10.1021/es035006d.

(142) Manning, B. A.; Goldberg, S. ARSENIC(III) AND ARSENIC(V) ADSORPTION ON THREE CALIFORNIA SOILS. *Soil Sci.* **1997**, *162* (12), 886.

(143) Savage, K. S.; Bird, D. K.; Ashley, R. P. Legacy of the California Gold Rush: Environmental Geochemistry of Arsenic in the Southern Mother Lode Gold District. *Int. Geol. Rev.* **2000**, *42* (5), 31.

(144) Duff, M. C.; Amrhein, C.; Bertsch, P. M.; Hunter, D. B. The Chemistry of Uranium in Evaporation Pond Sediment in the San Joaquin Valley, California, USA, Using X-Ray Fluorescence and XANES Techniques. *Geochim. Cosmochim. Acta* **1997**, *61* (1), 73–81. https://doi.org/10.1016/S0016-7037(96)00330-4.

(145) Auger, Y.; Bodineau, L.; Leclercq, S.; Wartel, M. Some Aspects of Vanadium and Chromium Chemistry in the English Channel. *Cont. Shelf Res.* **1999**, *19* (15), 2003–2018. https://doi.org/10.1016/S0278-4343(99)00050-3.

(146) Trefry, J. H.; Metz, S. Role of Hydrothermal Precipitates in the Geochemical Cycling of Vanadium. *Nature* **1989**, *342* (6249), 531–533. https://doi.org/10.1038/342531a0.

(147) Mikkonen, H. G.; van de Graaff, R.; Collins, R. N.; Dasika, R.; Wallis, C. J.; Howard, D. L.; Reichman, S. M. Immobilisation of Geogenic Arsenic and Vanadium in Iron-Rich Sediments and Iron Stone Deposits. *Sci. Total Environ.* **2018**. https://doi.org/10.1016/j.scitotenv.2018.10.427.

(148) Cappuyns, V.; Slabbinck, E. Occurrence of Vanadium in Belgian and European Alluvial Soils https://www.hindawi.com/journals/aess/2012/979501/ (accessed 2020 -04 -28). https://doi.org/10.1155/2012/979501.

(149) Cappuyns, V.; Swennen, R. Release of Vanadium from Oxidized Sediments: Insights from Different Extraction and Leaching Procedures. *Environ. Sci. Pollut. Res.* **2014**, *21* (3), 2272–2282. https://doi.org/10.1007/s11356-013-2149-0.

(150) Larsson, M. A.; Hadialhejazi, G.; Gustafsson, J. P. Vanadium Sorption by Mineral Soils: Development of a Predictive Model. *Chemosphere* **2017**, *168*, 925–932. https://doi.org/10.1016/j.chemosphere.2016.10.117.

(151) Mikkonen, A.; Tummavuori, J. Retention of Vanadium (V) by Three Finnish Mineral Soils. *Eur. J. Soil Sci.* **1994**, *45* (3), 361–368. https://doi.org/10.1111/j.1365-2389.1994.tb00520.x.

(152) Rietra, R. P. J. J. *The Relationship between the Molecular Structure and Ion Adsorption on Goethite*; 2001.

(153) Vessey, C. J.; Schmidt, M. P.; Abdolahnezhad, M.; Peak, D.; Lindsay, M. B. J. Adsorption of (Poly)Vanadate onto Ferrihydrite and Hematite: An In Situ ATR–FTIR Study. *ACS Earth Space Chem.* **2020**. https://doi.org/10.1021/acsearthspacechem.0c00027.

(154) White, A. F.; Peterson, M. L. Reduction of Aqueous Transition Metal Species on the Surfaces of Fe(II) -Containing Oxides. *Geochim. Cosmochim. Acta* **1996**, *60* (20), 3799–3814. https://doi.org/10.1016/0016-7037(96)00213-X.

(155) Calvin, S. *EXAFS for Everyone*; CRC Press.

(156) Kelly, S. D.; Hesterberg, D.; Ravel, B.; Ulery, A. L.; Richard Drees, L. Analysis of Soils and Minerals Using X-Ray Absorption Spectroscopy. In *SSSA Book*

Series; Soil Science Society of America, 2008. https://doi.org/10.2136/sssabookser5.5.c14.

(157) Sparks, D. L. Environmental Soil Chemistry. **2003**, 367.

(158) Rees, J. A.; Wandzilak, A.; Maganas, D.; Wurster, N. I. C.; Hugenbruch, S.; Kowalska, J. K.; Pollock, C. J.; Lima, F. A.; Finkelstein, K. D.; DeBeer, S. Experimental and Theoretical Correlations between Vanadium K-edge X-ray Absorption and Kβ Emission Spectra. *JBIC J. Biol. Inorg. Chem.* **2016**, *21* (5), 793–805. https://doi.org/10.1007/s00775-016-1358-7.

(159) Ankudinov, A. L.; Ravel, B.; Rehr, J. J.; Conradson, S. D. Real-Space Multiple-Scattering Calculation and Interpretation of x-Ray-Absorption near-Edge Structure. *Phys. Rev. B* **1998**, *58* (12), 7565–7576. https://doi.org/10.1103/PhysRevB.58.7565.

(160) Zabinsky, S. I.; Rehr, J. J.; Ankudinov, A.; Albers, R. C.; Eller, M. J. Multiple-Scattering Calculations of x-Ray-Absorption Spectra. *Phys. Rev. B* **1995**, *52* (4), 2995–3009. https://doi.org/10.1103/PhysRevB.52.2995.

(161) Chaurand, P.; Rose, J.; Briois, V.; Salome, M.; Proux, O.; Nassif, V.; Olivi, L.; Susini, J.; Hazemann, J.-L.; Bottero, J.-Y. New Methodological Approach for the Vanadium K-Edge X-Ray Absorption Near-Edge Structure Interpretation: Application to the Speciation of Vanadium in Oxide Phases from Steel Slag. *J. Phys. Chem. B* **2007**, *111* (19), 5101–5110. https://doi.org/10.1021/jp063186i.

(162) Fendorf, S.; Eick, M. J.; Grossl, P.; Sparks, D. L. Arsenate and Chromate Retention Mechanisms on Goethite. 1. Surface Structure. *Environ. Sci. Technol.* **1997**, *31* (2), 315–320. https://doi.org/10.1021/es950653t.

(163) Kelly, S. D.; Kemner, K. M.; Fein, J. B.; Fowle, D. A.; Boyanov, M. I.; Bunker, B. A.; Yee, N. X-Ray Absorption Fine Structure Determination of PH-Dependent U-Bacterial Cell Wall Interactions. *Geochim. Cosmochim. Acta* **2002**, *66* (22), 3855–3871. https://doi.org/10.1016/S0016-7037(02)00947-X.

(164) Ravel, B.; Kelly, S. D. The Difficult Chore of Measuring Coordination by EXAFS. In *AIP Conference Proceedings*; AIP: Stanford, California (USA), 2007; Vol. 882, pp 150–152. https://doi.org/10.1063/1.2644458.

(165) Siebecker, M.; Li, W.; Khalid, S.; Sparks, D. Real-Time QEXAFS Spectroscopy Measures Rapid Precipitate Formation at the Mineral–Water Interface. *Nat. Commun.* **2014**, *5* (1), 5003. https://doi.org/10.1038/ncomms6003.

(166) Siebecker, M. G.; Sparks, D. L. Structural Differentiation between Layered Single (Ni) and Double Metal Hydroxides (Ni–Al LDHs) Using Wavelet

Transformation. *J. Phys. Chem. A* **2017**, *121* (37), 6992–6999. https://doi.org/10.1021/acs.jpca.7b07940.

(167) Benfatto, M.; Della Longa, S. Geometrical Fitting of Experimental XANES Spectra by a Full Multiple-Scattering Procedure. *J. Synchrotron Radiat.* **2001**, *8* (4), 1087–1094. https://doi.org/10.1107/S0909049501006422.

(168) Benfatto, M.; Della Longa, S.; Natoli, C. R. The MXAN Procedure: A New Method for Analysing the XANES Spectra of Metallo-proteins to Obtain Structural Quantitative Information. *J. Synchrotron Radiat.* **2003**, *10* (1), 51–57. https://doi.org/10.1107/S0909049502018137.

(169) Benzi, F.; Giuli, G.; Della Longa, S.; Paris, E. Vanadium K-Edge XANES in Vanadium-Bearing Model Compounds: A Full Multiple Scattering Study. *J. Synchrotron Radiat.* **2016**, *23* (4), 947–952. https://doi.org/10.1107/S1600577516008134.

(170) Prietzel, J.; Botzaki, A.; Tyufekchieva, N.; Brettholle, M.; Thieme, J.; Klysubun, W. Sulfur Speciation in Soil by S K-Edge XANES Spectroscopy: Comparison of Spectral Deconvolution and Linear Combination Fitting. *Environ. Sci. Technol.* **2011**, *45* (7), 2878–2886. https://doi.org/10.1021/es102180a.

(171) Sherman, D. M.; Randall, S. R. Surface Complexation of Arsenic(V) to Iron(III) (Hydr)Oxides: Structural Mechanism from Ab Initio Molecular Geometries and EXAFS Spectroscopy. *Geochim. Cosmochim. Acta* **2003**, *67* (22), 4223–4230. https://doi.org/10.1016/S0016-7037(03)00237-0.

(172) O'Day, P. A.; Vlassopoulos, D.; Root, R.; Rivera, N. The Influence of Sulfur and Iron on Dissolved Arsenic Concentrations in the Shallow Subsurface under Changing Redox Conditions. *Proc. Natl. Acad. Sci.* **2004**, *101* (38), 13703–13708. https://doi.org/10.1073/pnas.0402775101.

(173) Scheinost, A. C.; Sparks, D. L. Formation of Layered Single- and Double-Metal Hydroxide Precipitates at the Mineral/Water Interface: A Multiple-Scattering XAFS Analysis. *J. Colloid Interface Sci.* **2000**, *223* (2), 167–178. https://doi.org/10.1006/jcis.1999.6638.

(174) Ravel, B. Composing Complex EXAFS Problems with Severe Information Constraints. *J. Phys. Conf. Ser.* **2009**, *190*, 012026. https://doi.org/10.1088/1742-6596/190/1/012026.

(175) Newville, M. IFEFFIT : Interactive XAFS Analysis and FEFF Fitting. *J. Synchrotron Radiat.* **2001**, *8* (2), 322–324. https://doi.org/10.1107/S0909049500016964.

(176) Ravel, B.; Newville, M. ATHENA, ARTEMIS, HEPHAESTUS: Data Analysis for X-Ray Absorption Spectroscopy Using IFEFFIT. *J. Synchrotron Radiat.* **2005**, *12* (4), 537–541. https://doi.org/10.1107/S0909049505012719.

(177) Rehr, J. J.; Albers, R. C. Theoretical Approaches to X-Ray Absorption Fine Structure. *Rev. Mod. Phys.* **2000**, *72* (3), 621–654. https://doi.org/10.1103/RevModPhys.72.621.

Chapter 2: Vanadate retention by Iron and Manganese Oxides

I. Introduction

Geogenic and anthropogenic emission of vanadium (V) into the biosphere poses an increasing threat to water quality, [1–3] human health, [4] and sensitive ecological systems. [5,6] Vanadium has demonstrable toxicity at exposures as low as 1.2-80 μg/L for sensitive aquatic species, [5–7] and elevated concentrations have been shown to alter microbial community structure [8,9] and reduce crop yields. [10,11] Increases in steel demand and the extraction and combustion of fossil fuels have drastically increased the mobilization of V from the Earth's crust over the past century. [7,12–14] Recent estimates suggest that anthropogenic emissions of V into the biosphere now exceed V emissions from geologic processes. [13] However, with few exceptions, the source of mobile V in subsurface environments appears to be dominated by weathering processes. [7,14] This is most relevant to regions with aquifers developing on parent material rich in Fe^{III} and Al^{III} (hydr)oxides due to the high weight percentages of V^{III} and V^{IV} substitution that can occur in these minerals. [15–22] Weathering processes affecting these mineral phases release V into the groundwater-sediment matrix at elevated concentrations. [23–25] Such sediment weathering has resulted in V mobilization to aquifer pore spaces resulting in well water contamination throughout California. [1,2]

Vanadium is a redox active metal present in the +3, +4 and +5 oxidation states in terrestrial environments. [2,7] The solubility, and thus mobility of V is highly dependent on its oxidation state, with solubility increasing with oxidation state at circumneutral pH.

Additionally, V mobility in soils is greater in the absence of organic matter. [7,26,27] Species of V^{V} are the most mobile forms of V in terrestrial and aquatic environments, and their high degree of toxicity makes them a particular concern for human health. [5,7,28] Typically, V^{V} is observed as a vanadic acid derivative ($H_nVO_4^{n-3}$) at environmentally relevant concentrations. However, even at concentrations as low as 50 μM, a small percentage of the total vanadate polymerizes to form polyvanadate species that have unique biological and geochemical behaviors. [29–31] Accordingly, V^{V} in this text will refer to total vanadate concentrations as a way to describe this distribution, which is dominated by $H_2VO_4^-$ at circumneutral pH.

The fate of vanadate in the environment is largely controlled by surface processes. [32] Early work by Wehrli and Stumm considered the effects of adsorption on V^{IV} retention and oxidation, [32,33] and following work by Peacock and Sherman (2004) [34] examined the effects of vanadate complexation by the Fe^{III}-hydroxide goethite. More recent work has primarily focused on V retention by whole soils, [19,25,35–38] or individual minerals. [31,39,40] In all cases, surface interactions with the soil phases result in attenuation of vanadate from the aqueous phase, decreasing the soil toxicity potential. [36,37,41] While few spectroscopic studies have examined the mechanisms of vanadate retention by soil phases in detail, what has been done demonstrates that V forms covalent, inner sphere complexes with a host of mineral phases. [31,39–41] In the case of Fe^{II} bearing Fe oxides, this can result in electron transfer from the sorbent to the vanadate, resulting in adsorbed, or incorporated V^{IV}. [40] However, many details related to these surface-mediated retention processes are unknown. As such, more research has been called for by both scientists [3,7] and regulators [42,43] to

further our understanding of the geochemical controls that govern the mobility of V in the subsurface with the goal of improving the management of and reclamation processes for sites impacted by V contamination.

The goal of this study is to examine the mechanisms of V^V retention by selected Fe and Mn (hydr)oxide phases that have proven to have strong influences on the fate and transport of other, well-studied contaminants. [34,39,44–49] Thermodynamic parameters derived from Langmuir theory are used to assess the role of sorbent crystallinity and surface area on the the complexation V^V by manganese and iron oxides. Changes to the dominant modes of surface complextation with increasing V^V concentration are assessed spectroscopically to corroborate the adsorption affinities observed under equilibrium conditions.

II. Methods

Mineral Acquisition and Synthesis

Pyrolusite (Pyr) was purchased as ≥ 99% MnO_2 from Sigma-Aldrich and goethite (Gt) was purchased from Strem Chemicals. Hematite (Hm), 2-line ferrihydrite (Fhy), and hexagonal K-birnessite (Birn) were synthesized following the protocols of Cornell and Schwertmann, and Mckenzie respectively. [50,51] All oxides were finely ground with an agate mortar and pestle prior to characterization and use. Mineral synthesis is summarized in Appendix section VII.

Mineral Characterization

Each mineral was characterized by powder x-ray diffraction (XRD) using a Siemens D500 diffractometer equipped with a Cu Kα x-ray source operating at 40 kV.

Randomly oriented powders were mounted in an aluminum sample holder, and data were collected between 2 and 80 °2θ and 0.01° step size. Alignment of the diffractometer was previously calibrated using a quartz standard. JADE software (Materials Data, Inc.) was used for background subtraction, and peak positions and intensities were matched against reference data from the Joint Committee on Diffraction Standards Mineral Database, as well as the American Mineralogist Crystal Structure Database.

Surface area and pore-size analysis was performed using a Quantachrome Nova 2000e analyzer. Surface area analysis and collection of the corresponding pore-size distribution was conducted at 77.35 K using multi-point BET and adsorption-desorption Barrett-Joyner-Halenda (BJH) methods. All characterization supplementary data is presented in Table 2.1 and Appendix Figure 2.1.

Sorption Experiments

Ten concentrations of Na_3VO_4 were prepared, ranging from 5 to 2000 μM, and a no V control. Treatment solutions were composed of ultrapure water buffered with 10 mM PIPES that was brought to a pH of 7.00 using less than 400 μL 12 M NaOH per liter of solution. Ionic strength was adjusted with the addition of NaCl to a final concentration of 25 mM. The sorption experiments were carried out in static batch reactors using 50 ml vials with oxide loadings of 1 g L^{-1} for birnessite, goethite and ferrihydrite, and 100 mg L^{-1} for hematite and 2 g L^{-1} for pyrolusite due to their high and low surface areas, respectively.

All sorption experiments were performed in triplicate and stored in the dark with daily manual shaking. The sorption experiments were allowed to equilibrate for at least 3 weeks before syringe-filtration through a 0.22 μm PES membrane. All solutions were

analyzed for dissolved V, Mn, and Fe using ICP-OES. Solid phase samples were harvested for analysis by x-ray adsorption spectroscopy (XAS) via filter deposition onto 0.45 and 0.22 μm MCE membranes.

Plots of adsorbed V^V (q_{eq}) as a function of the equilibrium concentration (C_{eq}) were evaluated for the suitability of a single or two-site Langmuir model by examining the isotherms according to their Scatchard transformations ($\frac{q_{eq}}{C_{eq}}$ vs q_{eq}, equation 2) . [52,53] All data were found to exhibit two-site characteristics (see below),[52] and were modelled using the two-site Langmuir (2L) model described by equation 1. [54]

$$\text{Eq 1. } q_{eq} = \frac{q_{\max\_1} K_{L\_1} C_{eq}}{(1+K_{L\_1} C_{eq})} + \frac{q_{\max\_2} K_{L\_2} C_{eq}}{(1+K_{L\_2} C_{eq})}$$

Where: q_{eq} is the amount of V^V adsorbed to the oxide surface at equilibrium

C_{eq} is the aqueous equilibrium concentration of V^V

q_{max} is the adsorption capacity of a given site

K_L is the Langmuir constant of a given site

This model has the advantage of being easy to implement and interpret, while also yielding parameters that are amenable to energy calculations and reactive transport modelling. [55–58] A generalized reduced-gradient non-linear least-squares fitting algorithm [59] was used to fit the adsorption models to each data set using a global optimization method. [60] Optimization was performed by minimizing the weighted sum of squared residuals. Further details on calculations can be found in Appendix 1.

Aqueous V^V Speciation

Visual Minteq version 3.1 was used to calculate the V^V speciation for each equilibrium V^V_{aq} concentration obtained in the Langmuir isotherm experiments. Parameters for the calculation included 25 mM NaCl of background electrolyte, and the pH was fixed at 7 to account for the 10 mM of PIPES buffer. Results are presented in section III of Appendix 1.

X-ray Absorption Spectroscopy

X-ray absorption spectroscopy was conducted at the Stanford Synchrotron Radiation Lightsource. All samples were sealed in 13 μm thick Kapton tape. Room temperature vanadium K-edge EXAFS were collected at beamline 4-3 with a He purge box to reduce oxygen infiltration (< 0.15 %). Spectra were collected from 5235 eV to 6300 eV in fluorescence mode using a 7-channel Si drift detector (Canberra) and energy selection provided by a Si(111) crystal set oriented to φ = 90°. After each scan, the samples were moved vertically by 1 mm to avoid beam-induced photo-reduction. An in-line V^0 foil was used for energy calibration by setting the peak of the first derivative to 5465 eV. Background subtraction and normalization was performed using Athena software (Windows v9.26). [61]

Nonlinear least squares shell-by-shell fitting was performed using Artemis as an interface to Feff6 and IFEFFIT. [61] E_0 was set at the value of the absorption edge inflection point (~ 5482 eV) for each spectrum. Fourier transform of k^3-weighted χ(k) data was taken using a sine windowing function to acquire the pseudoradial structure function. Backscattering paths were then fit to the transformed data using multiple *k*-weighting to

derive relevant interatomic distances and coordination numbers. No solid-phase V^V precipitate was observed in the EXAFS data.

III. Results

Metal Oxide Sorbents characterization

The properties of the Fe and Mn oxides used in sorption experiments are presented in Table 2.1. XRD analysis confirmed the identity of each mineral phase (Appendix 1 Figure 2.3-7). Birn was synthesized with potassium in the interlayer space, matching previously reported hkl reflections. [62] The hexagonal symmetry of the Birn was verified by the ratio of d-spacings for the (11,20) and (31,02) reflections approximating $\sqrt{3}$ with a value of 1.69. [63–65] Further, the (31,02) reflection is symmetric and lacks the splitting indicative of orthogonal symmetry. [63] The (001) reflection was used to calculate the d_{001} and the coherent scattering domain (CSD) along the c* axis, which were 7.2 Å and 6.4 nm respectively and are consistent with previously reported d_{100} values [64] and 8.8 coherently stacked layers along the c* axis. [63,64,66,67] The CSD of the ab plane was calculated to be 6.1 nm from the (11,20) peak, in agreement with previous reports. [67] The BJH pore size distribution confirms a multimodal distribution of pore sizes between 2 and 8 nm with averages at 3.7 and 5.3 nm confirmed by BJH adsorption and desorption, respectively. The identity of Pyr was confirmed via the (110), (101), (200), (111), and (210) hkl reflections, [68] with bulk terminations defined by the (110), (101), and (100) faces. [69–71] The corresponding BJH distribution confirms the low porosity of the Pyr (Appendix 1 Figure 2.2), with an average porosity between 2-3 nm, and a pore volume 10% to that of Birn.

Ferrihydrite was confirmed by the presence of two broad reflections in the XRD pattern characteristic of 2-line Fhy corresponding to the (110) and (115) reflections. [72,73] The pore size distribution is centered at 1.5 nm. The second peak at 5.9 nm is a single data point observed only during the adsorption portion of the BJH analysis and likely represents an artifact. The total pore volume of the Fhy is comparable to Birn at > 0.1 $cm^3\ g^{-1}$.

Goethite was confirmed by XRD to match previously published patterns of the pure mineral. [74,75] The narrow FWHM of the (110) hkl reflection indicates the predominance of this crystal face at the Gt surface, a characteristic of this Fe phase that has been reported previously. [74,76–78] The pore volume of Gt is approximately four times greater than that of Pyr, and half that of Fhy with pore diameters ranging from 2 and 4.5 nm depending on the BJH method used.

The purity of the Hm phase was confirmed at the resolution of XRD, with the ratio of the (012), (104), and (110) hkl reflections supporting a rhombohedral morphology.[79] This geometry has been described previously for Hm synthesized using low-temperature aqueous methods. [50,80–82] Studies of pH effects on Hm particle size resulting from $Fe(NO_3)_3$ hydrolysis have similarly shown rhombohedral particles of ∼20 nm forming from conditions identical to those used in this study ($pH_{formation} = 2.7$).[83] Although pore size was observed to be ∼1 nm, the pore volume was comparable to that of Fhy. A possible explanation for this arises from the high surface area of our sample (61 $m^2\ g^{-1}$), which is two times greater than has been reported previously using the same synthesis method; [50,82] however, similar low-temperature hydrothermal methods have produced particles with comparable surface area. [80] Thus, a smaller particle size is expected and was observed with

a small fraction of particles passing through the 0.22 μm membranes. Therefore sedimentation was also used to separate the aqueous and solid phases on these samples prior to ICP-OES analysis.

Isotherm Modelling

Across all sorbents, the observed C_{eq} values ranged in value by six orders of magnitude. The isotherm results are presented in Figure 2.1 and each isotherm is characterized by a steep initial slope and a plateau characteristic of H-type isotherms. [84] The 2-site Langmuir model (2L model) was selected to model the adsorption interaction based on the multilinearity of the corresponding Langmuir isotherm (q_{eq} as a function of C_{eq}; Eq. 2) for each V-oxide interaction (Appendix 1 Figure 2.8) [52,84,85]

$$\text{Eq. 2 } K_d = \frac{q_{eq}}{C_{eq}}$$

where q_{eq} is in units of (μmol g^{-1}), and C_{eq} is in μM.

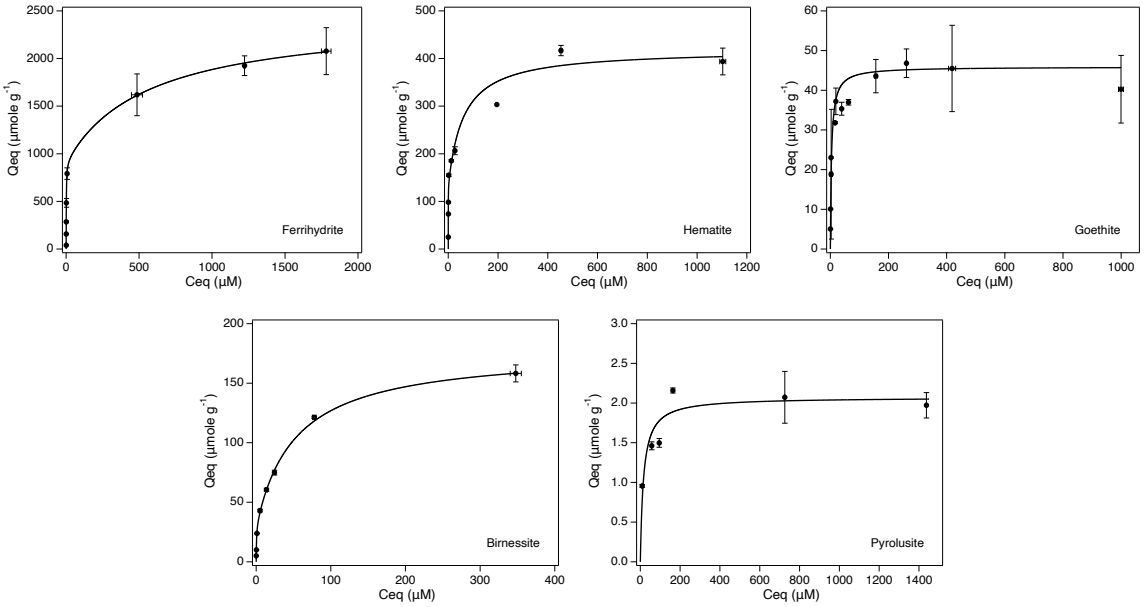

Figure 2.1 Plots of the aqueous equilibrium V^V concentration (µM) vs the adsorbed V^V (µmole g^{-1}). Note that the scale of x and y axes vary.

The suitability of the Langmuir model to the data is confirmed by a linear relationship between of C_{eq} and $\frac{Ceq}{q}$ (Appendix 1 Figure 2.9). Deviations from this linearity at low concentrations indicate the saturation of a small proportion of high-affinity sites which requires the application of the 2L model to accurately obtain model parameters q_{max} and K_L. The resulting values of q_{max} and K_L obtained from the model are reported in Table 2.1.

As expected, V^V showed greater retention on the oxide phases with lowest crystallinity, Birn and Fhy. When normalized for surface area, Fhy and Birn were found to contain more sites per nm^2 than their more crystalline counterparts, with overall site density following the order of Fhy > Hm > Birn > Gt > Pyr. Hematite and Fhy were found to have

> 1 site nm^{-1} for both high and low-affinity sites, while among the Mn oxides, only birnessite's low-affinity site had a density of > 1 nm^{-1}.

In a side-by-side comparison of the linearized Langmuir isotherms (Appendix 1 figure 2.9), the steeper slope of the Pyr isotherm is indicative of a low-affinity interaction across the entire range of V^V loading. Unlike the other oxides, a one-site Langmuir model was sufficient to model the data, with the addition of a second site consistently resulting in a q_{max} of 0 when the 2L model was applied. Application of one-site model revealed Pyr had an abundance of 1.07 sites nm^2 that reach half-saturation at 15.8 μM C_{eq}, corresponding to a surface loading of 1.04 μmole g^{-1}, whereas Birn exhibits a steep slope at low C_{eq} which inflects to a shallower slope after 13 μM C_{eq}. This suggests that Birn contains a relatively small number of high-affinity sites which become saturated below this concentration threshold. Applying the half-saturation formalism described by Sugihara et al., [86] the C_{eq} corresponding to half-saturation for the high-affinity sites on Birn is actually found to be much lower, at ~0.4 μM (Table 2.1), while 13 μM C_{eq} corresponds to approximately 12% of the total low-affinity site coverage.

Table 2.1 Fit parameters obtained via NLLS regression of the C_{eq} vs q data using a 2-site Langmuir model. Q_{max} is the maximum adsorption capacity for a given site, K_L is the Langmuir constant, K is the dimensionless equilibrium coefficient, $\Delta G°_{ads}$ is the free energy of adsorption and the RMSE and R^2 are goodness of fit parameters.

	(m^2 g^{-1})	mol g^{-1}		L mol^{-1}		$\Delta G°_{ad}$ (Kj mol^{-1})		Ratio of high to low $\Delta G°_{ad}$
	Surface Area	$q_{max}1$	$q_{max}2$	$Ln(K_L1)$	$Ln(K_L2)$	Site 1	Site 2	
Ferrihydrite	176.896	9.18E-04	1.52E-03	13.70	7.46	-33.96	-18.67	1.82
Hematite	61.286	2.85E-04	1.34E-04	9.71	15.99	-24.18	-39.56	1.64
Goethite	28.874	2.94E-05	1.65E-05	12.09	13.15	-30.01	-32.60	1.09
Birnessite	37.802	3.07E-05	1.47E-04	14.78	9.85	-36.61	-24.52	1.49
Pyrolusite	1.161	2.07E-06		11.05	-	-27.47	-	-

	Half-saturation Concentration (mole L^{-1})		sites/nm^2		Goodness of Fit	
	Site 1	Site 2	Site 1	Site 2	RMSE	R^2
Ferrihydrite	1.12E-06	5.74E-04	3.12	5.19	181.97	0.972
Hematite	6.06E-05	1.14E-07	2.80	1.31	43.98	0.937
Goethite	5.62E-06	1.95E-06	0.61	0.34	5.17	0.899
Birnessite	3.81E-07	5.26E-05	0.49	2.34	1.70	0.999
Pyrolusite	1.58E-05	-	1.07	-	0.22	0.810

The Gt Scatchard transformation shows that two distinct site types are present (Appendix 1 figure 2.8). Though the linearization of the Langmuir function results in a good fit ($R^2 = 0.9967$), the Scatchard transformation shows a steep initial descending slope suggestive of high-affinity sites, which are saturated when q_{eq} = 32 μmole g^{-1} (corresponding to a C_{eq} of 16 μM). The half-saturation concentration of Gt's high-affinity site (1.9 μM) corresponds to the rising edge of the isotherm with the half-saturation of the low-affinity site occurring after C_{eq} = 5.6 μM.

Hematite, which is highly crystalline (Appendix 1 figure 2.6), retained more V per gram of oxide than Gt (Table 2.1), likely due to the smaller particle size and higher surface area. In the linearized Langmuir plot (Appendix 1 figure 2.9), Hm displays an inflection in slope steepness akin to that observed for Birn at low V^V concentrations. This, along with the Scatchard transformation, affirms the need for a 2-site model. The high-affinity site on Hm has the highest affinity for V^V at low concentrations of all oxides examined, reaching half-saturation when C_{eq}= 100 nM. However, Hm low-affinity sites are of much lower affinity than Gt's low-affinity sites (Table 2.1), indicating that the larger q_{max} of Hm relative to Gt is a function of its higher surface area.

Two-line Fhy exhibited the highest q_{max} of any oxide, as well as the largest surface area (Table 2.1). Like Gt, Langmuir linearization resulted in a good fit ($R^2 = 0.995$), though the Scatchard plot again suggests that multiple sites are required to model the Fhy-V^V isotherm. The inflection between the rising edge and asymptotic portions of the data occur between C_{eq} = 6.5 μM and C_{eq}= 486 μM. The Fhy high-affinity sites reach half-saturation when C_{eq} = 1.1 μM, corresponding to a surface coverage of ~480 μmole g^{-1}; Fhy low-

affinity sites reach half-saturation when C_{eq} reaches 573 μM, corresponding to a Qeq of ~1700 μmole g^{-1}. Thus, when C_{eq}= 6.5 μM, the high-affinity sites are expected to be fully saturated.

Thermodynamic Calculations

Once the K_L were obtained from the 2L models, the equilibrium Gibbs free energy of adsorption was estimated for V^V at each site using the equation developed in Liu 2009:[87]

$$\text{Eq 3. } \Delta G°_{ads} = -RTln\left[\frac{K_L}{\gamma_e}\right]$$

Where R is the gas constant (8.314 J K^{-1} mol^{-1}), T is the absolute temperature in kelvin, K is the dimensionless equilibrium coefficient, and γ_e is the activity coefficient calculated using the Davies equation at an ionic strength of 0.025 M.[87]

Thermodynamic parameters determined for each V^V-sorbent interaction are provided in Table 2.1. When site affinity is calculated as a function of the free energy of adsorption $\Delta G°_{ads}$ (kJ mol^{-1}) the ratio of high-affinity to low-affinity sites across oxides follow the order observed for site density. Notably, Hm, Gt, and Birn have affinity ratios of ~1.5 or greater (Table 2.1), while Gt is approximately isoenergetic between the two sites (~1.09). This suggests that the surface site-type distribution for Gt towards V^V is relatively homogenous compared to Birn, Fhy, and Hm. This is likely a result of greater surface heterogeneity on Birn, Fhy, and Hm arising from a larger range of truncating hkl surfaces, particularly for Hm [79] relative to the predominance of the (110) plane at the surface of Gt. While a site affinity ratio could not be calculated for pyrolusite, it is likely comparable to Hm given the variety of hkl planes present at the oxide surface. [69]

Results from EXAFS

EXAFS spectra were collected on all samples with initial V^V concentrations of 1.5 mM, 100 μM and 50 μM. The distribution of expected aqueous V^V species was calculated using Visual MINTEQ 3.1 (Appendix 1 Section III) and were used to inform the shell-by-shell modelling of EXAFS spectra. Additionally, prior studies using EXAFS to characterize vanadate adsorption by ferrihydrite and goethite provided a baseline for comparison to the data in this study.[34,39,40] Results of the fitting are presented in Table 2.2 and Figure 2.2 A-B. Coordination numbers were constrained to the crystallographic values of vanadate for the V-O single scattering and intra-tetrahedral multiple scattering paths, and to the expected V-Me values for a given type of surface complex. Vanadium EXAFS spectra of the 1.5 mM pyrolusite sample could not be collected due high crystallinity and large particle size of pyrolusite leading to excessive elastic scattering of the incident x-rays, leading to detector saturation. While both bidentate-binuclear corner sharing complexes (^{2}C) and bidentate mononuclear edge sharing complexes (^{2}E) were observed between vanadate and the Fe oxides, vanadate primarily forms ^{2}E complexes on Mn oxides.

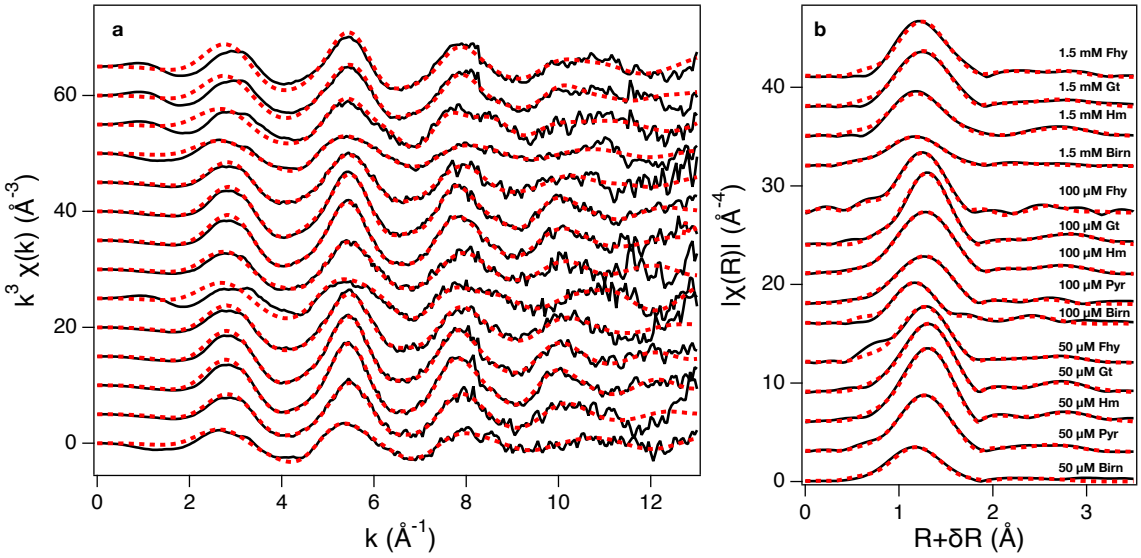

Figure 2.2 k^3-weighted V K-edge EXAFS of VV adsorbed onto metal oxides sorbents at different initial concentrations. b) Pseudoradial structure function of the EXAFS for samples. For consistency, samples are arranged identically in each panel.

Table 2.2 Results from non-linear least squares shell-by-shell fitting of the V K-edge EXAFS. CN is the coordination number, R is the interatomic distance in Å, σ^2 is a measure of the static and thermal disorder for each coordinating interatomic path, ΔE is a shift parameter to align the EXAFS theory with the data and S_0^2 is the amplitude reduction term.

Sample	CN	R(Å)	σ^2 (Å^2) x10^{-3}	S_0^2	ΔE	K range	R-factor	χ^2_{red}
1.5 mM Fhy								
V-O	2.2 (2)	1.66 (2)	0.9 (5)					
V-O	1.9 (2)	1.80 (3)	0.9 (5)					
V-O-O	12	3.174 (5)	1.7 (9)	0.9 (1)	-4 (5)	3-12.5	0.008	30.6
V-Fe	1	2.78 (5)	14.5 (5)					
V-Fe	2	3.33 (8)	22 (9)					
1.5 mM Goethite								
V-O	2.0 (8)	1.65 (6)	0.9 (6)					
V-O	2.0 (8)	1.78 (7)	0.9 (6)					
V-O-O	12	3.174 (6)	2 (1)	0.8 (1)	-4 (8)	3-11.5	0.007	41
V-Fe	1	2.8 (1)	20 (10)					
V-Fe	2	3.29 (7)	16 (8)					
1.5 mM Hem								
V-O	2.0 (5)	1.62 (5)	1.0 (5)					
V-O	2.0 (5)	1.76 (6)	1.0 (5)					
V-O-O	12	3.174 (5)	1.8 (9)	0.7 (2)	-9 (8)	3-12	0.011	51.5
V-Fe	1	2.66 (4)	14 (6)					
V-Fe	2	3.38 (9)	14 (6)					

1.5 mM Birn								
V-O	2.6 (1)	1.63 (2)	5.0 (2)					
V-O	1.4 (1)	1.79 (4)	5.0 (2)	0.71(1)	-9(1)	3.5-11	0.008	20
V-O-O	12	3.174 (5)	9.3 (5)					
100 uM Fhy								
V-O	2.1 (3)	1.66 (2)	1.0 (4)					
V-O	1.9 (3)	1.79 (2)	1.0 (4)					
V-O-O	12	3.124 (4)	1.8 (8)	0.72 (6)	-3 (1)	3-11	0.006	36.4
V-Fe	1	2.78 (8)	20 (10)					
100 uM Goethite								
V-O	2.0 (2)	1.67 (2)	1.0 (3)					
V-O	2.0 (2)	1.79 (2)	1.0 (3)					
V-O-O	12	3.174 (3)	1.9 (5)	0.83 (5)	-1 (2)	3-12.5	0.005	7.8
V-Fe	1	2.77 (3)	16 (4)					
V-Fe	2	3.37 (2)	13 (2)					
100 uM Hem								
V-O	2.1 (5)	1.67 (3)	1.0 (4)					
V-O	1.9 (5)	1.79 (3)	1.0 (4)					
V-O-O	12	3.17 (3)	1.8 (7)	0.88 (5)	-2 (2)	3-11	0.002	25.1
V-Fe	1	2.79 (3)	17 (5)					
V-Fe	2	3.40 (3)	19 (4)					
100 uM Pyr								
V-O	1.5 (2)	1.61 (2)	1.0 (2)					
V-O	2.5 (2)	1.74 (3)	1.0 (2)					
V-O-O	12	3.124 (2)	1.8(3)	0.70 (7)	-6 (3)	3-11.5	0.004	3
V-Mn	1	2.76 (4)	18 (2)					
100 uM Birn								
V-O	2.3 (1)	1.63 (2)	1.1 (2)					
V-O	1.7 (1)	1.80 (3)	1.1 (2)					
V-O-O	12	3.16 (5)	2.0 (4)	0.72 (8)	-7 (6)	3.5-12.5	0.014	4.2
V-Mn	1	2.65 (4)	14 (4)					
50 uM Fhy								
V-O	2.1 (3)	1.66 (2)	2 (2)					
V-O	1.9 (3)	1.78 (2)	2 (2)					
V-O-O	12	3.16 (2)	3 (3)	0.81 (7)	-3 (2)	3-12.5	0.001	5.2
V-Fe	1	2.78 (2)	18 (4)					
V-Fe	2	3.35 (2)	21 (4)					
50 uM Goethite								
V-O	1.7 (3)	1.65 (2)	1.0 (2)					
V-O	2.3 (3)	1.77 (1)	1.0 (2)					
V-O-O	12	3.16 (3)	1.8 (5)	0.90 (5)	-3 (2)	3-12.5	0.001	13.3
V-Fe	1	2.79 (3)	18 (5)					
V-Fe	2	3.37 (3)	17 (3)					
50 uM Hem								
V-O	1.7 (3)	1.65 (2)	0.9 (4)					
V-O	2.3 (3)	1.77 (2)	0.9 (4)					
V-O-O	12	3.17 (3)	1.7 (7)	0.93 (6)	-3 (2)	3-12.5	0.002	32.4
V-Fe	1	2.77 (3)	15 (3)					
V-Fe	2	3.37 (3)	17 (3)					
50 uM Pyr								
V-O	1.9 (9)	1.65 (5)	1.0 (3)					
V-O	2.1 (9)	1.77 (5)	1.0 (3)					
V-O-O	12	3.15 (5)	1.8 (6)	0.72 (9)	-3 (4)	3-11.5	0.003	28.7
V-Mn	1	2.79 (7)	18 (3)					
V-Mn	2	3.35 (7)	20 (10)					
50 uM Birn								
V-O	2.4 (1)	1.63 (2)	3.1 (4)					
V-O	1.6 (1)	1.77 (3)	3.1 (4)	0.71 (2)	-8 (1)	3.5-12	0.011	9.2
V-O-O	12	3.13 (4)	5.7 (8)					

IV. Discussion

Iron Oxides

The free energy of adsorption, $\Delta G°_{ads}$ was negative for all observed interactions, indicating a thermodynamically spontaneous process. Hematite and Gt exhibited similar $\Delta G°_{ads}$ for V^V, while the $\Delta G°_{ads}$ for Fhy was ~20% less, suggesting that affinity increases with crystallinity, which has been observed in other adsorption systems. A similar phenomena has been observed for As^{III} adsorption on these minerals despite the typically anhydrous nature of Hm, and likely has to do with their ability to accommodate similar modes of adsorption. [88] For the Hm used in this study, the ratio of the intensities of the (104) and (113) peaks was ~3.1, where a ratio of ~4 would be indicative of pure anhydrous α-Fe_2O_3.[50] This indicates that the Hm used here is partially hydrated, with Fe vacancies to balance the presence of H^+ and a partially hydroxylated surface that can better accommodate the adsorption of the V^V oxyanion along the (001) and (110) faces. [80,88–90] In contrast, the (110) face of Gt is both the most abundant face and is also hydroxylated, which supports oxyanion adsorption with minor contributions from the (101) face. [78,88,91,92]

The difference in site affinity between the Gt and Hm can be described by differences in their points of zero charge (pzc). Typical pzc for Gt range 7.5-9.5, where 8.5 was used in a study modeling the adsorption of vanadate by Gt. [34,90,93] Pzc of Hm is generally slightly higher, with a range of 8.4-9.4. [90,93] The higher pzc of Hm results in increased attraction for the $H_2VO_4^-$ anion (pK_{a1}= 7.91,[94] pK_{a2} = 8.06, [12] pK_{a3} = 8.8[7]) which dominates the species distribution of V^V_{aq} when $[V^V] < 1.5$ mM at pH 7 (Appendix 1 Section III). Additionally, imperfections in the (001) and (110) faces of Hm as a result of

Fe vacancies and hydration increase the pzc leading to longer singly coordinated Fe-O bonds at the Hm surface, resulting in pzc ~ 11 for select faces. [90]

Due to the predicted presence of polyvanadate species at all but the lowest concentrations tested, it remains a possibility that Hm can retain highly-charged polymeric vanadate species more efficiently than Gt. Precedence for this was previously established by the observations of Peacock and Sherman[34], who noted a decreased retention of V by Gt at pH 7 when concentrations allowed for polymeric species to form. Using a combination of *ab initio* modelling and EXAFS measurements, Peacock and Sherman ruled out the formation of vanadate ^{2}E complexes on Gt in favor of ^{2}C complexes in the pH range of 2.85 to 8.9 and V^V concentrations of approximately 50 and 500 μM. [34] The authors argued that the formation of ^{2}E complex should not be considered based on modelled energetic favorability and the *a priori* requirement that multiple scattering paths should be included in FEFF calculations, where failure to do so would result in spurious detection of a ^{2}E complex. [34] However, another study of vanadate adsorption on ferrihydrite utilized multiple scattering and wavelet transform (WT) analysis,[39] concluding that a ^{2}E $Fe^{III}(O,OH)_6$-vanadate complex exists for ferrihydrite, with the vanadate tetrahedron distorted into an approximately square-planar geometry. Their results supported the conclusion that multiple scattering within the vanadate tetrahedron hides the EXAFS contribution from the iron in the second shell of the EXAFS pseudo-RSF plot, and no ^{2}C complex was reported. [39] Later work by Vessey and Lindsay [40] corroborated these results for ferrihydrite. However, whereas Larsson et al. had included several multiple scattering paths to improve the fit that went beyond the intra-tetrahedral V-O-O path at ~ 3.15 Å

(including V-O-Fe and V-O-O hinge/rattle paths between 3 and 4 Å), Vessey and Lindsay was able to fit a ^{2}C V-Fe complex, and reported both ^{2}E and ^{2}C V-Fe distances that were comparable to the *ab initio* calculated V-Fe distances of Peacock and Sherman. [34,39,40]

In our analysis, both ^{2}E and ^{2}C complexes were observed for Fhy, Gt, and Hm. Twelve intra-tetrahedra V-O-O MS paths were included in all fits, and did not interfere with the detection of the ^{2}E complex, which was similar to what was observed by Larsson et al. [39] Further, our observed V-Fe distance for the ^{2}E complex on Fhy was similar to that reported by Larsson et al. [39] at 2.78 Å, and longer than that reported by Vessey and Lindsay, which may be due to the lower ionic strength (IS) employed by this study and in Larsson et al. 2017 (10 mM, as compared to IS = 50 mM in Vessey and Lindsay 2020).[39,40] Lower IS leads to an increase in the thickness of the Stern layer at the mineral surface, and has been attributed to differences in vanadate adsorption modes in earlier studies. [95]

Our study agreed with the conclusion of Peacock and Sherman [34] and Larsson et al. [39] regarding the importance of the MS paths to the quality of the fit. Specifically, the twelve intra-tetrahedral V-O-O paths at 3.12-3.17 Å were found to be the most important. While Peacock and Sherman described the importance of the various MS paths, they did not report the fitted half-path lengths nor the values of σ^2 for these paths, making comparisons difficult. Given the distance resolution of EXAFS allowable by Eq. 4:

$$\text{Eq.4 } \Delta R = \frac{\pi}{2\Delta K}$$

the intra-tetrahedral MS paths ranging 3.12-3.17 Å is relatively comparable to the ^{2}C V-Fe distance of ~3.30 Å making then difficult to distinguish unless a Δk greater than 10 is used, which is difficult to achieve at low surface loadings. Similarly, the V-O-Fe path for the ^{2}E

complex, while a weak contributor to the overall EXAFS signal can occur from 3.19-3.25 Å, further interfering with the detection of the ^{2}C complex unless the signal is sufficiently strong. One method that has used to resolve such interreferences by fitting the EXAFS spectra with multiple k-weights simultaneously, where different *k*-weightings will amplify specific segments of the spectrum. For example, MS paths are typically strongest at low values of *k*, and thus are most emphasized by low *k*-weighting, while single-scattering paths are present throughout the spectra and can be emphasized by higher k weights. When this approach was applied in this study, the results for V adsorption on Fhy are comparable to that presented by Larsson et al. [39] However, we did not observe an improvement to the fit with the inclusion of further MS paths. Iterations of our fits included all combinations of ^{2}E, ^{2}C, ^{2}E V-O-Fe at 3.25 Å, ^{2}C V-O-Fe at 3.50 Å and intra-tetrahedral hinge and rattle V-O-O contributions at 3.45 Å. Further, we found that the 4+12 V-O-O rattle and hinge paths at 3.45 described by Larsson et al.[39] occur predominately in the Na_3VO_4 crystal structure often used as a source of V-O and V-O-O paths for V^V EXAFS. As such we do not expect them to occur in a surface complex with any of the minerals tested.

Like Larsson et al. [39] and Vessey and Lindsay, [40] we observed relatively large Debye-Waller factors for the ^{2}E V^V-Fe complex, which may be a result of heterogeneity in the V binding environment. Although we also observed large Debye-Waller factors for the V^V ^{2}C complexes as well, we attribute this to the room-temperature data collection, and relatively short ΔK range refined in the fitting due to degradation of the data quality at values of *k* greater than 11.5 Å^{-1} in many cases.

Inner-sphere adsorption of polymeric oxometallates has been observed at the surface of Hm for polyvanadate and polytungstate. [31,96] Specifically, Hm appears to effectively retain $H_2V_2O_7^{2-}$ and $V_4O_{12}^{4-}$ at its surface. [31] These species constituting ~5% of total V^V_{aq} below 100 μM and ~30% below 1000 μM (Appendix 1 Section III). The affinity for these polyvanadate species for Hm is attributed to an association with the (001) surface and is greater than at the Fhy surface. [31] This provides an explanation for the greater affinity of V on Fhy in this study, as the Hm produced here exhibited minimal basal (001) character, despite a low amount of platy morphology implied by the presence of a small (006) peak in the powder XRD pattern (Appendix 1 Figure 2.6). Instead, surfaces appear to be dominated by (024), (104), (110) and possibly (014) faces (Appendix 1 Figure 2.6). [79,97] As noted by Venema et al.[90] and Ona-Nguema et al.[88], singly-coordinated reactive oxygens at the (110) surface are ideal for supporting ^{2}C surface complexes and are the most likely candidate for hosting adsorbed monomeric V in the ^{2}C configuration. The ratio of singly-coordinated O to doubly-coordinated O of the Fe face-sharing octahedra is 2:1 per unit cell. The ^{2}E complexes may form at this face and the (001) face, which is predicted to have 3 singly-coordinated O atoms per unit cell forming the face of a single Fe octahedron with less likely formation at the (110) face due to the lower favorability presented by the doubly-coordinated O atoms.

Ferrihydrite displayed the greatest adsorption capacity for V^V. This is a function of its high surface area, site density, Fe vacancies, and abundance of singly- and doubly-coordinated -OH groups present at its surface. [39,73,88] The pH_{pzc} for 2-line Fhy ranges from 7-8; [98] therefore, the Fhy surface holds a slight positive charge at pH 7 and is expected to

electrostatically attract aqueous V^V anions. Given the high degree of disorder in the stacking of Fhy lattice planes,[99] the formation of the ^2E complex with vanadate reported previously[39] and in this work likely occurs at the (100) surface. [88] Several structural motifs have been reported for 2-line Fhy including a maghemite-like structure, a hexagonally-stacked double-chain like structure, a Baker-Figgis δ-Keggin-like cluster, and closely-packed anionic sheets with high amounts of stacking disorder and interlayer Fe. [73,99,100] Thus, it is difficult to determine which hkl surface is most favorable for V^V adsorption; however, it is likely that the presence of Fe vacancies and singly-coordinated oxygen makes the (100) and (010) faces more likely to host adsorbed V^V than the (001) face due to the relative lack of singly-coordinated O on the (001) face.[73,100] In the model proposed by Michel et al. [100], the (100) and (010) faces host doubly and singly coordinated O in a 7:1 ratio with equivalent positions for ^2E or ^2C adsorption.

It is possible that the high capacity of Fhy for V^V is due to polymeric V complexation. While observed for other polymerizing d-block elements (Mo, W) on Hm,[96,101] the paucity of comparable observations for polymeric V on Fhy is likely due to the and concentration ranges tested (≤100 μM). [39,40,95] However, recent evidence supports the retention of tetrahedrally-coordinated polyvanadate species such as pyrovanadate (V_2) but not octahedrally-coordinated V^V species such as decavanadate (V_{10}) at the surface of Fhy. [31] Unlike Mo, epitaxial and surface-catalyzed growth of the polyvanadate species is not expected under the conditions examined in the present study[101] due to the rapid kinetics of polymeric V^V formation, [102] and steric hindrance due to the large size of decavanadate.

[31] Thus, it is likely that the process of V_2 complexation is an adsorption process as opposed to surface-catalyzed polymerization.

The limitations of EXAFS also complicate the resolution of polyvanadate surface species. It is difficult to distinguish between atoms of similar atomic number using EXAFS, and thus it can be challenging to discern between V and Fe at a similar half-path length. [103] However, the adsorption of V_2 has been shown as pyrovanadate bound to an octahedrally-coordinated oxo-manganese (similar in atomic number to V and Fe indicating low steric hindrance). [104] Finally, an examination of the ^{2}C distances obtained for the 1.5 mM V^V treatments of Fhy and Gt reveal V-Fe distances of 3.29 to 3.33, which are comparable to previous studies; [34,40] however, the ^{2}C distance for V^V on Hm was 3.38 Å. While it is possible that the V-Fe distance is greater with Hm than Fhy or Gt, 3.38 Å is also the average between a V-Fe ^{2}C distance at 3.33 Å and the crystallographic V-V distance of pyrovanadate at 3.42 Å. Given the difficulty in distinguishing between V and Fe by EXAFS, it is likely the resultant distance is contributed by both backscattering atomic pairs, providing evidence for polyvanadate retention by Hm.

Manganese Oxides

Vanadium(V) retention on Mn oxides increased as a function of decreasing crystallinity similar to adsorption of V^V on Fe (oxyhydr)oxides, with more exergonic V^V adsorption on Birn than on Pyr. Although methods used to calculate estimates of the dimensionless equilibrium coefficient (K) from the Langmuir constant have been rigorously established, [56,87,105,106] some variability between methods exists (primarily K_L's derivation from a linearized Langmuir equation). [105] While K_L was not derived from linear

regression in this study, it appears to be the most common approach, allowing for the results of this study to be compared to values obtained for other adsorption phenomena.

The $\Delta G°_{ads}$ for the low-energy site of Birn was approximately equal to that of the high energy site on Pyr. The lower affinity of Pyr for V^V adsorption is likely due to the anhydrous nature of the bulk mineral. While the formation of an amorphous, hydrous layer has been reported in nanophase Pyr when exposed to solvation by water, no such amorphous MnOOH formation has been reported for the surface of bulk-phase Pyr. [107] Therefore, singly coordinated O and reactive -OH groups available on Pyr is expected to be low, which likely explains the low amount of V^V retained. This hypothesis is further supported by bond valance calculations yielding high degrees of terminal O bond saturation in Pyr relative to 2-line Fhy and Birn. [98] This leads to lower likelihood that terminal O at the Pyr surface will form the new bonds needed for inner-sphere adsorption. Furthermore, Pyr has been reported as having higher surface energy than Birn, [107,108] which leads to stronger retention of water from hydrating layer. This results in greater energy barrier for V^V to displace hydrating water molecules on Birn during inner-sphere complexation. In the 100 μM V^V-Birn incubation, the ^{2}E V-Mn distance was 2.65 Å, compared to 2.76 Å with Pyr. However, V EXAFS of solids from 50 μM and 1.5 mM V^V-Birn incubations did not reveal a distinct V-Mn peak. This may indicate the formation of a vanadate outer-sphere complex at the birnessite surface, given only contributions from the coordinating oxygen and V-O-O MS paths were observed. The $\chi(k)$ data for these samples resembles the selenate EXAFS of Hayes et al. 1987, which were similarly attributed to an outer sphere complex due to a lack of Se-Me contributions.[109] Only one prior study has looked at vanadate

associated with birnessite using V EXAFS. [110] Yin et al. examined how birnessite synthesized with various degrees of V^V doping would affect the oxide's ability to scavenge metal cation contaminants. They found that Pb^{2+} scavenging was enhanced in the doped birnessite and cited spectroscopic evidence to support the formation of an MnO_6-V_6O_{16}-Pb^{II} oxyanion bridge. They attribute this to a surface coating of $V_6O_{16}^{2-}$ hexameric vanadate polymers, yielding possible V-Mn distances of 2.97-3.06 and 3.43-3.5 Å, much longer than what was observed in this study. [110]

Synthetic Pyr generally has a higher pH_{pzc} than Birn, with reported values ranging from 5.98 to 4.3 [111] (Birn pH_{pzc} ~ 2 - 4). [67,112,113] However, a much higher pH_{pzc} for Birn edge sites has been proposed ranging from 6 - 7. [67,98,114] At pH 7, the surface of Pyr is thus expected to be dominated by negatively-charged, saturated oxygens, which can electrostatically repel $H_2VO_4^-$. As a result, we attribute ^{2}C and ^{2}E complexes at the surface of Pyr to form at the (110) and (100) faces, with the ^{2}C forming more favorably due to the solvent-facing orientation of the singly coordinated O at these faces. In contrast, reactive terminal hydroxyl groups on Birn are available for inner-sphere adsorption and ligand exchange. This also explains why no V^V adsorption moieties were observed at the Birn layer vacancies with in the *ab* plane, as these are a source of negative layer charge that contributes heavily to the low pH_{pzc} of the bulk Birn, repelling the negatively charged V^V. [67,115]

The results from the V k-edge EXAFS corroborate the expected sorption affinities predicted by a comparison of the surface pzc's of the minerals. The peak corresponding to the nearest Mn neighbor in the pseudo-RSF plot is markedly lower in amplitude for the Pyr

samples than it is for results from 100 μM V^V-Birn incubation, reflecting a lower surface loading (Figure 2.2). However, σ^2 values for the V-Mn paths are greater for Pyr than Birn (Table 2.2). This could be due to measurements being conducted at room temperature as well as the perturbation of the Pyr surface by hydration leading to heterogenous bonding environments. The authors who first reported hydration-induced perturbation of the surface of nano-Pyr, but not bulk Pyr, utilized XRD as their primary method of detection. [107] While this was sufficient for the nano-Pyr due to its large surface area, the low surface area of bulk-phase Pyr was below detection limit by XRD. However, a hydrated amorphous phase developing at the Pyr surface would be situated ideally to interact with adsorbents such as the V^V examined here, which is theoretically measurable with EXAFS. Thus, competition for aqueous vanadate between a discontinuous, amorphous Mn phase and exposed faces of unreacted Pyr, taken in conjunction with the EXAFS measurements being taken at room temperature may explain the relatively large σ^2 and interatomic distance error. Future studies probing the alteration of the surface of macro-crystalline Pyr by hydration, and it's resulting effects on adsorption are needed to verify this hypothesis. Finally, we were unable to resolve an alternative explanation for the low retention V by Pyr that relies on an outer-sphere adsorption mechanism due to the resolution of the V EXAFS at the concentrations examined.

V. Conclusion

Previous studies examining the interactions of aqueous V^V at the water-solid interface have focused primarily on Gt and Fhy, [34,39] and rarely discuss the role of polynuclear V^V species in adsorption. [31] Additionally, no studies to our knowledge have

characterized the interactions of V^V with Mn oxides in an environmental context. The present study examined the adsorption of V^V on several common Fe (oxyhydr)oxides and Mn (hydr)oxides using an isotherm approach paired with EXAFS to determine uptake affinities and coordination geometries. While mononuclear V^V was the only species detected via EXAFS at and below 100 μM V^V, evidence for polyvanadate adsorption could be detected with 1.5 mM V^V. Overall, we observed higher adsorption capacity of V^V by mineral phases that exhibited low crystallinity and high surface area. The exergonic adsorption of V^V onto both the Fe and Mn (hydr)oxides examined suggests that V adsorption is thermodynamically favorable for a range of surfaces that display differing levels of hydration and Me-O bond saturations. The ability of V^V to adsorb onto Fe (oxyhydr)oxides and Mn (hydr)oxides octahedra has implications for competitive adsorption-desorption interactions in the presence of common oxyanions such as phosphate, with potential for complex competitive interactions to occur with coexisting oxoanionic contaminants such as arsenate, molybdate or tungstate. Due to the ubiquity of ferrihydrite and hematite in terrestrial systems and the high affinity of V^V for these minerals, they are likely to be the dominant sorbent phases in most systems.

VI. Supporting Information

The Supporting Information for chapter 2 is available in Appendix 1

VII. References

(1) Wright, M. T.; Belitz, K. Factors Controlling the Regional Distribution of Vanadium in Groundwater. *Ground Water* **2010**, *48* (4), 515–525. https://doi.org/10.1111/j.1745-6584.2009.00666.x.

(2) Wright, M. T.; Stollenwerk, K. G.; Belitz, K. Assessing the Solubility Controls on Vanadium in Groundwater, Northeastern San Joaquin Valley, CA. *Applied Geochemistry* **2014**, *48*, 41–52. https://doi.org/10.1016/j.apgeochem.2014.06.025.

(3) Watt, J. A. J.; Burke, I. T.; Edwards, R. A.; Malcolm, H. M.; Mayes, W. M.; Olszewska, J. P.; Pan, G.; Graham, M. C.; Heal, K. V.; Rose, N. L.; Turner, S. D.; Spears, B. M. Vanadium: A Re-Emerging Environmental Hazard. *Environ. Sci. Technol.* **2018**, *52* (21), 11973–11974. https://doi.org/10.1021/acs.est.8b05560.

(4) Rehder, D. The Role of Vanadium in Biology. *Metallomics* **2015**, *7* (5), 730–742. https://doi.org/10.1039/C4MT00304G.

(5) Smit, C. Environmental Risk Limits for Vanadium in Water : A Proposal for Water Quality Standards in Accordance with the Water Framework Directive. *Milieurisicogrenzen voor vanadium : Een voorstel voor waterkwaliteitsnormen volgens de Kaderrichtlijn water* **2012**.

(6) Schiffer, S.; Liber, K. Estimation of Vanadium Water Quality Benchmarks for the Protection of Aquatic Life with Relevance to the Athabasca Oil Sands Region Using Species Sensitivity Distributions. *Environmental Toxicology and Chemistry* **2017**, *36* (11), 3034–3044. https://doi.org/10.1002/etc.3871.

(7) Gustafsson, J. P. Vanadium Geochemistry in the Biogeosphere –Speciation, Solid-Solution Interactions, and Ecotoxicity. *Applied Geochemistry* **2019**, *102*, 1–25. https://doi.org/10.1016/j.apgeochem.2018.12.027.

(8) Larsson, M. A.; Baken, S.; Gustafsson, J. P.; Hadialhejazi, G.; Smolders, E. Vanadium Bioavailability and Toxicity to Soil Microorganisms and Plants. *Environmental Toxicology and Chemistry* **2013**, *32* (10), 2266–2273. https://doi.org/10.1002/etc.2322.

(9) Zhang, B.; Qiu, R.; Lu, L.; Chen, X.; He, C.; Lu, J.; Ren, Z. J. Autotrophic Vanadium(V) Bioreduction in Groundwater by Elemental Sulfur and Zerovalent Iron. *Environ. Sci. Technol.* **2018**, *52* (13), 7434–7442. https://doi.org/10.1021/acs.est.8b01317.

(10) Singh, B. B. Effect of Vanadium on the Growth, Yield and Chemical Composition of Maize (Zea Mays L.). *Plant Soil* **1971**, *34* (1), 209–213. https://doi.org/10.1007/BF01372773.

(11) Martin, H. W.; Kaplan, D. I. Temporal Changes in Cadmium, Thallium, and Vanadium Mobility in Soil and Phytoavailability under Field Conditions. *Water, Air, & Soil Pollution* **1998**, *101* (1), 399–410. https://doi.org/10.1023/A:1004906313547.

(12) Huang, J.-H.; Huang, F.; Evans, L.; Glasauer, S. Vanadium: Global (Bio)Geochemistry. *Chemical Geology* **2015**, *417*, 68–89. https://doi.org/10.1016/j.chemgeo.2015.09.019.

(13) Schlesinger, W. H.; Klein, E. M.; Vengosh, A. Global Biogeochemical Cycle of Vanadium. *Proceedings of the National Academy of Sciences* **2017**, *114* (52), E11092–E11100. https://doi.org/10.1073/pnas.1715500114.

(14) Nesbitt, J. A.; Lindsay, M. B. J. Vanadium Geochemistry of Oil Sands Fluid Petroleum Coke. *Environ. Sci. Technol.* **2017**, *51* (5), 3102–3109. https://doi.org/10.1021/acs.est.6b05682.

(15) Gehring, A. U. The Chemical Form of Vanadium (IV) in Kaolinite. *Clays and Clay Minerals* **1993**, *41* (6), 662–667. https://doi.org/10.1346/CCMN.1993.0410604.

(16) Gehring, A. U.; Fry, I. V.; Luster, J.; Sposito, G. Vanadium in Sepiolite: A Redox-Indicator for an Ancient Closed Brine System in the Madrid Basin, Central Spain. *Geochimica et Cosmochimica Acta* **1994**, *58* (16), 3345–3351. https://doi.org/10.1016/0016-7037(94)90090-6.

(17) Balan, E.; Villiers, J. P. R. D.; Eeckhout, S. G.; Glatzel, P.; Toplis, M. J.; Fritsch, E.; Allard, T.; Galoisy, L.; Calas, G. The Oxidation State of Vanadium in Titanomagnetite from Layered Basic Intrusions. *American Mineralogist* **2006**, *91* (5–6), 953–956. https://doi.org/10.2138/am.2006.2192.

(18) Yang, J.; Tang, Y.; Yang, K.; Rouff, A. A.; Elzinga, E. J.; Huang, J.-H. Leaching Characteristics of Vanadium in Mine Tailings and Soils near a Vanadium Titanomagnetite Mining Site. *Journal of Hazardous Materials* **2014**, *264*, 498–504. https://doi.org/10.1016/j.jhazmat.2013.09.063.

(19) Wisawapipat, W.; Kretzschmar, R. Solid Phase Speciation and Solubility of Vanadium in Highly Weathered Soils. *Environ. Sci. Technol.* **2017**, *51* (15), 8254–8262. https://doi.org/10.1021/acs.est.7b01005.

(20) Bordage, A.; Balan, E.; de Villiers, J. P. R.; Cromarty, R.; Juhin, A.; Carvallo, C.; Calas, G.; Sunder Raju, P. V.; Glatzel, P. V Oxidation State in Fe–Ti Oxides by High-Energy Resolution Fluorescence-Detected X-Ray Absorption Spectroscopy. *Phys Chem Minerals* **2011**, *38* (6), 449–458. https://doi.org/10.1007/s00269-011-0418-3.

(21) Schwertmann, U.; Pfab, G. Structural Vanadium and Chromium in Lateritic Iron Oxides: Genetic Implications. *Geochimica et Cosmochimica Acta* **1996**, *60* (21), 4279–4283. https://doi.org/10.1016/S0016-7037(96)00259-1.

(22) Canil, D. Vanadium Partitioning between Orthopyroxene, Spinel and Silicate Melt and the Redox States of Mantle Source Regions for Primary Magmas. *Geochimica et Cosmochimica Acta* **1999**, *63* (3), 557–572. https://doi.org/10.1016/S0016-7037(98)00287-7.

(23) Telfeyan, K.; Johannesson, K. H.; Mohajerin, T. J.; Palmore, C. D. Vanadium Geochemistry along Groundwater Flow Paths in Contrasting Aquifers of the United States: Carrizo Sand (Texas) and Oasis Valley (Nevada) Aquifers. *Chemical Geology* **2015**, *410*, 63–78. https://doi.org/10.1016/j.chemgeo.2015.05.024.

(24) Groover, K. D.; Izbicki, J. A. Selected Trace-Elements in Alluvium and Rocks, Western Mojave Desert, Southern California. *Journal of Geochemical Exploration* **2018**. https://doi.org/10.1016/j.gexplo.2018.09.005.

(25) Hudson-Edwards, K. A.; Byrne, P.; Bird, G.; Brewer, P. A.; Burke, I. T.; Jamieson, H.; Macklin, M.; Williams, R. Origin and Fate of Vanadium in the Hazeltine Creek Catchment Following the 2014 Mount Polley Mine Tailings Spill, British Columbia, Canada. *Environ. Sci. Technol.* **2019**. https://doi.org/10.1021/acs.est.8b06391.

(26) Shi, Y. X.; Mangal, V.; Guéguen, C. Influence of Dissolved Organic Matter on Dissolved Vanadium Speciation in the Churchill River Estuary (Manitoba, Canada). *Chemosphere* **2016**, *154*, 367–374. https://doi.org/10.1016/j.chemosphere.2016.03.124.

(27) Pourret, O.; Dia, A.; Gruau, G.; Davranche, M.; Bouhnik-Le Coz, M. Assessment of Vanadium Distribution in Shallow Groundwaters. *Chemical Geology* **2012**, *294–295*, 89–102. https://doi.org/10.1016/j.chemgeo.2011.11.033.

(28) Aureliano, M. Decavanadate Toxicology and Pharmacological Activities: V10 or V1, Both or None? https://www.hindawi.com/journals/omcl/2016/6103457/abs/ (accessed 2019 -01 -28). https://doi.org/10.1155/2016/6103457.

(29) Aureliano, M.; Crans, D. C. Decavanadate (V10O286-) and Oxovanadates: Oxometalates with Many Biological Activities. *Journal of Inorganic Biochemistry* **2009**, *103* (4), 536–546. https://doi.org/10.1016/j.jinorgbio.2008.11.010.

(30) Howarth, O. W. Vanadium-51 NMR. *Progress in Nuclear Magnetic Resonance Spectroscopy* **1990**, *22* (5), 453–485. https://doi.org/10.1016/0079-6565(90)80007-5.

(31) Vessey, C. J.; Schmidt, M. P.; Abdolahnezhad, M.; Peak, D.; Lindsay, M. B. J. Adsorption of (Poly)Vanadate onto Ferrihydrite and Hematite: An In Situ ATR–FTIR Study. *ACS Earth Space Chem*. **2020**. https://doi.org/10.1021/acsearthspacechem.0c00027.

(32) Wehrli, B.; Stumm, W. Vanadyl in Natural Waters: Adsorption and Hydrolysis Promote Oxygenation. *Geochimica et Cosmochimica Acta* **1989**, *53* (1), 69–77. https://doi.org/10.1016/0016-7037(89)90273-1.

(33) Wehrli, B.; Stumm, W. Oxygenation of Vanadyl(IV). Effect of Coordinated Surface Hydroxyl Groups and Hydroxide Ion. *Langmuir* **1988**, *4* (3), 753–758. https://doi.org/10.1021/la00081a045.

(34) Peacock, C. L.; Sherman, D. M. Vanadium(V) Adsorption onto Goethite (α-FeOOH) at PH 1.5 to 12: A Surface Complexation Model Based on Ab Initio Molecular Geometries and EXAFS Spectroscopy. *Geochimica et Cosmochimica Acta* **2004**, *68* (8), 1723–1733. https://doi.org/10.1016/j.gca.2003.10.018.

(35) Burke, I. T.; Mayes, W. M.; Peacock, C. L.; Brown, A. P.; Jarvis, A. P.; Gruiz, K. Speciation of Arsenic, Chromium, and Vanadium in Red Mud Samples from the Ajka Spill Site, Hungary. *Environ. Sci. Technol.* **2012**, *46* (6), 3085–3092. https://doi.org/10.1021/es3003475.

(36) Larsson, M. A.; Baken, S.; Smolders, E.; Cubadda, F.; Gustafsson, J. P. Vanadium Bioavailability in Soils Amended with Blast Furnace Slag. *Journal of Hazardous Materials* **2015**, *296*, 158–165. https://doi.org/10.1016/j.jhazmat.2015.04.034.

(37) Larsson, M. A.; D'Amato, M.; Cubadda, F.; Raggi, A.; Öborn, I.; Kleja, D. B.; Gustafsson, J. P. Long-Term Fate and Transformations of Vanadium in a Pine Forest Soil with Added Converter Lime. *Geoderma* **2015**, *259–260*, 271–278. https://doi.org/10.1016/j.geoderma.2015.06.012.

(38) Larsson, M. A.; Hadialhejazi, G.; Gustafsson, J. P. Vanadium Sorption by Mineral Soils: Development of a Predictive Model. *Chemosphere* **2017**, *168*, 925–932. https://doi.org/10.1016/j.chemosphere.2016.10.117.

(39) Larsson, M. A.; Persson, I.; Sjöstedt, C.; Gustafsson, J. P. Vanadate Complexation to Ferrihydrite: X-Ray Absorption Spectroscopy and CD-MUSIC Modelling. *Environ. Chem.* **2017**, *14* (3), 141–150. https://doi.org/10.1071/EN16174.

(40) Vessey, C. J.; Lindsay, M. B. J. Aqueous Vanadate Removal by Iron(II)-Bearing Phases under Anoxic Conditions. *Environ. Sci. Technol.* **2020**. https://doi.org/10.1021/acs.est.9b06250.

(41) Baken, S.; Larsson, M. A.; Gustafsson, J. P.; Cubadda, F.; Smolders, E. Ageing of Vanadium in Soils and Consequences for Bioavailability. *European Journal of Soil Science* **2012**, *63* (6), 839–847. https://doi.org/10.1111/j.1365-2389.2012.01491.x.

(42) Howd, R. palvanadium.pdf https://oehha.ca.gov/media/downloads/water/chemicals/nl/palvanadium.pdf (accessed 2019 -02 -15).

(43) 07.28.15_Risk explanation FAQ__.pdf https://files.nc.gov/ncdeq/document-library/07.28.15_Risk%20explanation%20FAQ__.pdf (accessed 2019 -09 -09).

(44) Lafferty, B. J.; Ginder-Vogel, M.; Zhu, M.; Livi, K. J. T.; Sparks, D. L. Arsenite Oxidation by a Poorly Crystalline Manganese-Oxide. 2. Results from X-Ray Absorption Spectroscopy and X-Ray Diffraction. *Environ. Sci. Technol.* **2010**, *44* (22), 8467–8472. https://doi.org/10.1021/es102016c.

(45) Lafferty, B. J.; Ginder-Vogel, M.; Sparks, D. L. Arsenite Oxidation by a Poorly Crystalline Manganese-Oxide 1. Stirred-Flow Experiments. *Environ. Sci. Technol.* **2010**, *44* (22), 8460–8466. https://doi.org/10.1021/es102013p.

(46) Stahl, R. S.; James, B. R. Zinc Sorption by Manganese-Oxide-Coated Sand as a Function of PH. *Soil Science Society of America Journal* **1991**, *55* (5), 1291–1294. https://doi.org/10.2136/sssaj1991.03615995005500050016x.

(47) Catalano, J. G.; Luo, Y.; Otemuyiwa, B. Effect of Aqueous Fe(II) on Arsenate Sorption on Goethite and Hematite. *Environ. Sci. Technol.* **2011**, *45* (20), 8826–8833. https://doi.org/10.1021/es202445w.

(48) Guha, H.; Jayachandran, K.; Maurrasse, F. Microbiological Reduction of Chromium(VI) in Presence of Pyrolusite-Coated Sand by Shewanella Alga

Simidu ATCC 55627 in Laboratory Column Experiments. *Chemosphere* **2003**, *52* (1), 175–183. https://doi.org/10.1016/S0045-6535(03)00104-8.

(49) Kim, J. G.; Dixon, J. B.; Chusuei, C. C.; Deng, Y. Oxidation of Chromium(III) to (VI) by Manganese Oxides. *SOIL SCI. SOC. AM. J.* **2002**, *66*, 10.

(50) Schwertmann, U.; Cornell, R. *Iron Oxides in the Laboratory: Preparation and Characterization*; Wiley.

(51) McKenzie, R. M. The Synthesis of Birnessite, Cryptomelane, and Some Other Oxides and Hydroxides of Manganese. *Mineralogical Magazine* **1971**, *38* (296), 493–502. https://doi.org/10.1180/minmag.1971.038.296.12.

(52) Kumar, K. V.; de Castro, M. M.; Martinez-Escandell, M.; Molina-Sabio, M.; Rodriguez-Reinoso, F. A Continuous Binding Site Affinity Distribution Function from the Freundlich Isotherm for the Supercritical Adsorption of Hydrogen on Activated Carbon. *J. Phys. Chem. C* **2010**, *114* (32), 13759–13765. https://doi.org/10.1021/jp104014f.

(53) Scatchard, G. THE ATTRACTIONS OF PROTELNS FOR SMALL MOLECULES AND IONS https://www.gwern.net/docs/biology/1949-scatchard.pdf (accessed 2019 -12 -03).

(54) Kinniburgh, D. G. General Purpose Adsorption Isotherms. *Environ. Sci. Technol.* **1986**, *20* (9), 895–904. https://doi.org/10.1021/es00151a008.

(55) Liu, C.-H.; Chuang, Y.-H.; Chen, T.-Y.; Tian, Y.; Li, H.; Wang, M.-K.; Zhang, W. Mechanism of Arsenic Adsorption on Magnetite Nanoparticles from Water: Thermodynamic and Spectroscopic Studies. *Environ. Sci. Technol.* **2015**, *49* (13), 7726–7734. https://doi.org/10.1021/acs.est.5b00381.

(56) Milonjic, S. A Consideration of the Correct Calculation of Thermodynamic Parameters of Adsorption. *J. Serb. Chem. Soc.* **2007**, *72* (12), 1363–1367. https://doi.org/10.2298/JSC0712363M.

(57) Goldberg, S.; Criscenti, L. J.; Turner, D. R.; Davis, J. A.; Cantrell, K. J. Adsorption-Desorption Processes in Subsurface Reactive Transport Modeling. *Vadose Zone Journal* **2007**, *6* (3), 407–435. https://doi.org/10.2136/vzj2006.0085.

(58) Parkhurst, D.; Appelo, C. A. J. User's Guide to PHREEQC (Version 2) : A Computer Program for Speciation, Batch-Reaction, One-Dimensional Transport, and Inverse Geochemical Calculations. **1999**. https://doi.org/10.3133/wri994259.

(59) Lasdon, L. S.; Waren, A. D.; Jain, A.; Ratner, M. Design and Testing of a Generalized Reduced Gradient Code for Nonlinear Programming. *ACM Trans. Math. Softw.* **1978**, *4* (1), 34–50. https://doi.org/10.1145/355769.355773.

(60) Brown, A. M. A Step-by-Step Guide to Non-Linear Regression Analysis of Experimental Data Using a Microsoft Excel Spreadsheet. *Computer Methods and Programs in Biomedicine* **2001**, *65* (3), 191–200. https://doi.org/10.1016/S0169-2607(00)00124-3.

(61) Ravel, B.; Newville, M. ATHENA, ARTEMIS, HEPHAESTUS: Data Analysis for X-Ray Absorption Spectroscopy Using IFEFFIT. *J Synchrotron Rad* **2005**, *12* (4), 537–541. https://doi.org/10.1107/S0909049505012719.

(62) Lopano, C. L.; Heaney, P. J.; Post, J. E.; Hanson, J.; Komarneni, S. Time-Resolved Structural Analysis of K- and Ba-Exchange Reactions with Synthetic Na-Birnessite Using Synchrotron X-Ray Diffraction. *American Mineralogist* **2007**, *92* (2–3), 380–387. https://doi.org/10.2138/am.2007.2242.

(63) Grangeon, S.; Lanson, B.; Lanson, M.; Manceau, A. Crystal Structure of Ni-Sorbed Synthetic Vernadite: A Powder X-Ray Diffraction Study. *Mineral. mag.* **2008**, *72* (6), 1279–1291. https://doi.org/10.1180/minmag.2008.072.6.1279.

(64) Villalobos, M.; Lanson, B.; Manceau, A.; Toner, B.; Sposito, G. Structural Model for the Biogenic Mn Oxide Produced by Pseudomonas Putida. *American Mineralogist* **2006**, *91* (4), 489–502. https://doi.org/10.2138/am.2006.1925.

(65) Drits, V. A.; Lanson, B.; Gaillot, A.-C. Birnessite Polytype Systematics and Identification by Powder X-Ray Diffraction. *American Mineralogist* **2007**, *92* (5–6), 771–788. https://doi.org/10.2138/am.2007.2207.

(66) Lanson, B.; Marcus, M. A.; Fakra, S.; Panfili, F.; Geoffroy, N.; Manceau, A. Formation of Zn–Ca Phyllomanganate Nanoparticles in Grass Roots. *Geochimica et Cosmochimica Acta* **2008**, *72* (10), 2478–2490. https://doi.org/10.1016/j.gca.2008.02.022.

(67) Marafatto, F. F.; Lanson, B.; Peña, J. Crystal Growth and Aggregation in Suspensions of δ-MnO2 Nanoparticles: Implications for Surface Reactivity. *Environ. Sci.: Nano* **2018**, *5* (2), 497–508. https://doi.org/10.1039/C7EN00817A.

(68) Wyckoff, R. Crystal Structures. **1963**.

(69) Schaefer, M. V.; Handler, R. M.; Scherer, M. M. Fe(II) Reduction of Pyrolusite (β-MnO2) and Secondary Mineral Evolution. *Geochem Trans* **2017**, *18*. https://doi.org/10.1186/s12932-017-0045-0.

(70) Yamada, N.; Ohmasa, M.; Horiuchi, S. Textures in Natural Pyrolusite, β-MnO2, Examined by 1 MV HRTEM. *Acta Cryst B* **1986**, *42* (1), 58–61. https://doi.org/10.1107/S0108768186098579.

(71) Maphanga, R. R.; Parker, S. C.; Ngoepe, P. E. Atomistic Simulation of the Surface Structure of Electrolytic Manganese Dioxide. *Surface Science* **2009**, *603* (21), 3184–3190. https://doi.org/10.1016/j.susc.2009.07.038.

(72) Wooyong Um, M. M. S. Adsorption Mechanisms and Transport Behavior between Selenate and Selenite on Different Sorbents. *Int J Waste Resources* **2014**, *04* (02). https://doi.org/10.4172/2252-5211.1000144.

(73) Janney, D. E.; Cowley, J. M.; Buseck, P. R. Structure of Synthetic 2-Line Ferrihydrite by Electron Nanodiffraction. 8.

(74) Gualtieri, A. F.; Venturelli, P. In Situ Study of the Goethite-Hematite Phase Transformation by Real Time Synchrotron Powder Diffraction. *American Mineralogist* **1999**, *84* (5–6), 895–904. https://doi.org/10.2138/am-1999-5-624.

(75) Notini, L.; Latta, D. E.; Neumann, A.; Pearce, C. I.; Sassi, M.; N'Diaye, A. T.; Rosso, K. M.; Scherer, M. M. The Role of Defects in Fe(II)–Goethite Electron Transfer. *Environ. Sci. Technol.* **2018**, *52* (5), 2751–2759. https://doi.org/10.1021/acs.est.7b05772.

(76) Burleson, D. J.; Penn, R. L. Two-Step Growth of Goethite from Ferrihydrite. *Langmuir* **2006**, *22* (1), 402–409. https://doi.org/10.1021/la051883g.

(77) Ostergren, J. D.; Trainor, T. P.; Bargar, J. R.; Brown, G. E.; Parks, G. A. Inorganic Ligand Effects on Pb(II) Sorption to Goethite (α-FeOOH): I. Carbonate. *Journal of Colloid and Interface Science* **2000**, *225* (2), 466–482. https://doi.org/10.1006/jcis.1999.6701.

(78) Weidler, P. G.; Hug, S. J.; Wetche, T. P.; Hiemstra, T. Determination of Growth Rates of (100) and (110) Faces of Synthetic Goethite by Scanning Force Microscopy. *Geochimica et Cosmochimica Acta* **1998**, *62* (21), 3407–3412. https://doi.org/10.1016/S0016-7037(98)00251-8.

(79) Sugimoto, T.; Muramatsu, A.; Sakata, K.; Shindo, D. Characterization of Hematite Particles of Different Shapes. *Journal of Colloid and Interface Science* **1993**, *158* (2), 420–428. https://doi.org/10.1006/jcis.1993.1274.

(80) Frierdich, A. J.; Helgeson, M.; Liu, C.; Wang, C.; Rosso, K. M.; Scherer, M. M. Iron Atom Exchange between Hematite and Aqueous Fe(II). *Environ. Sci. Technol.* **2015**, *49* (14), 8479–8486. https://doi.org/10.1021/acs.est.5b01276.

(81) Jang, J.-H.; Dempsey, B. A.; Burgos, W. D. Solubility of Hematite Revisited: Effects of Hydration. *Environ. Sci. Technol.* **2007**, *41* (21), 7303–7308. https://doi.org/10.1021/es070535t.

(82) Baltrusaitis, J.; M. Cwiertny, D.; H. Grassian, V. Adsorption of Sulfur Dioxide on Hematite and Goethite Particle Surfaces. *Physical Chemistry Chemical Physics* **2007**, *9* (41), 5542–5554. https://doi.org/10.1039/B709167B.

(83) Jolivet, J.-P.; Chanéac, C.; Tronc, E. Iron Oxide Chemistry. From Molecular Clusters to Extended Solid Networks. *Chemical Communications* **2004**, *0* (5), 481–483. https://doi.org/10.1039/B304532N.

(84) Essington, M. E. *Soil and Water Chemistry: An Integrative Approach*; CRC Press: Boca Raton, 2004.

(85) García-Calzón, J. A.; Díaz-García, M. E. Characterization of Binding Sites in Molecularly Imprinted Polymers. *Sensors and Actuators B: Chemical* **2007**, *123* (2), 1180–1194. https://doi.org/10.1016/j.snb.2006.10.068.

(86) Sugihara, G.; Shigematsu, D.-S.; Nagadome, S.; Lee, S.; Sasaki, Y.; Igimi, H. Thermodynamic Study on the Langmuir Adsorption of Various Bile Salts Including Taurine and Glycine Conjugates onto Graphite in Water. *Langmuir* **2000**, *16* (4), 1825–1833. https://doi.org/10.1021/la990358c.

(87) Liu, Y. Is the Free Energy Change of Adsorption Correctly Calculated? *J. Chem. Eng. Data* **2009**, *54* (7), 1981–1985. https://doi.org/10.1021/je800661q.

(88) Ona-Nguema, G.; Morin, G.; Juillot, F.; Calas, G.; Brown, G. E. EXAFS Analysis of Arsenite Adsorption onto Two-Line Ferrihydrite, Hematite, Goethite, and Lepidocrocite. *Environ. Sci. Technol.* **2005**, *39* (23), 9147–9155. https://doi.org/10.1021/es050889p.

(89) Trainor, T. P.; Chaka, A. M.; Eng, P. J.; Newville, M.; Waychunas, G. A.; Catalano, J. G.; Brown, G. E. Structure and Reactivity of the Hydrated Hematite (0001) Surface. *Surface Science* **2004**, *573* (2), 204–224. https://doi.org/10.1016/j.susc.2004.09.040.

(90) Venema, P.; Hiemstra, T.; Weidler, P. G.; van Riemsdijk, W. H. Intrinsic Proton Affinity of Reactive Surface Groups of Metal (Hydr)Oxides: Application to Iron (Hydr)Oxides. *Journal of Colloid and Interface Science* **1998**, *198* (2), 282–295. https://doi.org/10.1006/jcis.1997.5245.

(91) Cornell, R. M.; Schwertmann, U. *The Iron Oxides: Structure, Properties, Reactions, Occurences and Uses*, 1st ed.; Wiley, 2003. https://doi.org/10.1002/3527602097.

(92) Davantès, A.; Lefèvre, G. Molecular Orientation of Molybdate Ions Adsorbed on Goethite Nanoparticles Revealed by Polarized in Situ ATR-IR Spectroscopy. *Surface Science* **2016**, *653*, 88–91. https://doi.org/10.1016/j.susc.2016.06.007.

(93) Sahai, N.; Sverjensky, D. A. Evaluation of Internally Consistent Parameters for the Triple-Layer Model by the Systematic Analysis of Oxide Surface Titration Data. *Geochimica et Cosmochimica Acta* **1997**, *61* (14), 2801–2826. https://doi.org/10.1016/S0016-7037(97)00128-2.

(94) Crans, D. C.; Tracey, A. S. The Chemistry of Vanadium in Aqueous and Nonaqueous Solution. In *Vanadium Compounds*; ACS Symposium Series; American Chemical Society, 1998; Vol. 711, pp 2–29. https://doi.org/10.1021/bk-1998-0711.ch001.

(95) Brinza, L.; Vu, H. P.; Neamtu, M.; Benning, L. G. Experimental and Simulation Results of the Adsorption of Mo and V onto Ferrihydrite. *Scientific Reports* **2019**, *9* (1), 1365. https://doi.org/10.1038/s41598-018-37875-y.

(96) Rakshit, S.; Sallman, B.; Davantés, A.; Lefèvre, G. Tungstate (VI) Sorption on Hematite: An in Situ ATR-FTIR Probe on the Mechanism. *Chemosphere* **2017**, *168*, 685–691. https://doi.org/10.1016/j.chemosphere.2016.11.007.

(97) Rodriguez, R. D.; Demaille, D.; Lacaze, E.; Jupille, J.; Chaneac, C.; Jolivet, J.-P. Rhombohedral Shape of Hematite Nanocrystals Synthesized via Thermolysis of an Additive-Free Ferric Chloride Solution. *J. Phys. Chem. C* **2007**, *111* (45), 16866–16870. https://doi.org/10.1021/jp075381i.

(98) Genuchten, C. M. van; Peña, J. Sorption Selectivity of Birnessite Particle Edges: A d-PDF Analysis of Cd(Ii) and Pb(Ii) Sorption by δ-MnO 2 and Ferrihydrite. *Environmental Science: Processes & Impacts* **2016**, *18* (8), 1030–1041. https://doi.org/10.1039/C6EM00136J.

(99) Janney, D. E.; Cowley, J. M.; Buseck, P. R. Transmission Electron Microscopy of Synthetic 2- and 6-Line Ferrihydrite. *Clays Clay Miner.* **2000**, *48* (1), 111–119. https://doi.org/10.1346/CCMN.2000.0480114.

(100) Michel, F. M.; Ehm, L.; Antao, S. M.; Lee, P. L.; Chupas, P. J.; Liu, G.; Strongin, D. R.; Schoonen, M. A. A.; Phillips, B. L.; Parise, J. B. The Structure of Ferrihydrite, a Nanocrystalline Material. *Science* **2007**, *316* (5832), 1726–1729. https://doi.org/10.1126/science.1142525.

(101) Davantès, A.; Costa, D.; Sallman, B.; Rakshit, S.; Lefèvre, G. Surface Polymerization of Mo(VI) and W(VI) Anions on Hematite Revealed by in Situ Infrared Spectroscopy and DFT+U Theoretical Study. *J. Phys. Chem. C* **2017**, *121* (1), 324–332. https://doi.org/10.1021/acs.jpcc.6b09721.

(102) Whittaker, M. P.; Asay, J.; Eyring, E. M. A Kinetic Study of Vanadate Polymerization in Aqueous Solution [1]. *The Journal of Physical Chemistry* **1966**, *70* (4), 1005–1008. https://doi.org/10.1021/j100876a009.

(103) Calvin, S. *EXAFS for Everyone*; CRC Press.

(104) Akabayov, B.; Kulczyk, A. W.; Akabayov, S. R.; Theile, C.; McLaughlin, L. W.; Beauchamp, B.; van Oijen, A. M.; Richardson, C. C. Pyrovanadolysis, a Pyrophosphorolysis-like Reaction Mediated by Pyrovanadate, Mn2+, and DNA Polymerase of Bacteriophage T7. *J Biol Chem* **2011**, *286* (33), 29146–29157. https://doi.org/10.1074/jbc.M111.250944.

(105) Tran, H. N.; You, S.-J.; Chao, H.-P. Thermodynamic Parameters of Cadmium Adsorption onto Orange Peel Calculated from Various Methods: A Comparison Study. *Journal of Environmental Chemical Engineering* **2016**, *4* (3), 2671–2682. https://doi.org/10.1016/j.jece.2016.05.009.

(106) Zhou, X.; Zhou, X. The Unit Problem in the Thermodynamic Calculation of Adsorption Using the Langmuir Equation. *Chemical Engineering Communications* **2014**, *201* (11), 1459–1467. https://doi.org/10.1080/00986445.2013.818541.

(107) Birkner, N.; Navrotsky, A. Thermodynamics of Manganese Oxides: Effects of Particle Size and Hydration on Oxidation-Reduction Equilibria among Hausmannite, Bixbyite, and Pyrolusite. *American Mineralogist* **2012**, *97* (8–9), 1291–1298. https://doi.org/10.2138/am.2012.3982.

(108) Birkner, N.; Navrotsky, A. Thermodynamics of Manganese Oxides: Sodium, Potassium, and Calcium Birnessite and Cryptomelane. *PNAS* **2017**, *114* (7), E1046–E1053. https://doi.org/10.1073/pnas.1620427114.

(109) Hayes, K.; Roe, L.; Brown, G. E.; Hodgson, K. O.; Leckie, J. O.; Parks, G. A. In Situ X-Ray Absorption Study of Surface Complexes: Selenium Oxyanions on α-FeOOH. *Science* **1987**, *238*, 783–786. https://doi.org/10.1126/science.238.4828.783.

(110) Yin, H.; Feng, X.; Tan, W.; Koopal, L. K.; Hu, T.; Zhu, M.; Liu, F. Structure and Properties of Vanadium(V)-Doped Hexagonal Turbostratic Birnessite and Its Enhanced Scavenging of Pb2+ from Solutions. *Journal of Hazardous Materials* **2015**, *288*, 80–88. https://doi.org/10.1016/j.jhazmat.2015.01.068.

(111) Cristiano, E.; Hu, Y.-J.; Siegfried, M.; Kaplan, D.; Nitsche, H. A Comparison of Point of Zero Charge Measurement Methodology. *Clays Clay Miner*. **2011**, *59* (2), 107–115. https://doi.org/10.1346/CCMN.2011.0590201.

(112) Tonkin, J. W.; Balistrieri, L. S.; Murray, J. W. Modeling Sorption of Divalent Metal Cations on Hydrous Manganese Oxide Using the Diffuse Double Layer Model. *Applied Geochemistry* **2004**, *19* (1), 29–53. https://doi.org/10.1016/S0883-2927(03)00115-X.

(113) Murray, J. W. The Surface Chemistry of Hydrous Manganese Dioxide. *Journal of Colloid and Interface Science* **1974**, *46* (3), 357–371. https://doi.org/10.1016/0021-9797(74)90045-9.

(114) Villalobos, M. The Role of Surface Edge Sites in Metal(Loid) Sorption to Poorly-Crystalline Birnessites. In *Advances in the Environmental Biogeochemistry of Manganese Oxides*; ACS Symposium Series; American Chemical Society, 2015; Vol. 1197, pp 65–87. https://doi.org/10.1021/bk-2015-1197.ch004.

(115) Lanson, B.; Drits, V. A.; Silvester, E.; Manceau, A. Structure of H-Exchanged Hexagonal Birnessite and Its Mechanism of Formation from Na-Rich Monoclinic Buserite at Low PH. *American Mineralogist* **2000**, *85* (5–6), 826–838. https://doi.org/10.2138/am-2000-5-625.

Chapter 3: The Oxidation of V(IV) by Birnessite: Kinetics and Surface Complexation

Abstract

Vanadium is a redox-active metal that has been added to the EPA's Contaminant Candidate List with a notification level of 50 μg L^{-1} due to mounting evidence that V^{V} exposure can lead to adverse health outcomes. Groundwater V concentration exceeds the notification level in many locations, yet geochemical controls on its mobility are poorly understood. Here, we examined the redox interaction between V^{IV} and birnessite (MnO_2), a well-characterized oxidant and scavenger of many trace metals. In our findings, birnessite quickly oxidized sparingly soluble V^{IV} species such as häggite [$V_2O_3(OH)_2$] into highly mobile and toxic vanadate ($H_nVO_4^{(3-n)-}$) in continuously stirred batch reactors under neutral pH conditions. Synchrotron X-ray absorption spectroscopic (XAS) analysis of *in situ* and *ex situ* experiments showed that oxidation of V^{IV} occurs in two stages which are both rapid relative to the measured dissolution rate of the V^{IV} solid. Concomitantly, the reduction of birnessite during V^{IV} oxidation generated soluble Mn^{II}, which led to the formation of the Mn^{III} oxyhydroxide feitknechtite (β-MnOOH) upon back-reaction with birnessite. XAS analysis confirmed a bidentate-mononuclear edge-sharing complex formed between V^{V} and birnessite, although retention of V^{V} was minimal relative to the aqueous quantities generated. In summary, we demonstrate that Mn oxides are effective oxidants of V^{IV} in the environment with the potential to increase dissolved V concentrations in aquifers subject to redox oscillations.

I. Introduction

Vanadium (V) is ubiquitous in terrestrial environments, and is increasingly recognized as a contaminant in subsurface environments due to both natural processes and anthropogenic activities.[1,2] In aquatic ecosystems, sensitive species are vulnerable to aqueous V exposures as low as 1.2-80 μg L^{-1}.[1,3,4] In either environment, vanadium toxicity is dependent on the concentration, oxidation state, and species of V, with V^{V} species eliciting the largest degree of toxicity as well as the highest degree of solubility.[5–8] As a result, V was added to the U.S. Environmental Protection Agency Contaminant Candidate List (CCL1) in 1998 with a corresponding notification level of 50 μg L^{-1} and several U.S. states have since recommended lower notification levels.[9–11]

In the environment, V is present in the +II, +III, +IV, and +V oxidation states, but only V^{III}, V^{IV}, and V^{V} are common in soils and sediments.[12–14] V^{III} is released from mineral phases into the soil solution upon weathering and dissolution of host material, which quickly oxidizes to V^{IV} or V^{V} under suboxic to oxic conditions.[14–16] Despite the prominence of V^{III} as the most abundant form of V in geologic parent material, its solubility decreases above pH 4.9, limiting its mobility under all but the most reducing and acidic conditions, although precise thermodynamic parameters are not known.[1] As a result, V^{IV} and V^{V} are the most common species found in groundwater systems.[14,17]

V^{IV} and V^{V} exhibit differences in solubility, speciation, and chemical interactions with organic matter and mineral phases.[1] V^{IV} species are stable under moderately reducing and acidic conditions, and have been shown to be the most stable form of V in suboxic to anoxic groundwater, as well as waters with dissolved organic carbon (DOC).[1,18]

Oxovanadium^{IV} (VO^{2+}_{aq}) hydrolyzes above pH 5.7 to form $VOOH^{+}_{aq}$ and $VO(OH)_{2\,(s)}$. However, $VO(OH)_{2(s)}$ precipitation can be inhibited by V^{IV} complexation with DOC, and as such precipitation occurs primarily under low DOC conditions.[18,19]

Under oxic conditions and solution pH above 6, V^{V} species exist predominantly as the oxyanion vanadate ($H_nVO_4^{(3-n)-}$) which is reducible to V^{IV} by organic ligands or by Fe^{II}, with a HVO_4^{2-}/VO^{2+} standard potential (E^0) of 1.90 V. [1,20,21] Further, V^{V} is known to polymerize to form oligomeric polyoxometalate V^{V} species at concentrations as low as 100 μM.[22,23] While retention of V^{V} species in the environment is dependent on sorption-desorption and reduction processes, [14,24,25] conditions which lead to changes in redox potential are expected to affect the oxidation state and, therefore, the mobility of V similar to other redox active metal(loid)s such as arsenic and chromium. [26,27]

Manganese(IV) oxides are strong oxidants and scavengers of metal(loids) like As and Cr in terrestrial systems.[28,29] The ubiquity and reactivity of Mn^{IV} oxides make them likely candidates to influence the fate of V in these environments. For example, elevated levels of geogenic V (> 50 ppb) have been detected throughout aquifers in California.[13,17] Many of these aquifers are subject to seasonal redox fluctuations that can lead to the accumulation of Mn^{IV} oxides in close spatial proximity to V.[17,29,30] However, previous studies examining the reactivity of V^{IV} and V^{V} with soil mineral phases [20,31–37] have not examined the role of Mn^{IV} oxides in V^{IV} oxidation or V^{V} adsorption despite their importance in controlling the fate of other metal(loid)s. In this study we investigated the reaction kinetics, sorption processes, and resultant Mn and V solid phase alterations following the reaction of V^{IV} with birnessite. Accordingly, we combine *in situ* and *ex situ*

aqueous and solid phase measurements to construct a model that describes the oxidation of V^{IV} by birnessite.

II. Material and Methods

Birnessite synthesis

Birnessite was prepared as described by McKenzie et al.[38] Briefly, 63 g of $KMnO_4$ (Fisher) was dissolved into 1 L of ultrapure water (18.2 MΩ*cm, Millipore) and heated to 90°C. Over the course of ten minutes, 66 mL of concentrated trace metal grade HCl was added to the $KMnO_4$ solution. The mixture was kept at 90°C for 10 minutes before being cooled to 21°C. Manganese oxides in the solution were collected using vacuum filtration and repeatedly rinsed with ultrapure water to remove excess $KMnO_4$ then dried and crushed with a mortar and pestle. Birnessite was confirmed by X-ray diffraction (XRD) using Cu Kα radiation on a Siemens D500 X-ray diffractometer (Appendix 2 Figure 3.5) and specific surface area was 37.8 m^2g^{-1} (r^2 = 0.999) using the BET surface area analysis (Quantachrome Nova 2000e).

In situ and *ex situ* experiments

Two sets of stirred batch reactors were carried out under anoxic conditions to determine the reaction kinetics of V^{IV}'s oxidation by birnessite using chemicals that were ACS grade or higher. For both sets of experiments, anoxic 25 mM NaCl was used as a background electrolyte and 50 mM PIPES was used to buffer the solutions at pH 7. One set of experiments (hereafter referred to as *in situ*) were performed at beamline 2-2 at the Stanford Synchrotron Radiation Lightsource (SSRL) using semi-quick (~90 s per scan) X-ray absorption near-edge structure (XANES) spectroscopy at the V K-edge. The progression

of the reaction was tracked in real time by monitoring the increase in the pre-edge peak intensity to determine the V^{IV}:V^{V} ratio. These experiments were initiated by suspending birnessite at final loadings of 0.5, 1, 3, or 10 g L^{-1} in anoxic buffer at 75% of the final volume. V^{IV} was added to the remaining 25% of separately aliquoted buffer solution as the hydrated salt $VOSO_4 \bullet 5H_2O$. However, the pH of the buffer caused it to immediately precipitate into variety of solid V^{IV} oxyhydroxides, the identity of which is further discussed in Appendix 2 section 3. The final concentration of V^{IV} was 3.2 mM, with final Mn:V ratios of 2.2, 3.7, 11.9 and 47.1, which are common to concentrations of V and Mn that have been observed in California's aquifers. [17,39]

The second set of experiments (hereafter referred to as *ex situ*) were conducted in the laboratory in an identical manner with the solids loading of birnessite fixed at 1 g L^{-1} and the concentration of V^{IV} varied between 1 and 3.5 mM for final Mn:V ratios of 11.1 and 3.2 respectively. While elevated, these concentrations were chosen to get adequate x-ray fluorescence signal based on the single-channel silicon drift detector that was used in the collection of both *in situ* and *ex situ* V XAS data collection, and is a reason for the similarly elevated concentrations used in prior studies.[40] Additionally, the chosen V concentrations were necessary to reach our targeted Mn:V ratios based on the amount of birnessite that was used. Further details of the reactors and analysis methods are available in Section 1 of Appendix 2. Samples were collected from the *ex situ* experiments for both aqueous and solid phases analysis. Briefly, total aqueous V and aqueous V^{V} speciation was quantified using ICP-OES and ^{51}V NMR; solid phase characterization and V speciation

included X-ray diffraction, XANES spectroscopy, and extended X-ray absorption fine structure (EXAFS) analyses.

Kinetic Modelling

Rate constants were initially calculated by fitting both first and second order rate models to the V and Mn data. However, the interaction of V^{IV} and V^{V} with birnessite may proceed through a variety of pathways that include oxidation, adsorption, desorption, and surface passivation. We therefore developed a model that accounts for mixed-order Langmuir adsorption kinetics, surface passivation, and pseudo-second order oxidation, which is presented as equation 1.

Eq 1. $$\ln\frac{[V^{IV}]_i-[V^V]_{aq,t}-\left(q_{eq}\left(\frac{1-e^{-k_s t}}{1-f_{eq}e^{-k_s t}}\right)[Birnessite]_{t,(gL^{-1})}\right)}{[Birnessite]_t} = t(k_0 e^{-bt})([V^{IV}]_i - 2[Birnessite]_i) + \ln\frac{[V^{IV}]_i}{[Birnessite]_i}$$

Where:

q_{eq} is the amount of vanadate adsorbed by birnessite at equilibrium (mmole g^{-1})

k_s is the first order adsorption rate constant (min^{-1})

f_{eq} is the the batch equilibrium factor and represents the level of second-order contribution to the adsorption of V^V to birnessite. F_{eq} falls between $[0 \leq F_{eq} \leq 1]$, with 0 yielding a pure first order and 1 yielding a pure second order form (dimensionless)

K_0 is the initial pseudo-second order rate constant (mM^{-1} min^{-1})

b is the pseudo-first order birnessite surface passivation constant (min^{-1})

$_i$ *denotes initial concentrations*

$_t$ denotes concentrations at time *t*

**Note that the concentration of birnessite is reported in g L^{-1} in the numerator on left side of the model and in molar units otherwise.*

All parameters from the pseudo-second order surface oxidation (PSOSO) model (Table 3.1) were determined via inverse modelling with residual sum of squares (RSS) minimization. The reaction orders for V and birnessite were determined by standard natural-log transformations of the initial concentration and the rates of reaction from both the *in situ* and *ex* situ experiments followed by linear regression, with the slope being equal to the reaction order.[40,41] The adsorption-desorption parameters (q_{eq}, k_s and f_{eq}) were determined by fitting data from kinetic adsorption and equilibrium adsorption experiments (Appendix 2 section 1). K_0 and *b* were determined from regressing the model in equation 1 on the data from each experiment using the initial rate method (Phase 1 only) or the entire time series. Additional details on the model construction can be found in Appendix 2, and values are reported in Table 3.1.

III. Results & Discussion

Kinetics of VIV oxidation by birnessite

Ex situ batch experiments showed that the reaction of 3.5 mM V^{IV} with birnessite (1 g L^{-1}) under anoxic conditions led to the production of 3.3 mM dissolved V^{V} and 1 mM dissolved Mn^{II} within two hours, while the 1 mM initial V^{IV} experiments led to the production of 0.9 mM dissolved V^{V} and ~0.05 mM Mn^{II}_{aq} (Figure 3.1). After accounting for the adsorbed V^{V} fraction, all V^{IV} was found to be oxidized within 2 h (Appendix 2 section 2 eq. 11). V_{aq} (total aqueous V concentration) increased before plateauing after

approximately 101 min, which coincided with a decrease in Mn_{aq} for both concentrations of V^{IV} tested (Figure 3.1).

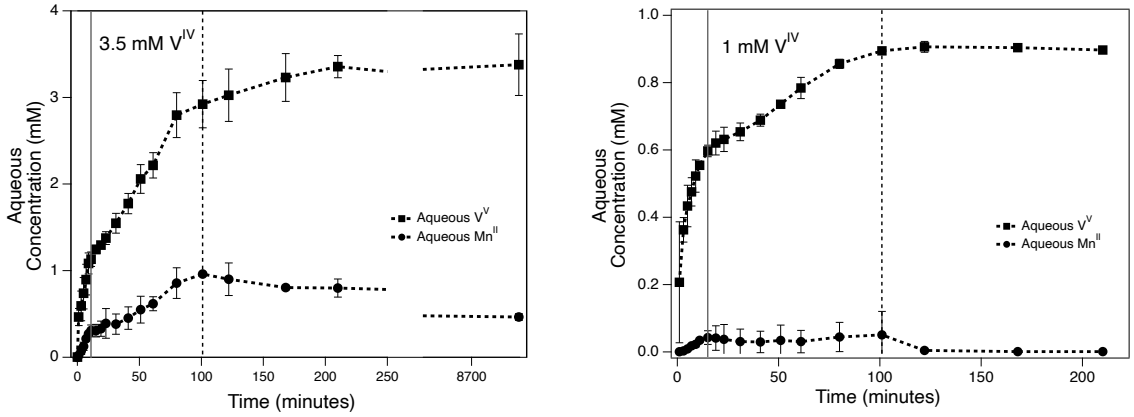

Figure 3.1 Aqueous V and Mn during reaction of 3.5 mM (left) and 1 mM (right) V^{IV} with 1 g L^{-1} birnessite at pH 7 in the *ex situ* experiments. Note the x-axis is split at 250 minutes for the 3.5 mM V^{IV} treatment (left). The solid gray vertical line denotes the end of *Phase 1* and the dashed vertical line denotes the end of *Phase 2* of reaction.

V_{aq} production occurred in two phases during the *ex situ* expeirments: 1) rapid initial production from 0 to 11 minutes (3.5 mM V^{IV}) or 15 minutes (1mM V^{IV}), followed by 2) slower production until 101 minutes. After these phases, V_{aq} production plateaued with no V^{IV} remaining. In the 3.5 mM V^{IV} experiments, an average rate of 0.079 ± 0.01 mM V^{V} min^{-1} was achieved during the first phase, followed by a rate of 0.022 ± 0.002 mM V min^{-1} during the second phase (calculations provided in SI). In the 1 mM V *ex situ* experiments, an average rate of 0.029 ± 0.003 mM V min^{-1} was observed during the first phase, which decreased to 0.0039 ± 0.0005 mM V min^{-1} in the second phase. This represents a rate decrease of 72% and 87%, respectively for the two sets of experiments. By combining data from *ex situ* and *in situ* measurements, a reaction order for vanadium of 0.70 (R^2 = 0.912) was calculated for the first phase, which increased to 1.37 (R^2 = 0.992)

in the second phase. The V reaction order for phase 1 approximates the two-thirds reaction order observed in geometric contraction kinetic models, indicating that the reduction of birnessite by V^{IV} results in a change to the birnessite particle size, likely as Mn^{IV} is reduced to Mn^{II}_{aq} at the particle edges. [42] Aqueous speciation of dissolved V using ^{51}V-NMR confirmed the production of $H_2VO_4^-$ within the first 2 min, followed by the production of $H_2V_2O_7^{2-}$ and $V_4O_{12}^{4-}$ (Appendix 2 Figure 3.4 a-c).[43–45]

Aqueous Mn was also observed in the *ex situ* experiments which increased linearly until the end of the first phase (Figure 3.1). This suggests that side reactions like the formation of Mn^{III} hydroxides were not significant during the first phase, affirming our use of the initial rate method over this time frame. This is further supported by the surface passivation rate constant and Mn XANES analyses discussed below. For the 1mM experiments, the concentration of Mn_{aq} plateaued during the second phase before decreasing after 101 minutes. Likewise, the rate of Mn_{aq} production slowed in the 3.5 mM experiments during the second phase, with the concentration of Mn_{aq} gradually decreasing after 101 minutes. The decrease in Mn_{aq} in both systems after the consumption of V^{IV} by the end of the second phase is likely due to comproportionation reactions between the Mn^{II}_{aq} and birnessite, resulting in $Mn^{III}OOH$ phases further described below. Maximum Mn_{aq} produced by the 1 mM and 3.5 mM experiments were 0.05 mM and 0.96 mM respectively, or 5% and 27% of the total V^{IV} added to each set of systems. Since two moles of V^V are produced per mole of Mn^{II} released, and both spectroscopic and kinetic data suggest that all V^{IV} was oxidized to V^V (Figure 3.2b), the remaining reduced Mn must therefore be associated with the solid phase, which is supported by the Mn XAS and XRD

findings. The differences in Mn^{II}_{aq} between the high and low concentration *ex situ* experiments, particularly during phase 2 is likely a result of the lowered likelihood of two molar equivalents of V^{IV} transferring their electrons to the same structural Mn atom at lower V^{IV}:Birnessite ratios. This would result in the formation of more structural Mn^{III} than Mn^{II}_{aq}, especially as Mn^{II}_{aq} is removed from solution through back reactions with additional equivalents of structural Mn^{IV} as seen by the decrease in Mn^{II}_{aq} after phase 2 and the formation of β-MnOOH.

Measurements of the vanadium average oxidation state (AOS) were obtained using pre-edge peak fitting of XANES spectra collected during the *in situ* experiments, which accounts for V in both aqueous and solid phases (Appendix 2 Eq. S12). Reaction rates and initial concentrations are presented in Table 3.1 and Figure 3.2. In all treatments, the pre-edge analysis revealed a monotonic V^{V} increase followed by a plateau with an average V AOS increase of 1.19 ± 0.04 valence units. Comparison of the rates across experiments revealed an increase in the observed V^{IV} oxidation rate of 0.0039 mM V min^{-1} per unit increase in the Mn:V ratio ($R^2 = 0.966$). The reaction order for birnessite was calculated to be 0.55 ($R^2 = 0.988$). Since only a single phase of V^{V} production was observed in the time frame over which the *in situ* experiments were conducted, any increase in the reaction order for birnessite at later stages of the reaction was poorly-defined. Regardless, when combined with the V reaction order the overall reaction order increased from 1.25 to 1.92 between phase 1 and phase 2, approximating a designation as second order overall.

Several trends emerge upon application of the PSOSO model to the *ex situ* data. First, the values of the initial pseudo-second order rate constant (K_0) and the pseudo first

order surface passivation rate constant (*b*) are dependent on the time frame over which the model is applied. Thus, we will discuss values obtained from the application of the model to phase 1 only, as well as those obtained via the application of the model over the whole experimental time frame. When applied to only the first phase of the *ex situ* data and the single phase of V^V production in the *in situ* experiments, a K_0 of 0.0035 (mM^{-1} min^{-1}) was obtained. Over this time frame the calculated value of *b* was 0.000 min^{-1}, supporting our conclusion that side and backreactions are minimized over this period. However, when applied to the entire time series, K_0 decreased to 0.0028 (mM^{-1} min^{-1}), and a value of 0.009 min^{-1} was obtained for *b* indicating the increased role of surface passivation with time.

The rate of solid-phase V^{IV} dissolution was found to be 0.0017 mM V min^{-1} (R^2 = 0.952) over the first phase (11 min) of the control experiment in the absence of birnessite (Appendix 2 Figure 3.3). We speculate that the difference between this dissolution rate and the observed oxidation rates may be a result of solid-solid interactions due to particle collisions in the stirred reactor, implying that electron transfer between V^{IV} oxyhydroxides and birnessite takes place. Additionally, although the V^{IV} oxyhydroxides are predominantly in the solid phase when introduced into the birnessite slurry, the presence of the of oxidant rapidly removes the low concentration of V^{IV} present before it can back-react with the V^{IV} solids, spurring the state of the V^{IV}_{aq}-V^{IV}_{solid} system in the presence of birnessite towards dissolution.

Using the results from the V^{IV} dissolution control experiment, we calculated a pseudo first order dissolution constant of 0.115 min^{-1} for the first phase. However, a steady increase of V^{IV}_{aq} was not observed after this phase. Instead, V^{IV}_{aq} reached a maximum

concentration of 27 μM before equilibrating to 22 ± 4 μM for 23 hrs, followed by a slow decrease to 7 μM by the end at 125 hrs (Appendix 2 Figure 3.3a). The slow V^{IV}_{aq} decrease is attributed to re-uptake by the V^{IV} precipitate, leading to an increase in its crystallinity (additional details provided in Section 3 of Appendix 2), possibly via Ostwald ripening. Both dissolution and re-uptake processes were modelled using the second order rate law for mineral dissolution, yielding desorption and resorption constants 0.021 μM^{-1} min^{-1} and 3.9 x 10^{-7} μM^{-1} min^{-1}, respectively. [46]

Table 3.1 Kinetic parameters derived from modelling the *in situ* and *ex situ* experiments.

Experiment	Birnessite Loading	V Concentration (mM)	Mn Concentration (mM)	Rate (mM min^{-1}) from Pre-Edge Analysis	Phase 1 Rate (mM V min^{-1})	Phase 2 Rate (mM V min^{-1})	Mn:V ratio
in situ	0.5 g L^{-1}	2.633	5.747	0.042	-	-	2.183
in situ	1 g L^{-1}	3.112	11.494	0.074	-	-	3.693
in situ	3 g L^{-1}	2.890	34.483	0.116	-	-	11.934
in situ	10 g L^{-1}	2.440	114.943	0.232	-	-	47.110
ex situ	1 g L^{-1}	3.513	11.123	-	0.079	0.022	3.167
ex situ	1 g L^{-1}	0.998	11.128	-	0.029	0.004	11.149

Reaction order	V	R^2	Birnessite	R^2
Phase 1	0.701	0.913	0.529	0.969
Phase 2	1.371	0.992		

Entire Time Series ($x10^{-3}$)		Phase 1 only ($x10^{-3}$)	
Passivation Rate constant *b* (min^{-1})	9.039	Passivation Rate constant *b* (min^{-1})	0.000
K_0 (mM^{-1} min^{-1})	2.755	K_0 (mM^{-1} min^{-1})	3.529

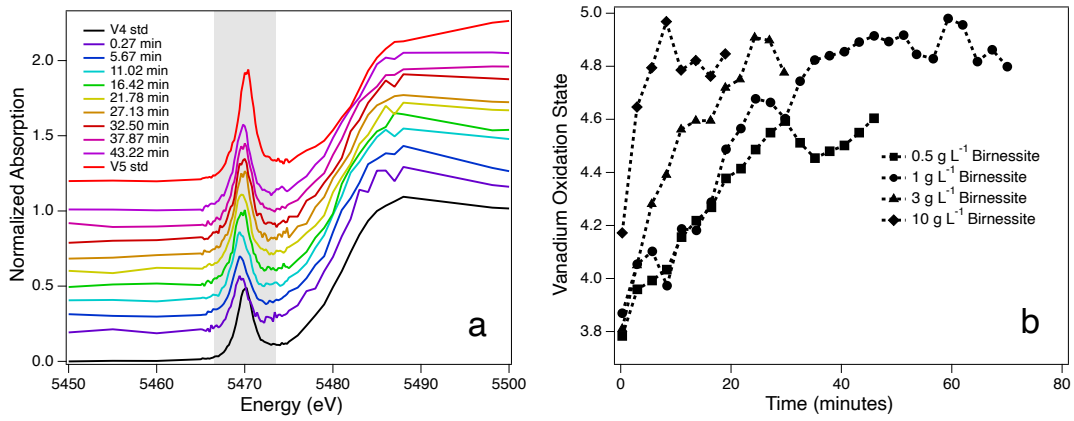

Figure 3.2 *In situ* V K-edge XANES time series. (a) XANES spectra collected during oxidation of V^{IV} by 0.5 g L^{-1} birnessite. Oxidation of V^{IV} to V^{V} is primarily observed as an increase in the intensity of the pre-edge feature at 5469 eV over time (shaded area). (b) The increase in the oxidation number of V across the *in situ* experiments calculated from analysis of the pre-edge feature.

Manganese Transformations

Vanadium(IV) oxidation is coupled with the reduction of Mn^{IV} to structural and aqueous $Mn^{II/III}$. Understanding the fate of reduced Mn products provides insights into the underlying controls on the observed rate, extent, and products of V(IV) oxidation by birnessite. Manganese XANES analysis of the unreacted and reacted birnessite shows a shift in edge position by −1.7 eV, with E_0 (taken as the peak of the first derivative) decreasing from 6553.16 eV to 6549.68 (Appendix 2 Figure 3.5b,c). Since the concentrations of V^{V}_{aq} and Mn^{II}_{aq} are not stoichiometric (Figure 3.1), the remaining reduced-Mn equivalents must remain associated with the solid phase. The AOS of Mn in the unreacted birnessite was calculated as 3.75 using the Combo method of Manceau et al.[47] (Appendix 2 section 1). Given the complete oxidation of the V^{IV} and the concentrations presented in Table 3.1, a final Mn AOS of 3.45 and 3.67 is expected in the 3.5 mM and 1 mM *ex situ* experiments, respectively. The solid phase associated reduced

Mn equivalents were then calculated at each time point using the values of Mn^{II}_{aq} and V^{V}_{total} (Appendix 2 equation 11; Figure 3.3), yielding AOS values for the 1 mM and 3.5 mM *ex situ* batch experiments of 3.66 and 3.53, respectively. These values were validated by applying the Combo method to the Mn XANES the reacted birnessite from the 3.5 mM *ex situ* batch experiment, for which an AOS of 3.52 was obtained.

The accumulation of $Mn^{III}_{structural}$ in the birnessite was observed in both the Mn EXAFS and XRD as well. The presence of corner-sharing $Mn^{II/III}$ octahedra at interlayer vacancy sites is exhibited by the appearance of a shoulder at 6.3 $Å^{-1}$ in Mn EXAFS spectra at the end of the reaction (Appendix 2 Figure 3.5), along with an increase in the intensity of the peak at 3.1 Å R+δR in the RSF (Appendix 2 Figure 3.5 and Appendix 2 Table 3.5).[48–52] In addition, a triple corner-sharing Mn octahedra capping a birnessite vacancy site is observed at a distance of 3.50 Å, comparable to previously published distances.[53] The intensity of a Mn-Mn-Mn multiple scattering peak at 5.1 Å R+δR increased over the reaction suggesting that these vacancies were filled by disordered arrangements of $Mn^{II/III}$ as the reaction progressed.[49,53,54] We then used XRD to see if these changes affected the long-range structure of the Mn oxide.

Sorption and incorporation of Mn^{II} and Mn^{III} into birnessite was observed in the XRD patterns as well. A dip at 45° and a broad feature between 37° and 66° 2θ was found in the reacted birnessite (Appendix 2 Figure 3.5), which are associated with $Mn^{II/III}$ sorption at interlayer vacancy sites at levels close to saturation.[54–58] The lack of the dip at 45° in the unreacted birnessite indicates a low amount of $Mn^{II/III}$ initially present.[56] We didn't detect a symmetry change from hexagonal to triclinic in the birnessite after the reaction, which

has been shown to occur when Mn^{II}_{aq} reacts with hexagonal birnessite above a pH of 8.0. [50] Rather, comproportionation between the adsorbed Mn^{II} and birnessite resulted in the formation of the Mn^{III} oxide phase feitknechtite, a product that has been observed in similar studies.[50,59,60] The feitknechtite was observed via the reflection of the [100] plane at 18° 2θ (Appendix 2 Figure 3.5). In contrast to previous studies that investigated the reduction of birnessite by Mn^{II}, no manganite (γ-MnOOH) was observed in this study. [50,59,60] We attribute the absence of manganite primarily to relatively short experimental time, whereas longer reaction times are necessary for the feitknechtite-to-manganite aging process to occur. [59–61] While competition between divalent cations and Mn^{II} for vacancy sites has also been shown to lead to the preferential formation of feitknechtite over manganite,[61,62] V EXAFS results suggest that V^{V} preferentially interacts with edge sites rather than vacancy sites; thus, manganite formation would be expected if the aging process continued. Furthermore, we expect aqueous V^{IV} species to preferentially react at birnessite edge sites over surface vacancy sites due to the increased reactivity of undersaturated edge oxygens present at the particle edge, similar to the mechanism of the oxidation of As^{III} by birnessite.[56]

Reductive manganese oxide transformation initiated by V^{IV} oxidation and sustained by reaction with V^{IV} and Mn^{II} (and likely Mn^{III}) result in a complex reaction cycle that has implications for controlling both V and Mn concentrations in groundwater. The reaction can lead to the accumulation of secondary Mn phases at the surface of birnessite which is expected to add complexity to the rate of oxidation and adsorption of $V^{IV/V}$, which is reflected in part by the V EXAFS described below.

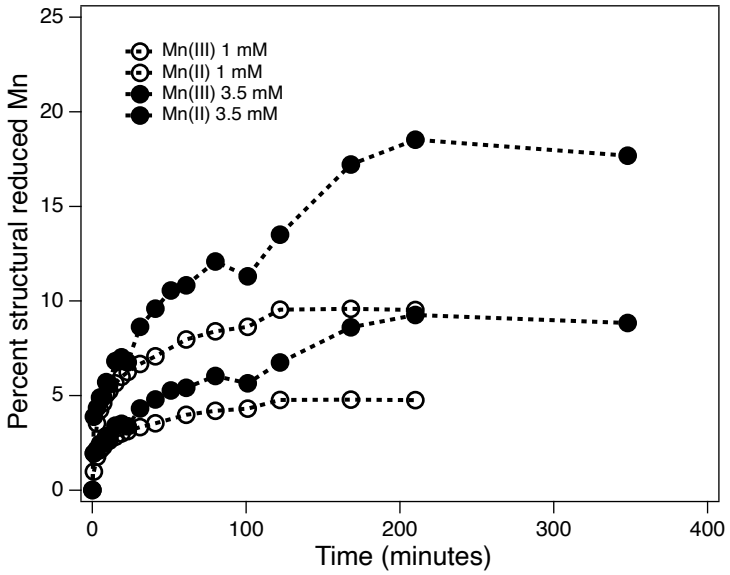

Figure 3.3 Percentage increase in reduced structural Mn in birnessite over time (with reduced Mn presented as either Mn^{II}_{sorbed} or $Mn^{III}_{structural}$) for *ex situ* experiments. The increase in reduced structural Mn was determined by calculating the amount of structural Mn^{II} or Mn^{III} from the V^{V}_{total} and Mn^{II}_{aq} at each time step.

Vanadium Solid Phase Dynamics

The presence of an oxidant influences the development of the V^{IV} hydroxide at early stages of its formation. In the presence of birnessite, the V^{IV} precipitate differs considerably from the V^{IV} oxyhydroxide observed in the V^{IV} dissolution control experiment when samples taken 1-minute post-initiation are compared. Specifically, V^{IV} was present as an octahedrally-coordinated semi-crystalline solid primarily composed of häggite in the V^{IV} dissolution control experiment (Appendix 2 Section 3), whereas V^{IV} solids appeared more amorphous in the presence of birnessite. In the presence of birnessite, V^{IV} exhibited a trigonal planar coordination while retaining some characteristics of häggite, such as the linear axial arrangement of V^{IV} octahedra responsible for producing a strong focused multiple scattering contribution in the EXAFS signal at 3.7 Å (Figure 3.4,

Appendix 2 Table 3.6). In both the control and oxidative experiments, equatorially neighboring V^{IV} are present at distances similar to häggite and Gain's hydrate. [63] The remaining oxygens constituting the octahedral coordination sphere of V^{IV} in the presence of birnessite are likely contributed by transient waters.[64] Although trigonal V^{IV} surface complexes have been observed on $Fe^{II/III}$ (oxy)hydroxides, the inclusion of V^{IV}-Mn backscattering atoms did not statistically improved the fit as evaluated by the Hamilton test.[20] Specifically, we considered the formation of a ^{2}C V^{IV}-Mn complex given the apparent V-V distance at 3.32 Å (Appendix 2 Table 3.6) at the early stages of the reaction, and the absence of that scattering contribution in the early stages of the control experiment, as well as it's similarity to the V^{IV}-Fe^{II} distance in in the ^{2}C complexes reported by Vessey and Lindsay. [20] However, the coordination number when the path is fit as Mn instead of V does not rise above 0.8, which is over a unit less than is required by the formation of a ^{2}C complex. Given this, we assigned this path to a V^{IV}-V^{IV} backscattering interaction, which takes into account the findings of Besnardiere et al. for a V^{IV}-V^{IV} backscattering interaction at 3.37 Å in a häggite sample with a coordination number of one.[63] Likewise, while V^{V}-Mn^{II} phases exist, they were not detected in the experiments through EXAFS or XANES analyses.[65]

The difference in oxygen coordination between the initial forms of V^{IV} in the presence and absence of birnessite is likely due the relative rates of crystallization versus oxidation when in the presence of birnessite. In the control experiment, V^{IV} precipitated and ripened in solution before being dried under an anoxic atmosphere prior to EXAFS analysis. Whereas, in the presence of birnessite, the V^{IV} recrystallization pathway was in

direct competition with the oxidation pathway provided by contact with the birnessite. A comparison of the 2nd order rate constants presented in Table 3.1 and Appendix 2 Table 3.4 for oxidation by birnessite and V^{IV} re-uptake by the V^{IV} solid (a proxy for the recrystallization process) reveals that oxidation is more than 7000 times faster; thus, aging of the initial V^{IV} precipitate is inhibited in the presence of the Mn oxide.

Tetrahedrally coordinated vanadate $H_2VO_4^-$ was the predominate end-product in the 1 mM and 3.5 mM *ex situ* experiments, also forming a surface complex with the birnessite. However, some V^V polymerization occurred by the end of the reaction. Equilibrium speciation modeling predicted approximately 20% of aqueous V^V to be pyrovanadate ($H_2V_2O_7^{2-}$) and 15-47% (1 mM V^V and 3.5 m M V^V respectively) to be present as tetravanadate ($V_4O_{12}^{4-}$). The proportions of pyrovanadate and tetravandate determined by ^{51}V NMR were found to be less than predicted, reaching 7.7% and 4.2% of the total V respectively (Appendix 2 Figure 3.4). Several possible reasons for this discrepancy include the formation of surface-bound pyrovanadate-birnessite complexes and paramagnetic interreference in the NMR spectra by the elevated concentrations of Mn^{II}_{aq}. V^V surface complexation by birnessite was dominated by a vanadate bidentate mononuclear edge-sharing complex (^{2}E), likely localized to birnessite edge-sites (Figure 3.4). The EXAFS signal for this complex included a significant contribution from vanadate intra-tetrahedral multiple scattering, a phenomena observed for vanadate adsorbed on Fe oxides.[20,33] When a Mn-O length of 1.90 Å is applied (Appendix 2 Table 3.5), a ∠V-O-Mn angle of 102.8° results which is comparable to the ^{2}E complex of vanadate adsorption on ferrihydrite.[33] While EXAFS spectra with greater k ranges are needed to definitively

identify whether pyrovanadate was also complexed to the birnessite surface, the addition of a neighboring V backscattering atom at the V-V pyrovanadate distance of 3.43 Å lead to an improvement in the overall fit and decreased uncertainties calculated for the floated variables (Appendix 2 Table 3.6, $I_r = 0.53$). Formation of bidentate corner sharing (^{2}C) V-Mn complexes are also possible, though inclusion of these paths did not statistically enhance the EXAFS fit ($I_r = 0.71$). Larsson et al.[33] previously noted that the EXAFS contribution from intra-tetrahedral multiple scattering obscured the ability to resolve any ^{2}C complexes between V^V and ferrihydrite. Likewise, the presence of several types of intra-tetrahedral multiple scattering with a half-path length of 3.4-3.5 Å [33] as well as a V-O-Mn multiple scattering path at 3.36 Å would make the determination of a pyrovanadate V-V distance at 3.4 Å difficult without higher resolution data. A summary of the oxidation of V^{IV} by birnessite and interactions of the products are illustrated in Appendix 2 Figure 3.6.

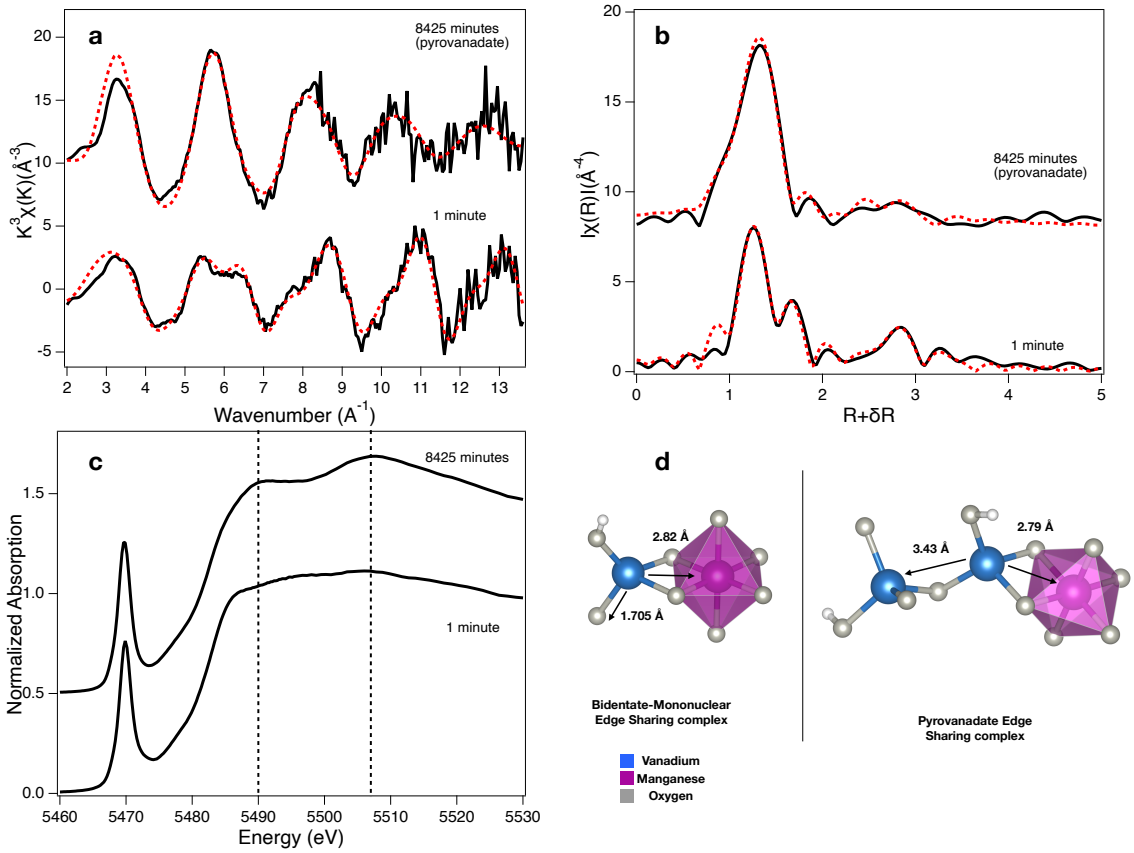

Figure 3.4 Comparison of V speciation of solids collected at start (1 min) and end (140 h) of the reaction between V^{IV} and birnessite with 3.5 mM V^{IV} initial concentration and 1 g L^{-1} birnessite. (a) k^3-weighted EXAFS spectra showing the transition from V^{IV} octahedra at 1 min to V^{V} tetrahedra at 140 h. (b) Radial structure function (RSF) plot of (a). (c) XANES spectra showing oxidation of V^{IV} to V^{V} indicated by shift in edge position and development of absorption features at 5490 and 5507 eV corresponding to 1s to $4P_z$ and $4P_{xy}$ transitions. (d) Structural models of V^{V} adsorbed on birnessite as determined by shell-fitting of EXAFS. Red dashed lines represent the fit and black solid lines represent the data.

Comparison to other metal(loid) contaminants

While no studies have examined V surface complexes formed on Mn oxides, several studies have characterized V^{IV} and V^{V} adsorption on Fe oxides.[20,33,34,66] Vessey and Lindsay[20] reported the formation of V^{IV} and V^{V} adsorption complexes in ^{2}C and ^{2}E

configurations on the surface of mixed-valence Fe^{II}/Fe^{III} oxides. Larsson et al. found that V^V did not form a ^2C complex on ferrihydrite, which they attributed to the longer V-O bond of V relative to the Me-O distance of an element like As which predominantly forms a ^2C complex on the mineral.[33] Our results indicate that V^V primarily forms a ^2E complex at birnessite edge sites, which is in agreement with work by Larsson et al.[33] The V-Mn distance identified in this study (2.79 - 2.82 Å) is comparable to ^2E V-Fe distance (2.789 Å) on ferrihydrite at neutral pH, but approximately 0.12 Å greater than the ferrihydrite V-Fe ^2E distances published by Vessey and Lindsay[20] and approximately 0.1 Å greater than the ^2E complex formed by As^V on what was hypothesized to be γ-MnOOH-passivated birnessite.[20,56] This confirms that the sorption behavior of V^V is more similar to that of other tetrahedrally coordinated metal(loid)s than octahedrally coordinated metals like Cd or Ni, which have Cd-Mn and Ni-Mn distances of 3.66 and 3.49 Å respectively.[61,67] Likewise, our predicted ∠V-O-Mn angles range from 101.3° to 102.8°, which are approximately 4° greater than for the V-O-Fe angle with ferrihydrite. This difference indicates that the formation of the ^2E complex induces a greater level of Jahn-Teller distortion into the Mn octahedra than when adsorbed onto Fe^{III} octahedra.[33] The greater distortion could be caused by a shorter average Mn-O distance (1.90 Å) in birnessite than the Fe-O distances of ferrihydrite (1.91 Å, 1.92 Å or 2.04 Å depending on the Fe center).[68]

Many studies have examined metal anion and cation adsorption on birnessite surfaces that provide insight into other possible V complexes that may have formed. Terminal hydroxyl groups of birnessite can carry a positive charge when doubly protonated and are therefore the most likely sites where anion adsorption is expected to occur (e.g.,

As, Mo, and Sb).[69–72] Accordingly, we expect V^{V} to be primarily bound at edge sites. However, V^{IV} is cationic and could electrostatically attracted to negatively charged surface vacancy sites in a manner similar to Mn^{II}, Zn^{II} and Ni^{II}. This would be physically feasible given a hydrated diameter of < 4.2 Å for aqueous V^{IV} and an interlayer d_{100} spacing of 7.2 Å for birnessite that yields a 5.2 Å cation gap.[61,62,64] However, it likely reacts at the edge sites, given the reactivity of these sites towards other oxyanions.[71,72] We were unable to detect any V^{IV} sorption complexes on birnessite, which may have been due to relatively fast V^{IV} oxidation by birnessite compared to the speed of XAS data acquisition. A previous study reported that the fast rate of As^{III} oxidation by birnessite precluded the observation of any As^{III} - Mn complex using EXAFS.[56] However, the role of edge sites in the oxidation of V^{IV} may be observable in the aqueous *ex situ* data (Figure 3.1) via the presence of the two phases discussed above. Rapid accumulation of structural Mn^{III} at particle edge sites during the first phase of the reaction would lead to the decreased reaction rate observed in the second phase, given the lower potential of Mn^{III} to oxidize V^{IV}. The accumulation of Mn^{III} at birnessite particle edges in response electron transfer from aqueous reductants is well documented, and has likewise been shown to influence the adsorption and oxidation of other environmental contaminants such as Sb and Ni.[71,73]

The oxidation of metal oxides has been shown to be limited by the solubility of one or both members of the redox couple.[29] For example, the initial rate of V^{IV} oxidation (K_0) was 80 to 200 times slower than the published rates of As^{III} oxidation, which highlights how V^{IV} oxyhydroxide oxidation is likely limited by solubility.[74,75] The decreasing solubility of the V^{IV} oxyhydroxide as it ages from an amorphous precipitate into a more

crystalline solid solution of V^{IV} hydroxides imposes constraints on its subsequent oxidation similar to the constraints imposed on the oxidation of Cr^{III} by birnessite due to the exceptionally low solubility of Cr^{III}.[26,76] The observed dissolution rate of the amorphous V^{IV} precipitate is more than 3 orders of magnitude greater than the dissolution rate of Cr^{III} from minerals such as chromite, although the solubility of the V^{IV} precipitate is reduced as it ages (Appendix 2 Figure 3.3).[76]

IV. Environmental Implications

In the environment, the concentration of aqueous V^{IV} is controlled by the solubility of V^{IV} oxyhydroxides, [1] pH, [77] pO_2, [18] and the reactivity of other soil mineral phases.[31,35,78] The heterogenous oxidation of sparingly soluble V^{IV} by birnessite increased aqueous V^{V} concentrations as well as promoted the reductive release of Mn^{II}, an underrecognized groundwater contaminant into solution.[79,80] Although birnessite adsorbs a portion of aqueous V^{V} and Mn^{II}, back-reactions and the formation of new mineralogical phases like Mn^{III} hydroxides may alter the reactivity and retention capacity of birnessite. Our findings suggest that in environments subject to redox cycling, such as sediments in aquifers subject to seasonal draw-down and recharge, V can be abiotically oxidized via interactions with Mn oxides, which are also known to accumulate in such environments. [13,17,29,30] We hope that the information presented here can be used to help parameterize predictive models to better predict the extent of groundwater V contamination in areas where Mn oxide content is well defined.

V. Acknowledgements

The authors thank R. Root for synchrotron XRD of V^{IV} solids on beamline 11-3 at SSRL and Ryan Davis, Matthew Latimer, Erik Nelson and Sharon Bone for help with data collection at SSRL. Portions of this research were carried out at the Stanford Synchrotron Radiation Lightsource, a Directorate of SLAC National Accelerator Laboratory and an Office of Science User Facility operated for the U.S. Department of Energy Office of Science by Stanford University under Contract No. DE-AC02-76SF00515. This work was funded in part by the USDA NIFA Hatch Project CA-R-ENS-5151-H and UCR Regents Faculty Fellowship to S.C.Y. M.J.A. was supported by a T32 Training Grant from the National Institutes of Health (T32 ES018827). M.V.S. was supported in part by the John D. Montgomery Postdoctoral Fellowship from the Pacific Basin Research Center, Soka University of America.

VI. Supporting Information

The Supporting Information for chapter 3 is available in Appendix 2

VII. References

(1) Gustafsson, J. P. Vanadium Geochemistry in the Biogeosphere –Speciation, Solid-Solution Interactions, and Ecotoxicity. *Applied Geochemistry* **2019**, *102*, 1–25. https://doi.org/10.1016/j.apgeochem.2018.12.027.

(2) Schlesinger, W. H.; Klein, E. M.; Vengosh, A. Global Biogeochemical Cycle of Vanadium. *Proceedings of the National Academy of Sciences* **2017**, *114* (52), E11092–E11100. https://doi.org/10.1073/pnas.1715500114.

(3) Smit, C. Environmental Risk Limits for Vanadium in Water : A Proposal for Water Quality Standards in Accordance with the Water Framework Directive. *Milieurisicogrenzen voor vanadium : Een voorstel voor waterkwaliteitsnormen volgens de Kaderrichtlijn water* **2012**.

(4) Schiffer, S.; Liber, K. Estimation of Vanadium Water Quality Benchmarks for the Protection of Aquatic Life with Relevance to the Athabasca Oil Sands Region Using Species Sensitivity Distributions. *Environmental Toxicology and Chemistry* **2017**, *36* (11), 3034–3044. https://doi.org/10.1002/etc.3871.

(5) Pessoa, J. C.; Etcheverry, S.; Gambino, D. Vanadium Compounds in Medicine. *Coordination Chemistry Reviews* **2015**, *301–302*, 24–48. https://doi.org/10.1016/j.ccr.2014.12.002.

(6) Rehder, D. The Role of Vanadium in Biology. *Metallomics* **2015**, *7* (5), 730–742. https://doi.org/10.1039/C4MT00304G.

(7) Aureliano, M.; Crans, D. C. Decavanadate (V10O286-) and Oxovanadates: Oxometalates with Many Biological Activities. *Journal of Inorganic Biochemistry* **2009**, *103* (4), 536–546. https://doi.org/10.1016/j.jinorgbio.2008.11.010.

(8) Capella, M. A. M.; Capella, L. S.; Valente, R. C.; Gefé, M.; Lopes, A. G. Vanadate-Induced Cell Death Is Dissociated from H2O2 Generation. *Cell Biol Toxicol* **2007**, *23* (6), 413–420. https://doi.org/10.1007/s10565-007-9003-4.

(9) Howd, R. palvanadium.pdf https://oehha.ca.gov/media/downloads/water/chemicals/nl/palvanadium.pdf (accessed 2019 -02 -15).

(10) Tabri, A.; Daunt, P.; Zwayer, B. *Health Effects Assessinent Sumtnary Tables FY-1997 UPDATE*; 1997.

(11) *Amendments to 15A NCAC 02L .0202 Groundwater Quality Standards: Part 1*; 2020.

(12) Canil, D. Vanadium in Peridotites, Mantle Redox and Tectonic Environments: Archean to Present. *Earth and Planetary Science Letters* **2002**, *195* (1), 75–90. https://doi.org/10.1016/S0012-821X(01)00582-9.

(13) Wright, M. T.; Stollenwerk, K. G.; Belitz, K. Assessing the Solubility Controls on Vanadium in Groundwater, Northeastern San Joaquin Valley, CA. *Applied Geochemistry* **2014**, *48*, 41–52. https://doi.org/10.1016/j.apgeochem.2014.06.025.

(14) Shaheen, S. M.; Alessi, D. S.; Tack, F. M. G.; Ok, Y. S.; Kim, K.-H.; Gustafsson, J. P.; Sparks, D. L.; Rinklebe, J. Redox Chemistry of Vanadium in Soils and Sediments: Interactions with Colloidal Materials, Mobilization, Speciation, and Relevant Environmental Implications- A Review. *Advances in Colloid and Interface Science* **2019**, *265*, 1–13. https://doi.org/10.1016/j.cis.2019.01.002.

(15) Telfeyan, K.; Johannesson, K. H.; Mohajerin, T. J.; Palmore, C. D. Vanadium Geochemistry along Groundwater Flow Paths in Contrasting Aquifers of the United States: Carrizo Sand (Texas) and Oasis Valley (Nevada) Aquifers. *Chemical Geology* **2015**, *410*, 63–78. https://doi.org/10.1016/j.chemgeo.2015.05.024.

(16) Groover, K. D.; Izbicki, J. A. Selected Trace-Elements in Alluvium and Rocks, Western Mojave Desert, Southern California. *Journal of Geochemical Exploration* **2018**. https://doi.org/10.1016/j.gexplo.2018.09.005.

(17) Wright, M. T.; Belitz, K. Factors Controlling the Regional Distribution of Vanadium in Groundwater. *Ground Water* **2010**, *48* (4), 515–525. https://doi.org/10.1111/j.1745-6584.2009.00666.x.

(18) Wehrli, B.; Stumm, W. Vanadyl in Natural Waters: Adsorption and Hydrolysis Promote Oxygenation. *Geochimica et Cosmochimica Acta* **1989**, *53* (1), 69–77. https://doi.org/10.1016/0016-7037(89)90273-1.

(19) Pourret, O.; Dia, A.; Gruau, G.; Davranche, M.; Bouhnik-Le Coz, M. Assessment of Vanadium Distribution in Shallow Groundwaters. *Chemical Geology* **2012**, *294–295*, 89–102. https://doi.org/10.1016/j.chemgeo.2011.11.033.

(20) Vessey, C. J.; Lindsay, M. B. J. Aqueous Vanadate Removal by Iron(II)-Bearing Phases under Anoxic Conditions. *Environ. Sci. Technol.* **2020**. https://doi.org/10.1021/acs.est.9b06250.

(21) Lu, X.; Johnson, W. D.; Hook, J. Reaction of Vanadate with Aquatic Humic Substances: An ESR and 51V NMR Study. *Environ. Sci. Technol.* **1998**, *32* (15), 2257–2263. https://doi.org/10.1021/es970930r.

(22) McCann, N.; Wagner, M.; Hasse, H. A Thermodynamic Model for Vanadate in Aqueous Solution – Equilibria and Reaction Enthalpies. *Dalton Trans.* **2013**, *42* (7), 2622–2628. https://doi.org/10.1039/C2DT31993D.

(23) Cruywagen, J. J.; Heyns, J. B. B. Vanadium(V) Equilibria. Spectrophotometric and Enthalpimetric Investigation of the Dimerization and Deprotonation of HVO42−. *Polyhedron* **1991**, *10* (2), 249–253. https://doi.org/10.1016/S0277-5387(00)81596-X.

(24) Blackmore, D. P. T.; Ellis, J.; Riley, P. J. Treatment of a Vanadium-Containing Effluent by Adsorption/Coprecipitation with Iron Oxyhydroxide. *Water Research* **1996**, *30* (10), 2512–2516. https://doi.org/10.1016/0043-1354(96)00080-2.

(25) Shieh, C.; Duedall, I. W. Role of Amorphous Ferric Oxyhydroxide in Removal of Anthropogenic Vanadium from Seawater. *Marine Chemistry* **1988**, *25* (2), 121–139. https://doi.org/10.1016/0304-4203(88)90060-6.

(26) Hausladen, D. M.; Fendorf, S. Hexavalent Chromium Generation within Naturally Structured Soils and Sediments. *Environ. Sci. Technol.* **2017**, *51* (4), 2058–2067. https://doi.org/10.1021/acs.est.6b04039.

(27) Manning, B. A.; Fendorf, S. E.; Bostick, B.; Suarez, D. L. Arsenic(III) Oxidation and Arsenic(V) Adsorption Reactions on Synthetic Birnessite. *Environ. Sci. Technol.* **2002**, *36* (5), 976–981. https://doi.org/10.1021/es0110170.

(28) Mock, R. P.; Schaefer, M. V.; Pacheco, J. L.; Lake, L.; Lee, I.; Ying, S. C. Influence of Fe(II) on Arsenic(III) Oxidation by Birnessite in Diffusion-Limited Systems. *ACS Earth Space Chem.* **2019**, *3* (4), 550–561. https://doi.org/10.1021/acsearthspacechem.8b00184.

(29) McClain, C. N.; Fendorf, S.; Webb, S. M.; Maher, K. Quantifying Cr(VI) Production and Export from Serpentine Soil of the California Coast Range. *Environ. Sci. Technol.* **2017**, *51* (1), 141–149. https://doi.org/10.1021/acs.est.6b03484.

(30) Manning, A. H.; Mills, C. T.; Morrison, J. M.; Ball, L. B. Insights into Controls on Hexavalent Chromium in Groundwater Provided by Environmental Tracers, Sacramento Valley, California, USA. *Applied Geochemistry* **2015**, *62*, 186–199. https://doi.org/10.1016/j.apgeochem.2015.05.010.

(31) Wisawapipat, W.; Kretzschmar, R. Solid Phase Speciation and Solubility of Vanadium in Highly Weathered Soils. *Environ. Sci. Technol.* **2017**, *51* (15), 8254–8262. https://doi.org/10.1021/acs.est.7b01005.

(32) Vessey, C. J.; Schmidt, M. P.; Abdolahnezhad, M.; Peak, D.; Lindsay, M. B. J. Adsorption of (Poly)Vanadate onto Ferrihydrite and Hematite: An In Situ ATR–FTIR Study. *ACS Earth Space Chem.* **2020**. https://doi.org/10.1021/acsearthspacechem.0c00027.

(33) Larsson, M. A.; Persson, I.; Sjöstedt, C.; Gustafsson, J. P. Vanadate Complexation to Ferrihydrite: X-Ray Absorption Spectroscopy and CD-MUSIC Modelling. *Environ. Chem.* **2017**, *14* (3), 141–150. https://doi.org/10.1071/EN16174.

(34) Peacock, C. L.; Sherman, D. M. Vanadium(V) Adsorption onto Goethite (α-FeOOH) at PH 1.5 to 12: A Surface Complexation Model Based on Ab Initio Molecular Geometries and EXAFS Spectroscopy. *Geochimica et Cosmochimica Acta* **2004**, *68* (8), 1723–1733. https://doi.org/10.1016/j.gca.2003.10.018.

(35) Larsson, M. A.; Hadialhejazi, G.; Gustafsson, J. P. Vanadium Sorption by Mineral Soils: Development of a Predictive Model. *Chemosphere* **2017**, *168*, 925–932. https://doi.org/10.1016/j.chemosphere.2016.10.117.

(36) Wehrli, B.; Stumm, W. Oxygenation of Vanadyl(IV). Effect of Coordinated Surface Hydroxyl Groups and Hydroxide Ion. *Langmuir* **1988**, *4* (3), 753–758. https://doi.org/10.1021/la00081a045.

(37) Terzano, R.; Spagnuolo, M.; Vekemans, B.; De Nolf, W.; Janssens, K.; Falkenberg, G.; Fiore, S.; Ruggiero, P. Assessing the Origin and Fate of Cr, Ni, Cu, Zn, Pb, and V in Industrial Polluted Soil by Combined Microspectroscopic Techniques and Bulk Extraction Methods. *Environ. Sci. Technol.* **2007**, *41* (19), 6762–6769. https://doi.org/10.1021/es070260h.

(38) McKenzie, R. M. The Synthesis of Birnessite, Cryptomelane, and Some Other Oxides and Hydroxides of Manganese. *Mineralogical Magazine* **1971**, *38* (296), 493–502. https://doi.org/10.1180/minmag.1971.038.296.12.

(39) Rosecrans, C. Z.; Nolan, B. T.; Gronberg, J. M. Prediction and Visualization of Redox Conditions in the Groundwater of Central Valley, California. *Journal of Hydrology* **2017**, *546*, 341–356. https://doi.org/10.1016/j.jhydrol.2017.01.014.

(40) Landrot, G.; Ginder-Vogel, M.; Sparks, D. L. Kinetics of Chromium(III) Oxidation by Manganese(IV) Oxides Using Quick Scanning X-Ray Absorption

Fine Structure Spectroscopy (Q-XAFS). *Environ. Sci. Technol.* **2010**, *44* (1), 143–149. https://doi.org/10.1021/es901759w.

(41) Wright, M. *An Introduction to Chemical Kinetics*; Wiley, 2004.

(42) Khawam, A.; Flanagan, D. R. Solid-State Kinetic Models: Basics and Mathematical Fundamentals. *J. Phys. Chem. B* **2006**, *110* (35), 17315–17328. https://doi.org/10.1021/jp062746a.

(43) Crans, D. C.; Tracey, A. S. The Chemistry of Vanadium in Aqueous and Nonaqueous Solution. In *Vanadium Compounds*; ACS Symposium Series; American Chemical Society, 1998; Vol. 711, pp 2–29. https://doi.org/10.1021/bk-1998-0711.ch001.

(44) Howarth, O. W. Vanadium-51 NMR. *Progress in Nuclear Magnetic Resonance Spectroscopy* **1990**, *22* (5), 453–485. https://doi.org/10.1016/0079-6565(90)80007-5.

(45) Tracey, A. S.; Jaswal, J. S.; Angus-Dunne, S. J. Influences of PH and Ionic Strength on Aqueous Vanadate Equilibria. *Inorg. Chem.* **1995**, *34* (22), 5680–5685. https://doi.org/10.1021/ic00126a043.

(46) Frierdich, A. J.; Catalano, J. G. Fe(II)-Mediated Reduction and Repartitioning of Structurally Incorporated Cu, Co, and Mn in Iron Oxides. *Environ. Sci. Technol.* **2012**, *46* (20), 11070–11077. https://doi.org/10.1021/es302236v.

(47) Manceau, A.; Marcus, M. A.; Grangeon, S. Determination of Mn Valence States in Mixed-Valent Manganates by XANES Spectroscopy. *American Mineralogist* **2012**, *97* (5–6), 816–827. https://doi.org/10.2138/am.2012.3903.

(48) Toner, B.; Manceau, A.; Webb, S. M.; Sposito, G. Zinc Sorption to Biogenic Hexagonal-Birnessite Particles within a Hydrated Bacterial Biofilm. *Geochimica et Cosmochimica Acta* **2006**, *70* (1), 27–43. https://doi.org/10.1016/j.gca.2005.08.029.

(49) Zhu, M.; Ginder-Vogel, M.; Parikh, S. J.; Feng, X.-H.; Sparks, D. L. Cation Effects on the Layer Structure of Biogenic Mn-Oxides. *Environmental Science & Technology* **2010**, *44* (12), 4465–4471. https://doi.org/10.1021/es1009955.

(50) Zhao, H.; Zhu, M.; Li, W.; Elzinga, E. J.; Villalobos, M.; Liu, F.; Zhang, J.; Feng, X.; Sparks, D. L. Redox Reactions between Mn(II) and Hexagonal Birnessite Change Its Layer Symmetry. *Environ. Sci. Technol.* **2016**, *50* (4), 1750–1758. https://doi.org/10.1021/acs.est.5b04436.

(51) Manceau, A.; Drits, V. A.; Silvester, E. Structural Mechanism of Co21 Oxidation by the Phyllomanganate Buserite. 26.

(52) Marcus, M. A.; Manceau, A.; Kersten, M. Mn, Fe, Zn and As Speciation in a Fast-Growing Ferromanganese Marine Nodule1 1Associate Editor: G. R. Helz. *Geochimica et Cosmochimica Acta* **2004**, *68* (14), 3125–3136. https://doi.org/10.1016/j.gca.2004.01.015.

(53) Webb, S. M. Structural Characterization of Biogenic Mn Oxides Produced in Seawater by the Marine Bacillus Sp. Strain SG-1. *American Mineralogist* **2005**, *90* (8–9), 1342–1357. https://doi.org/10.2138/am.2005.1669.

(54) Villalobos, M.; Lanson, B.; Manceau, A.; Toner, B.; Sposito, G. Structural Model for the Biogenic Mn Oxide Produced by Pseudomonas Putida. *American Mineralogist* **2006**, *91* (4), 489–502. https://doi.org/10.2138/am.2006.1925.

(55) Yin, H.; Wang, X.; Qin, Z.; Ginder-Vogel, M.; Zhang, S.; Jiang, S.; Liu, F.; Li, S.; Zhang, J.; Wang, Y. Coordination Geometry of Zn2+ on Hexagonal Turbostratic Birnessites with Different Mn Average Oxidation States and Its Stability under Acid Dissolution. *Journal of Environmental Sciences* **2018**, *65*, 282–292. https://doi.org/10.1016/j.jes.2017.02.017.

(56) Lafferty, B. J.; Ginder-Vogel, M.; Zhu, M.; Livi, K. J. T.; Sparks, D. L. Arsenite Oxidation by a Poorly Crystalline Manganese-Oxide. 2. Results from X-Ray Absorption Spectroscopy and X-Ray Diffraction. *Environ. Sci. Technol.* **2010**, *44* (22), 8467–8472. https://doi.org/10.1021/es102016c.

(57) Elzinga, E. J. 54Mn Radiotracers Demonstrate Continuous Dissolution and Reprecipitation of Vernadite (δ-MnO2) during Interaction with Aqueous Mn(II). *Environ. Sci. Technol.* **2016**, *50* (16), 8670–8677. https://doi.org/10.1021/acs.est.6b02874.

(58) Drits, V. A.; Lanson, B.; Gaillot, A.-C. Birnessite Polytype Systematics and Identification by Powder X-Ray Diffraction. *American Mineralogist* **2007**, *92* (5–6), 771–788. https://doi.org/10.2138/am.2007.2207.

(59) Elzinga, E. J. Reductive Transformation of Birnessite by Aqueous Mn(II). *Environ. Sci. Technol.* **2011**, *45* (15), 6366–6372. https://doi.org/10.1021/es2013038.

(60) Lefkowitz, J. P.; Rouff, A. A.; Elzinga, E. J. Influence of PH on the Reductive Transformation of Birnessite by Aqueous Mn(II). *Environ. Sci. Technol.* **2013**, *47* (18), 10364–10371. https://doi.org/10.1021/es402108d.

(61) Lefkowitz, J. P.; Elzinga, E. J. Structural Alteration of Hexagonal Birnessite by Aqueous Mn(II): Impacts on Ni(II) Sorption. *Chemical Geology* **2017**, *466*, 524–532. https://doi.org/10.1016/j.chemgeo.2017.07.002.

(62) Lefkowitz, J. P.; Elzinga, E. J. Impacts of Aqueous Mn(II) on the Sorption of Zn(II) by Hexagonal Birnessite. *Environ. Sci. Technol.* **2015**, *49* (8), 4886–4893. https://doi.org/10.1021/es506019j.

(63) Besnardiere, J.; Petrissans, X.; Ribot, F.; Briois, V.; Surcin, C.; Morcrette, M.; Buissette, V.; Le Mercier, T.; Cassaignon, S.; Portehault, D. Nanoparticles of Low-Valence Vanadium Oxyhydroxides: Reaction Mechanisms and Polymorphism Control by Low-Temperature Aqueous Chemistry. *Inorg. Chem.* **2016**, *55* (21), 11502–11512. https://doi.org/10.1021/acs.inorgchem.6b02059.

(64) Krakowiak, J.; Lundberg, D.; Persson, I. A Coordination Chemistry Study of Hydrated and Solvated Cationic Vanadium Ions in Oxidation States +III, +IV, and +V in Solution and Solid State. *Inorg. Chem.* **2012**, *51* (18), 9598–9609. https://doi.org/10.1021/ic300202f.

(65) Brugger, J.; Elliott, P.; Meisser, N.; Ansermet, S. Argandite, Mn7(VO4)2(OH)8, the V Analogue of Allactite from the Metamorphosed Mn Ores at Pipji, Turtmann Valley, Switzerland. *American Mineralogist* **2011**, *96* (11–12), 1894–1900. https://doi.org/10.2138/am.2011.3841.

(66) White, A. F.; Peterson, M. L. Reduction of Aqueous Transition Metal Species on the Surfaces of Fe(II) -Containing Oxides. *Geochimica et Cosmochimica Acta* **1996**, *60* (20), 3799–3814. https://doi.org/10.1016/0016-7037(96)00213-X.

(67) Genuchten, C. M. van; Peña, J. Sorption Selectivity of Birnessite Particle Edges: A d-PDF Analysis of Cd(Ii) and Pb(Ii) Sorption by δ-MnO 2 and Ferrihydrite. *Environmental Science: Processes & Impacts* **2016**, *18* (8), 1030–1041. https://doi.org/10.1039/C6EM00136J.

(68) Michel, F. M.; Ehm, L.; Antao, S. M.; Lee, P. L.; Chupas, P. J.; Liu, G.; Strongin, D. R.; Schoonen, M. A. A.; Phillips, B. L.; Parise, J. B. The Structure of Ferrihydrite, a Nanocrystalline Material. *Science* **2007**, *316* (5832), 1726–1729. https://doi.org/10.1126/science.1142525.

(69) Villalobos, M. The Role of Surface Edge Sites in Metal(Loid) Sorption to Poorly-Crystalline Birnessites. In *Advances in the Environmental Biogeochemistry of Manganese Oxides*; ACS Symposium Series; American Chemical Society, 2015; Vol. 1197, pp 65–87. https://doi.org/10.1021/bk-2015-1197.ch004.

(70) Wasylenki, L. E.; Weeks, C. L.; Bargar, J. R.; Spiro, T. G.; Hein, J. R.; Anbar, A. D. The Molecular Mechanism of Mo Isotope Fractionation during Adsorption to

Birnessite. *Geochimica et Cosmochimica Acta* **2011**, *75* (17), 5019–5031. https://doi.org/10.1016/j.gca.2011.06.020.

(71) Sun, Q.; Liu, C.; Alves, M. E.; Ata-Ul-Karim, S. T.; Zhou, D.-M.; He, J.-Z.; Cui, P.-X.; Wang, Y.-J. The Oxidation and Sorption Mechanism of Sb on δ-MnO2. *Chemical Engineering Journal* **2018**, *342*, 429–437. https://doi.org/10.1016/j.cej.2018.02.091.

(72) Villalobos, M.; Escobar-Quiroz, I. N.; Salazar-Camacho, C. The Influence of Particle Size and Structure on the Sorption and Oxidation Behavior of Birnessite: I. Adsorption of As(V) and Oxidation of As(III). *Geochimica et Cosmochimica Acta* **2014**, *125*, 564–581. https://doi.org/10.1016/j.gca.2013.10.029.

(73) Simanova, A. A.; Kwon, K. D.; Bone, S. E.; Bargar, J. R.; Refson, K.; Sposito, G.; Peña, J. Probing the Sorption Reactivity of the Edge Surfaces in Birnessite Nanoparticles Using Nickel(II). *Geochimica et Cosmochimica Acta* **2015**, *164*, 191–204. https://doi.org/10.1016/j.gca.2015.04.050.

(74) Feng, X.; Wang, P.; Shi, Z.; Kwon, K. D.; Zhao, H.; Yin, H.; Lin, Z.; Zhu, M.; Liang, X.; Liu, F.; Sparks, D. L. A Quantitative Model for the Coupled Kinetics of Arsenic Adsorption/Desorption and Oxidation on Manganese Oxides. *Environ. Sci. Technol. Lett.* **2018**, *5* (3), 175–180. https://doi.org/10.1021/acs.estlett.8b00058.

(75) Ginder-Vogel, M.; Landrot, G.; Fischel, J. S.; Sparks, D. L. Quantification of Rapid Environmental Redox Processes with Quick-Scanning x-Ray Absorption Spectroscopy (Q-XAS). *Proceedings of the National Academy of Sciences* **2009**, *106* (38), 16124–16128. https://doi.org/10.1073/pnas.0908186106.

(76) Oze, C.; Bird, D. K.; Fendorf, S. Genesis of Hexavalent Chromium from Natural Sources in Soil and Groundwater. *PNAS* **2007**, *104* (16), 6544–6549. https://doi.org/10.1073/pnas.0701085104.

(77) Huang, J.-H.; Huang, F.; Evans, L.; Glasauer, S. Vanadium: Global (Bio)Geochemistry. *Chemical Geology* **2015**, *417*, 68–89. https://doi.org/10.1016/j.chemgeo.2015.09.019.

(78) Larsson, M. A.; D'Amato, M.; Cubadda, F.; Raggi, A.; Öborn, I.; Kleja, D. B.; Gustafsson, J. P. Long-Term Fate and Transformations of Vanadium in a Pine Forest Soil with Added Converter Lime. *Geoderma* **2015**, *259–260*, 271–278. https://doi.org/10.1016/j.geoderma.2015.06.012.

(79) McMahon, P. B.; Belitz, K.; Reddy, J. E.; Johnson, T. D. Elevated Manganese Concentrations in United States Groundwater, Role of Land Surface–Soil–

Aquifer Connections. *Environ. Sci. Technol.* **2019**, *53* (1), 29–38. https://doi.org/10.1021/acs.est.8b04055.

(80) Ying, S. C.; Schaefer, M. V.; Cock-Esteb, A.; Li, J.; Fendorf, S. Depth Stratification Leads to Distinct Zones of Manganese and Arsenic Contaminated Groundwater. *Environ. Sci. Technol.* **2017**, *51* (16), 8926–8932. https://doi.org/10.1021/acs.est.7b01121.

Chapter 4: Redox Dynamics of Vanadium in a Diffusion-Limited Environment

Abstract

Manganese and iron oxides are common components of terrestrial environments and play an important role in the fate of vanadium (V) in soil systems. Despite the growth in vanadium geochemical studies, a mechanistic understanding of the factors controlling V fate in mixed-phase systems is still lacking. In this study, we examined the effects of competitive, abiotic oxidation, reduction and retention of V by Mn and Fe oxides in a diffusion limited environment. The relative rates of oxidation, reduction, and surface complexation are evaluated for their impacts on vanadate attenuation within the context of diffusive transport. Multi-chamber reactors were constructed that allowed V to react with two mineral phases separately, while allowing any aqueous V species to diffusive between mineral chambers. To evaluate the role of oxidation and adsorption on Mn oxides, birnessite was selected for one chamber, while goethite, a non-redox active adsorption control, or magnetite, a reduction mediator and adsorbent, were used in the opposite chamber. Spiking V^{IV} into the chambers led to the rapid production of aqueous vanadate, which diffuses into the Fe oxide chamber and quickly saturates the Fe oxide surface. Adsorption of the vanadate by birnessite is slower, but it saturates slowly and ultimately retains more than the two Fe oxides. The rate of vanadate production by birnessite far outpaces the rate of vanadate reduction by the structural Fe^{II} of magnetite, suggesting that adsorption and surface complexation, even by birnessite itself is a more

significant attenuation pathway than abiotic reduction to insoluble V^{IV} oxyhydroxides or surface complexation by Fe oxides.

I. Introduction

Vanadium (V) is a naturally occurring metal that poses a threat to human health and the environment.[1,2] While human activities including industrial production and mining operations are increasing V emissions, geogenic V is the predominant source of V contamination in groundwater.[3–5] In subsurface environments, V enters groundwater as V^{III}-rich Fe^{III} mineral phases weather.[6,7] In human-impacted sites, V can enter the groundwater through anthropogenic routes including weathering of mine tailings or steel slag and bauxite ore processing waste.[6,8–11] In soil and sediment environments subject to oxic conditions, reduced, insoluble forms of V (V^{III} and V^{IV}) are oxidized to soluble V^{V} (vanadate, $H_nVO_4^{(3-n)-}$) which is then able to contaminate groundwater resources relied on for irrigation and human consumption. The United States Environmental Protection Agency and California Department of Public Health has established a 50 μg L^{-1} notification level for V^{V} drinking water due to evidence that vanadate is toxic to humans[12] through multiple pathways including disruption of phosphatase activity and in the proper functioning of p53.[13–16] The notification levels for V in drinking water vary widely across the US; California has proposed decreasing that state's notification level from 50 to 15 μg L^{-1}, while North Carolina has established a groundwater standard of 7 μg L^{-1}, and Canada provides a water quality guideline for freshwater of 120 μg L^{-1}.[14,17,18]

In redox fluctuating soil environments, V may cycle between oxidized (V^{V}) and reduced (V^{III} and V^{IV}) forms.[4,5,19] Mn^{IV} oxides and mixed-valent $Fe^{II/III}$ oxides commonly

co-occur within redox cycling environments and can form in close proximity to redox sensitive elements like V .[4,20–22] Several Fe oxide mineral phases have been shown to effectively remove V^{V} from solution through surface complexation at circumneutral pH.[23,24] Fe^{II}-bearing mineral phases can not only adsorb V^{V}, but can also reduce it to V^{IV} via a surface-mediated electron transfer mechanism.[25,26] In general, the presence of Fe oxides have been shown to result in vanadate attenuation. In a recent study, we showed that birnessite, a poorly-crystalline Mn^{IV} oxide commonly found in soils and sediments can oxidize V^{IV} oxyhydroxide minerals to aqueous V^{V} relatively quickly. We found that Mn oxides are capable of oxidizing a higher concentration of V^{IV} than can be retained through surface complexation.[27] These findings demonstrate that V may undergo abiotically driven redox cycling when Mn oxides and reduced Fe phases are present within soils, and that there may be competition between the phases for V adsorption. Identifying the factors that determine whether V^{V} or V^{IV} ultimately dominates in the soils can inform which conditions promote V^{V} mobilization.

The structure of soils combined with biogeochemical processes controls the transport of contaminants in the subsurface by influencing tortuosity,[28] pore structure,[29–31] precipitation and dissolution reactions,[32] advection and dispersion,[32,33] non-equilibrium and preferential flow,[34,35] storage,[36] stochasticity and scale,[37] surfaces,[38] and pedological processes,[39] among other factors. Although all factors influence contaminant mobility, diffusion-limited transport is the dominating factor at the aggregate scale,[33,40–42] which can often be described using a dual-pore domain approach.[43] In a dual-pore model, large pores support advective flow, while relatively slow diffusion-limited transport dominates in

smaller pore channels.[43] Diffusion-limited transport can result in oxygen depletion within the aggregate's interior due to aerobic microbial respiration.[44,45] These transport limitations lead to the formation of steep redox interfaces within aggregates where reduced species, such as V^{IV} oxyhydroxides and partially oxidized species such as Mn and Fe oxides could potentially occur in close proximity.

The relative rates of kinetic reactions (e.g., abiotic oxidation or reduction of metals by soil minerals) compared to rates of transport can be assessed using the Thiele modulus,[46–49] Damköhler numbers,[50] and Péclet number.[32] The Damköhler numbers and the Thiele modulus involve a comparison of the reaction and diffusion time scales, which allows the user to assess whether kinetic or diffusion limitation determines the rate of product formation.[47,48,50] These dimensionless parameters have been extensively used to evaluate aspects of reactive transport in environmental and synthetic systems.[32,48–51] With many pathways for abiotic oxidation, reduction and adsorption-desorption already defined, a remaining yet poorly defined variable in determining the fate of V in the subsurface is the role of diffusion. In this study, adsorption and desorption processes of V is coupled to redox cycling between the +4 and +5 charge states in a diffusion-limited environment to investigate how this type of transport impacts the partitioning of V between oxidation states, mineral sorbents and the aqueous versus solid phase.

II. Materials and Methods

Mineral Characterization

Birnessite was synthesized following past methods.[52] Briefly, 63 g of $KMnO_4$ (Fisher) was dissolved in 1 L of double deionized (DDI) water (18.2 MΩ resistivity; EMD Millipore) in a 4 L flask. The solution was heated to 90° C while 66 ml of trace metal grade concentrated hydrochloric acid (Fisher) was added over the course of 10 minutes with rapid stirring. The mixture was maintained at 90° C for an additional 10 min after which it was cooled to room temperature for 30 min, then vacuum filtered to collect solids. Excess $KMnO_4$ was removed by rinsing solids repeatedly with DDI water. The solids were then air-dried in a covered container before being ground with an agate mortar and pestle. The identity and phase purity of the dry powder was verified by X-ray diffraction using a Siemens D500 with Cu Kα radiation and surface area was measured using multi-point Brunauer-Emmett-Teller (BET) N_2 adsorption. The powder was identified as hexagonal birnessite with an average oxidation state of 3.72 and a surface area of 37.80 $m^2\ g^{-1}$. The average oxidation state was determined via the Combo method developed by Manceau et al. and used as implemented previously.[27,53] Goethite and magnetite were purchased from Strem Chemicals (99.9% purity) and all phases were confirmed by powder X-ray diffraction. Surface area of goethite and magnetite were 28.87 $m^2\ g^{-1}$ and 0.92 $m^2\ g^{-1}$, respectively. The ferrous Fe content of the magnetite was 23.4 %.

Multi-chamber reactor experiments

All experiments were performed in an anerobic glovebag (Coy Laboratory Products, Inc.) with O_2 maintained below 1 ppmv using a Pd catalyst with an atmospheric

content of 3.5% H_2 and 96.5% N_2. Multi-chamber reactors were constructed as described previously (Ying et al., 2011, 2012) and are described here briefly. Reactors were constructed from two acid-washed PVC pipes (capacity of 330 ml per chamber) separated by a 0.1 μm VTCP membrane held in place by a union. The membrane allows the diffusion of dissolved species between the chambers while larger solids are kept separated in their respective chambers (Appendix 3 Figure 4.5).

Multi-chamber experiments were used to test the complementive oxidation/reduction and adsorption of V in the presence of (1) birnessite (MnO_2) and goethite (α-FeOOH) and (2) birnessite and magnetite (Fe_3O_4). The background electrolyte solution for the birnessite|goethite reactor was prepared with 25 mM NaCl and buffered at pH 7.00 with 10 mM PIPES [piperazine-N,N′-bis (2-ethanesulfonic acid)] sodium salt. The background electrolyte for the birnessite|magnetite reactor consisted of 2.7 mM KCl, 7.9 mM NaCl and 400 μM $CaCl_2$ and was buffered at a pH of 7.1 using 10 mM MOPS [3-(N-morpholino) propanesulfonic acid]. All reagents were 99.5% purity or greater. The transition from PIPES to MOPS was made in response to recent work demonstrating the ability of the piperazine group of many Good's buffers to act as an electron donor to Mn^{IV} octahedra at birnessite edge sites,[54] leading to the accumulation of Mn^{III}. Although this effect is minimized at short (< 100 min) time scales,[55] recent studies have also shown that MOPS does not interfere with oxyanion adsorption at neutral pH.[26,56]

Minerals were added to achieve solid loadings similar previous studies: 1 g L^{-1} birnessite [27] and 4.47 g L^{-1} of goethite was used to match the birnessite:goethite ratios used previously [42] and 4 g L^{-1} of magnetite was used to match previous V kinetic studies [26] as

well as to ensure an excess of ferrous iron. Vanadium was added as $VOSO_4 \cdot 5H_2O$ to initiate all experiments, except one birnessite|magnetite experiment, where a 100 mM stock solution of Na_3VO_4 was used. This stock was pH adjusted prior to use to ensure the proportion of decavanadate was minimized. For the birnessite|goethite, $VOSO_4 \cdot 5H_2O$ was added to final concentrations of 10, 100 and 300 μM to reflect what has been observed in environments with elevated V contamination (Burke et al. 2012, Burke et al. 2013).[10,57] The birnessite|magnetite reactor initiated with V^V was constrained to an initial concentration of 300 μM.

All buffer solutions were then degassed under vacuum for 3 hrs and then placed in an anerobic chamber to equilibrate overnight. Each chamber was prepared by adding 210 ml of buffer and initiating stirring in each chamber with an overhead PTFE paddle system. Minerals were sonically dispersed in 50 mL anoxic buffer solution for 15 minutes and before being added to each respective chamber. $VOSO_4 \cdot 5H_2O$ was dissolved in 50 mL of anoxic buffer, which immediately precipitated beige V^{IV} oxyhydroxides characterized in Abernathy et al. 2021.[27] The reaction was initiated by simultaneously adding each 50 ml aliquot of V^{IV} oxyhydroxide slurry to its respective reactor chamber for a final chamber volume of 310 ml. In the case of the Na_3VO_4 initiated birnessite|magnetite reactor, 930 μL of Na_3VO_4 stock was added to 310 ml of mineral slurry prepared by adding 50 ml of sonically dispersed mineral to 260 ml of buffer with stirring. At each time point, 1 ml of slurry was sampled for total digestion and 3 ml was sampled and immediately filtered through a 0.22 μm PES membrane to acquire the aqueous fraction. At select time points, an additional 3 ml was filter deposited onto 0.22 μm nitrocellulose paper and dried

anoxically in the dark for later XAS analysis. Total and aqueous V, Mn and Fe were then measured using a Perkin-Elmer Optima 7300DV ICP-OES. Synchrotron X-ray based analyses including extended X-ray absorption fine structure (EXAFS), X-ray absorption near-edge structure (XANES) spectroscopy, and synchrotron powder-XRD were conducted at beamlines 4-1, 4-3, 7-3, 11-2, and 11-3 at the Stanford Synchrotron Radiation Lightsource as described previously.[27] Aqueous vanadium was assumed to be dominated by V^{V} given the insolubility of V^{IV} at pH 7.0 seen in similar systems.[25,26] Additional details including diffusion control experiments are described in Appendix 3.

Kinetic Batch Experiments

Stirred batch experiments were carried out to determine the rate of adsorption of vanadate onto birnessite and goethite. All reactors were run oxically as described in Abernathy et al. 2021.[27] Briefly, 500 ml polypropylene vessels were wrapped in aluminum foil to prevent any photochemical effects and filled with a background electrolyte consisting of 25 mM NaCl and buffered to pH 7.00 with 10 mM MOPS. Birnessite or goethite were added to achieve solid loadings identical to that used in the multi-chamber reactors, with goethite also being evaluated at loadings of 1 g L^{-1}. Mineral slurry was stirred and homogenized, and the reaction was initiated by adding aliquots of the 100 mM Na_3VO_4 stock described above to a final concentration of 10, 100 or 300 μM V. At each time point, 5 ml of the slurry was filtered through a 0.22 μm PES membrane to quench the reaction. Samples were prepared for ICP-OES analysis by measuring 4 ml of the filtrate, diluting to 5 ml with ultrapure H_2O and acidifying to 3% v/v with HNO_3. Reaction kinetics were calculated for the disappearance of V^{V} from solution using to the first order rate law, as

well as the Integrated Langmuir Kinetic model from Marczewski 2010.[58] A detailed presentation of this model is available in Abernathy et al. 2021.[27]

III. Results

Kinetic Batch Experiments

The adsorption of V^V onto birnessite and goethite was rapid and well described using a pseudo-first order kinetic model, the rate constants derived from which (k_{ads}) are presented in Tables 4.1 and 4.3. When normalized by mass, the k_{ads} for birnessite was 1.67 times greater than k_{ads} goethite. However, at the mass loadings used in the multi-chamber reactors the k_{ads} for V^V on goethite was 1.83 times greater than birnessite. Likewise, the first order k_{ads} for V^V adsorption onto magnetite as reported by Vessey and Lindsay 2020 [26] was 1.48 times greater than the k_{ads} for birnessite. Although the mass loadings were different, the k_{ads} for goethite was 1.24 times greater than the k_{ads} for magnetite at the loadings used in the multi-chamber reactor experiments.

Table 4.1 Results of the kinetic adsorption experiments.

Kinetic adsorption experiment	Mass Loading gL^{-1}	$C_{initial}$ (μM)	C_{eq} (μM)	q_{eq} (μmole g^{-1})	q_{max} (μmole g^{-1})	K_L (L μmole^{-1})	k_{ads} (s^{-1})	f_{eq} (dimensionless)	K_s ($k_{1,app}$) (s^{-1})	rss
10 μM Birn	1.00	11.16	3.88	7.29	169.74	3.72E-02	5.17E-04	2.80E-02	1.99E-03	1.25E-01
100 μM Birn	1.00	104.14	66.40	37.90	169.74	3.72E-02	2.96E-04	8.09E-02	1.06E-03	7.06E-02
300 μM Goet	1.00	312.41	265.06	47.32	43.81	2.85E-01	1.78E-04	1.52E-01	5.18E-03	2.13E-01
300 μM Goet	4.47	312.41	115.99	43.91	43.81	2.85E-01	5.43E-04	6.29E-01	3.25E-02	5.08E-02

The batch equilibrium factors (f_{eq}) for all reactions fell between 0 and 1, indicating their suitability for analysis via Marczewski's Integrated Langmuir Kinetic model. In all cases, the first-order kinetic coefficient, $k_{1,app}$ derived from this method was greater than the corresponding first order rate constant $k_{ads,}$ while the positive value of f_{eq} indicates a second-order contribution to the adsorption reaction (Marczewski 2013).[59] The adsorption data and fits are presented in Appendix 3 Figure 4.1.

Multi-Chamber Reactor Experiments

The competitive adsorption-oxidation-reduction reactions controlling the fate of V were investigated by injecting V^{IV} or V^{V} into the multichamber reactors containing the sorbent and environmental oxidant birnessite, as well as either the sorbent goethite or the sorbent and reductant magnetite. In all cases, V^{IV} added to the birnessite chamber was quickly oxidized to vanadate at rates comparable to those observed previously.[27] The rate at which V^{IV} was oxidized in this chamber was dependent on the initial concentration, and generally increased with $[V^{IV}]_{initial}$. In all cases, the maximum concentration V^{V}_{aq} was greater as a percentage of initial $[V^{IV}]_{initial}$ in the birnessite chamber, reaching a maximum in under 3 hrs. For all V^{IV} reactors with initial concentrations greater than 100 μM, a pulse of V^{V}_{aq} was observed in the birnessite chamber, which decreased concomitantly with an increase in V_{aq} within the Fe oxide chamber, indicating the role of diffusion in supplying the Fe chamber with aqueous V^{V} (Figure 4.1). Subsequently, the maximum V^{V}_{aq} within the Fe oxide chamber trailed the maximum V^{V}_{aq} in the birnessite chamber by 21-47 hrs. Diffusion of V^{V} between the chambers was crucial to the fate of V as it partitioned between the aqueous and solid phases of the chambers. In the absence of any

mineral sorbents, the rate of V^{V}_{aq} diffusion across the 0.1 µm VTCP membrane was 165.3 nmol min^{-1} with an initial concentration gradient of 280-320 µM. Using the method of Ying et al. 2011, these diffusion data in the absence of any sorbents were used to calculate a diffusion coefficient for V^{V} of 0.08 cm^2 s^{-1} (8.1 x 10^{-6} m^2 s^{-1}), approximately 27 times greater than As^{III} and As^{V} in a similar experimental setup.[49] The diffusion curves are presented in Appendix 3 Figure 4.4.

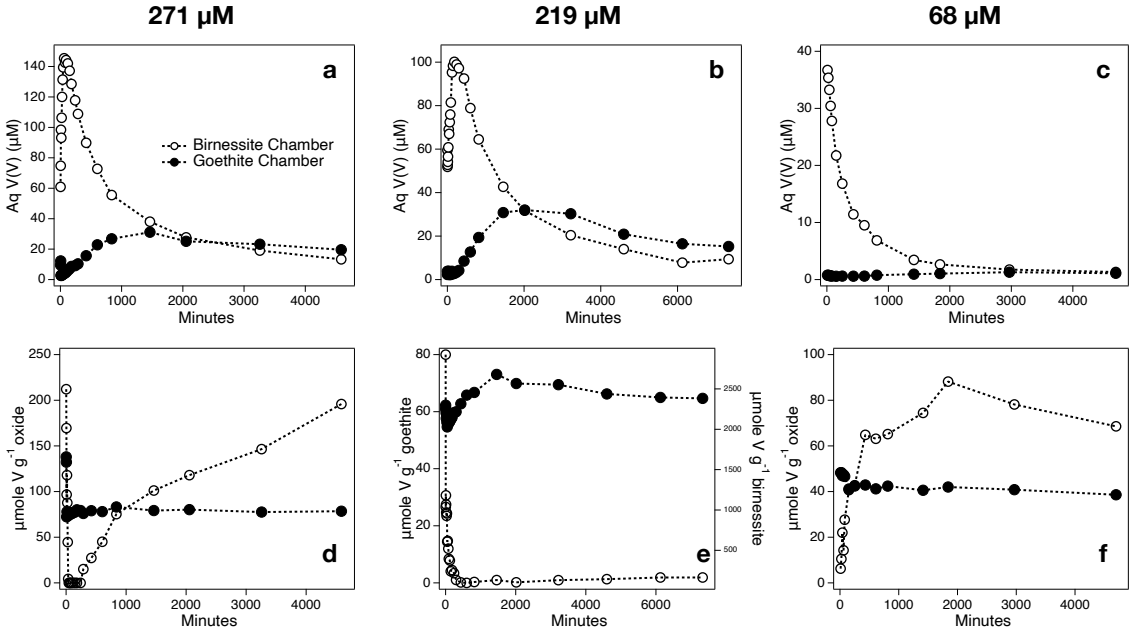

Figure 4.1 Aqueous and solid phase dynamics for vanadium in the Birnessite|goethite multi-chamber rectors. The open circles represent V in the birnessite chambers, and the closed circles represent the V in the goethite chambers. Plots a, b and c represent the aqueous V in the 271, 219 and 68 µM reactors, respectively. Plots d, e and f correspond to plots a, b and c respectively, and represent the solid phase associated V. Note that, at least in the early stages of the reaction this is not equivalent to adsorbed V, as V^{IV} is present primarily as the V^{IV} oxyhydroxide häggite.

Linear regression of the initial V^{IV} concentration to the maximum observed V^{V}_{aq} demonstrated that for every 1 µM increase in initial V^{IV} concentration, the maximum V^{V}_{aq} in the birnessite chamber increased by 0.8 µM (R^2 = 0.827) (Figure 4.1). The

remaining 0.2 μM not observed as aqueous V^{V} in the birnessite chamber adsorbed to the birnessite or diffused into the Fe oxide chamber. The rapid decrease in the solid phase V in the birnessite chamber at the beginning of the reaction is evidence for oxidative dissolution of V^{IV} oxyhydroxides (Figure 4.1 d, e, f). In the birnessite chamber of the 219 μM V^{IV} birnessite|goethite reactor, V^{IV} oxidation follows a first order k_{ox} of 1.2 x 10^{-4} s^{-1} over the first 6 hours, coinciding with the accumulation of aqueous V^{V} to the maximum observed aqueous concentration at that time. This increases to 1.6 x 10^{-3} s^{-1} when the $V^{IV}_{initial}$ is increased to 271 μM.

The remainder of this section will focus on the 219 μM birnessite|goethite experiment (Figure 4.1b, e). In the goethite chamber the solid-phase associated V decreases at a rate of 155 nmoles V g^{-1} goethite min^{-1} for the first 45 minutes before reaching a minimum of 54.7 μmole V g^{-1} goethite (Figure 4.1). During this time V_{aq} in the chamber is nearly constant at 2.9 ±0.6 μM, which is likely due to rapid adsorption of aqueous V^{V} diffusing in from the birnessite chamber. Then from 45 minutes to 24 hours, the amount of solid-phase associated V increased linearly from 54.7 to 73.1 umol V per g goethite (rate =13 nmoles V g^{-1} goethite min^{-1}) as V^{V} diffused from the birnessite chamber and adsorbed to goethite. However, the aqueous V concentration does not increase until the 5 hr mark, indicating near immediate sorption of V to goethite following diffusion from the birnessite chamber. At 5 hrs, the high affinity sites and approximately half of the low affinity adsorption sites on goethite were saturated, explaining the linear increase in aqueous V^{V} concentration from 5-24 hrs at a rate of 1.36 μM hr^{-1} before reaching a maximum of 32 μM at 33.6 hrs. Over the following 89 hr (3.7

days), V^{V}_{aq} decreased from 32 to 15 μM at a rate of 211 nM hr^{-1} while the amount of goethite-associated V remained relatively constant, decreasing at a rate of 66.4 nmole g^{-1} goethite hr^{-1} over the same period (Figure 4.1).

Oxidation of V(IV) in the birnessite chamber resulted in a maximum V^{V}_{aq} concentration at 3 hr followed by monotonic decrease to below 10 μM by 102 hrs (4.3 days). The decrease in V^{V}_{aq} in the birnessite chamber after 3 hrs coincided with an increase in both aqueous and solid phase V in the goethite chamber. Therefore, we infer that the majority of aqueous V present in the birnessite chamber at the 3hr mark diffused into the goethite chamber and adsorbed to the goethite. However, after the 24hrs, this trend reversed as the birnessite-associated V^{V} increased linearly at a rate of 681.7 nmole V g^{-1} birnessite hr^{-1} until the end of the experiment. This was likely due to the uptake of the V^{V} that was observed leaving the aqueous and solid phases of the goethite chamber over this time period, as well as the decrease in the V^{V} in the aqueous phase of birnessite chamber V^{V}. At the end of the experiment, the solid-phase associated V in the birnessite chamber was the largest pool of V in the reactor, retaining 2.5 times the vanadium as the goethite chamber. In general, this trend was also observed in the 68 and 271 μM birnessite|goethite reactors (Figure 4.1).

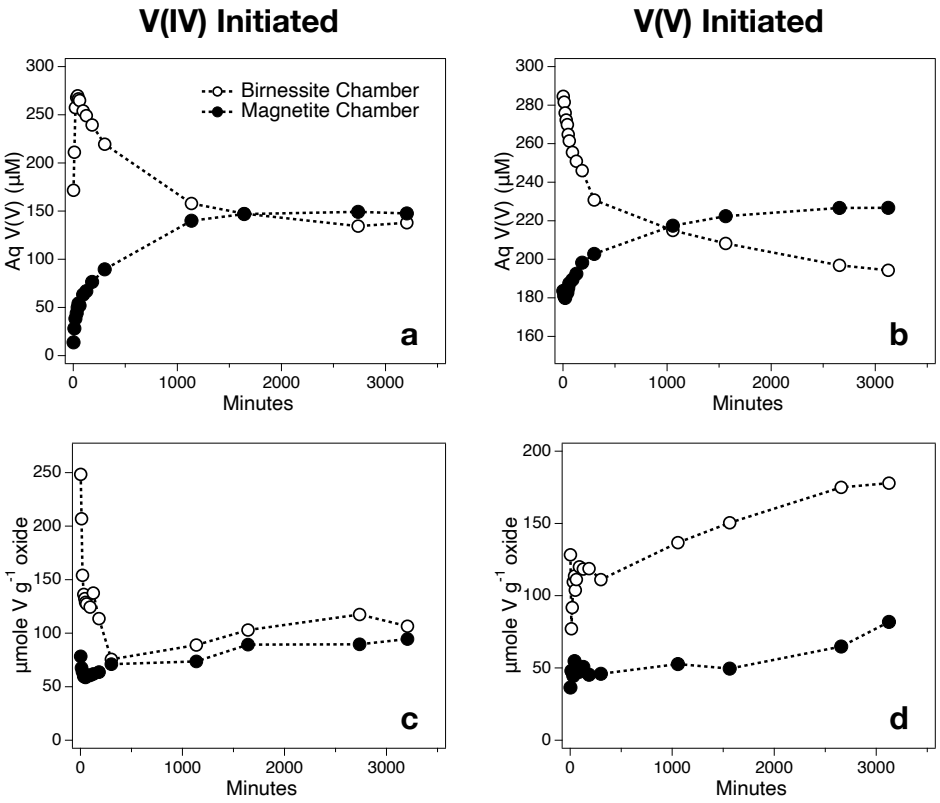

Figure 4.2 Aqueous and solid phase dynamics for vanadium in the Birnessite|Magnetite multichamber reactors. The open circles represent V in the birnessite chambers, and the closed circles represent the V in the magnetite chambers. Plots a and b represent the aqueous V in the V^{IV} and V^{V} initiated reactors, respectively. Plots c and d show the solid-phase associated, or adsorbed V in corresponding experiments.

In the birnessite|magnetite reactors, the behavior of V in the solid and aqueous phases is sensitive to its initial oxidation state (Figure 4.2). In the birnessite chamber of the V^{IV} initiated experiment, solid-phase associated V removal follows a first order kinetic model yielding a k_{ox} of 3.4 x 10^{-4} s^{-1} over the first 32 min, corresponding to a linear removal rate of -3.81 μmole V g^{-1} birnessite min^{-1}. When initiated with V^{V}, solid phase associated V increased with corresponding removal of V from the aqueous phase at

a rate of 342 nM min^{-1} over the first 90 min, yielding a first order $k_{removal}$ of 2.1 x 10^{-5} s^{-1}. By 5 hrs, the V^{IV} experiment reached a minimum solid-phase associated V of 75.6 μmole V g^{-1} birnessite, whereas the V^{V} initiated experiment exhibited a plateau in adsorbed V^{V} from 1.5 to 5 hrs of approximately 118 μmole V g^{-1} birnessite. However, in both experiments the adsorbed V increased from 5 hrs until the end of the reaction, comparable to the birnessite|goethite reactor. The rate of increase differed between the V^{IV} and V^{V} birnessite|magnetite reactors by a factor of 2, yielding rates of 0.745 and 1.43 μmole V g^{-1} birnessite for the V^{IV} and V^{V} initiated reactors respectively. In the V^{V} initiated reactor, this coincides with a decrease in the aqueous V concentration of −0.751 μM hr^{-1}, while the rate of decrease in V_{aq} in the V^{IV} reactor was −1.52 μM hr^{-1}. In the magnetite chamber of the V^{IV} reactor, aqueous V increased monotonically over the first 42 min at a rate of 85 nM min^{-1} as V^{V} diffused from the birnessite chamber. In the V^{V} experiment, V^{V}_{aq} decreased over the first 20 min at 205 nM min^{-1} as the vanadate adsorbed to the magnetite surface. V_{aq} then increased linearly until 3 hrs at a rate of 107 nM min^{-1} as V^{V} diffused from the birnessite chamber where V^{V}_{aq} was decreasing at a rate of 182 nM min^{-1}, indicating that removal from that chamber is a function of both diffusion and adsorption to birnessite. In the V^{IV} experiment, solid-phase associated V decreased linearly at a rate of −364 nmole V g^{-1} magnetite min^{-1} for the first 50 minutes, and then increased until the end of the experiment in two phases: 50 min to 3 hrs at 45 nmole V g^{-1} magnetite min^{-1} which then slowed to 8.2 nmole V g^{-1} magnetite min^{-1} from 3 hr to 53 hrs. In the V^{V} experiment, rapid uptake of the V^{V} is observed in the solid phase

over the first 10 minutes, saturating at about 49 ± 3 μmole V g^{-1} magnetite for the first 26 hrs. This increased sharply after 26 hrs at a rate of 1.17 μmole V g^{-1} magnetite hr^{-1}.

Reduction of birnessite by V^{IV} produced aqueous Mn^{II}, which diffused into the Fe oxide chamber and adsorbed (Appendix 3 Figures 4.2 and 4.3). Total digestion of unreacted magnetite revealed Mn contamination of approximately 150 ppm. X-ray absorption spectroscopy revealed this to be predominately structural Mn with an average valence of +2.5 using the Combo method of Manceau et al.[53] Thus, the Mn^{II} contribution due to reductive dissolution of the birnessite and diffusion into the magnetite chamber is presented as a difference in magnetite-normalized Mn between timepoints rather than in the total amount of Mn present (Appendix 3 Figure 4.3). In the V^{IV} initiated birnessite|magnetite reactor aqueous Mn^{II} production was similar to aqueous V^{V}, reaching a maximum concentration of 6.6 μM by 3 hrs and decreasing at a rate of 196 nM hr^{-1} between 3 and 27 hrs before plateauing at 2 μM. Produced Mn^{II} diffused into the magnetite chamber yielding aqueous Mn concentration of 1.65 μM by 90 min, after which it decreased at a rate of 26 nM hr^{-1} for the remainder of the experiment. Adsorption of Mn to magnetite follows a decrease in magnetite-associated Mn from 0 to 50 minutes, after which it increased at a rate of 58 μmole g^{-1} magnetite min^{-1} until plateauing at 5hrs.

X-ray Absorption Spectroscopy

Vanadium formed primarily tetrahedral vanadate surface complexes with goethite and birnessite at the end of the birnessite|goethite experiments. First shell V-O distances were best fit by 2 O at 1.68 Å and 2 O at 1.79 Å. On goethite, a bidenate binuclear corner sharing complex (^{2}C) was observed with V-Fe distance of 3.33 Å, while a ^{2}C V-Mn

complex was fit with V-Mn distance of 3.43 Å (Figure 4.3, Appendix 3 Table 4.1). A possible bidentate mononuclear edge sharing (^{1}E) complex on birnessite was also observed with a V-Mn distance of 2.97 Å. This V-Mn distance is longer than previously reported distance of 2.8 Å.[27] We attribute the longer V-Mn distances to highly strained surface complexes that form in response to the strong electrostatic repulsion between the +4 charge of the Mn and the +5 charge of the V atom. The V oxidation state was obtained by fitting the pre-edge peak of the XANES spectra with a Voight function to yield the normalized area.[11,26,60] Using this method, a decrease in valence from +5.1 to +4.8 was observed in the magnetite chamber over the course of the V^V initiated birnessite|magnetite experiment, whereas the valence remained unchanged in the birnessite chamber. In the V^{IV} initiated birnessite|magnetite experiment, the observed vanadium valence rose from +4.9 to +5.1 in the birnessite chamber, indicative of the oxidation that took place. Meanwhile, the average valence decreased from +4.8 to + 4.6 in the magnetite chamber, indicating that the V^V which had diffused in from the birnessite chamber had been reduced by the magnetite over time (Table 4.2). No pure V^{IV} was observed on any of the birnessite samples, likely due to being in contact with the birnessite between the end of the experiment and analysis at the synchrotron, a period of one week.

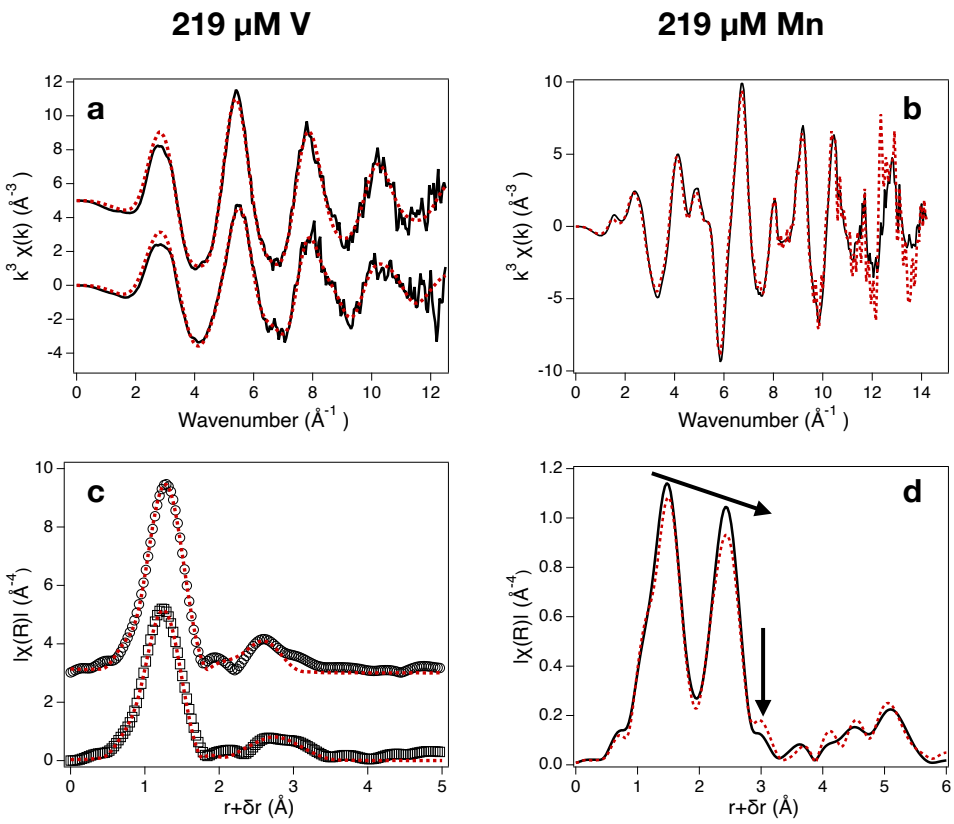

Figure 4.3 a, c) Results of shell by-shell nonlinear least-squares fitting of the V k-edge EXAFS taken of the final product in the birnessite (top spectra) and goethite (bottom spectra) chambers. The red line is the fit and black line or circles are the data. Additional fit details available in Appendix 3 Table 4.1. b, d) Mn EXAFS of the unreacted (red) and reacted (black) birnessite taken from the 219 µM V^{IV} experiment. The tilted arrow denotes the decrease in the Mn-Mn scattering peak at 2.5 Å r+δr relative to the Mn-O peak at 1.5 r+δr. The second arrow denotes the position of Mn^{II} adsorbed at surface vacancy sites.

Table 4.2 Calculated vanadium valance from least-squares fitting of the pre-edge feature with a single Voigt function.

Sample	Time point	Calculated Valence
219 μM goethite	end	4.90
219 μM birnessite	end	5.14
V(IV) MB birnessite	initial	4.92
V(IV) MB birnessite	end	5.06
V(IV) MB magnetite	initial	4.75
V(IV) MB magnetite	end	4.60
V(V) MB magnteite	initial	5.10
V(V) MB magnteite	end	4.82
V(V) MB birnessite	initial	5.10
V(V) MB birnessite	end	5.07
Unreacted magnetite	–	4.68

The Mn XAS of birnessite from the 219 μM birnessite|goethite experiment corroborates the transformation implied by the aqueous data. First, application of Manceau et al.'s Combo method[53] for determining Mn average oxidation state (AOS) shows a decrease of birnessite's AOS by 0.08 valence units over the course of the experiment. According to the V XAS, all the V^{IV} had oxidized by the end of the experiment, meaning that all 219 μM of electrons can be assumed to have transferred to the birnessite. Given an initial concentration of birnessite of 7.1 mM, a 3.08% reduction in AOS, equivalent to a decrease of 0.11 valence units is expected if all the electrons were retained by the Mn oxide. However, given an initial AOS of 3.715, only a 2.26% reduction in AOS was observed (0.08 valence units), equating to a difference between the predicted and observed decrease of 0.03 valence units. This difference can be accounted for by the 1.78 μM Mn^{II}_{aq} present at the end of the reaction which constitutes 0.025

valence units of the 0.03 valence unit difference, with the balance likely contributed by limited reduction of the birnessite by the piperazine ring of the PIPES buffer and Mn^{II} that was removed from solution via adsorption to goethite.

The reduction in birnessite's AOS is also observed in the Mn EXAFS, where the increase in the peak at 3.1 Å r+δr indicates the capture of aqueous Mn^{II} at surface vacancies (Figure 4.3).[61,62] This is also present as the growth of a shoulder at 6.5 $Å^{-1}$ in the χ(k) spectrum. As Mn^{II}_{aq} undergoes back reaction with birnessite, Mn^{II}_{aq} is incorporated as ordered structural Mn^{III}, which results in elongated Mn-O and Mn-Mn distances, resulting in a decrease in the intensity and slight rightward shift of the Mn-Mn peak at 2.5 Å r+δr.[63,64] Goethite-associated Mn was too low to collect EXAFS data, but XANES analysis reveal an AOS of 3.59, suggesting that surface-catalyzed oxidation of the Mn^{II} occurred at the Fe oxide surface, a phenomenon observed previously.[65,66] In the magnetite chambers, the signal from the structural Mn was strong enough to washout any slight differences from adsorbed Mn^{II} over the course of the reaction, with all XANES and EXAFS mapping perfectly onto the Mn XAS of the pure magnetite (Figure 4.4).

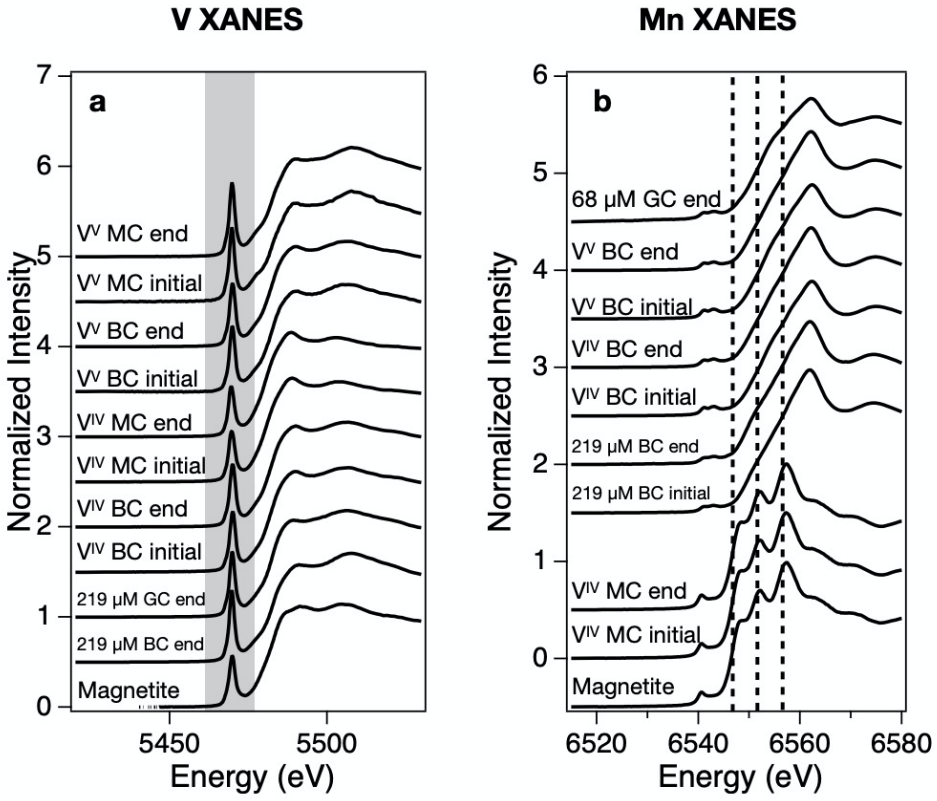

Figure 4.4 a) V K-edge XANES with the shaded region highlighting the pre-edge feature. b) Mn k-edge XANES with dashed lines representing the edge inflection points for the +2, +3 and +4 oxidation states. MC: Magnetite Chamber; BC: Birnessite Chamber; GC: Goethite Chamber

IV. Discussion

The fate of vanadium in diffusion limited environments is dependent on both surface complexation by and redox interactions with adjacent mineral phases. The purpose of this experiment was to investigate the chemical interactions and partitioning of V with Fe and Mn oxides in a diffusion limited setting. Regardless of whether Fe oxides were able to participate in electron exchange with V^V, both goethite and magnetite quickly became surface saturated with V^V, while birnessite continued uptake of V^V throughout the duration of the experiments. Therefore, while Fe oxides offer rapid

sorption capacity for vanadate removal, on a mole-per-mole basis, Mn oxides act as longer-term scavengers capable of sustained uptake. This result is consistent with the kinetic Langmuir analysis, where the K_{ads} values of vanadate onto goethite and magnetite were comparable at 5.4 and 4.4 x 10^{-4} s^{-1}, respectively but were 50-80% greater than the 3.0 x 10^{-4} s^{-1} of vanadate on birnessite.

As the reaction proceeds diffusion becomes increasingly important as the appearance of vanadate in the Fe oxide chambers is offset from its generation in the birnessite chamber. In natural systems, diffusion becomes an increasingly important transport factor as the spatial scale of soil-mediated processes is decreased. This is particularly relevant at the level of soil aggregates, where diffusion gradients and external conditions such as redox fluctuations give rise to redox gradients.[44,49,67] Therefore, within a system designed to mimic these processes the extent of kinetic or diffusive limitation on the reactions in question must be evaluated. As described above, Thiele's modulus and the diffusion Damköhler numbers are useful tools to compare diffusion and kinetic limitation, respectively. Both metrics make use of a (pseudo) first order rate constant (k), effective diffusivity (D_e) and length of diffusion R (radius of aggregate.[41,49,50] The Thiele modulus (φ) is calculated according to:

$$\varphi = R\sqrt{\frac{k}{D_e}}$$

And the diffusion Damköhler number, Da_{diff} is calculated by:

$$Da_{diff} = \frac{\text{reactive mass flux}}{\text{transport mass flux}} = \frac{k \times R^2}{D_e}$$

Several generalized conditions have been outlined for the Thiele modulus,[48,49] wherein:

$$\varphi > 3\ ;\ \text{diffusion controlled}$$

$$\varphi < 0.3\ \text{kinetically limited}$$

Tokunaga et al. established that processes with a $k > 10^{-4}$ or an $L > 5$ mm are diffusion controlled.[48] An alternative interpretation of the modulus holds that if $\varphi < 1$ then the reaction rates are controlled by the inherent kinetics of the reaction in question (product formation is kinetically limited). Conversely, if $\varphi > 1$ then physical diffusion of reactants becomes rate limiting (product formation is diffusion limited).[68] Likewise, general bounds on $D_{a_{diff}}$ have been established such that if $\mathrm{D_{a_{diff}}} \gg 1$ then the reaction rate is greater than the diffusion rate (product formation is diffusion limited); and if $\mathrm{D_{a_{diff}}} \ll 1$ then the rate of diffusion is greater than the reaction rate (product formation is kinetically limited).[32,41,51]

Using an effective diffusivity D_e of 8.1×10^{-2} and 1.3×10^{-2} $cm^2\ s^{-1}$ for V^{IV} and V^{V} respectively (Appendix 3 section IV), and an L equal to the half-length of the reactor (12.5 cm), φ and Da_{diff} were calculated for each redox or adsorption reaction, the values of which are presented in Table 4.3.

Table 4.3 Parameters used in the calculation of the Thiele moduli and Damköhler numbers.

Reaction	k (s^{-1})	φ	Da_{diff}	Source
V(IV) oxidation by birnessite	6.22E-04	2.75	7.58	Abernathy et al. 2021
V(IV) oxyhydroxide dissolution	3.19E-05	0.62	0.39	Abernathy et al. 2021
Kinetic adsorption of 100 μM by 1gL birn	2.96E-04	0.75	0.57	This study
kinetic adsorption of 300 μM 4.47 gL Goet	5.43E-04	1.02	1.04	This study
kinetic adsorption of 100 μM 2 gL Mag	4.39E-04	0.92	0.84	Vessey and Lindsay 2020

Generally, all V^{V} adsorption reactions were kinetically limited, while the oxidation of V^{IV} by birnessite was diffusion-limited for this system, confirming that diffusion determines the rate of flux of V^{V} between the chambers of the reactor. This also suggests that the rate of V^{V} production by birnessite determines how much V^{V} will be available to diffuse and interact with Fe oxides. At very low initial concentrations of V^{IV}, the rate of V^{V} production may be low enough that it is all retained by the birnessite. However, such low concentrations were not examined in this study. At the lowest V^{IV} initial concentration examined, V^{IV} was rapidly oxidized to V^{V} by birnessite and adsorbed to goethite, saturating the surface in the first 10 minutes with 48 μmole V g^{-1} (Figure 4.1). As the reaction proceeded V desorbed from the goethite and back-diffused into the birnessite chamber to adsorbed onto birnessite, indicating that V^{V} has a greater affinity for birnessite than goethite, which was also seen in chapter 2. Similarly, V^{V} quickly saturated the surface of magnetite in approximately 10 min,[26] but reached lower surface coverages than observed for either goethite or birnessite.

Ying et al. examined the competitive oxidation and adsorption processes in a similar birnessite|goethite reactor system that examined As^{III} oxidation.[42] They found that goethite retained more As^{V} at low initial As^{III} concentrations, while at higher initial As^{III}

concentrations birnessite was the dominant sorbent phase. The results of the current study demonstrate that the trends are similar for V^{V}. In experiments with both magnetite and goethite the Fe oxide saturated quickly while birnessite scavenged V^{V} from the aqueous phase over much longer time scales, eventually surpassing the Fe oxide in V^{V} retained on a mass normalized basis.

The rate of V^{IV} oxidation by birnessite can be contrasted against the slow rate of V^{V} reduction by magnetite. Quantifying the rate of V^{V} reduction by Fe^{II} bearing mineral phases has been a challenge, with the few prior studies that have examined this focusing on the rate of aqueous V^{V} removal and measuring the final V valence [26] or by calculating a reduction rate via the appearance of low concentrations of aqueous V^{IV} without decoupling the adsorption-desorption rates from the actual reduction rate.[25] In both cases the overall reaction was slow. This was confirmed in our birnessite|magnetite reactors, where all of the V^{IV} was oxidized but only ~20% of the V^{V} was then reduced by the magnetite over the experimental timescale. While this difference is likely inherent to the kinetics of the magnetite-vanadate reduction reaction, several other factors contribute to the low efficacy of the Fe oxide in removing V^{V} via reduction. Magnetite has a lower specific surface area than goethite, resulting in fewer available adsorption sites when normalized by mass. Additionally, the magnetite used in this study was partially oxidized, having a Fe^{II} : Fe^{III} stoichiometry (x) of 0.31 compared to stoichiometric magnetite where x = 0.5. Magnetite stoichiometry greatly influences the redox potential of the mineral and has been found to vary from the theoretical 0.5 to as low as 0.17.[69–71] In a study by Latta et al., a precipitous decline in the reduction rate of U^{VI} by magnetite

was observed when x was lowered from 0.33 to 0.28, with little to no noticeable reduction occurring below $x \leq 0.33$.[72] Likewise, magnetite with increasing stoichiometries produce greater rates of contaminant reduction.[70]

However, greater values of x do not always result in greater rates of V reduction. For example, White and Peterson observed the first-order removal of aqueous V^V by magnetite with a k_{obs} of 9.9×10^{-7} s^{-1}, despite a magnetite stoichiometry of 0.45.[25,73] This is approximately 443 time slower than what was observed by Vessey and Lindsay,[26] and slower than what was observed in this study. Two factors likely cause this discrepancy: available surface area and aging. The specific surface area reported for the Ishpeming magnetite used by White and Peterson was 0.1 m^2 g^{-1}, 110 times lower than the magnetite used by Vessey and Lindsay and 9 times lower than this study, resulting in significantly less surface area for reduction to occur and presumably resulting in faster surface passivation rates. The second factor, aging, can lower the reactivity of magnetite over time due to surface oxidation, anoxic Fe^{II} release, phase transformation, reaction with other redox sensitive elements and blocking of surface sites through adsorption.[25,74–76] While the characterization of the material by the authors was extensive, trace amounts of goethite and lepidocrocite were detected on some weathered samples, while passivating maghemite crusts formed in response to contact with trace amounts of redox active elements.[25] Work by Gorski et al. suggests that surface passivation of magnetite by such contaminants may not result in bulk structural changes to the magnetite, making them difficult to detect.[70] It is therefore likely that the reduced reactivity of the naturally occurring magnetite used by White and Peterson is likely a result of *in situ* environmental

aging prior to use in their study. Based on this analysis, we conclude that both the adsorption of V^V to magnetite and its subsequent reduction are kinetically limited even at low concentrations of V^V and in systems where V^{IV} oxidation is diffusion limited.

V. Environmental Implications

Reducing conditions are protective of groundwater quality with respect to vanadium due to the insolubility of V^{IV} and V^{III}.[5] Across a range of V concentrations, birnessite is more effective at removing aqueous V^V than both reducing and non-reducing Fe oxides, despite the ability of birnessite to oxidize reduced V to more soluble V^V. However, birnessite can oxidize more V^{IV} than it can retain through surface complexation of V^V. Our findings suggest that in environments subject to redox cycling or the establishment of redox gradients, the timescales for abiotic V^V reduction are greater than those needed for V^{IV} oxidation. This holds to be true even when there is a greater proportion of Fe oxides than Mn oxides due to the greater reactivity of Mn oxides towards oxidizing V^{IV} than $Fe^{II/III}$ oxides towards reducing V^V.

Vanadium typically enters groundwater via the *in situ* weathering of Fe-bearing mineral phases.[6,9,11] Even in the absence of significant advection, diffusive transport of V^V away from these Fe oxide phases may be faster than re-adsorption, creating conditions sufficient to result in release of V. This suggests that the mineralogical composition of the soil or sediments around a source of V^V can contribute as much, if not more to aqueous V^V attenuation as the Fe oxides that had weathered to produce that V^V, despite the closer spatial proximity of V^V to its parent Fe oxide upon its formation. The results of this study can be used to better parameterize reactive transport models used to

predict the distribution of V contamination in groundwater impacted by naturally occurring or anthropogenic vanadium contamination [4,6] with the goal of improving management strategies for affected waters.

VI. Supporting Information

The Supporting Information for chapter 4 is available in Appendix 3

VI. References

(1) Watt, J. A. J.; Burke, I. T.; Edwards, R. A.; Malcolm, H. M.; Mayes, W. M.; Olszewska, J. P.; Pan, G.; Graham, M. C.; Heal, K. V.; Rose, N. L.; Turner, S. D.; Spears, B. M. Vanadium: A Re-Emerging Environmental Hazard. *Environ. Sci. Technol.* **2018**, *52* (21), 11973–11974. https://doi.org/10.1021/acs.est.8b05560.

(2) Smit, C. Environmental Risk Limits for Vanadium in Water : A Proposal for Water Quality Standards in Accordance with the Water Framework Directive. *Milieurisicogrenzen voor vanadium : Een voorstel voor waterkwaliteitsnormen volgens de Kaderrichtlijn water* **2012**.

(3) Schlesinger, W. H.; Klein, E. M.; Vengosh, A. Global Biogeochemical Cycle of Vanadium. *Proceedings of the National Academy of Sciences* **2017**, *114* (52), E11092–E11100. https://doi.org/10.1073/pnas.1715500114.

(4) Wright, M. T.; Belitz, K. Factors Controlling the Regional Distribution of Vanadium in Groundwater. *Ground Water* **2010**, *48* (4), 515–525. https://doi.org/10.1111/j.1745-6584.2009.00666.x.

(5) Wright, M. T.; Stollenwerk, K. G.; Belitz, K. Assessing the Solubility Controls on Vanadium in Groundwater, Northeastern San Joaquin Valley, CA. *Applied Geochemistry* **2014**, *48*, 41–52. https://doi.org/10.1016/j.apgeochem.2014.06.025.

(6) Hudson-Edwards, K. A.; Byrne, P.; Bird, G.; Brewer, P. A.; Burke, I. T.; Jamieson, H.; Macklin, M.; Williams, R. Origin and Fate of Vanadium in the Hazeltine Creek Catchment Following the 2014 Mount Polley Mine Tailings Spill, British Columbia, Canada. *Environ. Sci. Technol.* **2019**. https://doi.org/10.1021/acs.est.8b06391.

(7) Balan, E.; Villiers, J. P. R. D.; Eeckhout, S. G.; Glatzel, P.; Toplis, M. J.; Fritsch, E.; Allard, T.; Galoisy, L.; Calas, G. The Oxidation State of Vanadium in Titanomagnetite from Layered Basic Intrusions. *American Mineralogist* **2006**, *91* (5–6), 953–956. https://doi.org/10.2138/am.2006.2192.

(8) Nesbitt, J. A.; Lindsay, M. B. J. Vanadium Geochemistry of Oil Sands Fluid Petroleum Coke. *Environ. Sci. Technol.* **2017**, *51* (5), 3102–3109. https://doi.org/10.1021/acs.est.6b05682.

(9) Hobson, A. J.; Stewart, D. I.; Bray, A. W.; Mortimer, R. J. G.; Mayes, W. M.; Rogerson, M.; Burke, I. T. Mechanism of Vanadium Leaching during Surface Weathering of Basic Oxygen Furnace Steel Slag Blocks: A Microfocus X-Ray Absorption Spectroscopy and Electron Microscopy Study. *Environ. Sci. Technol.* **2017**, *51* (14), 7823–7830. https://doi.org/10.1021/acs.est.7b00874.

(10) Burke, I. T.; Mayes, W. M.; Peacock, C. L.; Brown, A. P.; Jarvis, A. P.; Gruiz, K. Speciation of Arsenic, Chromium, and Vanadium in Red Mud Samples from the Ajka Spill Site, Hungary. *Environ. Sci. Technol.* **2012**, *46* (6), 3085–3092. https://doi.org/10.1021/es3003475.

(11) Chaurand, P.; Rose, J.; Briois, V.; Salome, M.; Proux, O.; Nassif, V.; Olivi, L.; Susini, J.; Hazemann, J.-L.; Bottero, J.-Y. New Methodological Approach for the Vanadium K-Edge X-Ray Absorption Near-Edge Structure Interpretation: Application to the Speciation of Vanadium in Oxide Phases from Steel Slag. *J. Phys. Chem. B* **2007**, *111* (19), 5101–5110. https://doi.org/10.1021/jp063186i.

(12) Portier, C.; Taylor, J.; Keith, S.; Cseh, L.; Ingerman, L.; Chappell, L.; Rhoades, J.; Hueber, A. *Agency for Toxic Substances and Disease Registry (ATSDR). Toxicological Profile for Vanadium*; 2012; p 255.

(13) Morita, A.; Yamamoto, S.; Wang, B.; Tanaka, K.; Suzuki, N.; Aoki, S.; Ito, A.; Nanao, T.; Ohya, S.; Yoshino, M.; Zhu, J.; Enomoto, A.; Matsumoto, Y.; Funatsu, O.; Hosoi, Y.; Ikekita, M. Sodium Orthovanadate Inhibits P53-Mediated Apoptosis. *Cancer Res* **2010**, *70* (1), 257–265. https://doi.org/10.1158/0008-5472.CAN-08-3771.

(14) Howd, R. palvanadium.pdf https://oehha.ca.gov/media/downloads/water/chemicals/nl/palvanadium.pdf (accessed 2019 -02 -15).

(15) Tabri, A.; Daunt, P.; Zwayer, B. *Health Effects Assessinent Sumtnary Tables FY-1997 UPDATE*; 1997.

(16) Seargeant, L. E.; Stinson, R. A. Inhibition of Human Alkaline Phosphatases by Vanadate. *Biochemical Journal* **1979**, *181* (1), 247–250. https://doi.org/10.1042/bj1810247.

(17) *Amendments to 15A NCAC 02L .0202 Groundwater Quality Standards: Part 1*; 2020.

(18) *Environment and Climate Change Canada. Canadian Environ- Mental Protection Act (1999)*; Federal Environmental Quality Guidelines: Vanadium, 2016.

(19) Gustafsson, J. P. Vanadium Geochemistry in the Biogeosphere –Speciation, Solid-Solution Interactions, and Ecotoxicity. *Applied Geochemistry* **2019**, *102*, 1–25. https://doi.org/10.1016/j.apgeochem.2018.12.027.

(20) Kontny, A.; Schneider, M.; Eiche, E.; Stopelli, E.; Glodowska, M.; Rathi, B.; Göttlicher, J.; Byrne, J. M.; Kappler, A.; Berg, M.; Thi, D. V.; Trang, P. T. K.; Viet, P. H.; Neumann, T. Iron Mineral Transformations and Their Impact on As (Im)Mobilization at Redox Interfaces in As-Contaminated Aquifers. *Geochimica et Cosmochimica Acta* **2021**, *296*, 189–209. https://doi.org/10.1016/j.gca.2020.12.029.

(21) Manning, A. H.; Mills, C. T.; Morrison, J. M.; Ball, L. B. Insights into Controls on Hexavalent Chromium in Groundwater Provided by Environmental Tracers, Sacramento Valley, California, USA. *Applied Geochemistry* **2015**, *62*, 186–199. https://doi.org/10.1016/j.apgeochem.2015.05.010.

(22) McClain, C. N.; Fendorf, S.; Webb, S. M.; Maher, K. Quantifying Cr(VI) Production and Export from Serpentine Soil of the California Coast Range. *Environ. Sci. Technol.* **2017**, *51* (1), 141–149. https://doi.org/10.1021/acs.est.6b03484.

(23) Larsson, M. A.; Persson, I.; Sjöstedt, C.; Gustafsson, J. P. Vanadate Complexation to Ferrihydrite: X-Ray Absorption Spectroscopy and CD-MUSIC Modelling. *Environ. Chem.* **2017**, *14* (3), 141–150. https://doi.org/10.1071/EN16174.

(24) Peacock, C. L.; Sherman, D. M. Vanadium(V) Adsorption onto Goethite (goethite) at PH 1.5 to 12: A Surface Complexation Model Based on Ab Initio Molecular Geometries and EXAFS Spectroscopy. *Geochimica et Cosmochimica Acta* **2004**, *68* (8), 1723–1733. https://doi.org/10.1016/j.gca.2003.10.018.

(25) White, A. F.; Peterson, M. L. Reduction of Aqueous Transition Metal Species on the Surfaces of Fe(II) -Containing Oxides. *Geochimica et Cosmochimica Acta* **1996**, *60* (20), 3799–3814. https://doi.org/10.1016/0016-7037(96)00213-X.

(26) Vessey, C. J.; Lindsay, M. B. J. Aqueous Vanadate Removal by Iron(II)-Bearing Phases under Anoxic Conditions. *Environ. Sci. Technol.* **2020**. https://doi.org/10.1021/acs.est.9b06250.

(27) Abernathy, M. J.; Schaefer, M. V.; Vessey, C. J.; Liu, H.; Ying, S. C. Oxidation of V(IV) by Birnessite: Kinetics and Surface Complexation. *Environ. Sci. Technol.* **2021**. https://doi.org/10.1021/acs.est.1c02464.

(28) Backeberg, N. R.; Iacoviello, F.; Rittner, M.; Mitchell, T. M.; Jones, A. P.; Day, R.; Wheeler, J.; Shearing, P. R.; Vermeesch, P.; Striolo, A. Quantifying the Anisotropy and Tortuosity of Permeable Pathways in Clay-Rich Mudstones Using Models Based on X-Ray Tomography. *Sci Rep* **2017**, *7* (1), 14838. https://doi.org/10.1038/s41598-017-14810-1.

(29) Fatt, I. Influence of Dead-End Pores on Relative Permeability of Porous Media. *Science* **1961**, *134* (3492), 1750–1751. https://doi.org/10.1126/science.134.3492.1750.

(30) Hyman, J. D.; Winter, C. L. Stochastic Generation of Explicit Pore Structures by Thresholding Gaussian Random Fields. *Journal of Computational Physics* **2014**, *277*, 16–31. https://doi.org/10.1016/j.jcp.2014.07.046.

(31) Smolarkiewicz, P. K.; Larrabee Winter, C. Pores Resolving Simulation of Darcy Flows. *Journal of Computational Physics* **2010**, *229* (9), 3121–3133. https://doi.org/10.1016/j.jcp.2009.12.031.

(32) Battiato, I.; Tartakovsky, D. M. Applicability Regimes for Macroscopic Models of Reactive Transport in Porous Media. *Journal of Contaminant Hydrology* **2011**, *120–121*, 18–26. https://doi.org/10.1016/j.jconhyd.2010.05.005.

(33) Michalak, A. M.; Kitanidis, P. K. Macroscopic Behavior and Random-Walk Particle Tracking of Kinetically Sorbing Solutes. *Water Resour. Res.* **2000**, *36* (8), 2133–2146. https://doi.org/10.1029/2000WR900109.

(34) Šimůnek, J.; van Genuchten, M. Th. Modeling Nonequilibrium Flow and Transport Processes Using HYDRUS. *Vadose Zone Journal* **2008**, *7* (2), 782. https://doi.org/10.2136/vzj2007.0074.

(35) Šimůnek, J.; Jarvis, N. J.; van Genuchten, M. Th.; Gärdenäs, A. Review and Comparison of Models for Describing Non-Equilibrium and Preferential Flow and Transport in the Vadose Zone. *Journal of Hydrology* **2003**, *272* (1), 14–35. https://doi.org/10.1016/S0022-1694(02)00252-4.

(36) Zachara, J.; Brantley, S.; Chorover, J.; Ewing, R.; Kerisit, S.; Liu, C.; Perfect, E.; Rother, G.; Stack, A. G. Internal Domains of Natural Porous Media Revealed: Critical Locations for Transport, Storage, and Chemical Reaction. *Environ. Sci. Technol.* **2016**, *50* (6), 2811–2829. https://doi.org/10.1021/acs.est.5b05015.

(37) Hilfer, R. Review on Scale Dependent Characterization of the Microstructure of Porous Media. **2002**, 18.

(38) Huang, W.; Schlautman, M. A.; Weber, W. J. A Distributed Reactivity Model for Sorption by Soils and Sediments. 5. The Influence of Near-Surface Characteristics in Mineral Domains. 8.

(39) van OORT, F.; Foy, E.; Labanowski, J.; Leguédois, S.; Jongmans, T. Soil Processes, Pedofeatures and Microscale Metal Distributions: Relevant Study of Contaminant-Dynamics Calls for Pedology-Based Soil-Depth Sampling Strategies. *Soil Syst.* **2018**, *2* (1), 17. https://doi.org/10.3390/soilsystems2010017.

(40) Aharoni, C.; Levinson, S.; Ravina, I.; Sparks, D. L. Kinetics of Soil Chemical Reactions: Relationships between Empirical Equations and Diffusion Models. *Soil Science Society of America Journal* **1991**, *55* (5), 1307. https://doi.org/10.2136/sssaj1991.03615995005500050019x.

(41) Oldham, C. E.; Farrow, D. E.; Peiffer, S. A Generalized Damköhler Number for Classifying Material Processing in Hydrological Systems. *Hydrology and Earth System Sciences* **2013**, *17* (3), 1133–1148. https://doi.org/10.5194/hess-17-1133-2013.

(42) Ying, S. C.; Kocar, B. D.; Fendorf, S. Oxidation and Competitive Retention of Arsenic between Iron- and Manganese Oxides. *Geochimica et Cosmochimica Acta* **2012**, *96*, 294–303. https://doi.org/10.1016/j.gca.2012.07.013.

(43) Gerke, H. H.; Genuchten, M. T. van. A Dual-Porosity Model for Simulating the Preferential Movement of Water and Solutes in Structured Porous Media. *Water Resources Research* **1993**, *29* (2), 305–319. https://doi.org/10.1029/92WR02339.

(44) Ying, S. C.; Masue-Slowey, Y.; Kocar, B. D.; Griffis, S. D.; Webb, S.; Marcus, M. A.; Francis, C. A.; Fendorf, S. Distributed Microbially- and Chemically-Mediated Redox Processes Controlling Arsenic Dynamics within Mn-/Fe-Oxide Constructed Aggregates. *Geochimica et Cosmochimica Acta* **2013**, *104*, 29–41. https://doi.org/10.1016/j.gca.2012.08.020.

(45) Sexstone, A. J.; Revsbech, N. P.; Parkin, T. B.; Tiedje, J. M. Direct Measurement of Oxygen Profiles and Denitrification Rates in Soil Aggregates. *Soil Sci. Soc. Am. j.* **1985**, *49* (3), 645–651. https://doi.org/10.2136/sssaj1985.03615995004900030024x.

(46) Thiele, E. W. Relation between Catalytic Activity and Size of Particle. *Ind. Eng. Chem.* **1939**, *31* (7), 916–920. https://doi.org/10.1021/ie50355a027.

(47) Weisz, P. Diffusion and Chemical Transformation. **1973**, 9.

(48) Tokunaga, T.; Newville, M.; Rao, W. Distribution of Chromium Contamination and Microbial Activity in Soil Aggregates https://www.osti.gov/servlets/purl/785303 (accessed 2019 -08 -07).

(49) Ying, S. C.; Kocar, B. D.; Griffis, S. D.; Fendorf, S. Competitive Microbially and Mn Oxide Mediated Redox Processes Controlling Arsenic Speciation and Partitioning. *Environ. Sci. Technol.* **2011**, *45* (13), 5572–5579. https://doi.org/10.1021/es200351m.

(50) Oldham, C.; Beer, J.; Blodau, C.; Fleckenstein, J.; Jones, L.; Neumann, C.; Peiffer, S. Controls on Iron(II) Fluxes into Waterways Impacted by Acid Mine Drainage: A Damköhler Analysis of Groundwater Seepage and Iron Kinetics. *Water Research* **2019**, *153*, 11–20. https://doi.org/10.1016/j.watres.2018.12.024.

(51) Ocampo, C. J.; Oldham, C. E.; Sivapalan, M. Nitrate Attenuation in Agricultural Catchments: Shifting Balances between Transport and Reaction. *Water Resources Research* **2006**, *42* (1). https://doi.org/10.1029/2004WR003773.

(52) McKenzie, R. M. The Synthesis of Birnessite, Cryptomelane, and Some Other Oxides and Hydroxides of Manganese. *Mineralogical Magazine* **1971**, *38* (296), 493–502. https://doi.org/10.1180/minmag.1971.038.296.12.

(53) Manceau, A.; Marcus, M. A.; Grangeon, S. Determination of Mn Valence States in Mixed-Valent Manganates by XANES Spectroscopy. *American Mineralogist* **2012**, *97* (5–6), 816–827. https://doi.org/10.2138/am.2012.3903.

(54) Simanova, A. A.; Kwon, K. D.; Bone, S. E.; Bargar, J. R.; Refson, K.; Sposito, G.; Peña, J. Probing the Sorption Reactivity of the Edge Surfaces in Birnessite Nanoparticles Using Nickel(II). *Geochimica et Cosmochimica Acta* **2015**, *164*, 191–204. https://doi.org/10.1016/j.gca.2015.04.050.

(55) Simanova, A. A.; Peña, J. Time-Resolved Investigation of Cobalt Oxidation by Mn(III)-Rich δ-Birnessite Using Quick X-Ray Absorption Spectroscopy. *Environ. Sci. Technol.* **2015**, *49* (18), 10867–10876. https://doi.org/10.1021/acs.est.5b01088.

(56) Wolthers, M.; Charlet, L.; van Der Weijden, C. H.; van der Linde, P. R.; Rickard, D. Arsenic Mobility in the Ambient Sulfidic Environment: Sorption of Arsenic(V) and Arsenic(III) onto Disordered Mackinawite. *Geochimica et Cosmochimica Acta* **2005**, *69* (14), 3483–3492. https://doi.org/10.1016/j.gca.2005.03.003.

(57) Burke, I. T.; Peacock, C. L.; Lockwood, C. L.; Stewart, D. I.; Mortimer, R. J. G.; Ward, M. B.; Renforth, P.; Gruiz, K.; Mayes, W. M. Behavior of Aluminum, Arsenic, and Vanadium during the Neutralization of Red Mud Leachate by HCl, Gypsum, or Seawater. *Environ. Sci. Technol.* **2013**, *47* (12), 6527–6535. https://doi.org/10.1021/es4010834.

(58) Marczewski, A. W. Analysis of Kinetic Langmuir Model. Part I: Integrated Kinetic Langmuir Equation (IKL): A New Complete Analytical Solution of the Langmuir Rate Equation. *Langmuir* **2010**, *26* (19), 15229–15238. https://doi.org/10.1021/la1010049.

(59) Marczewski, A. W.; Deryło-Marczewska, A.; Słota, A. Adsorption and Desorption Kinetics of Benzene Derivatives on Mesoporous Carbons. **2013**, 16.

(60) Levina, A.; McLeod, A. I.; Lay, P. A. Vanadium Speciation by XANES Spectroscopy: A Three-Dimensional Approach. *Chemistry – A European Journal* **2014**, *20* (38), 12056–12060. https://doi.org/10.1002/chem.201403993.

(61) Lafferty, B. J.; Ginder-Vogel, M.; Zhu, M.; Livi, K. J. T.; Sparks, D. L. Arsenite Oxidation by a Poorly Crystalline Manganese-Oxide. 2. Results from X-Ray Absorption Spectroscopy and X-Ray Diffraction. *Environ. Sci. Technol.* **2010**, *44* (22), 8467–8472. https://doi.org/10.1021/es102016c.

(62) Toner, B.; Manceau, A.; Webb, S. M.; Sposito, G. Zinc Sorption to Biogenic Hexagonal-Birnessite Particles within a Hydrated Bacterial Biofilm. *Geochimica et Cosmochimica Acta* **2006**, *70* (1), 27–43. https://doi.org/10.1016/j.gca.2005.08.029.

(63) Zhao, H.; Zhu, M.; Li, W.; Elzinga, E. J.; Villalobos, M.; Liu, F.; Zhang, J.; Feng, X.; Sparks, D. L. Redox Reactions between Mn(II) and Hexagonal Birnessite Change Its Layer Symmetry. *Environ. Sci. Technol.* **2016**, *50* (4), 1750–1758. https://doi.org/10.1021/acs.est.5b04436.

(64) Gaillot, A.-C.; Drits, V. A.; Manceau, A.; Lanson, B. Structure of the Synthetic K-Rich Phyllomanganate Birnessite Obtained by High-Temperature Decomposition of KMnO4: Substructures of K-Rich Birnessite from 1000°C Experiment. *Microporous and Mesoporous Materials* **2007**, *98* (1), 267–282. https://doi.org/10.1016/j.micromeso.2006.09.010.

(65) Schaefer, M. V.; Plaganas, M.; Abernathy, M.; Aiken, M. L.; Garniwan, A.; Lee, I.; Ying, S. C. Manganese, Arsenic, and Carbonate Interactions in Model Oxic Groundwater Systems. *Environ. Sci. Technol.* **2020**, acs.est.0c02084. https://doi.org/10.1021/acs.est.0c02084.

(66) Lan, S.; Wang, X.; Xiang, Q.; Yin, H.; Tan, W.; Qiu, G.; Liu, F.; Zhang, J.; Feng, X. Mechanisms of Mn(II) Catalytic Oxidation on Ferrihydrite Surfaces and the Formation of Manganese (Oxyhydr)Oxides. *Geochimica et Cosmochimica Acta* **2017**, *211*, 79–96. https://doi.org/10.1016/j.gca.2017.04.044.

(67) Masue-Slowey, Y.; Ying, S. C.; Kocar, B. D.; Pallud, C. E.; Fendorf, S. Dependence of Arsenic Fate and Transport on Biogeochemical Heterogeneity Arising from the Physical Structure of Soils and Sediments. *Journal of Environment Quality* **2013**, *42* (4), 1119. https://doi.org/10.2134/jeq2012.0253.

(68) Myrold, D. D.; Tiedje, J. M. Diffusional Constraints on Denitrification in Soil. *Soil Sci. Soc. Am. j.* **1985**, *49* (3), 651–657. https://doi.org/10.2136/sssaj1985.03615995004900030025x.

(69) Gorski, C. A.; Scherer, M. M. Influence of Magnetite Stoichiometry on Fe ^{II} Uptake and Nitrobenzene Reduction. *Environ. Sci. Technol.* **2009**, *43* (10), 3675–3680. https://doi.org/10.1021/es803613a.

(70) Gorski, C. A.; Nurmi, J. T.; Tratnyek, P. G.; Hofstetter, T. B.; Scherer, M. M. Redox Behavior of Magnetite: Implications for Contaminant Reduction. *Environ. Sci. Technol.* **2010**, *44* (1), 55–60. https://doi.org/10.1021/es9016848.

(71) Gorski, C. A.; Scherer, M. M. Determination of Nanoparticulate Magnetite Stoichiometry by Mössbauer Spectroscopy, Acidic Dissolution, and Powder X-Ray Diffraction: A Critical Review. *American Mineralogist* **2010**, *95*, 1017–1026. https://doi.org/10.2138/am.2010.3435.

(72) Latta, D. E.; Gorski, C. A.; Boyanov, M. I.; O'Loughlin, E. J.; Kemner, K. M.; Scherer, M. M. Influence of Magnetite Stoichiometry on U(VI) Reduction. *Environ. Sci. Technol.* **2012**, *46* (2), 778–786. https://doi.org/10.1021/es2024912.

(73) White, A. F.; Peterson, M. L.; Hochella, M. F. Electrochemistry and Dissolution Kinetics of Magnetite and Ilmenite. *Geochimica et Cosmochimica Acta* **1994**, *58* (8), 1859–1875. https://doi.org/10.1016/0016-7037(94)90420-0.

(74) Liu, C.-H.; Chuang, Y.-H.; Chen, T.-Y.; Tian, Y.; Li, H.; Wang, M.-K.; Zhang, W. Mechanism of Arsenic Adsorption on Magnetite Nanoparticles from Water: Thermodynamic and Spectroscopic Studies. *Environ. Sci. Technol.* **2015**, *49* (13), 7726–7734. https://doi.org/10.1021/acs.est.5b00381.

(75) Cornell, R. M.; Schwertmann, U. *The Iron Oxides: Structure, Properties, Reactions, Occurences and Uses*, 1st ed.; Wiley, 2003. https://doi.org/10.1002/3527602097.

(76) Peterson, M. L.; White, A. F.; Brown, G. E.; Parks, G. A. Surface Passivation of Magnetite by Reaction with Aqueous Cr(VI): XAFS and TEM Results. *Environ. Sci. Technol.* **1997**, *31* (5), 1573–1576. https://doi.org/10.1021/es960868i.

Chapter 5: Conclusions and Recommendations for Future Work

The primary goal of this work was to evaluate the geochemical behavior of vanadium by assessing the abiotic interactions of V with oxidative, reductive, and redox neutral mineral phases. The findings presented in this work support the conclusion that the surface interactions of vanadate with soil mineral phases constrain the mobility of the metal within the soil matrix, which has been supported by other studies as well. [1–4]

The mechanisms of surface complexation and the surface capacity of five mineral phases for vanadium adsorption were first evaluated for their potential to contribute to vanadate attenuation. The affinity of Fe and Mn oxide mineral surfaces for vanadate decreased as their crystallinity increased. Ferrihydrite, an amorphous Fe hydroxide, had the highest site density, while hematite, a crystalline Fe oxide of very small (submicron) particle size had the second highest site density. Given the high free energy of adsorption (ΔG) associated with both mineral phases, ferrihydrite and hematite are expected to contribute significantly to the attenuation of aqueous vanadate in soil solutions given their ubiquity, ease of formation, and stability in the environment.[5,6] This trend was also observed for amorphous versus highly crystalline Mn oxides. Birnessite, a poorly crystalline Mn oxide, had higher site densities and adsorption affinities than pyrolusite, a highly crystalline Mn oxide. Birnessite-like minerals have been shown to form under redox fluctuating conditions in soils and sediments including in aquifers impacted by metal contamination,[7,8] and are therefore expected to play an important role in vanadate attenuation as well.

Amorphous manganese oxides like birnessite may, however, also contribute to elevated pore water vanadate concentrations though V oxidation processes. Prior studies have demonstrated the efficacy of birnessite minerals in oxidizing a wide range of other common redox active contaminants such as arsenic and chromium.[9,10] The oxidation of V^{IV} by birnessite at circumneutral pH is complicated by the insolubility of V^{IV}, which forms a V^{IV} oxyhydroxide solid solutions of häggite, paramontroseite, and duttonite. Nevertheless, birnessite proved to be an effective oxidant for V^{IV}, though oxidation rates are 100 times slower than the well-studied oxidation of As^{III} by birnessite.[11,12] Importantly, the oxidative capacity of birnessite is much higher for vanadate than its surface capacity, retaining less than 5% of the total vanadate produced in the highest concentrations tested. This comparatively low surface capacity occurs despite the formation of secondary Mn^{III} oxide phases at the birnessite surface as it is reduced by V^{IV}. Therefore, the most likely scenario for birnessite to be protective of groundwater quality with respect to vanadate contamination would occur under conditions with high Mn:V ratios, such that there is more surface area available to retain the vanadate produced from V oxidation. In areas with low Mn:V ratios, the oxidative capacity of birnessite outstrips its adsorptive capacity. Under such scenarios, the other aquifer minerals such as Fe oxides and layer phyllosilicates will likely be dominant adsorbents of vanadate over poorly crystalline Mn oxides.

The final chapter of this dissertation focused on the role of diffusion-limited transport in controlling the rate of vanadate production and attenuation. Diffusion-limited transport dominates solute movement at the aggregate scale, and redox interfaces have

been shown to form within these diffusion-controlled matrices leading to the redox cycling of metals within small spatial scales. To gauge the relative contribution of adsorption versus surface-complex-mediated reduction on V immobilization, V was spiked into a diffusion-controlled system containing birnessite and either goethite (which interacts with V in a purely adsorptive manner) or magnetite (which reduces V^{V} through surface-mediated electron transfer).[13] We found that regardless of whether vanadate was produced via oxidation of solid V^{IV} oxyhydroxides by birnessite or added as V^{V} directly to the reactor system, diffusion was sufficient to limit adsorption onto the Fe oxide phases in favor of continued uptake by birnessite over long timescales. Initially when V is first added to the reactor system, the Fe oxides have greater affinity for vanadate and reach their adsorption capacity quickly. As the reaction progresses, V^{V} desorbs from the Fe oxides and birnessite becomes the major adsorbent similar to what has been observed for As in a related study.[14] The rate of vanadate reduction through abiotic Fe^{II}-mediated reduction was also much slower than the rate of vanadate production birnessite oxidation, suggesting that adsorption and surface complexation, even by birnessite itself is a more significant attenuation pathway than abiotic reduction to insoluble V^{IV} oxyhydroxides.

The goal with each of these studies was to provide equilibrium and kinetic parameters for the calibration of reactive transport models that are used to assess, manage, and reclaim V-impacted sites. Our understanding of the factors controlling V fate and transport has grown immensely in the last 10 years as an increasing number of studies are published on the biogeochemical cycling of V. However, further research is still needed in a number of areas regarding V fate and transport in soil surface and

subsurface environments. In particular, a comprehensive investigation into the role of biotic controls on vanadate attenuation and how those controls interact with abiotic factors to limit or promote vanadate mobility and concentrations in the soil solution is needed. Linking these two components (i.e. abiotic and biotic processes) is the next intensive research step that needs to be addressed to answer questions arising from field-based observations that show that V concentrations in groundwater can remain high even in the presence of Mn and Fe oxide rich aquifer sediments. The conclusions outlined by the studies within this dissertation contribute to our understanding of important abiotic interactions that can lead to vanadate attenuation even when in the presence of potent environmental oxidants like manganese oxides.

References

(1) Larsson, M. A.; D'Amato, M.; Cubadda, F.; Raggi, A.; Öborn, I.; Kleja, D. B.; Gustafsson, J. P. Long-Term Fate and Transformations of Vanadium in a Pine Forest Soil with Added Converter Lime. *Geoderma* **2015**, *259–260*, 271–278. https://doi.org/10.1016/j.geoderma.2015.06.012.

(2) Larsson, M. A.; Baken, S.; Gustafsson, J. P.; Hadialhejazi, G.; Smolders, E. Vanadium Bioavailability and Toxicity to Soil Microorganisms and Plants. *Environ. Toxicol. Chem.* **2013**, *32* (10), 2266–2273. https://doi.org/10.1002/etc.2322.

(3) Baken, S.; Larsson, M. A.; Gustafsson, J. P.; Cubadda, F.; Smolders, E. Ageing of Vanadium in Soils and Consequences for Bioavailability. *Eur. J. Soil Sci.* **2012**, *63* (6), 839–847. https://doi.org/10.1111/j.1365-2389.2012.01491.x.

(4) Yang, J.; Tang, Y.; Yang, K.; Rouff, A. A.; Elzinga, E. J.; Huang, J.-H. Leaching Characteristics of Vanadium in Mine Tailings and Soils near a Vanadium Titanomagnetite Mining Site. *J. Hazard. Mater.* **2014**, *264*, 498–504. https://doi.org/10.1016/j.jhazmat.2013.09.063.

(5) Sun, J.; Mailloux, B. J.; Chillrud, S. N.; van Geen, A.; Thompson, A.; Bostick, B. C. Simultaneously Quantifying Ferrihydrite and Goethite in Natural Sediments Using the Method of Standard Additions with X-Ray Absorption Spectroscopy. *Chem. Geol.* **2018**, *476*, 248–259. https://doi.org/10.1016/j.chemgeo.2017.11.021.

(6) Wang, R. B.; Hellman, A. Surface Terminations of Hematite (Fe2O3) Exposed to Oxygen, Hydrogen, or Water: Dependence on the Density Functional Theory Methodology. *J. Phys. Condens. Matter* **2018**, *30* (27), 275002. https://doi.org/10.1088/1361-648X/aac743.

(7) McClain, C. N.; Fendorf, S.; Webb, S. M.; Maher, K. Quantifying Cr(VI) Production and Export from Serpentine Soil of the California Coast Range. *Environ. Sci. Technol.* **2017**, *51* (1), 141–149. https://doi.org/10.1021/acs.est.6b03484.

(8) Villalobos, M.; Lanson, B.; Manceau, A.; Toner, B.; Sposito, G. Structural Model for the Biogenic Mn Oxide Produced by Pseudomonas Putida. *Am. Mineral.* **2006**, *91* (4), 489–502. https://doi.org/10.2138/am.2006.1925.

(9) Manning, B. A.; Fendorf, S. E.; Bostick, B.; Suarez, D. L. Arsenic(III) Oxidation and Arsenic(V) Adsorption Reactions on Synthetic Birnessite. *Environ. Sci. Technol.* **2002**, *36* (5), 976–981. https://doi.org/10.1021/es0110170.

(10) Landrot, G.; Ginder-Vogel, M.; Sparks, D. L. Kinetics of Chromium(III) Oxidation by Manganese(IV) Oxides Using Quick Scanning X-Ray Absorption Fine Structure Spectroscopy (Q-XAFS). *Environ. Sci. Technol.* **2010**, *44* (1), 143–149. https://doi.org/10.1021/es901759w.

(11) Feng, X.; Wang, P.; Shi, Z.; Kwon, K. D.; Zhao, H.; Yin, H.; Lin, Z.; Zhu, M.; Liang, X.; Liu, F.; Sparks, D. L. A Quantitative Model for the Coupled Kinetics of Arsenic Adsorption/Desorption and Oxidation on Manganese Oxides. *Environ. Sci. Technol. Lett.* **2018**, *5* (3), 175–180. https://doi.org/10.1021/acs.estlett.8b00058.

(12) Ginder-Vogel, M.; Landrot, G.; Fischel, J. S.; Sparks, D. L. Quantification of Rapid Environmental Redox Processes with Quick-Scanning x-Ray Absorption Spectroscopy (Q-XAS). *Proc. Natl. Acad. Sci.* **2009**, *106* (38), 16124–16128. https://doi.org/10.1073/pnas.0908186106.

(13) Vessey, C. J.; Lindsay, M. B. J. Aqueous Vanadate Removal by Iron(II)-Bearing Phases under Anoxic Conditions. *Environ. Sci. Technol.* **2020**. https://doi.org/10.1021/acs.est.9b06250.

(14) Ying, S. C.; Kocar, B. D.; Fendorf, S. Oxidation and Competitive Retention of Arsenic between Iron- and Manganese Oxides. *Geochim. Cosmochim. Acta* **2012**, *96*, 294–303. https://doi.org/10.1016/j.gca.2012.07.013.

Appendices

Appendix 1. Supporting Information for Chapter 2

Section I. Mineral Characterization

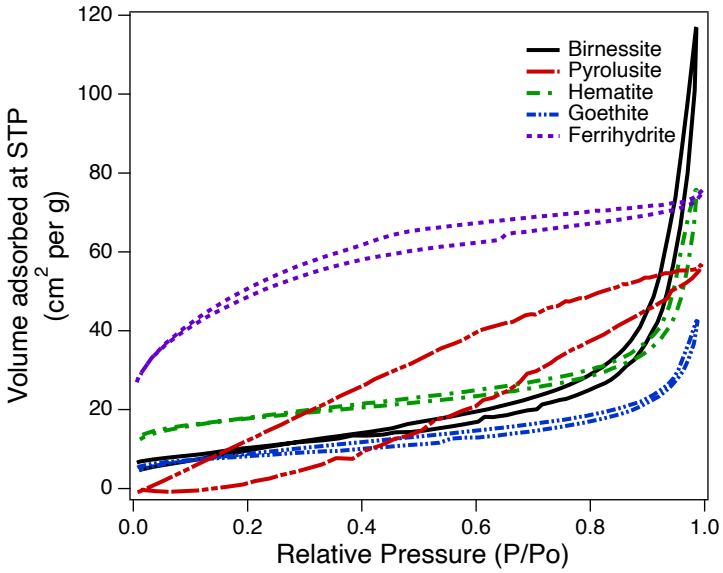

Appendix 1 Figure 2.1 Results of BET surface area analysis for each mineral species prior to reaction with V^V.

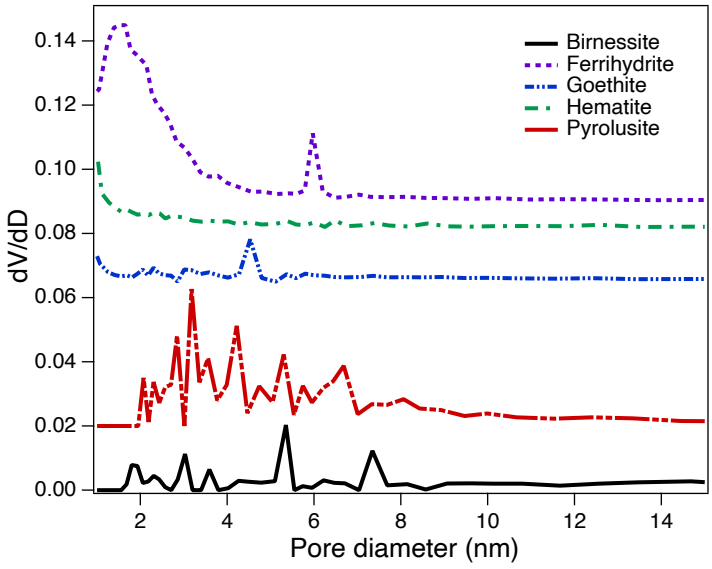

Appendix 1 Figure 2.2 Results of BJH porosity analysis for each mineral species prior to reaction with V^V.

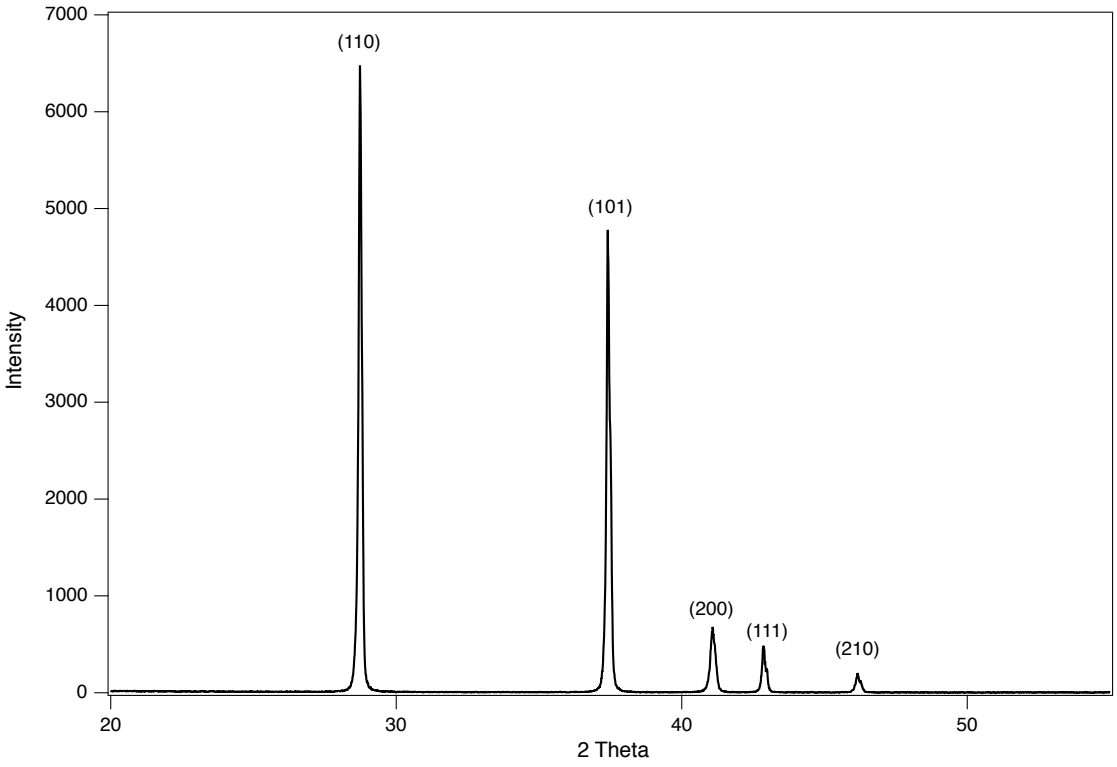

Appendix 1 Figure 2.3 XRD reflection for pyrolusite prior to reaction with V^{V}. Prominent (hkl) reflections are labelled.

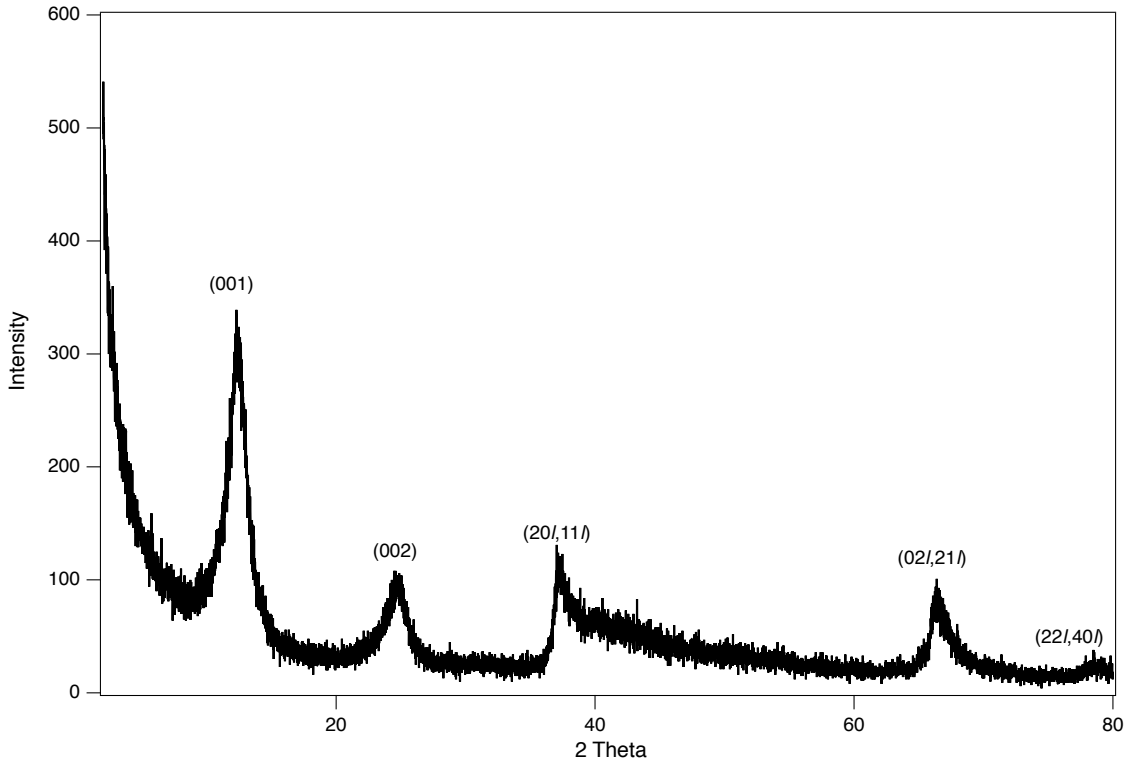

Appendix 1 Figure 2.4 XRD reflection for birnessite prior to reaction with V^{V}. Prominent (hkl) reflections are labelled.

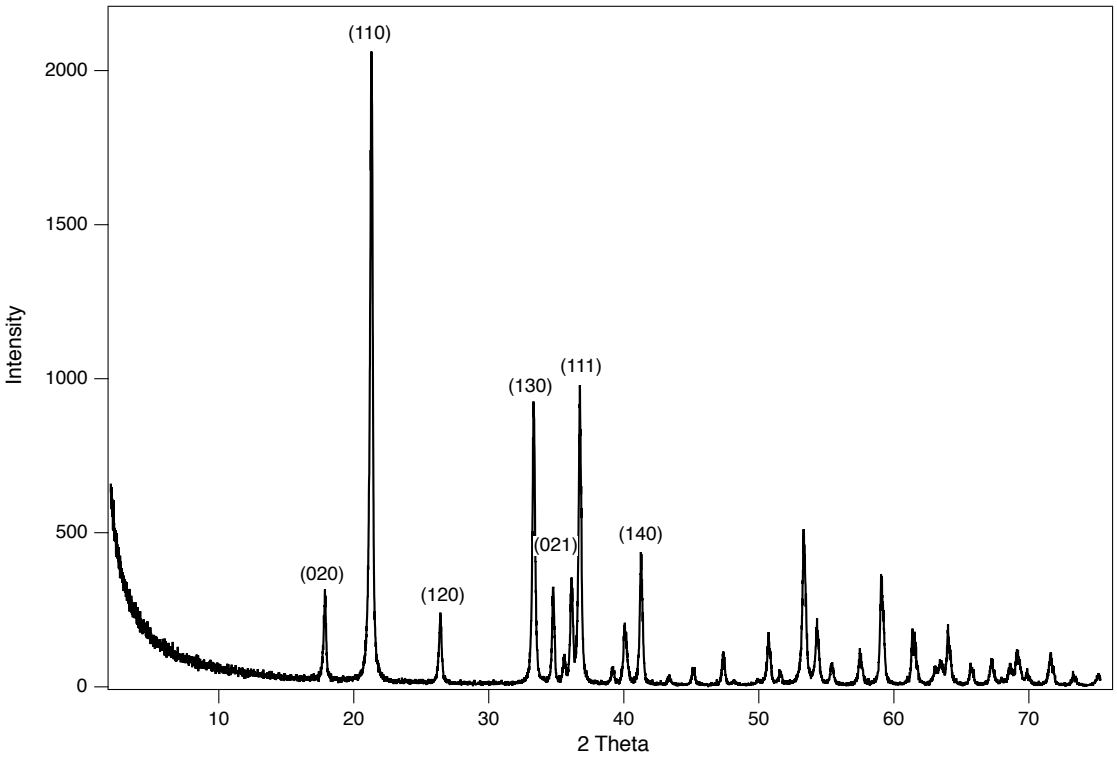

Appendix 1 Figure 2.5 XRD reflection for goethite prior to reaction with V^{V}. Prominent (hkl) reflections are labelled.

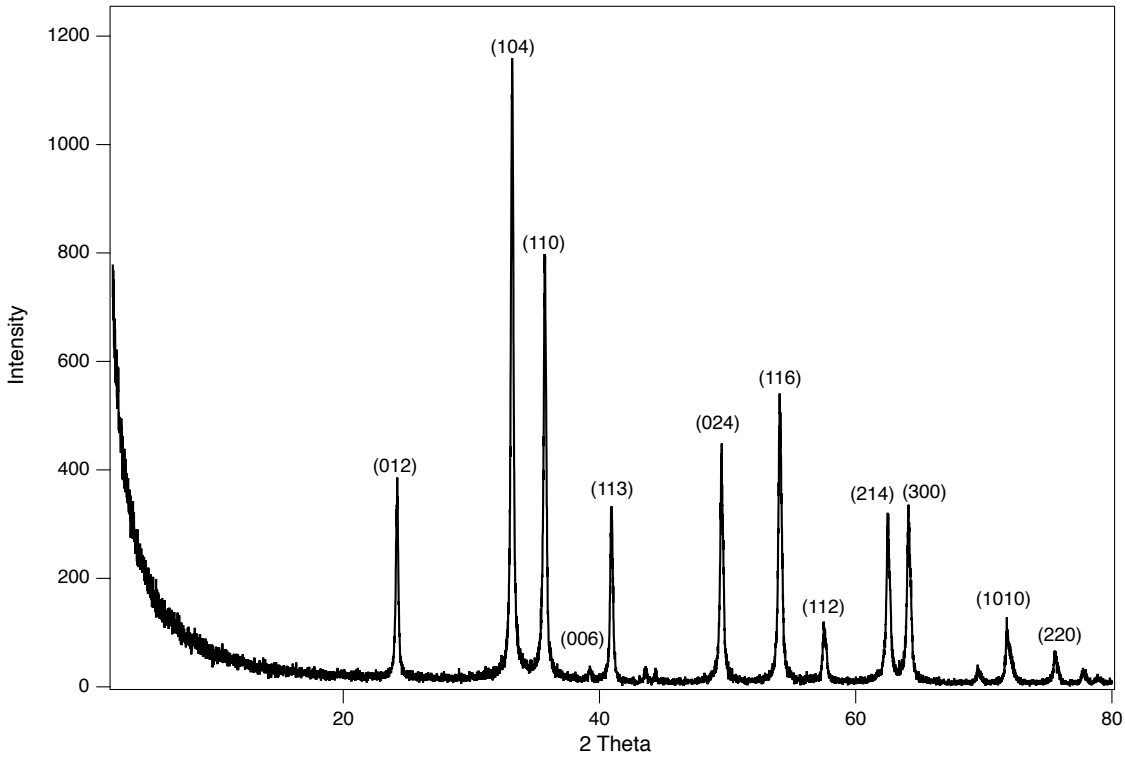

Appendix Figure 2.6 XRD reflection for hematite prior to reaction with V^V. Prominent (hkl) reflections are labelled.

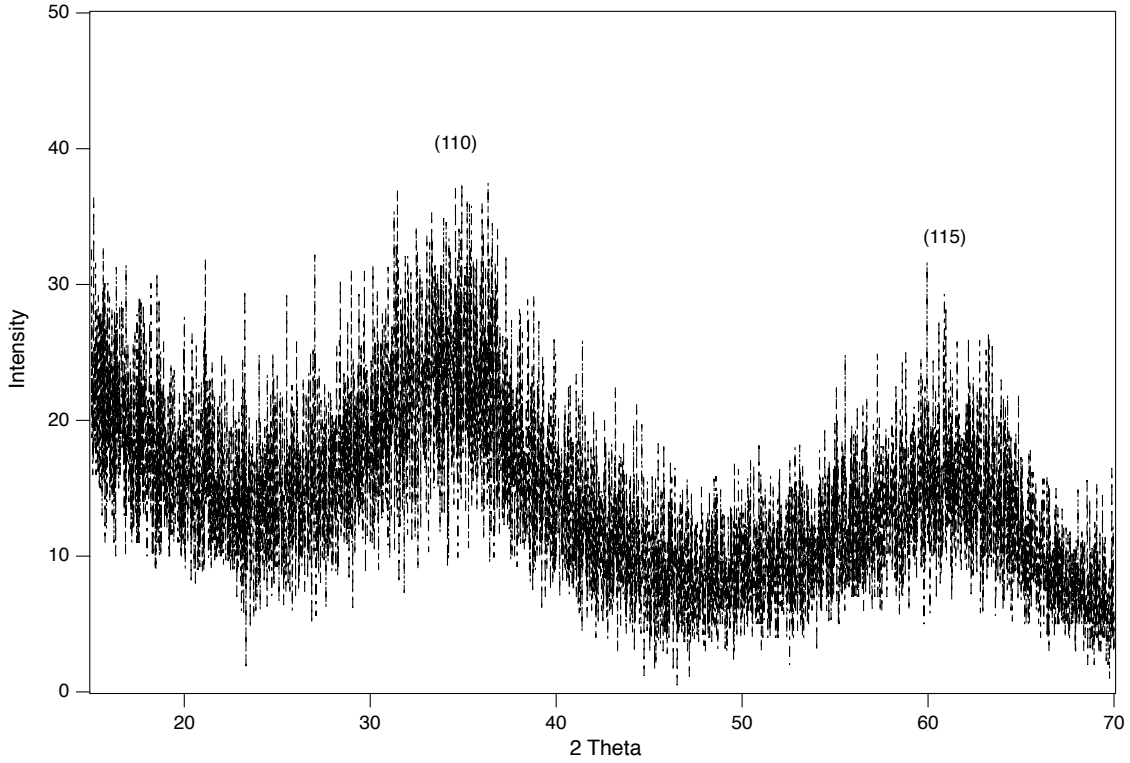

Appendix 1 Figure 2.7 XRD reflection for ferrihydrite prior to reaction with V^V. Prominent (hkl) reflections are labelled.

Section II. Transformed Isotherms

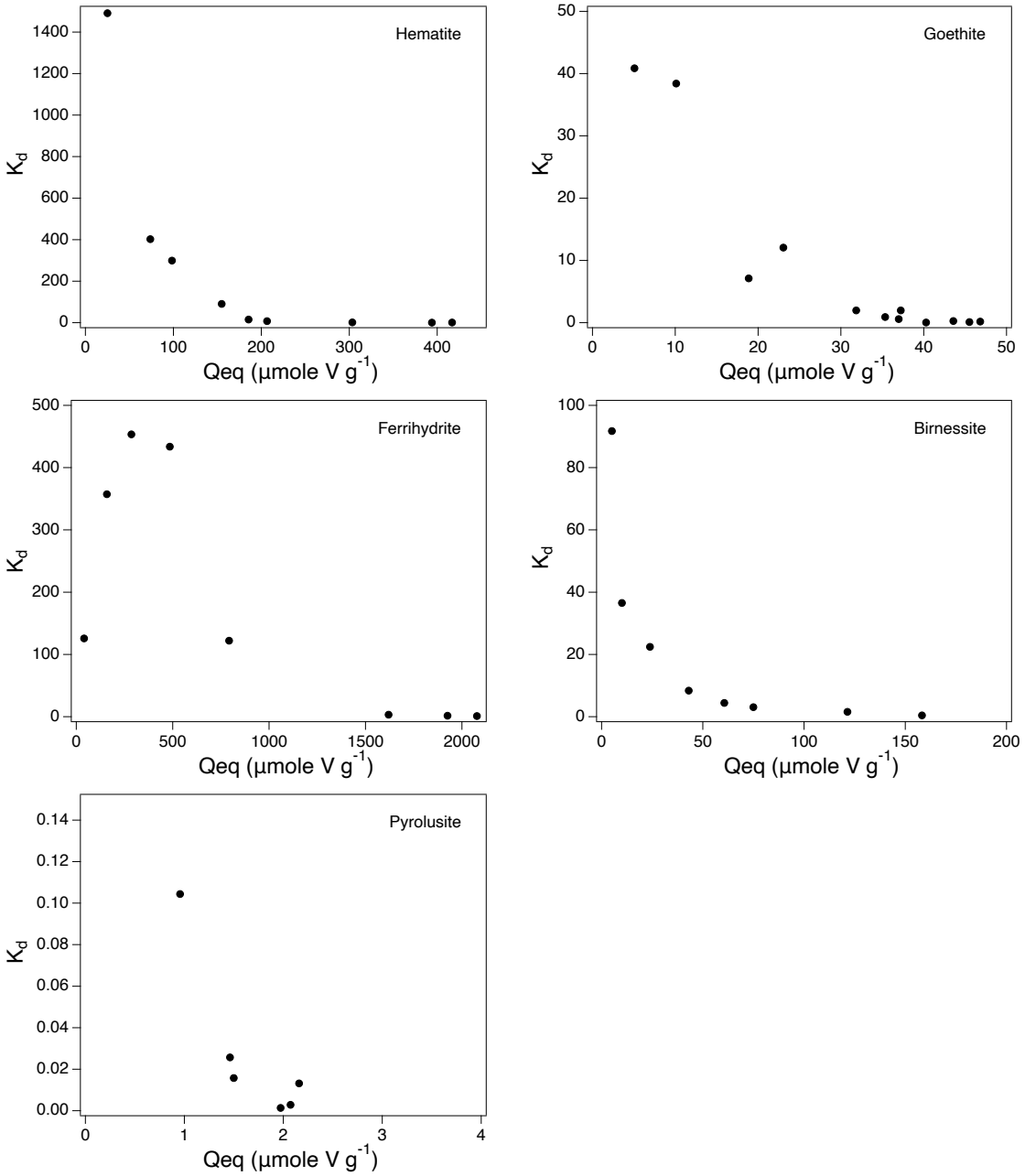

Appendix 1 Figure 2.8 Scatchard plots for the adsorption of V^V onto each mineral species.

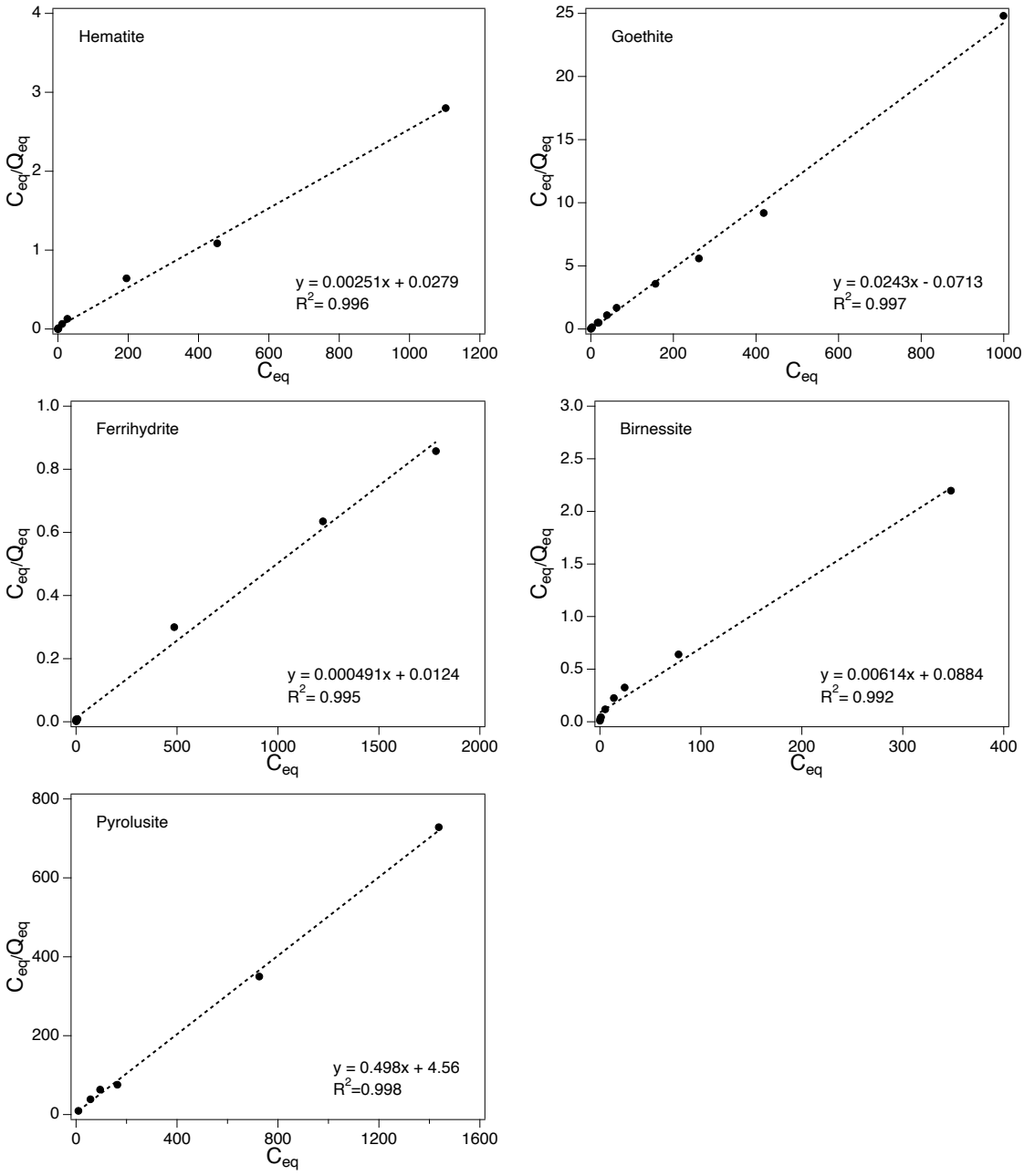

Appendix 1 Figure 2.9 Linearized Langmuir plots of V^V onto each mineral species.

Section III. Aqueous V^V Speciation

Visual Minteq version 3.1 was used to calculate the V^V speciation for each equilibrium V^V_{aq} concentration obtained in the Langmuir isotherm experiments. Parameters for the calculation included 25 mM NaCl of background electrolyte, and the pH was fixed at 7 to account for the 10 mM of PIPES buffer.

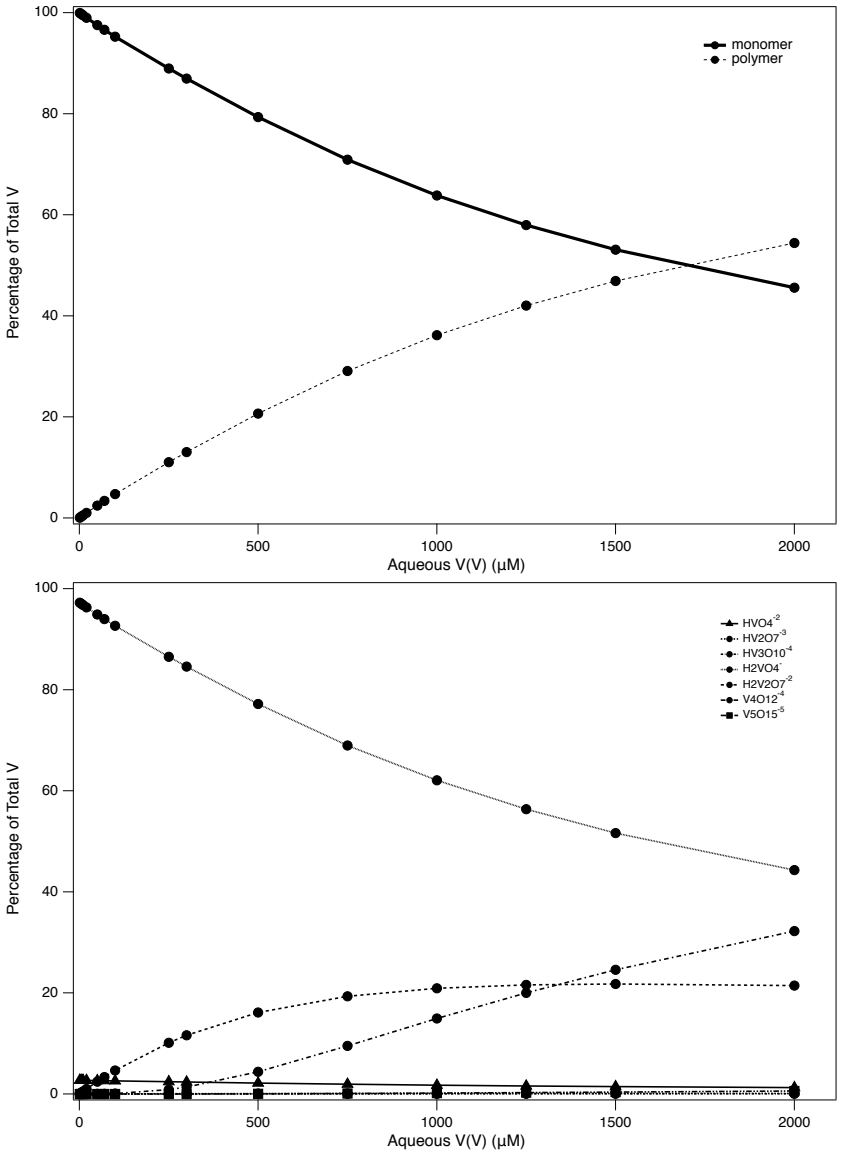

Appendix 1 Figure 2.10 A and B. Minteq speciation results for V^V at pH 7 and 25 mM NaCl. A) monomeric vs polymeric fraction of V^V, where each category is a sum of the fractions of monomeric or polymeric species. B) The fraction of each V^V species at each concentration of total V^V.

Appendix 1 Table 2.1 Minetq model results used to construct figures 2.10 A and B.

Total V	Percent of Total V								
uM V(V)	HVO4-2	H2VO4-	H2V2O7-2	HV2O7-3	V4O12-4	V5O15-5	HV3O10-4	monomer	polymer
1	2.722	97.227	0.051	0	0	0	0	99.949	0.051
5	2.716	97.028	0.254	0	0	0	0	99.744	0.254
10	2.709	96.782	0.506	0	0	0	0	99.491	0.506
20	2.696	96.296	1.002	0	0	0	0	98.992	1.002
50	2.657	94.887	2.433	0.013	0	0	0	97.544	2.446
70	2.631	93.982	3.342	0.018	0.026	0	0	96.613	3.386
100	2.595	92.665	4.642	0.025	0.072	0	0	95.26	4.739
250	2.425	86.527	10.123	0.054	0.863	0	0	88.952	11.04
300	2.371	84.582	11.609	0.062	1.363	0	0	86.953	13.034
500	2.166	77.182	16.124	0.087	4.395	0.033	0.013	79.348	20.652
750	1.939	68.974	19.337	0.104	9.525	0.098	0.021	70.913	29.085
1000	1.748	62.076	20.913	0.113	14.934	0.185	0.027	63.824	36.172
1250	1.591	56.371	21.588	0.117	20.012	0.283	0.032	57.962	42.032
1500	1.461	51.637	21.773	0.119	24.583	0.385	0.036	53.098	46.896
2000	1.26	44.307	21.445	0.118	32.234	0.585	0.041	45.567	54.423

Section IV. Method for Nonlinear Least Squares Fitting

Microsoft excel was used to organize and refine the isotherm data to each of the isotherm models.[1] The standard deviation was calculated for each C_{eq} and Q_{eq} value, for each isotherm. For each isotherm model used, a modelled Q_{eq} value was determined according to equations 1 and 2, with approximate initial guesses placed for each of the dependent variables (q_{max}, K, K_L, etc). the residual was then calculated, taken as:

$$\text{residual} = Q_{eq_{empirical}} - Q_{eq_{model}}$$

The residuals were then squared to make all values positive. The squared residuals were then weighted by a factor w_i, where w_i is equal to the standard error of $Q_{eq_{empirical}}$, although other methods of weighting have been discussed. [2,3] The standard error of $Q_{eq_{empirical}}$ is defined as:

$$\text{SE} = \frac{\text{sandard deviation of } Q_{eq_{empirical}}}{\sqrt{Number\ of\ of\ replicates\ at\ each\ concentration}}$$

$$= \frac{\text{sandard deviation of } Q_{eq_{empirical}}}{\sqrt{3}}$$

The weighted squared residuals were then summed (RSS), and the total number of data points in the isotherm (N) and total number of variables (m) used in the regression of $Q_{eq_{model}}$ on $Q_{eq_{empirical}}$ were counted. The root-mean squared error[2], also called the standard error[1] was then calculated according to:

$$\text{rmse} = \sqrt{\frac{RSS}{(N-m)}}$$

The rmse was then targeted as the parameter to be minimized by the optimization algorithm while adjusting the dependent variables. Additionally, the R^2 and 95% confidence intervals were calculated according to Brown. [1] However, the utility of an R^2 parameter in non-linear regression is low, primarily stemming from the requirement of an "mean" value of the empirically determined independent variable. The representativeness of such a mean value towards its dataset is low for nonlinear data. Nonetheless, these values are reported for completeness.

Section V. Isotherm Raw Data

Appendix 1 Table 2. 2 Isotherm raw data

Hematite																	
Ceq uM	Qeq umole/g oxide	stdev Ceq	stdev Qeq	Qeq Standard error	modelled 2 site L	residual	residuals^2	w_i*R^2	RMSE	mean Qeq	mean residual	square mean residual	R^2	T_{crit}	95% CI	CI Hi	CI Low
0.0168	24.9919	0.0290	0.1644	0.0949	17.1897	7.8023	60.8753	5.7777	43.9832	206.4466	-181.4547	32925.7966	0.9372	2.5706	113.0624	130.2520	-95.8727
0.1830	73.7092	0.0339	1.1600	0.6697	83.1387	-9.4295	88.9156	59.5503			-132.7374	17619.2155				196.2011	-29.9236
0.3282	98.3332	0.1225	1.5667	0.9046	100.6695	-2.3363	5.4583	4.9373			-108.1134	11688.5046				213.7319	-12.3928
1.7049	154.9287	1.3815	2.6880	1.5519	133.0223	21.9064	479.8921	744.7553			-51.5179	2654.0927				246.0846	19.9599
12.0671	185.4642	1.6524	2.2603	1.3050	179.7501	5.7141	32.6514	42.6094			-20.9824	440.2603				292.8124	66.6877
26.7491	206.4196	2.0149	8.3136	4.7998	220.4458	-14.0262	196.7338	944.2921			-0.0270	0.0007				333.5082	107.3834
194.9506	303.4232			0.0000	351.2163	-47.7931	2284.1808	0.0000			96.9766	9404.4670				464.2787	238.1540
452.8117	416.8177	4.2559	10.7870	6.2279	385.2254	31.5923	998.0735	6215.8909			210.3711	44255.9860				498.2877	272.1630
1102.7991	393.9316	12.0394	28.0050	16.1687	404.0482	-10.1166	102.3453	1654.7870			187.4850	35150.6276				517.1106	290.9858

Pyrolusite																	
Ceq uM	Qeq umole/g oxide	stdev Ceq	stdev Qeq	Qeq Standard error	modelled 2 site L	residual	residuals^2	w_i*R^2	RMSE	mean Qeq	mean residual	square mean residual	R^2	T_{crit}	95% CI	CI Hi	CI Low
9.1531	0.9557	0.0644	0.0179	0.5518	0.7590	0.1967	0.0387	0.0214	0.2287	1.6867	-0.7310	0.5344	0.8052	2.7764	0.6351	1.3940	0.1239
56.8940	1.4613	0.1874	0.0495	0.8437	1.6211	-0.1598	0.0255	0.0215			-0.2254	0.0508				2.2561	0.9860
95.1017	1.4988	0.2019	0.0555	0.8653	1.7765	-0.2777	0.0771	0.0667			-0.1879	0.0353				2.4116	1.1414
163.6549	2.1588	0.1271	0.0313	1.2464	1.8895	0.2693	0.0725	0.0904			0.4721	0.2229				2.5246	1.2544
725.7128	2.0732	1.2897	0.3265	1.1969	2.0281	0.0450	0.0020	0.0024			0.3864	0.1493				2.6632	1.3931
1437.0897	1.9725	0.6379	0.1596	1.1388	2.0498	-0.0773	0.0060	0.0068			0.2858	0.0817				2.6849	1.4147

Birnessite																	
Ceq uM	Qeq umole/g oxide	stdev Ceq	stdev Qeq	Qeq Standard error	modelled 2 site L	residual	residuals^2	w_i*R^2	RMSE	mean Qeq	mean residual	square mean residual	R^2	T_{crit}	95% CI	CI Hi	CI Low
0.0555	5.0950	0.0386	0.0362	0.0209	4.0650	1.0299	1.0608	0.0222	1.6996	62.1427	-57.0477	3254.4387	0.9994	2.7764	4.7187	9.8137	0.3763
0.2742	10.0167	0.0353	0.0339	0.0196	13.6211	-3.6044	12.9918	0.2541			-52.1260	2717.1160				14.7354	5.2980
1.0633	23.8695	0.1722	0.1273	0.0735	25.5246	-1.6551	2.7395	0.2013			-38.2732	1464.8381				28.5882	19.1507
5.1274	43.0182	1.3408	1.1054	0.6382	41.6391	1.3791	1.9019	1.2139			-19.1245	365.7446				47.7369	38.2995
13.6985	60.5744	1.1505	1.3707	0.7914	60.2466	0.3278	0.1075	0.0850			-1.5683	2.4596				65.2931	55.8556
24.4322	74.9574	1.6230	1.9953	1.1520	76.8573	-1.8998	3.6094	4.1579			12.8148	164.2184				79.6762	70.2387
77.7881	121.3755	2.3762	0.9889	0.5710	118.2604	3.1152	9.7043	5.5408			59.2329	3508.5318				126.0943	116.6568
347.6532	158.2346	7.4282	7.1622	4.1351	158.3727	-0.1381	0.0191	0.0789			96.0920	9233.6665				162.9534	153.5159

Goethite

Ceq uM	Qeq umole/g oxide	stdev Qeq	stdev Ceq Qeq Standard error	modelled 2 site L	residual	residuals^2	w_i*R^2	RMSE	mean Qeq	mean residual	square mean residual	R^2	T_{crit}	95% CI	CI Hi	CI Low
0.1238	5.0595	0.0321	0.0070	0.0185	1.6182	3.4413	11.8425	0.2195	5.1723	31.2172	-26.1577	684.2275	0.8990	2.3060	11.9273	13.5455	-10.3091
0.2629	10.0980	0.1292	0.0730	0.0746	3.2732	6.8248	46.5782	3.4741			-21.1192	446.0207				15.2005	-8.6541
1.9086	23.0389	0.1431	0.0863	0.0826	15.6124	7.4265	55.1530	4.5574			-8.1783	66.8849				27.5397	3.6851
2.6463	18.8556	16.3323	4.5834	9.4295	18.9094	-0.0538	0.0029	0.0273			-12.3616	152.8097				30.8367	6.9821
16.1342	31.8406	0.2226	0.5258	0.1285	36.5262	-4.6856	21.9550	2.8213			0.6234	0.3886				48.4535	24.5989
18.7761	37.2254	3.3412	0.2183	1.9291	37.5757	-0.3503	0.1227	0.2368			6.0082	36.0984				49.5030	25.6484
38.7962	35.3422	1.6278	1.7526	0.9398	41.3921	-6.0499	36.6008	34.3971			4.1250	17.0157				53.3194	29.4648
62.1860	36.9734	0.7009	0.4552	0.4047	42.9636	-5.9903	35.8833	14.5214			5.7561	33.1332				54.8909	31.0363
156.2523	43.5733	4.1951	4.2563	2.4221	44.6783	-1.1050	1.2210	2.9574			12.3561	152.6740				56.6056	32.7510
261.6484	46.8153	3.6040	1.6416	2.0808	45.1623	1.6531	2.7326	5.6860			15.5981	243.3017				57.0896	33.2350
418.3934	45.5073	10.8775	12.1613	6.2801	45.4364	0.0709	0.0050	0.0316			14.2901	204.2062				57.3637	33.5091
999.2776	40.2770	8.5260	8.7379	4.9225	45.7061	-5.4291	29.4748	145.0903			9.0598	82.0805				57.6334	33.7788

Ferrihydrite

Ceq uM	Qeq umole/g oxide	stdev Qeq	Ceq stdev Qeq Standard error	modelled 2 site L	residual	residuals^2	w_i*R^2	RMSE	mean Qeq	mean residual	square mean residual	R^2	T_{crit}	95% CI	CI Hi	CI Low
0.3179	39.9502	1.1001	0.0366	0.6351	203.7061	-163.7559	26815.9907	17031.2305	181.9719	922.7960	-882.8458	779416.7360	0.9724	2.7764	505.2350	545.1853	-465.2848
0.4429	158.3305	3.9534	0.0702	2.2825	261.2415	-102.9110	10590.6716	24173.1550			-764.4655	584407.5292				663.5656	-346.9045
0.6303	285.7785	9.3891	0.0707	5.4208	332.1180	-46.3394	2147.3424	11640.2656			-637.0175	405791.3189				791.0136	-219.4565
1.1171	484.5482	46.1262	0.9675	26.6309	461.1916	23.3567	545.5332	14528.0669			-438.2478	192061.1424				989.7833	-20.6868
6.4822	792.0829	61.3595	4.3410	35.4259	799.4257	-7.3428	53.9164	1910.0381			-130.7131	17085.9240				1297.3179	286.8479
485.7120	1619.2575	219.0132	37.9071	126.4473	1613.9818	5.2757	27.8332	3519.4324			696.4614	485058.5380				2124.4925	1114.0225
1222.4987	1924.7263	103.6201	6.2156	59.8251	1953.7000	-28.9737	839.4729	50221.5456			1001.9303	1003864.3013				2429.9614	1419.4913
1782.0110	2077.6941	246.3233	32.6198	142.2148	2069.5505	8.1436	66.3178	9431.3770			1154.8981	1333789.5554				2582.9291	1572.4591

Section VI. Method for Birnessite Characterization

Determination of the number of coherently stacked layers in our birnessite sample were done using the collected XRD data, and results from Villalobos et al. 2006.[4] Briefly, the crystallite sizes in the c* direction and for the ab plane were calculated using the Scherrer equation:

$$\tau = \frac{0.9\lambda}{\beta\cos(\theta)}$$

where τ is the crystallite size in nanometers, lambda is the wavelength of the x-rays used (Cu K_α = 0.154059 nm), β is the full width at half-maximum intensity of the XRD reflection in radians, and θ is the angle at which the reflection occurs, in radians. To calculate the distance along the c* direction, the (001) reflection was used, yielding a distance of 6.4 nm. To translate this into the number of turbostratically stacked layers, data from Villalobos et al. was used. Linear regression was applied to the reported values for length along the c* axis, and the corresponding number of layers. (crystallite size along the c* direction in nm = independent variable, number of layers = dependent variable)

c* nm	layers
1.9	2.6
2	2.8
4.2	5.8

Data collected by Villalobos et al. 2006 used to determine the number of coherently stacked layers of birnessite.

Regression results: number of layers = 1.378698*(c* nm) + 0.010848

Thus, an average of 8.8 layers were determined for our birnessite, having an average c* extent of 6.4 nm.

Section VII. Mineral Synthesis

Birnessite

63 g of $KMnO_2$ (Fisher) was dissolved into 1 L of ultrapure water (EMD Millipore) and heated to 90°C. Sixty-six ml of concentrated trace metal grade HCl was slowly added over the course of ten minutes. The mixture was then maintained at 90°C for 10 minutes before cooling to 21°C over the course of 30 minutes. Manganese oxides in the solution were collected using vacuum filtration. The Mn oxides were repeatedly rinsed with ultrapure water to remove excess $KMnO_4$ prior to air-drying.

Hematite

A 2 mM solution of trace metal grade HNO_3 was prepared, capped and brought to 98 °C in an oven. When the temperature was reached, 17 g of $Fe(NO_3)•9H_2O$ was added with stirring. The solution was then returned to the oven and held at 95-100 °C for a week. Solids were separated by centrifugation, and rinsed with ultrapure water before air-drying.

2-line Ferrihydrite

43.7 g of $Fe(NO_3)•9H_2O$ was dissolved in 500 ml of ultrapure water. 95 ml of 2 molar KOH was then added, with an additional 10 ml added dropwise. The resulting precipitate was then filtered, rinsed with ultrapure water and air dried.

Section VIII. References

(1) Brown, A. M. A Step-by-Step Guide to Non-Linear Regression Analysis of Experimental Data Using a Microsoft Excel Spreadsheet. *Computer Methods and Programs in Biomedicine* **2001**, *65* (3), 191–200. https://doi.org/10.1016/S0169-2607(00)00124-3.

(2) Kinniburgh, D. G. General Purpose Adsorption Isotherms. *Environ. Sci. Technol.* **1986**, *20* (9), 895–904. https://doi.org/10.1021/es00151a008.

(3) Tellinghuisen, J. Using Least Squares for Error Propagation. *J. Chem. Educ.* **2015**, *92* (5), 864–870. https://doi.org/10.1021/ed500888r.

(4) Villalobos, M.; Lanson, B.; Manceau, A.; Toner, B.; Sposito, G. Structural Model for the Biogenic Mn Oxide Produced by Pseudomonas Putida. *American Mineralogist* **2006**, *91* (4), 489–502. https://doi.org/10.2138/am.2006.1925.

Appendix 2. Supporting Information for Chapter 3

Section I Additional Methods

In situ XANES experiments

Batch reactions were conducted at beamline 2-2 at the Stanford Synchrotron Radiation Lightsource (SSRL) using semi-quick (~90 s per scan) X-ray absorption near edge structure (XANES) spectroscopy at the V K-edge to determine the kinetics of V^{IV} oxidation by birnessite. A Si(111) crystal set oriented to φ=90 was used for all experiments, and data were collected at ambient temperature. Energy was calibrated against a V reference foil placed at a 45° angle above I0 and backed by a photodiode, with reference scans being taken between each reaction to avoid attenuation by the reactor. Drift did not exceed 0.1 eV over the course of the experiments. XANES spectra targeted the V pre-edge 1s-3d peak and 1s-4p edge (5400-5700 eV energy region). Scans were collected until subsequent spectra showed no detectable change over a minimum of three scans. Experiments were conducted in 250 mL polypropylene bottles (with a 12.7 μm thick Kapton window) similar to previous experiments (Appendix 2 Figure 3.1).[1,2] An anoxic solution with 5 mM $VOSO_4$ was prepared as follows: a solution of 50 mM PIPES (RPI >99.9% purity) was adjusted to pH 7 using NaOH (Fisher ACS grade) and 25 mM NaCl (Macron ACS grade) was degassed (N_2 sparging for 30 min L^{-1}) then placed in a anoxic chamber with 95% N_2:5% H_2 atmosphere (COY) and 0.163 g $VOSO_4{\cdot}5H_2O$ (Acros Organics, < 20ppm impurities) was added to 50 mL of solution. 150 mL of degassed media was added to the reactor vessel within the anoxic chamber; containers were capped and

sealed during transport to the X-ray hutch. Within the hutch, birnessite was added to the reactor for a final solids loading of 0.5, 1, 3 or 10 g L^{-1}, yielding Mn:V molar ratios of 2.2, 3.7, 11.9 and 47.1. The vessel was then recapped and fit with a He purge line to limit O_2 intrusion. The reaction was initiated by adding the 50 mL aliquot of $VOSO_4$ slurry to the reactor, and subsequent collection of the XANES spectra began within 20 seconds of V^{IV} addition for all experiments. Spectra were also collected for V^{IV} ($VOSO_4$) or V^{V} (Na_3VO_4) standard solutions (in 50 mM PIPES, pH 7, 25 mM NaCl) at concentrations equal to the total V used in the experiments. No beam induced damage was observed in the course of scanning these standards.

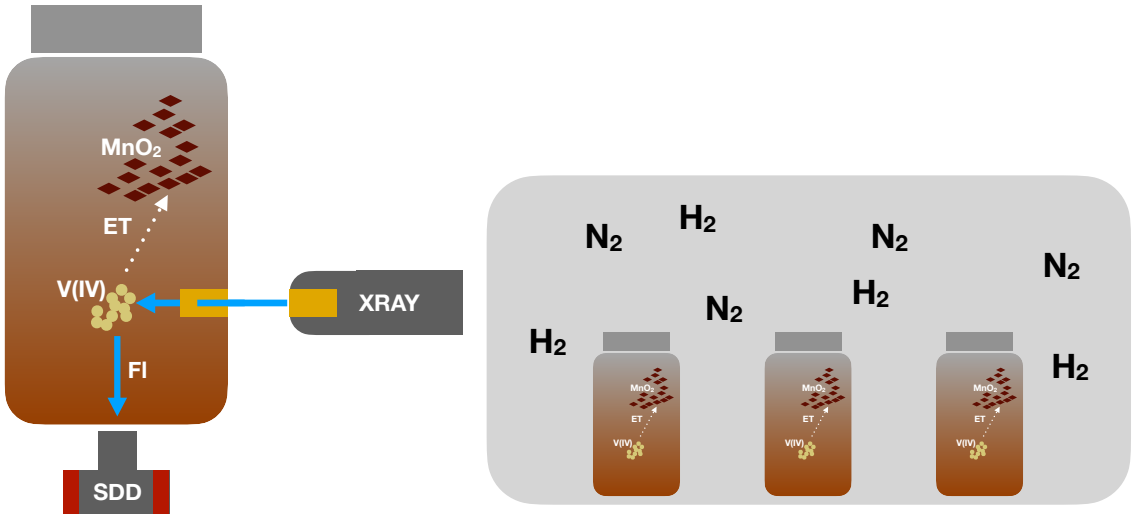

Appendix 2 Figure 3.1 Example of the experimental set up of the *in situ* (left) and *ex situ* (right) experiments at SSRL beamline 2-2. MnO_2 = birnessite, V(IV) = V^{IV} precipitate, ET=electron transfer, Fl = fluorescence, SDD = silicon drift detector, blue arrows = synchrotron x-rays.

Vanadium XAS Pre-Edge Analysis

The evolution of V oxidation state for the *in* situ experiments was assessed by analyzing pre-edge peak height and area.[3–5] Analysis was performed by integrating each normalized pre-edge peak for standards and samples using the Origin software package (Origin V.2020) which was used to generate linear regression curves, and 95% confidence and prediction intervals using chemical standards (Appendix 2 Table 3.3). Dissolved V^{IV} and V^{V} standards from each *in situ* experiment and powder samples ($V^{IV}{}_2O_4$, $V^{IV}OSO_4$, and $Na_3V^{V}O_4$) were plotted separately. Pre-edge intensity and area values for $V^{III}Cl_3$, $V^{IV}OSO_4$, $V^{IV}O(OH)_2$, $Na_3V^{V}O_4$, and V^{V} adsorbed to ferrihydrite (V^{V}-Fh) from Vessey and Lindsay (2020) and $H_2VO_4^-{}_{(aq)}$ and VO^{2+} from Brinza et al. 2019 were also used to produce the linear oxidation state calibration curve. [6,7] The regression ($R^2 = 0.971$) gave average oxidation state values of 4.22 (*in situ* V^{IV} standard), 5.06 (*in situ* V^{V} standard), 3.99 ($V^{IV}{}_2O_4$), 3.93 ($V^{IV}OSO_4$), and 4.95 ($Na_3V^{V}O_4$). These values are consistent with those published previously.

Stirred batch experiments

Herein, *ex situ* refers to batch experiments performed in the laboratory without real-time XAS data collection. *Ex situ* batch experiments were performed in triplicate to supplement the *in situ* experiments to explore the effect of different V:Mn ratios on V oxidation rate. *Ex situ* experiments were performed in an anoxic chamber (97% N_2:3% H_2; COY) with 50 mM PIPES (pH = 7.00 ± 1) and 25 mM NaCl solution in 1 L polypropylene containers. Solutions were degassed under vacuum for a minimum of 3 hrs before transfer into the anoxic chamber where it was equilibrated overnight. The birnessite slurry was

made by suspending 0.5000 ± 0.0005 g of birnessite in 50 mL of the reaction media, which was then removed from the anoxic chamber and sonically dispersed for 15 minutes in an air-tight container. Once dispersed, the birnessite slurry was added to additional reaction media in the anoxic chamber to a final volume of 450 mL and set to stir. In a separate 50 mL centrifuge tube, either 0.4074 g (Mn:V ratio 3.17) or 0.127 g (Mn:V ratio 11.15) of $VOSO_4 \bullet 5H_2O$ was dissolved in 50 mL of solution, which immediately hydrolyzed to $VOOH^{+}_{(aq)}$ and precipitated V^{IV} hydroxides primarily as $V_2O_3(OH)_{2(s)}$ (Appendix 2 Figure 3.2). To explore the role of this precipitate and it's rate of $V^{IV}_{(aq)}$ release, a V^{IV} dissolution control experiment was conducted. Details on this dissolution control experiment are presented below.

The reaction was initiated by adding the V^{IV} slurry to the birnessite slurry under vigorous stirring to ensure particles remained suspended. Photooxidation was prevented by covering the reactors with aluminum foil. Despite the tendency of V^{IV} species to strongly complex organic compounds[8], complexation by sulfonate functional groups is low and a PIPES-V^{IV} complex was not observed in ^{51}V NMR spectra (Appendix 2 Figure 3.3). [9]

The reactors were sampled 28 times over 6.2 days, with 13 samplings during the first hour. At each timepoint aliquots of well-mixed reaction slurry were removed for aqueous and solid-phase analyses. Ten mL of the slurry was filtered through a 0.22-µm PES membrane to recover the aqueous fraction, before being acidified with trace metal grade (TMG) HNO_3 to determine aqueous concentrations of Na, V, and Mn using ICP-OES. Solid-phase associated Na, V and Mn were determined by digesting 1 mL of the slurry with 0.5 mL of TMG HNO_3 which was then diluted with ultra-pure water, and

analyzed by ICP-OES. The detection limits for Na, V and Mn were 240, 0.6 and 1.5 μg L^{-1}, respectively. For XAS analysis, solids were filtered from 10 mL of reaction slurry using 0.22-μm cellulose acetate filters (GVS). The solids were covered by aluminum foil to prevent photooxidation and dried under anoxic conditions. Unreacted birnessite and the solids recovered at the final time point were analyzed using XRD (Appendix 2 Figure 3.2).

Manganese and Vanadium EXAFS

Solids collected on filters for XAS were encapsulated in 12.7 μm (V) or 25.4 μm (Mn) thick Kapton tape under anoxic conditions. Samples were transferred directly from an anoxic chamber to the beamline in an opaque anaerobic box (Mitsubishi) to minimize contact with O_2. Vanadium EXAFS spectra were collected at SSRL Beamline 4-3 using a channel cut Si(111) crystal set with a φ=90°. Fluorescence spectra were collected (minimum three scans) under a He atmosphere using a single-channel vortex silicon drift detector (Hitachi Vortex EX). After each scan, the beam spot was moved vertically 1 mm to minimize effects of beam-induced damage between scan replicates. Spectra were collected from 230 eV below the edge to 899 eV above the edge with an in-line V foil reference used to calibrate each scan to the peak of the first derivative of the V foil at 5465 eV.

Manganese EXAFS were collected at SSRL Beamline 4-1 using a Si(220) crystal set with a φ=0° that was detuned 40% to minimize contribution from higher-order harmonics. Energy calibration was achieved using an in-line Mn foil. Spectra were collected at 77 K using a liquid-N_2 cryostat from 230 eV below the edge to 656 eV above the edge in both transmission and fluorescence modes. Fluorescent X-rays were detected

using a Canberra 30-element solid-state Ge detector, and the influence of X-ray scattering was reduced by using a 3 absorption-length Cr filter and Soller slits. An in-line Mn foil was used to calibrate each spectra, setting the peak of its first derivative to 6539 eV.

The Demeter package (Windows v.9.26) was used to calibrate and normalize all spectra.[10] The average oxidation state and relative proportions of Mn^{II}, Mn^{III}, and Mn^{IV} in birnessite were determined using the procedure and standards in the Combo method of Manceau et al.[11] Four Mn standards from Manceau et al. 2012 were used for each oxidation state (Mn^{II}, Mn^{III} and Mn^{IV}): rhodochrosite, manganosite, $MnSO_{4\ aq}$, $MnSO_{4\ solid}$, feitknechtite, groutite, manganite, $MnPO_4$, pyrolusite, ramsdellite, K-birnessite and $Ca_2Mn_3O_8$. Least-squares, shell-by-shell fitting was performed using the Artemis interface to Feff6 and IFEFFIT as part of the Demeter software package.[10,12] In select cases, the Hamilton test was used to see if the additional paths, such as the inclusion of a ^{2}C V-Mn backscattering path, or a pyrovanadate V-V backscattering path would be statistically meaningful to the improvement of the fit.[13] This test generates a statistic I_r from a calculation of the regularized lower incomplete beta function ($0 < I_r < 1$), with lower values indicating a lower probability that the improvement in fit is from chance alone. [14]

^{51}V NMR Methods

Vanadium(V) in the aqueous phase was quantified using ^{51}V NMR spectroscopy. NMR spectra were collected on a Bruker Avance Neo 400 spectrometer at 105.2MHz equipped with a 5mm BBO probe at 298K. All samples were prepared for analysis by addition of 10% D_2O to facilitate spectra acquisition and all chemical shifts were referenced against $VOCl_3$ as an external standard ($\delta = 0$ ppm).[15] All spectra were collected

with 2000 to 3000 transients, a spectral width of 20.83 KHz, an acquisition time of 0.78 seconds, and a transmitter frequency offset of -57.13 KHz. All spectra were phased and polynomial-baseline corrected using standard ^{51}V procedures prior to peak selection, deconvolution, and integral calculation.[16] All data processing was conducted using Bruker Topspin 4.0.2. Due to paramagnetic interference from Mn^{II}, this method could only be applied to the 1 mM *ex situ* experiment.

Synchrotron XRD Methods

XRD on the initial V^{IV} oxyhydroxides was conducted at SSRL beamline 11-3, which utilized at 12.7 KeV beam. A 2D Raxyonics 225 detector was used for data collection. All patterns were calibrated using a LaB_6 standard and processed in WxDiff v1.20. Conversion of the resulting patterns to d_{hkl} and Cu Kα space was performed in Microsoft Excel. Peak matching was conducted in MDI Jade and manually using the AMCSD diffraction database.

Kinetic Batch Experiments

Kinetic adsorption batch experiments were carried out in duplicate at concentrations of 1 gL^{-1} birnessite, and 10 μM, 100 μM and 3.5 mM Na_3VO_4 in identical pH 7.01 reaction media to the oxidation experiments. Aqueous samples were taken at 0.5, 1, 1.5, 2, 2.5, 3, 4, 5, 6, 7, 8, 9, 10, 15, 20, 25, 30, 40, 50, 60, 71, 80, 90 and 101 minutes. The slurry was immediately filtered through a 0.22 μm PES filter and acidified to 3% acidity by volume using trace metal grade HNO_3. The concentration of V and Mn was measured via ICP-OES. The geometric kinetic Langmuir model of Kuan et al. and the Integrated Kinetic Langmuir (IKL) model of Marczewski were then fit to the resulting

adsorption curves via inverse modelling using the Solver function in Microsoft Excel, with the IKL yielding the better fit. [17,18] For this study, the IKL takes the form of:

Eq1. $$[V^V]_{ads,t} = q_{eq}\left(\frac{1-e^{-k_s t}}{1-f_{eq}e^{-k_s t}}\right)[Birnessite]_{t,(gL^{-1})}$$

Where [Birnessite] is in gL^{-1}. This yields the adsorption constant (K_s) and the batch equilibrium constant (f_{eq}) which were then used our the PSOSO model. The final values can be found in Appendix 2 Table 3.1. In the fits, k_s was allowed to vary, but F_{eq} was calculated according to Marczewski 2010.[18]

Appendix 2 Table 3.1 Results of Integrated Kinetic Langmuir model fit to data from the V^V-birnessite kinetic adsorption experiments

IKL Parameters	
K_s (min^{-1}) ($x10^{-2}$)	7.210
1 mM ex situ f_{eq} (dimensionless)	0.159
3.5 mM ex situ f_{eq} (dimensionless)	0.048

Langmuir Isotherm Experiments

The data to calculate the Langmuir constant (K_L) and maximum adsorptive capacity (q_{max}) of the birnessite for V^V was taken from another project. Briefly, these experiments were carried out at 10 different initial concentrations of V^V ranging from 5 to 2000 µM at pH 7.00 in a background media of 25 mM NaCl and 10 mM PIPES. A single-site Langmuir model was regressed on to the data using inverse modelling of K_L and q_{max} using the solver function in Microsoft excel, and the resulting values can be found in Appendix 2 Table 3.2.

Eq 2. $$q = \frac{q_{max} K_L C_{eq}}{(1+K_L C_{eq})}$$

Where q is the amount of V^V adsorbed at equilibrium and C_{eq} is the concentration of V^V at equilibrium.

Appendix 2 Table 3.2 Langmuir parameters obtained by fitting a single-site Langmuir model to a V^V-birnessite sorption isotherm.

Langmuir Parameters		95% CI
q_{max} (mmole g^{-1})	0.1697	[0.1701, 0.1693]
K_L (L $mmole^{-1}$)	37.15	[37.50, 36.80]
R^2	0.988	

Visual Minteq Calculations

Visual Minteq version 3.1 was used to calculate the V^V speciation for each equilibrium V^V_{aq} concentration obtained in the Langmuir isotherm experiments. Parameters for the calculation included 25 mM NaCl of background electrolyte, and the pH was held constant at 7 to account for the 10 mM of PIPES buffer.

Pre-Edge Fitting Standards

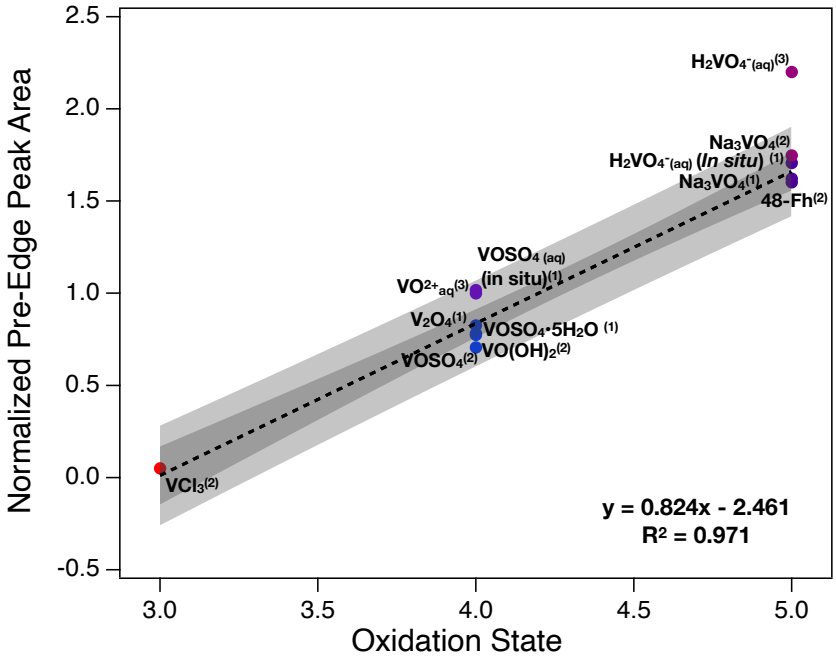

Appendix 2 Figure 3.2 Linear regression of normalized pre-edge peak area and oxidation state (dashed line) for vanadium standards used to calibrate the pre-edge peak fitting of the *in situ* V XANES. The dark grey shaded area is the 95% confidence interval, and the light-grey shaded area is the 95% prediction interval. The regression equation and R^2 are displayed. 1) This study, 2) Vessey and Lindsay 2020, 3) Brinza et al. 2019. [6,7]

Appendix 2 Table 3.3 Fit results from the V K-edge XANES pre-edge analysis.

	Pre-Edge Peak					
Identifier	Height	Area	Calculated Ox. State	Lower 95% CI	Upper 95% CI	References
$H_2VO_4^-$ (aq) *in situ*	0.69	1.71	5.06	4.86	5.25	This study
$VOSO_4$ (aq) *in situ*	0.42	1.02	4.22	3.94	4.50	This study
$VOSO_4 \bullet 5H_2O$	0.34	0.78	3.93	3.65	4.22	This study
V_2O_4	0.22	0.83	3.99	3.70	4.27	This study
Na_3VO_4	0.95	1.62	4.95	4.66	5.25	This study
Na_3VO_4	0.89	1.75	5.11	4.91	5.30	Vessey and Lindsay (2020)
48-Fh	0.66	1.60	4.93	4.64	5.22	Vessey and Lindsay (2020)
$VO(OH)_2$	0.32	0.77	3.92	3.64	4.21	Vessey and Lindsay (2020)
$VOSO_4$	0.31	0.71	3.84	3.56	4.13	Vessey and Lindsay (2020)
VCl_3	0.02	0.05	3.05	2.72	3.37	Vessey and Lindsay (2020)
$H_2VO_4^-$ (aq)	0.81	2.20	5.66	5.46	5.85	Brinza et al. (2008, 2019)
VO^{2+} (aq)	0.36	1.00	4.20	3.92	4.48	Brinza et al. (2008, 2019)

Section II. Oxidation Kinetic Model Description

The model employed here draws on previous work by Shi et al., Feng et al., Siebecker et al., Couture et al., and Marczewski. [18–22] The model is built in the form of the second order integrated rate equation for the chemical reaction:

Eq 3. $$aA + bB = Products$$

Eq 4. $$rate = k[A][B]$$

Which, when integrated yields the form:

Eq 5. $$\ln\left(\frac{[A]_t}{[B]_t}\right) = kt(b[A] - a[B]) + \ln\left(\frac{[A]_i}{[B]_i}\right)$$

Where $_t$ denotes the concentration at some time t, $_i$ denotes the initial concentration, and a and b are the stoichiometric coefficients for the reaction. Thus, when the simplified reaction between vanadium and birnessite is considered:

Eq 6. $$2V^{IV} + Mn^{IV}O_2 \rightarrow 2V^{V} + Mn^{II}$$

The integrated equation becomes:

Eq 7. $$\ln \frac{[V^{IV}]_t}{[Birnessite]_t} = kt([V_i^{IV}] - 2[Birnessite_i]) \ln \frac{[V^{IV}]_i}{[Birnessite]_i}$$

However, because multiple processes are at work in the removal of V^{IV}, we can model $[V^{IV}]_t$ as the difference between the initial V^{IV} concentration, the measured V^{V} concentration and the amount of V^{V} retained by the birnessite. This model assumes no V^{IV} is retained at the birnessite surface, and no V^{IV} present in the aqueous phase, which are supported by our control dissolution experiment and EXAFS data respectively:

Eq 8. $$[V^{IV}]_t = [V^{IV}]_i - [V^{V}]_{aq} - [V^{V}]_{ads}$$

While we have data on the initial concentrations of V^{IV}, dissolved V and birnessite, obtaining the amount of V^{V} adsorbed on the birnessite requires the IKL model mentioned above. Additionally, as has been shown for the oxidation of other metals and metalloids, birnessite experiences surface passivation as a result of Mn^{II} production, blockage of surface sites by oxidation products and mineralogical transformations due to Mn^{II}-MnO_2 back reactions. [19,20,23] While surface passivation is a complex set of competing processes, Shi et al. and Feng et al. were able to employ a first order estimation to model how passivation would modulate the pseudo-second order rate constant in the case of the oxidation of Sb and or As by birnessite. [19,20] In this approach, the pseudo-second order rate constant is described as:

Eq 9. $$k = k_0 e^{-bt}$$

Where k is the pseudo-second order rate constant at time t, K_0 is the initial pseudo-second order rate constant, and b is the pseudo first order surface passivation rate constant. Taken together, the final model is then:

Eq10. $$\ln \frac{[V^{IV}]_i - [V^V]_{aq,t} - \left(q_{eq}\left(\frac{1-e^{-k_S t}}{1-f_{eq}e^{-k_S t}}\right)[Birnessite]_{t,(gL^{-1})}\right)}{[Birnessite]_t} = t(k_0 e^{-bt})([V^{IV}]_i - 2[Birnessite]_i) + \ln \frac{[V^{IV}]_i}{[Birnessite]_i}$$

From which it can also be seen that the total $[V^V]$ can be calculated by:

Eq. 11 $$[V^V]_{total,t} = [V^V]_{aq,t} + \left(q_{eq}\left(\frac{1-e^{-k_S t}}{1-f_{eq}e^{-k_S t}}\right)[Birnessite]_{t,(gL^{-1})}\right)$$

And from which the simplified model for calculation of K_0 and *b* in the *in situ* experiments can derived:

Eq. 12 $$\ln \frac{[V^{IV}]_t}{[Birnessite]_t} = t(k_0 e^{-bt})([V^{IV}]_i - 2[Birnessite]_i) + \ln \frac{[V^{IV}]_i}{[Birnessite]_i}$$All related constants and fit variables are displayed in Tables 1, S1 and S2.

Section III. V^{IV} Control Experiment

Control Experiment Method

Reaction media was prepared in the same way as described for the *ex situ* experiments. The media contained 50 mM PIPES at pH 7.01 and 25 mM NaCl, and was degassed under vacuum for a minimum of 3 hours. The media was then transferred to the anoxic chamber (95% N_2: 5% H_2; COY) to equilibrate with stirring overnight. The control experiment was initiated in the anoxic chamber by dissolving 0.816 g of $VOSO_4 \bullet 5H_2O$ (Acros Organics, impurities < 20ppm) in 200 ml of the degassed media. As mentioned, the $V^{IV}O^{2+}$ cation immediately dissociated from the SO_4^{2-} and hydrolyzed to form a mixture of V^{IV} hydroxides (primarily $VOOH^{+}_{(aq)}$ and $V_2O_3(OH)_{2(s)}$) evident as a fine-textured, taupe precipitate suspended in the solution. This was then quickly added to 800 ml of vigorously stirring degassed media to commence the experiment. At select time points, samples were taken for analysis by ICP-OES and XAS, and trace metal grade HNO_3 was used to digest the V^{IV} precipitate. All procedures for analysis by XAS and ICP-OES were the same as detailed in the main text. Samples were taken at 1, 3, 5, 7, 9, 11, 15, 19, 24, 30, 40, 50, 60, 80, 103, 120, 150, 180, 240, 393, 630, 1372, 1848, 2813, 4211, 5715, and 7507 minutes. The release and resorption of V from the precipitate can be seen in Appendix 2 Figure 3.1b, with further details on the product below.

Modelling of the Control Experiment

The kinetics of dissolution and resorption of V^{IV} from the $VOSO_4$ hydrolysis precipitation product was modelled using an adapted form of the second order rate law for mineral dissolution. [24–26]

Eq 13. $$Rate = K_{obs}([V^{IV}]_{eq} - [V^{IV}]_t)^2$$

Which yields the integrated form:

Eq 14. $$[V^{IV}]_t = \frac{[V^{IV}]_{eq}{}^2 K_{obs} t}{1+[V^{IV}]_{eq} K_{obs} t}$$

Where rate is in mM min^{-1}, K_{obs} is the pseudo second order rate constant for dissolution in units of mM^{-1} min^{-1}, $[V^{IV}]_{eq}$ is the equilibrium aqueous V^{IV} concentration and $[V^{IV}]_t$ is the V^{IV} concentration at time t in mM.

Frierdich and Catalano adapted this equation for parallel pathways of dissolution from Fe oxides.[26] Here, we have adapted this equation to describe the rate of change in the V^{IV} concentration in terms of parallel dissolution and resorption reactions.

Eq 15. $$[V^{IV}]_t = \frac{[V^{IV}]_{eq}{}^2 K^*_{dis} t}{1+[V^{IV}]_{eq} K^*_{dis} t} - \frac{[V^{IV}]_{eq}{}^2 K_{res} t}{1+[V^{IV}]_{eq} K_{res} t}$$

Where K^*_{dis} is the pseudo second order dissolution rate constant (mM^{-1} min^{-1}) and K_{res} is the pseudo second order resorption rate constant (mM^{-1} min^{-1}).

V^{IV} Control	
Equillibrium release (μM)	24.155
K_{des} (μM^{-1} min^{-1}) ($x10^{-2}$)	2.083
Equillibrium resorption (μM)	90.378
K_{ads} (μM^{-1} min^{-1}) ($x10^{-7}$)	3.898

Appendix 2 Table 3.4 Second order fitted kinetic parameters used to model the V^{IV} control experiment.

Characterization of the V^{IV} precipitation product

All reactions were initiated by the dissolution of $V^{IV}OSO_4$ in reaction media at pH 7, which resulted in the immediate precipitation of a beige solid, which turned black over the course of 30 minutes under anoxic conditions and aged to green when dried under oxic conditions. Analysis of the anoxic product by Synchrotron XRD and XANES suggests that the compound is primarily häggite, a V^{IV} oxyhydroxide exhibiting prominent diffraction peaks corresponding to the 001 and -201 faces, as well as an E_0 of 5479.5 eV, and an $E_{1/2}$ of 5477.9 eV, which are similar to previously reported $E_{1/2}$ values for häggite and the similar oxide, duttonite.[27,28] Minor peaks in the diffraction pattern are attributed to the V^{IV} oxides doloresite, and paramontroseite (Appendix 2 Figure 3.3b). EXAFS of the material also show similar characteristics to EXAFS for häggite, namely the peaks at 2.3 $Å^{-1}$ and 2.9 $Å^{-1}$, the shoulder at 6.2 $Å^{-1}$ and the sloping oscillation between 7.5 $Å^{-1}$ and 9 $Å^{-1}$ (Appendix 2 Figure 3.3c).[28] Finally, the uncorrected radial structure plot (Appendix 2 Figure S3d) exhibits similarities to previously reported EXAFS taken of the V^{IV} oxides Gain's hydrate, or lenoblite ($V_2O_4•2H_2O$).[28] Theoretical fitting of the EXAFS reveals a V-V distance of 3.00 Å (Appendix 2 Table 3.6), comparable to previously published values for häggite.[29] Two sets of characteristic focused linear multiple scattering paths (fms paths) were also observed along the axially joined V-O-V (in the direction of the a axis, which can be seen looking down the c axis in Appendix 2 figure 3.3k – values presented in Appendix 2 Table 3.6). As the material recrystallized over the course of the reaction, the coordination number for the equatorially neighboring V increased from 0.8 to 1.4, approaching the crystallographic value of 2 (Appendix 2 Figures 3.3s-u). Additionally,

over the course of the control experiment, a new V-V distance at 3.36 Å appeared, which is in agreement with a previous study. [28] The XRD results indicate that our starting material is likely a solid solution, dominated by the oxyhydroxide Häggite, and indicates that the formation pathways for the various V^{IV} solid phases detected are competitive with one another.[28]

We interpret the change in the EXAFS signal of the precipitate as a result of a time-dependent increase in the crystallinity of the compound due to recrystallization as V^{IV}_{aq} is reincorporated from the aqueous phase (Appendix 2 Figure 3.3d). In addition to the increase in neighboring V coordination and the appearance of a V-V bond at 3.36 Å, the σ^2 of the fms paths decreased over the 5.2 day long experiment, while the amplitude increased (Appendix 2 Figure 3.3d,f). This indicates an increase in crystallinity of the final compound, as these paths are linear in Häggite, but are slightly distorted in similar V^{IV} solids, as discussed below. The spectra, and their pseudo-RSF plots are presented in Appendix 2 Figure 3.3c-f.

Despite being outside of our available fitting range, an increase in multiple scattering is observed between 5 and 6 Å R+δR which can be attributed to a V-V-V between equatorially neighboring V^{IV} octahedra in the ab plane along the b axis (Appendix 2 Figure 3.3f). In k-space, this and the fms paths contribute to a notable beat pattern that occurs between 8 and 8.5 $Å^{-1}$. This beat is denoted by arrows in Appendix 2 Figure 3.3 c, e, g and h. Similar beat patterns have been noted previously in metal hydroxides, and are indicative of a focused multiple-scattering phenomenon that can provide diagnostic clues about the structure of the metal (hydr)oxide in question.[30–32] In this case, the increase in

the beat pattern's depth to become a shoulder in the antinode spanning from 7.5 to 9.5 $Å^{-1}$ at the end of the experiment is diagnostic of an increase in the focused multiple scattering, both in the fms paths as well as the uncharacterized paths present between 5 and 6 Å R+δR. This beat pattern is only partially reproducible in the Fourier back-transforms constructed from paths below 3.5 Å R+δR (this includes the fms paths) (Appendix 2 Figure 3.3h). The Fourier back-transforms in the range of 5-6 Å R+δR shows a drastic increase in intensity between the initial and final time point (Appendix 2 Figure 3.3i), which when combined with the fms paths recreates the feature. The resulting wavelet peaks in amplitude at 8 $Å^{-1}$ (Appendix 2 Figure 3.3i). The signal contribution of the fms and multiple scattering paths is largely out of phase with the single-scattering signal contribution from the 1^{st} and 2^{nd} shells, particularly between 8 and 8.5 $Å^{-1}$ as can be seen in the Fourier-back transform plot done from 1-6 Å R+δR (Appendix 2 Figure 3.3g).

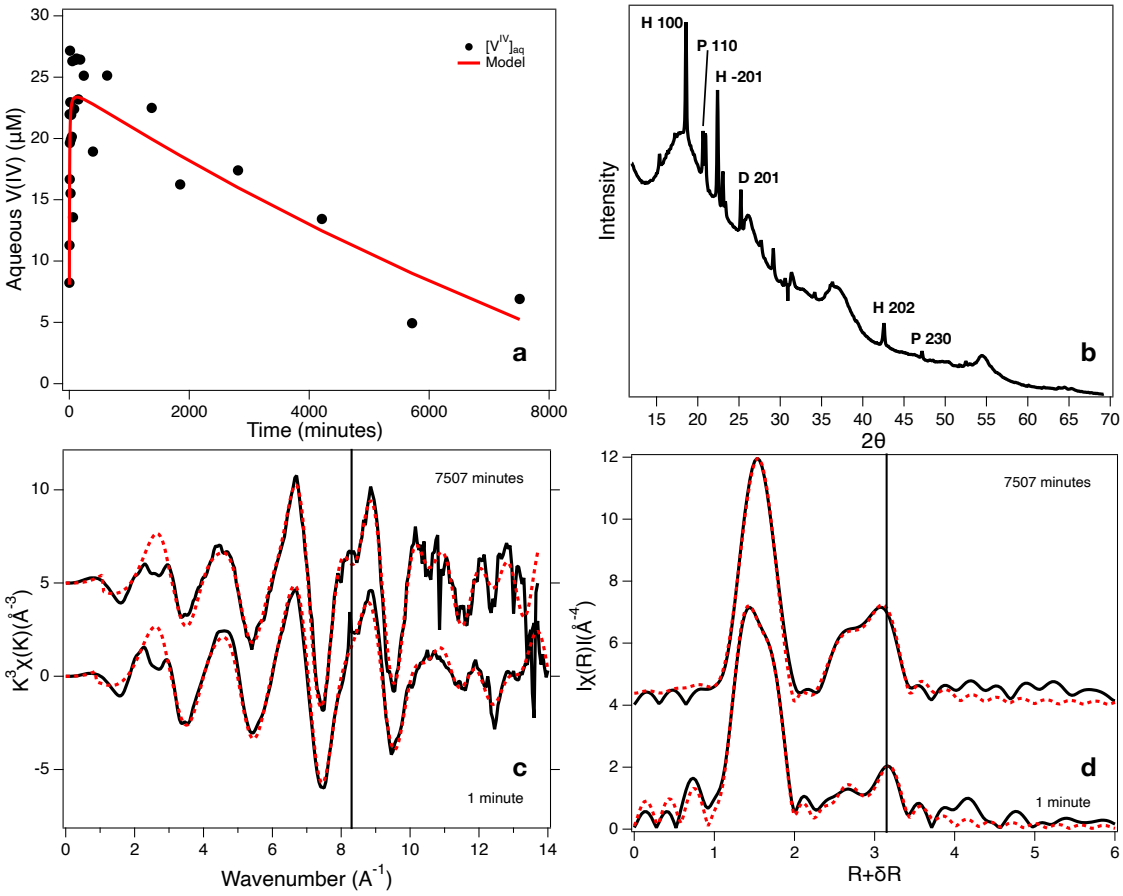

Appendix 2 Figure 3.3 a) Aqueous V^{IV} plot showing V dissolution and re-uptake over time at pH 7. The maximum concentration of dissolved V(IV) is 27μM after 11 minutes. b) Synchrotron XRD of the V^{IV} oxyhydroxides formed upon the hydrolysis of $VOSO_4$ in the reaction media at pH 7. Peak assignment demonstrates that the hydroxides are primarily Häggite, with traces of Doloresite and Paramontroseite. (H)= Häggite, (P)=Paramontroseite, (D)= Doloresite. c) K^3 weighted V EXAFS on the V^{IV} solid at the beginning and end of the dissolution control experiment. The vertical line denotes the position of the fms beat pattern. d) Corresponding rsf plots of the K^3 weighted EXAFS in panel c. The vertical line corresponds to the position of the V-V single scattering distance.

Thus, we attribute the increased intensity in the beat pattern to from increased linear ordering of the V(IV) octahedra in a way that allows for focused multiple scattering to

occur as the initially semi-amorphous collection of V^{IV} octahedra increase in their crystallinity via polymerization to form sheets. This interpretation follows previous work in metal oxides and oxyhydroxides.[30,32] Below, we will discuss the relationship between these scattering phenomena and the structure of the V^{IV} solid.

It's Besnardiere et al.[28] examined the dehydration of Gain's hydrate to form häggite. As characterized by the authors, häggite is composed of doublet chains of edge-sharing $V_2O_3(OH)_2$ octahedra that are apically connected to other doublet chains of edge-sharing octahedra at the vanadyl oxygen (along the shortest V-O bond) (Appendix 2 Figure 3.3j, k, l). focused multiple scattering is an in-plane the increase in fms over the 5.2 day reaction cannot indicate growth in the direction of the c axis, as this is the axis of sheet stacking (the c axis goes from left to right in Appendix 2 Figure 3.3j). Rather, it must indicate the increase in connections between the doublet chains in the ab plane (Appendix 2 Figure 3.3k). This is supported by the increase in the amplitude of the scattering atoms in the 2nd shell (Appendix 2 Figure 3.3d, f) with time, which correspond to the fitted equatorial V^{IV} octahedra and V-O-V fms paths. Crucially, our EXAFS didn't support the existence of V-V edge sharing neighbors present at 3.14 Å, although this is likely due to the resolution of our EXAFS (0.15 Å) which is at the threshold of 0.15 Å needed to distinguish the equatorial from edge-sharing V^{IV} octahedra that make up the doublet chains that extend along the b axis of the ab plane. structurally, we therefore interpret the increase of in the intensity of the second shell peaks over time with absences in the doublet chains of edge-sharing octahedra resulting in gaps which are filled as the material resorbs V^{IV}

from solution overtime. Leading to a structure that resembles the one published by Besnardiere et al.[28]

It's worth noting that the V^{IV} oxide doloresite is similar to the structure of häggite published by Besnardiere et al.[28], with the primary difference being the insertion of an additional, apically connected V^{IV} octahedra between each edge-sharing doublet (Appendix 2 Figure 3.3m,n). [33] In the EXAFS signal, this would have the result of fms scattering being dominated by the linear chain of 3, apically linked V octahedra rather than primarily by the edge-sharing doublet chains, which we did not observe. Paramontroseite is also structurally similar to häggite, although less so than doloresite. [34] It is composed of edge-sharing octahedra, where the shared edge is composed of an apical and equatorial oxygen, with additional edge-sharing of purely equatorial oxygens along the c axis (using the orientation schema of Evans and Morse) (Appendix 2 Figure 3.3o, p). Sheet structure in paramontroseite is attenuated by cross-linkages in the ab plane, which would likely attenuate the effects of focused multiple scattering as there are no continuous, apically linked chains of octahedra. Finally, duttonite is composed of polymeric sheets oriented in the bc-plane, with equatorial edge-sharing octahedra in the c-direction and apical corner sharing octahedra in the b-direction (Appendix 2 Figure 3.3 q, r). [27] However, in the structure reported by Evans and Morse, the V^{IV} atoms are canted with respect to their neighbors along the c axis (equatorial edge-sharing neighbors). This would severely reduce the intensity of focused multiple scattering in this direction, leaving only the b axis (apical, corner sharing octahedra) as a candidate along which this phenomenon could occur. However, the V-V single scattering distance along the b axis is 3.95 Å, and the V-V-V path

lengths in this direction are 7.9 Å long, which exceed the half path lengths of focused multiple scattering observed in our study. In contrast, the V-V-V distance for the equatorial, edge-sharing octahedra of Häggite doublets (along the b axis in the nomenclature of Evans and Morse [33]) is 5.98 Å, which fits in with our observations when the δR term is applied (Appendix 2 Figure 3.3d, f).

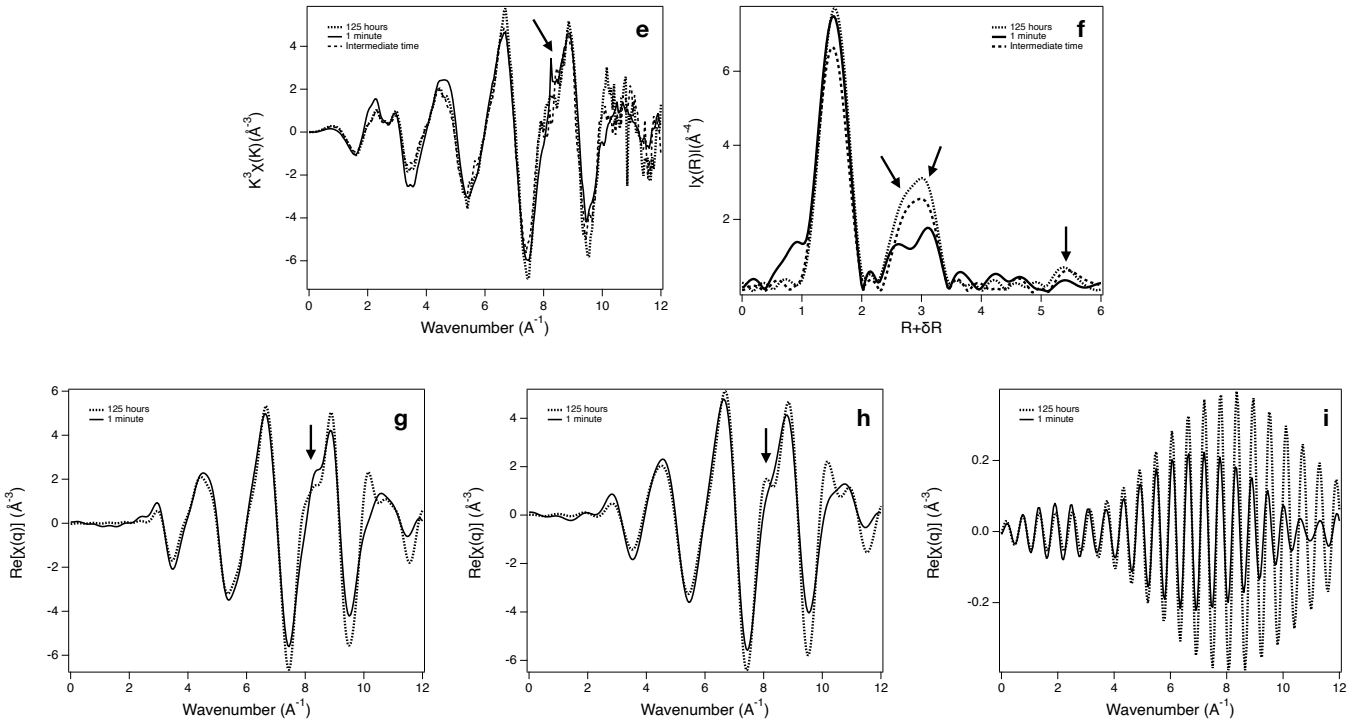

Appendix 2 Figure 3. 3 **e-i.** e) K^3-weighted EXAFS spectra of the V(IV) hydroxide precipitate over the course of 125 hours. The arrow denotes the location of the fms derived beat pattern. f) The corresponding pseudo-RSF plot. Arrows denote the positions of the apical and equatorially bound V(IV) octahedral neighbors, and the focused fms path. g) Fourier back transform for the R range 1-6 Å R+δR, with arrow denoting location of the beat. h) Fourier back transform plot using the R-range of 1-3.5 Å R+δR (1st and 2nd shell only), arrow denotes the position the beat would be, and it can be seen that the closely spaced V neighbors in the second shell lead to splitting of the antinode between 7.5 and 9.5 $Å^{-1}$. i) Fourier back transform plot using the R-range of 5-6 Å R+δR, which captures only the focused fms paths. Note the wavelet has the greatest amplitude near 8.5 $Å^{-1}$, which is the position of the beat in the k^3 weighted EXAFS spectra.

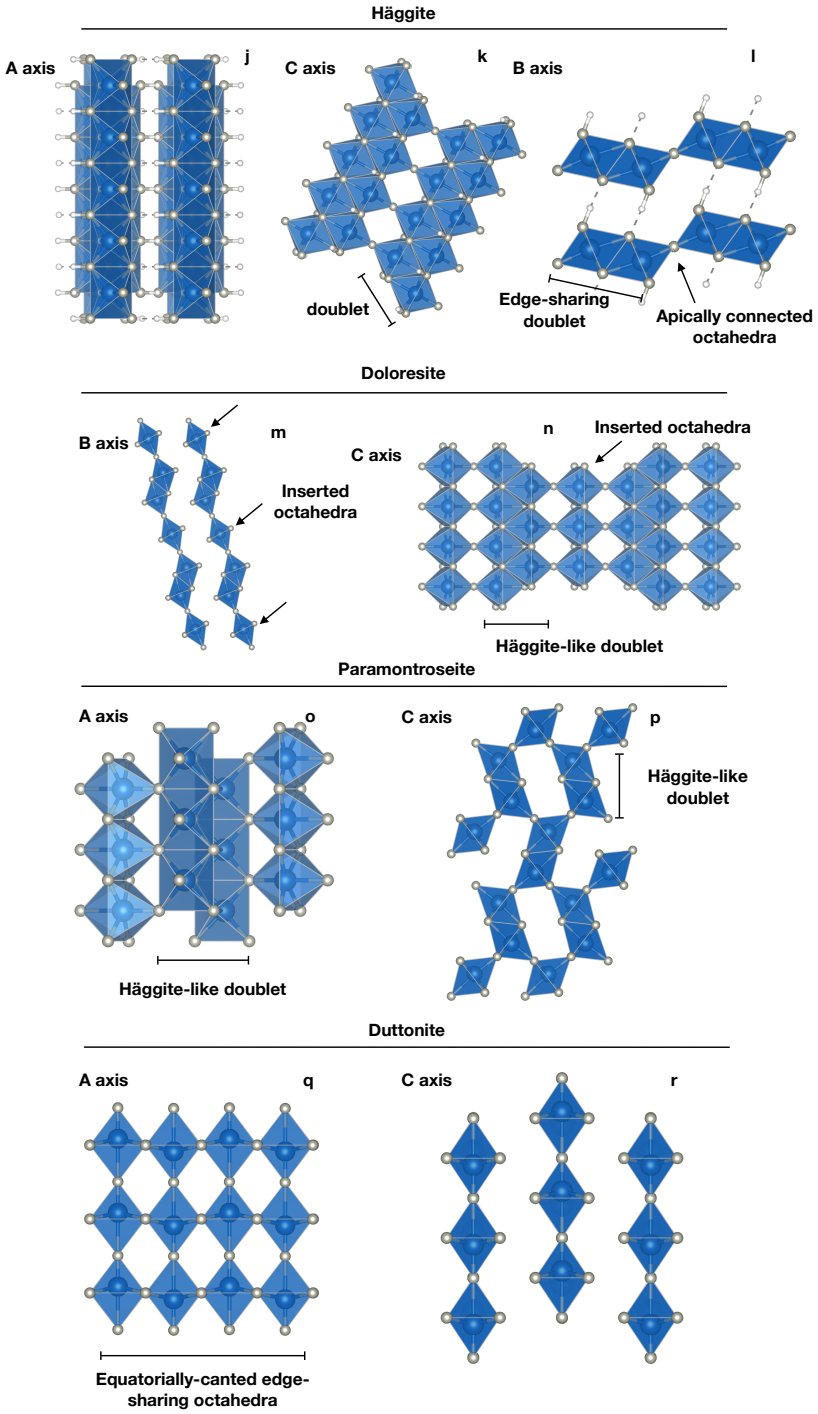

Appendix 2 Figure 3.3 j-r. j, k, l) Cross-sections of häggite emphasizing the edge-sharing and corner sharing interactions of the octahedra between edge-sharing chains extending in the b direction, and the apical connections between chains of doublets to form sheets. m,n) Cross-sections of doloresite emphasizing the inserted V^{IV} octahedra between the häggite-

like chains of doublets, this would result in an increased focused ms intensity. o,p) Cross-sections of Paramontroseite emphasizing the lack of apically-connected V^{IV} octahedra, with octahedra being connected apex to edge, or edge to edge. q,r) Cross-sections of duttonite to illustrate the lack of a octahedra-doublet chain structure seen in the other V^{IV} crystals. The formation of long sheets (Figure 3.3r) along the b direction indicates a strong focused multiple scattering contribution, but one that is much greater than what häggite would produce.

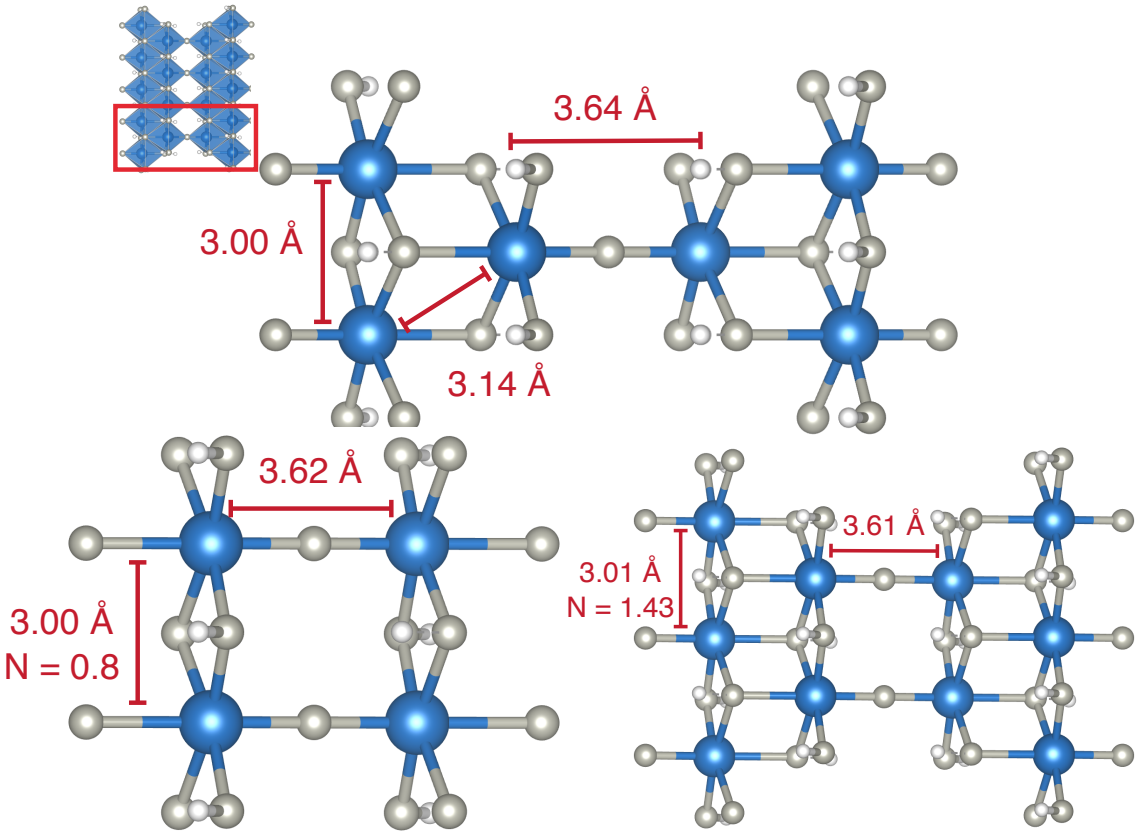

Appendix 2 Figure 3.3 s-u s) Top: crystallographic distances to nearest neighbors in Häggite. t) Left: Distances measured by EXAFS on solids taken 1 minute into the control reaction. u) Right: Distances measured by EXAFS on solids taken at the end of the control experiment, 5.2 days after start.

Section IV. Aqueous Vanadate Speciation (ex situ experiments)

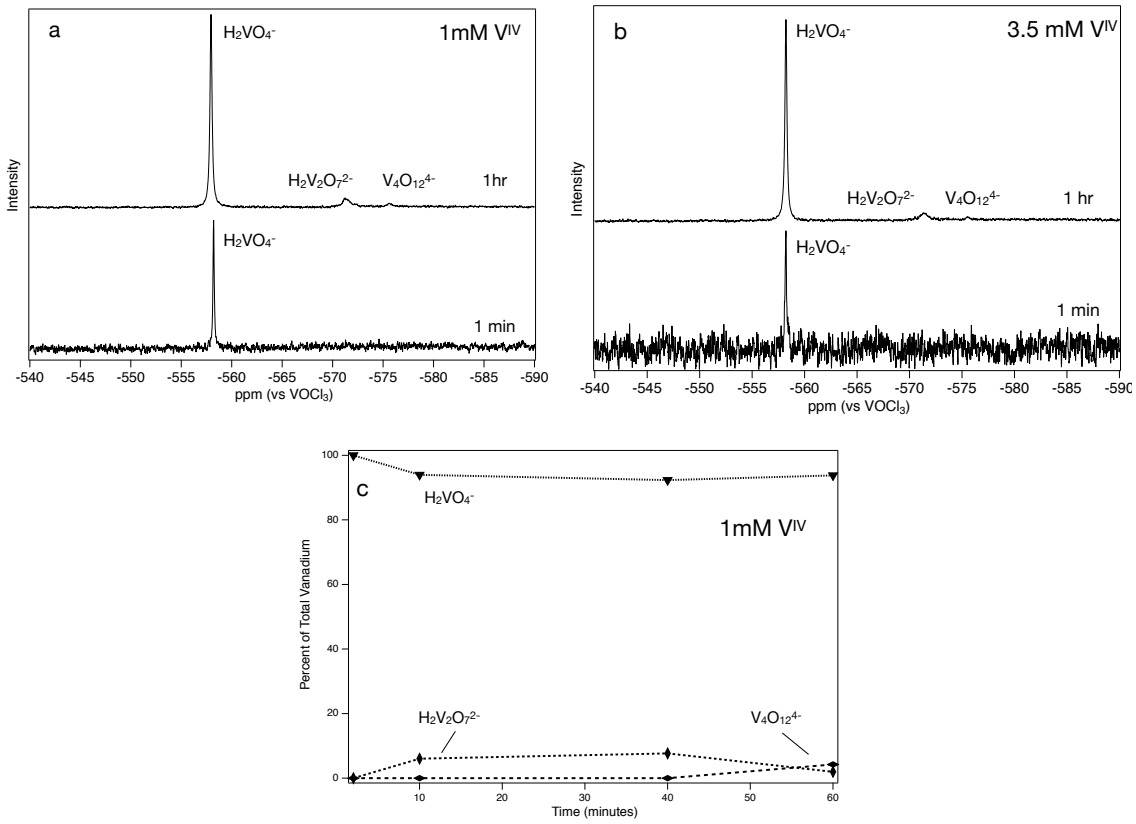

Appendix 2 Figure 3.4 ^{51}V NMR from the *ex situ* 1 mM (a) and 3.5 mM (b) V^{IV} experiments. The increased noise in the 3.5 mM spectra is due to paramagnetic interference caused by elevated levels of aqueous Mn^{II} relative to the 1mM experiment. ^{51}V-NMR confirmed the increased production of V^V over the course of the reaction, with peak development at -558.2 ppm indicative of $H_2VO_4^-$ formation within the first 2 minutes, and peaks at -571.4 ppm and -575.6 ppm indicating $H_2V_2O_7^{2-}$ and $V_4O_{12}^{4-}$ formation over the course of the first hour, reaching 93.8%, 4.3% and 1.9% respectively, with the proportions of the polymers increasing with time. [15,35,36] c) The proportion of each V^V species present as a function of total V extracted from ^{51}V NMR by peak integration.

Section V. Manganese Transformation

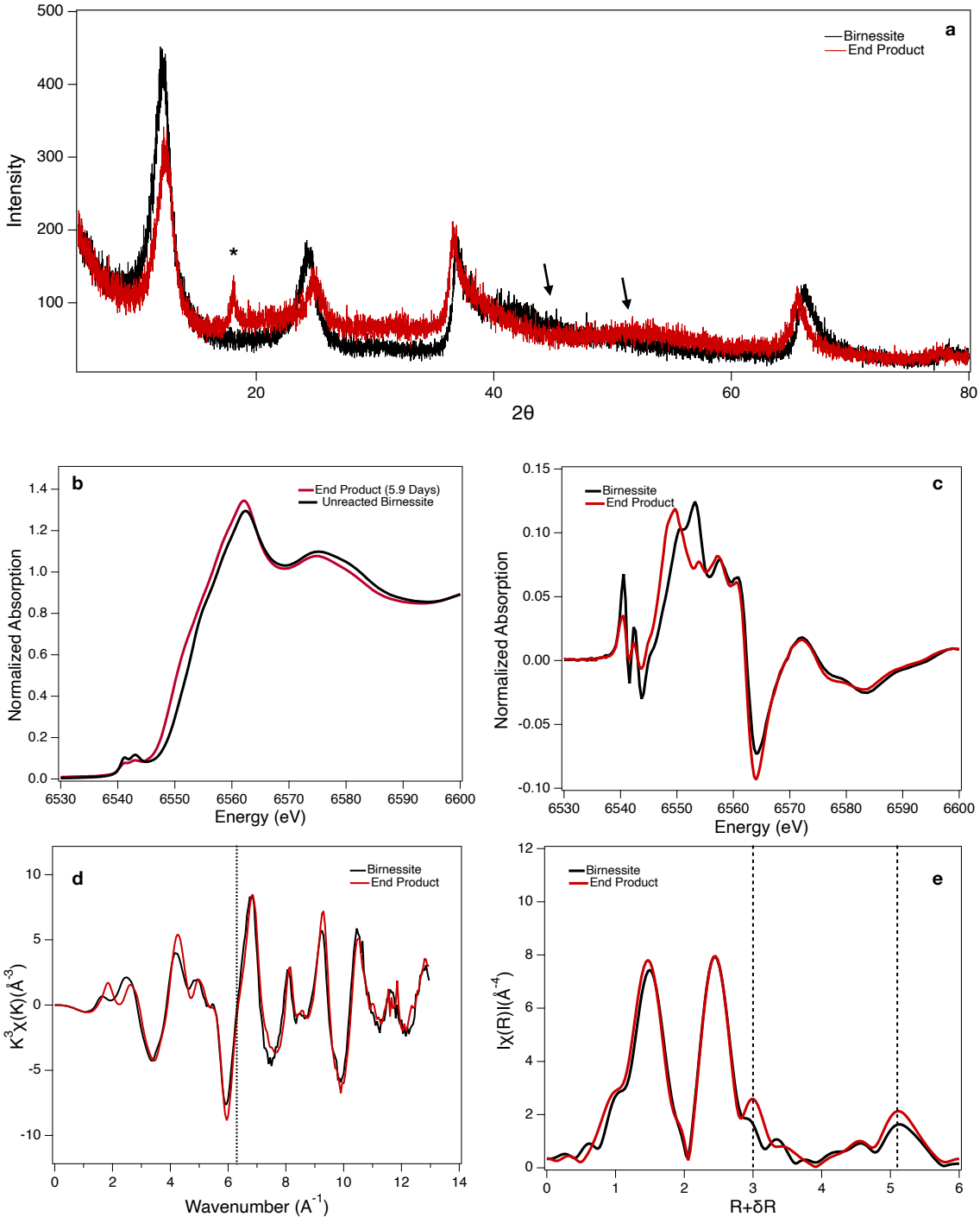

Appendix 2 Figure 3.5 a) The XRD pattern of birnessite before and after reaction with 3.5 mM V^{IV} at pH 7. The formation of the feiknechtite is indicated by the growth of a

peak at 18° denoted by *. The capping of Mn^{II} onto vacant sites is observed by the formation of a dip at 45°, and the formation of the broad feature between 37° and 66° denoted by arrows. b) Mn K-edge XANES taken from the 3.5 mM *ex situ* experiment. c) First derivative plot of the Mn XANES showing the shift of E_0 to lower energy as the birnessite is reduced by V^{IV}. d) Mn EXAFS of unreacted birnessite and the reacted birnessite from the end of the reaction. The dashed line at 6.3 $Å^{-1}$ denotes the development of the shoulder corresponding to $Mn^{II/III}$ adsorbed at vacant sites. e) RSF plots of the Mn EXAFS in 4d. The dashed lines correspond to the increase in adsorbed $Mn^{II/III}$ and an increase in Mn^3 multiple scattering.

Appendix 2 Table 3.5 Results of shell by shell least squares fitting on Mn EXAFS from the 3.5 mM *ex situ* experiments.

Birnessite

Path	N	S_0^2	σ^2 ($Å^2$) x10^{-3}	R (Å)	E0	K range
Mn-O	5.8 (0.14)	0.9	6.0 (1.0)	1.90(1)	0.3 (2.6)	3-12
Mn-Mn (edge)	3.7 (1.1)		4.3 (1.9)	2.86 (1)		
R-factor	0.022					
χ^2_{red}	314					

8425 minutes

Path	N	S_0^2	σ^2 ($Å^2$) x10^{-3}	R (Å)	E0	K range
Mn-O	5.8 (0.3)	0.9	7.7 (0.93)	1.90 (1)	-0.4 (2.0)	3-12
Mn-Mn edge	3.90 (0.96)		6.1 (1.7)	2.85 (1)		
Mn-Mn (corner)	0.8 (0.21)		1.5 (2.4)	3.50 (2)		
R-factor	0.026					
χ^2_{red}	174					

Section VI. V EXAFS

Appendix 2 Table 3.6 Results of shell by shell least squares fitting on the V EXAFS. The amplitude reduction value S_0^2 was determined by fitting the EXAFS of the in-line V calibration foil. The coordination number for each scattering path is denoted as N; σ^2 is the Debye-Waller factor; R is the half-path length (inter-atomic distance) in angstroms and E_0 is the energy-shift parameter.

Standards

Na3VO4

Path	N	S_0^2	σ^2 (Å^2) x10^{-3}	R (Å)	E0	K range
V-O	4	0.85	3.0 (3)	1.713 (5)	3 (2)	3-14
V-O-O	12		11 (15)	3.22 (8)		
R-factor	0.22					
χ^2_{red}	233					

Standards

VOSO4

Path	N	S_0^2	σ^2 (Å^2) x10^{-3}	R (Å)	E0	K range
V-O	1	0.95	3.0 (6)	1.609 (9)	5 (3)	3-14
V-O	1.5 (4)		3.0 (6)	1.89 (2)		
V-O	3.65 (5)		3.0 (6)	2.02 (1)		
V-S	2		14 (5)	3.23 (4)		
R-factor	0.018					
χ^2_{red}	289.8					

3.5 mM *ex situ* Experiment

1 minute

Path	N	S_0^2	σ^2 (Å^2) x10^{-3}	R (Å)	E0	K range
V-O	1.9 (3)	0.98 (8)	2.3 (8)	1.652 (7)	4 (3)	3-13.5
V-O	1.0 (3)		2.3 (8)	1.90 (1)		
V-V	1.2 (5)		4.9 (2)	3.09 (2)		
V-V	0.8 (6)		4.9 (2)	3.32 (2)		
V-O-V-O-V fms	1		14.1 (6)	3.72 (4)		
R-factor	0.019					
χ^2_{red}	6.5					

3.5 mM *ex situ* Experiment

8425 minutes

Path	N	S_0^2	σ^2 (Å^2) x10^{-3}	R (Å)	E0	K range
V-O	3.90 (9)	0.95 (7)	6.9 (7)	1.705 (9)	7 (2)	3-12.6
V-Mn	1.1 (5)		16 (8)	2.79 (3)		
V-O-O	12		13 (1)	3.25 (9)		
V-V	1		12 (9)	3.43 (6)		
R-factor	0.020		101.3° ∠V-O-Mn			
χ^2_{red}	3.1					

3.5 mM *ex situ* Experiment

8425 minutes

Path	N	S_0^2	σ^2 (Å^2) x10^{-3}	R (Å)	E0	K range
V-O	3.90 (9)	0.95 (7)	6.9 (7)	1.705 (9)	7.2 (2)	3-12.6
V-Mn	1.3 (8)		20 (3)	2.82 (5)		
V-O-O	12		13 (1)	3.17 (9)		
R-factor	0.26		102.8° ∠V-O-Mn			
χ^2_{red}	3.9					

V(IV) Control Experiment

1 minute

Path	N	S_0^2	σ^2 (Å^2) x10^{-3}	R (Å)	E0	K range
V-O	1.0 (1)	0.96 (7)	1.9 (5)	1.612 (3)	3 (1)	3-14
V-O	1.2 (1)		1.9 (5)	1.884 (5)		
V-O	2.6 (2)		1.9 (5)	2.015 (5)		
V-V	0.8 (3)		8 (3)	3.00 (1)		
V-O-V fms	2		4.3 (7)	3.62 (1)		
V-O-V-O-V fms	1		4.3 (7)	3.71 (2)		
R-factor	0.0036					
χ^2_{red}	15.8					

V(IV) Control Experiment

7507 minutes

Path	N	S_0^2	σ^2 (Å^2) x10^{-3}	R (Å)	E0	K range
V-O	1.4 (4)	0.9 (1)	5 (2)	1.63 (1)	4 (2)	3-13.2
V-O	4.0 (8)		5 (2)	1.991 (8)		
V-V	1.4 (3)		6 (3)	3.01 (1)		
V-V	1		12 (8)	3.36 (6)		
V-O-V fms	1		1 (1)	3.61 (2)		
V-O-V-O-V fms	1		1 (1)	3.69 (3)		
R-factor	0.011					
χ^2_{red}	9.8					

Section VII. Conceptual Diagram

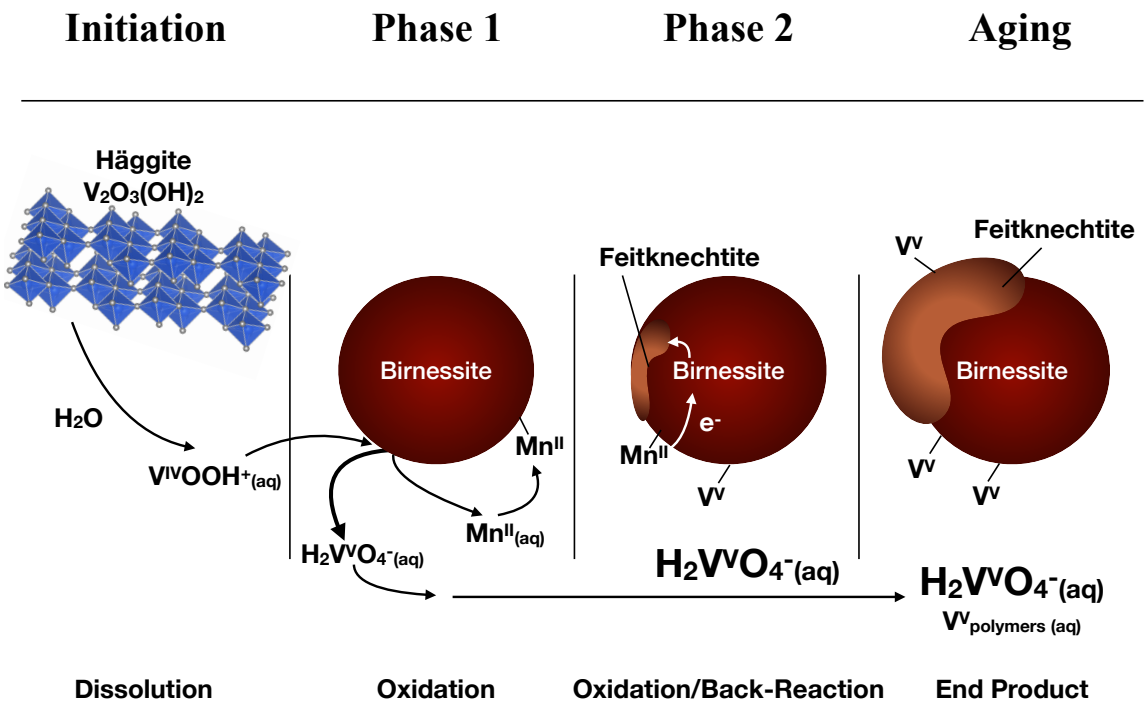

Appendix 2 Figure 3.6 Proposed reaction mechanism for V^{IV} oxidation by birnessite. Dissolution) VOSO4 has precipitated in the reaction media immediately prior to initiation by forming a mixture of V^{IV} oxyhydroxides that is primarily composed of Häggite, which dissolves to form $VOOH^{+}$. Phase 1) $VOOH^{+}$ is oxidized by birnessite to form aqueous Mn^{II} and V^{V}, which polymerizes in solution to form V_2 and V_4. No observable surface passivation. Phase 2) Mn^{II} induces the formation of feiknechtite via comproportionation with Mn^{IV}, while V^{V} adsorbs at the surface of the Mn oxides. Aging) V^{V} continues to adsorb onto and desorb from the surface of the Mn oxides. The Mn^{II}-birnessite back reaction continues, forming more MnOOH. The numbers at the top represent the time in minutes for each portion of the reaction (based on the 3.5 mM *ex situ* experiments).

Section VIII. References

(1) Larsson, M. A.; Hadialhejazi, G.; Gustafsson, J. P. Vanadium Sorption by Mineral Soils: Development of a Predictive Model. *Chemosphere* **2017**, *168*, 925–932. https://doi.org/10.1016/j.chemosphere.2016.10.117.

(2) Larsson, M. A.; Persson, I.; Sjöstedt, C.; Gustafsson, J. P. Vanadate Complexation to Ferrihydrite: X-Ray Absorption Spectroscopy and CD-MUSIC Modelling. *Environ. Chem.* **2017**, *14* (3), 141–150. https://doi.org/10.1071/EN16174.

(3) Chaurand, P.; Rose, J.; Briois, V.; Salome, M.; Proux, O.; Nassif, V.; Olivi, L.; Susini, J.; Hazemann, J.-L.; Bottero, J.-Y. New Methodological Approach for the Vanadium K-Edge X-Ray Absorption Near-Edge Structure Interpretation: Application to the Speciation of Vanadium in Oxide Phases from Steel Slag. *J. Phys. Chem. B* **2007**, *111* (19), 5101–5110. https://doi.org/10.1021/jp063186i.

(4) Bennett, W. W.; Lombi, E.; Burton, E. D.; Johnston, S. G.; Kappen, P.; Howard, D. L.; Canfield, D. E. Synchrotron X-Ray Spectroscopy for Investigating Vanadium Speciation in Marine Sediment: Limitations and Opportunities. *J. Anal. At. Spectrom.* **2018**, *33* (10), 1689–1699. https://doi.org/10.1039/C8JA00231B.

(5) Levina, A.; McLeod, A. I.; Lay, P. A. Vanadium Speciation by XANES Spectroscopy: A Three-Dimensional Approach. *Chemistry – A European Journal* **2014**, *20* (38), 12056–12060. https://doi.org/10.1002/chem.201403993.

(6) Vessey, C. J.; Lindsay, M. B. J. Aqueous Vanadate Removal by Iron(II)-Bearing Phases under Anoxic Conditions. *Environ. Sci. Technol.* **2020**. https://doi.org/10.1021/acs.est.9b06250.

(7) Brinza, L.; Vu, H. P.; Neamtu, M.; Benning, L. G. Experimental and Simulation Results of the Adsorption of Mo and V onto Ferrihydrite. *Scientific Reports* **2019**, *9* (1), 1365. https://doi.org/10.1038/s41598-018-37875-y.

(8) Gustafsson, J. P. Vanadium Geochemistry in the Biogeosphere –Speciation, Solid-Solution Interactions, and Ecotoxicity. *Applied Geochemistry* **2019**, *102*, 1–25. https://doi.org/10.1016/j.apgeochem.2018.12.027.

(9) Lawton, J. S.; Aaron, D. S.; Tang, Z.; Zawodzinski, T. A. Qualitative Behavior of Vanadium Ions in Nafion Membranes Using Electron Spin Resonance. *Journal of Membrane Science* **2013**, *428*, 38–45. https://doi.org/10.1016/j.memsci.2012.11.003.

(10) Ravel, B.; Newville, M. ATHENA, ARTEMIS, HEPHAESTUS: Data Analysis for X-Ray Absorption Spectroscopy Using IFEFFIT. *J Synchrotron Rad* **2005**, *12* (4), 537–541. https://doi.org/10.1107/S0909049505012719.

(11) Manceau, A.; Marcus, M. A.; Grangeon, S. Determination of Mn Valence States in Mixed-Valent Manganates by XANES Spectroscopy. *American Mineralogist* **2012**, *97* (5–6), 816–827. https://doi.org/10.2138/am.2012.3903.

(12) Ravel, B.; Newville, M. ATHENA and ARTEMIS: Interactive Graphical Data Analysis Using IFEFFIT. *Phys. Scr.* **2005**, *2005* (T115), 1007. https://doi.org/10.1238/Physica.Topical.115a01007.

(13) Hamilton, W. C. Significance Tests on the Crystallographic R Factor. *Acta Cryst* **1965**, *18* (3), 502–510. https://doi.org/10.1107/S0365110X65001081.

(14) Calvin, S. *EXAFS for Everyone*; CRC Press.

(15) Tracey, A. S.; Jaswal, J. S.; Angus-Dunne, S. J. Influences of PH and Ionic Strength on Aqueous Vanadate Equilibria. *Inorg. Chem.* **1995**, *34* (22), 5680–5685. https://doi.org/10.1021/ic00126a043.

(16) Ferreira, S.; Leite, A.; Moniz, T.; Andrade, M.; Amaral, L.; Castro, B. de; Rangel, M. EPR and 51 V NMR Studies of Prospective Anti-Diabetic Bis(3-Hydroxy-4-Pyridinonato)Oxidovanadium(Iv) Complexes in Aqueous Solution and Liposome Suspensions. *New Journal of Chemistry* **2018**, *42* (10), 8088–8097. https://doi.org/10.1039/C7NJ04678B.

(17) Kuan, W.-H.; Lo, S.-L.; Chang, C. M.; Wang, M. K. A Geometric Approach to Determine Adsorption and Desorption Kinetic Constants. *Chemosphere* **2000**, *41* (11), 1741–1747. https://doi.org/10.1016/S0045-6535(00)00054-0.

(18) Marczewski, A. W. Analysis of Kinetic Langmuir Model. Part I: Integrated Kinetic Langmuir Equation (IKL): A New Complete Analytical Solution of the Langmuir Rate Equation. *Langmuir* **2010**, *26* (19), 15229–15238. https://doi.org/10.1021/la1010049.

(19) Shi, Z.; Peng, S.; Wang, P.; Sun, Q.; Wang, Y.; Lu, G.; Dang, Z. Modeling Coupled Kinetics of Antimony Adsorption/Desorption and Oxidation on Manganese Oxides. *Environ. Sci.: Processes Impacts* **2018**, *20* (12), 1691–1696. https://doi.org/10.1039/C8EM00323H.

(20) Feng, X.; Wang, P.; Shi, Z.; Kwon, K. D.; Zhao, H.; Yin, H.; Lin, Z.; Zhu, M.; Liang, X.; Liu, F.; Sparks, D. L. A Quantitative Model for the Coupled Kinetics of Arsenic Adsorption/Desorption and Oxidation on Manganese Oxides. *Environ.*

Sci. Technol. Lett. **2018**, *5* (3), 175–180. https://doi.org/10.1021/acs.estlett.8b00058.

(21) Siebecker, M.; Madison, A. S.; Luther, G. W. Reduction Kinetics of Polymeric (Soluble) Manganese (IV) Oxide (MnO2) by Ferrous Iron (Fe2+). *Aquat Geochem* **2015**, *21* (2), 143–158. https://doi.org/10.1007/s10498-015-9257-z.

(22) Couture, R.-M.; Rose, J.; Kumar, N.; Mitchell, K.; Wallschläger, D.; Van Cappellen, P. Sorption of Arsenite, Arsenate, and Thioarsenates to Iron Oxides and Iron Sulfides: A Kinetic and Spectroscopic Investigation. *Environ. Sci. Technol.* **2013**, *47* (11), 5652–5659. https://doi.org/10.1021/es3049724.

(23) Mock, R. P.; Schaefer, M. V.; Pacheco, J. L.; Lake, L.; Lee, I.; Ying, S. C. Influence of Fe(II) on Arsenic(III) Oxidation by Birnessite in Diffusion-Limited Systems. *ACS Earth Space Chem.* **2019**, *3* (4), 550–561. https://doi.org/10.1021/acsearthspacechem.8b00184.

(24) Berner, R. A. Rate Control of Mineral Dissolution under Earth Surface Conditions. **1978**.

(25) Zhang, J. W.; Nancollas, G. H. Mechanisms of Growth and Dissolution of Sparingly Soluble Salts. *Reviews in Mineralogy and Geochemistry* **1990**, *23* (1), 365–396.

(26) Frierdich, A. J.; Catalano, J. G. Fe(II)-Mediated Reduction and Repartitioning of Structurally Incorporated Cu, Co, and Mn in Iron Oxides. *Environ. Sci. Technol.* **2012**, *46* (20), 11070–11077. https://doi.org/10.1021/es302236v.

(27) Evans, H. T.; Mrose, M. E. The Crystal Structures of Three New Vanadium Oxide Minerals. *Acta Crystallographica* **1958**, *11* (1), 56–58. https://doi.org/10.1107/S0365110X58000141.

(28) Besnardiere, J.; Petrissans, X.; Ribot, F.; Briois, V.; Surcin, C.; Morcrette, M.; Buissette, V.; Le Mercier, T.; Cassaignon, S.; Portehault, D. Nanoparticles of Low-Valence Vanadium Oxyhydroxides: Reaction Mechanisms and Polymorphism Control by Low-Temperature Aqueous Chemistry. *Inorg. Chem.* **2016**, *55* (21), 11502–11512. https://doi.org/10.1021/acs.inorgchem.6b02059.

(29) Wu, C.; Dai, J.; Zhang, X.; Yang, J.; Xie, Y. Synthetic Haggite V4O6(OH)4 Nanobelts: Oxyhydroxide as a New Catalog of Smart Electrical Switch Materials. *J. Am. Chem. Soc.* **2009**, *131* (21), 7218–7219. https://doi.org/10.1021/ja9020217.

(30) Scheinost, A. C.; Sparks, D. L. Formation of Layered Single- and Double-Metal Hydroxide Precipitates at the Mineral/Water Interface: A Multiple-Scattering

XAFS Analysis. *Journal of Colloid and Interface Science* **2000**, *223* (2), 167–178. https://doi.org/10.1006/jcis.1999.6638.

(31) O'Day, P. A.; Rehr, J. J.; Zabinsky, S. I.; Brown, G. E. Jr. Extended X-Ray Absorption Fine Structure (EXAFS) Analysis of Disorder and Multiple-Scattering in Complex Crystalline Solids. *J. Am. Chem. Soc.* **1994**, *116* (7), 2938–2949. https://doi.org/10.1021/ja00086a026.

(32) Villalobos, M.; Lanson, B.; Manceau, A.; Toner, B.; Sposito, G. Structural Model for the Biogenic Mn Oxide Produced by Pseudomonas Putida. *American Mineralogist* **2006**, *91* (4), 489–502. https://doi.org/10.2138/am.2006.1925.

(33) Evans, H. T.; Mrose, M. E. A Crystal Chemical Study of the Vanadium Oxide Minerals, Haggite and Doloresite. *American Mineralogist* **1960**, *45* (11–12), 1144–1166.

(34) Evans, H. T.; Mrose, M. E. A Crystal Chemical Study of Montroseite and Paramontroseite. *American Mineralogist* **1955**, *40* (9–10), 861–875.

(35) Crans, D. C.; Tracey, A. S. The Chemistry of Vanadium in Aqueous and Nonaqueous Solution. In *Vanadium Compounds*; ACS Symposium Series; American Chemical Society, 1998; Vol. 711, pp 2–29. https://doi.org/10.1021/bk-1998-0711.ch001.

(36) Howarth, O. W. Vanadium-51 NMR. *Progress in Nuclear Magnetic Resonance Spectroscopy* **1990**, *22* (5), 453–485. https://doi.org/10.1016/0079-6565(90)80007-5.

Appendix 3. Supporting Information for Chapter 4

Section I. Kinetic Adsorption Experiments

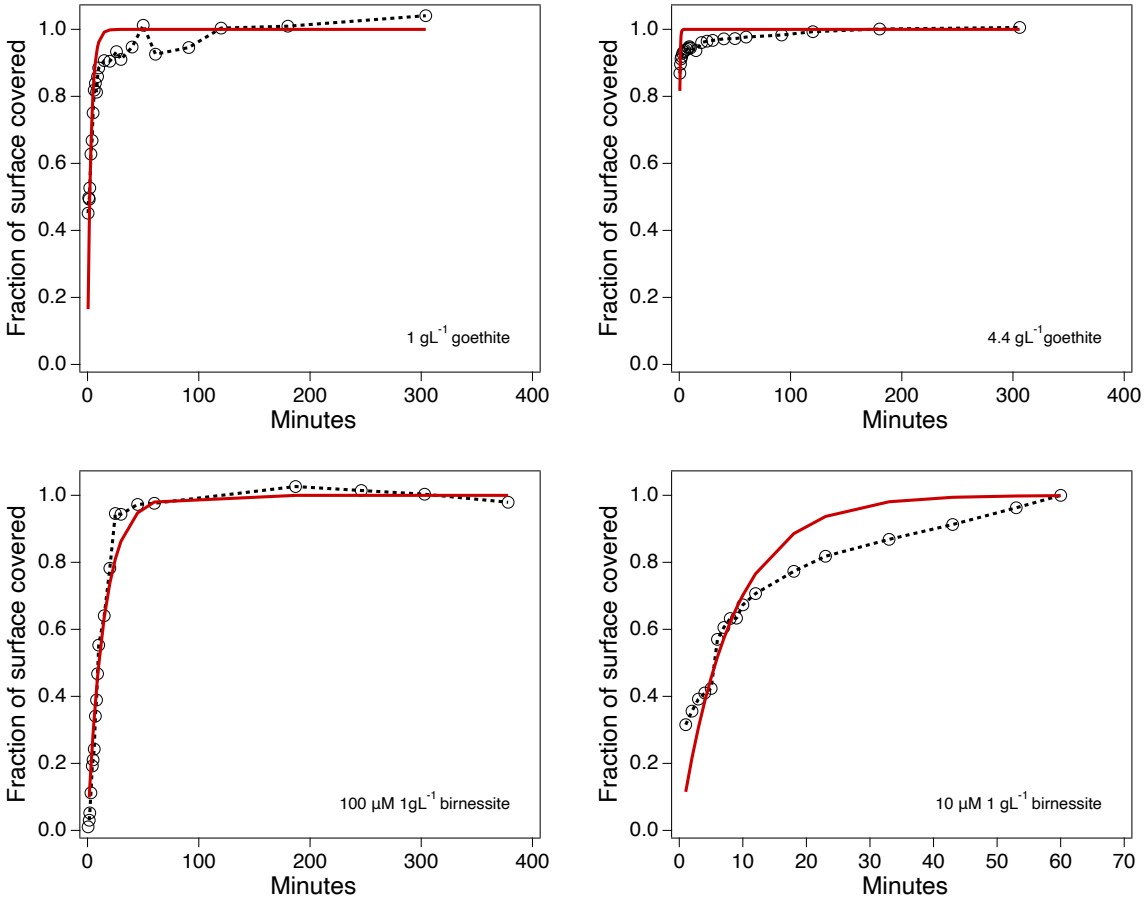

Appendix 3 Figure 4.1 Results from the kinetic adsorption batch experiments. The dotted lines with open circles are the data presented as fraction of total coverage (q_{eq} in the Langmuir equation) and the solid red lines is the application of the Integrated Kinetic Langmuir model.

Section II. Manganese Dynamics

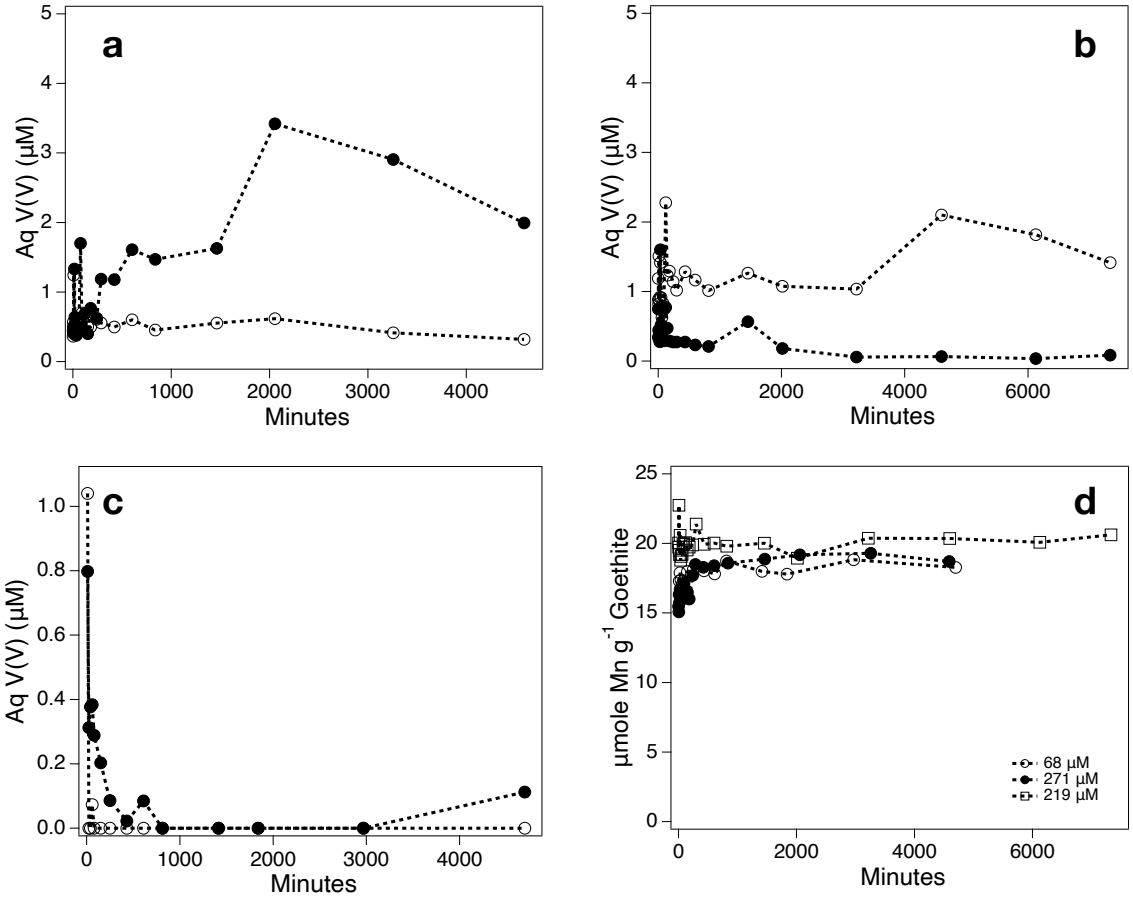

Appendix 3 Figure 4.2 Manganese results from all MnO_2|α-FeOOH multi-chamber reactors. Figures a, b and c are the plots for the aqueous Mn^{II} for the reactors initiated with 271, 219 and 68 µM V^{IV}, respectively. Open circles represent the Mn concentration in the birnessite chamber, while closed circles represent the aqueous Mn in the goethite chamber. Figure d presents the adsorbed Mn in the goethite chamber for all three reactors over time.

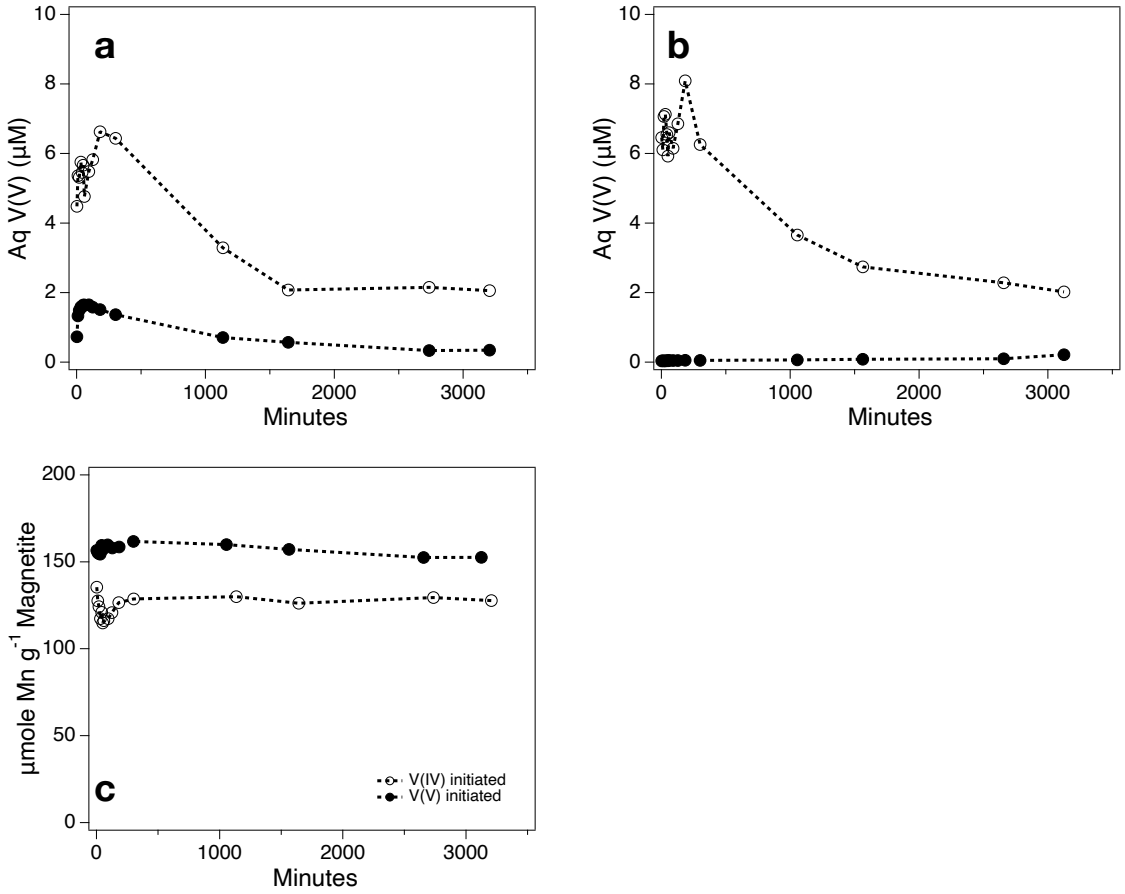

Appendix 3 Figure 4.3 Manganese results from all $MnO_2|Fe_3O_4$ multi-chamber reactors. Figures a and b are the plots for the aqueous Mn^{II} for the reactors initiated with 327 µM of V^{IV} and 369 µM V^{V} respectively. Open circles represent the Mn concentration in the birnessite chamber, while closed circles represent the aqueous Mn in the magnetite chamber. Figure c presents the magnetite-associated Mn for all three reactors over time.

Section III. V EXAFS results for 219 µM V^{IV} birnessite|goethite

Appendix 3 Table 4.1 Results from shell-by-shell nonlinear least squares fitting of the V K-edge EXAFS taken of the 219 µM V^{IV} initiated MnO_2|α-FeOOH reactor end products. CN is the coordination number, R is the interatomic distance, σ^2 is the mean-square relative displacement in the interatomic distance and is a combination of both thermal and static disorder, S_0^2 is the amplitude reduction factor and ΔE is the shift in energy needed to align the theory with the data.

Sample	CN	R(Å)	σ^2 (Å^2) x10^{-3}	S_0^2	ΔE	K range	R-factor	χ^2_{red}
V(V) Birnessite								
V-O	2.2 (2)	1.669 (6)	0.9 (3)					
V-O	1.8 (2)	1.795 (9)	0.9 (3)	0.804	-2.247	3-12.8	0.004	13.5
V-O-O	12	3.14 (2)	1.6 (5)					
V-Mn	2	3.43 (2)	16 (2)					
V(V) Goethite								
V-O	3.0 (6)	1.68 (2)	5.1 (4)					
V-O	1.0 (6)	1.79 (5)	5.1 (4)	0.750 (7)	-3.884	3-12	0.006	30.5
V-O-O	12	3.15 (3)	9.4 (7(					
V-Fe	2	3.33 (2)	15 (3)					

Section IV. Diffusion Control Experiments

Diffusion control experiments were conducted identically to the MnO_2|α-FeOOH reactors. In total, four controls were conducted. Two consisted of V^{IV} or V^{V} added to one chamber at a final concentration of 300 μM and diffusing into an empty chamber, and two consisted of V^{V} being added to one chamber to a final concentration of 100 μM and diffusing into a chamber with 1 gL of birnessite or 4.5 gL^{-1} of goethite. Samples were taken as-is, or filtered through a 0.22 μm PES membrane if mineral oxides were present, acidified to 3% by volume using trace metal grade HNO_3 and analyzed for V using a Perkin-Elmer Optima 7300DV.

The method employed by Ying et al. 2011 was used to determine the diffusion coefficient for vanadate across the 0.1 μm VTCP membrane.[1] The results of the 300 μM Na_3VO_4 diffusion control experiment are presented in figure 4.3. To transform the data in figure 4.3a into S3b, the natural log of the difference between the spiked and empty chambers, divided by 100 is taken (y-axis) and plotted against time (x-axis). The slope of this line is γ, which is used to calculate the diffusion coefficient according to Ying et al. 2011. The slope was found to be $-1.80 \pm 3 \times 10^{-5}$.

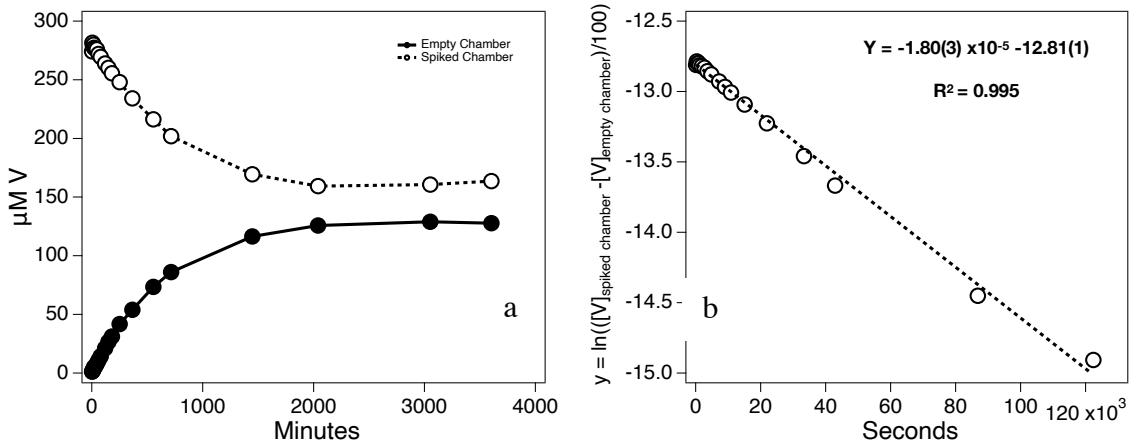

Appendix 3 Figure 4.4 A) Results of 300 μM Na_3VO_4 diffusion across a 0.1 μm VTCP membrane. B) Graphical representation of the determination of γ according to the method of Ying et al. 2011.

Section V. Multichamber Reactor Diagram

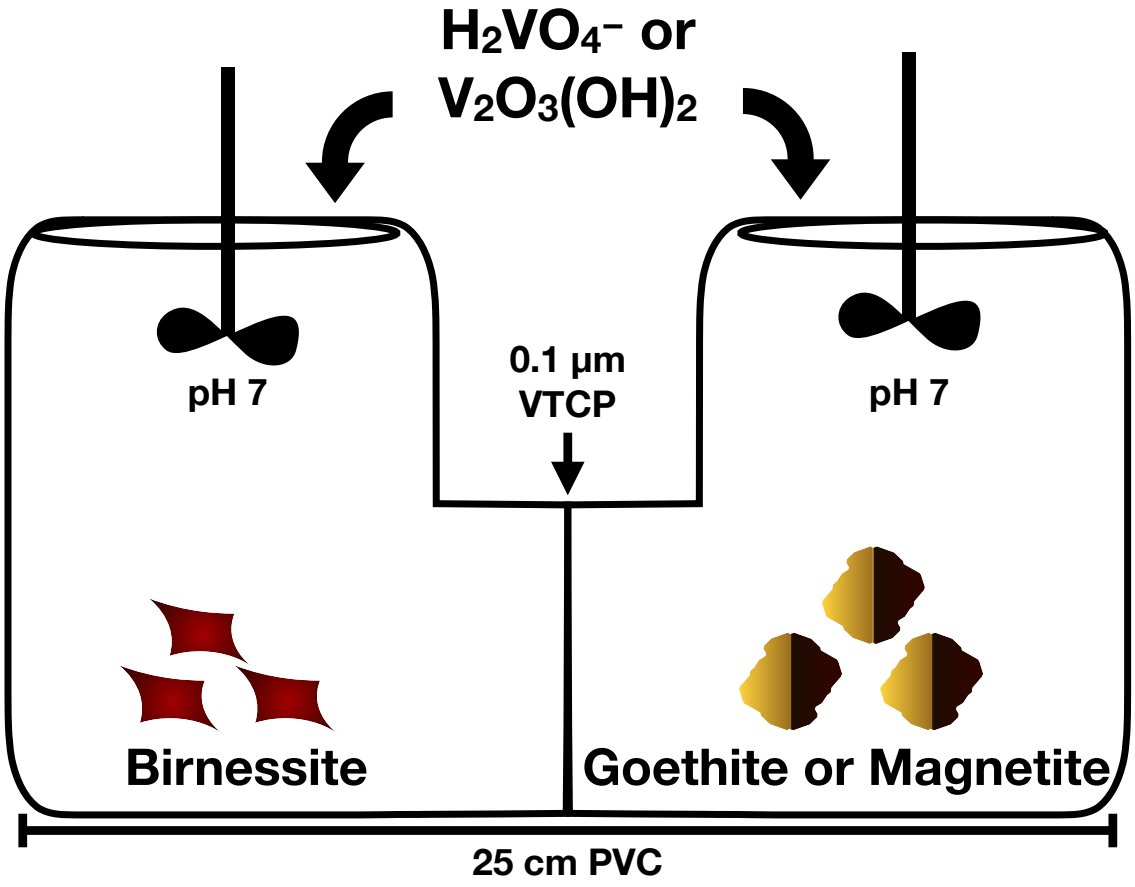

Appendix 3 Figure 4.5 Representation of the multi-chamber reactor.

Section VI. Reference

(1) Ying, S. C.; Kocar, B. D.; Griffis, S. D.; Fendorf, S. Competitive Microbially and Mn Oxide Mediated Redox Processes Controlling Arsenic Speciation and Partitioning. *Environ. Sci. Technol.* **2011**, *45* (13), 5572–5579. https://doi.org/10.1021/es200351m.